UNIVERSIDAD DE GRANADA

Tesis doctoral
Programa Oficial de Doctorado
en Física y Matemáticas (FisyMat)
Junio 2017

A multi-frequency study of the SFHs of galaxies in the integral field area survey CALIFA

[PhD THESIS]

Rafael López Fernández
Instituto de Astrofísica de Andalucía (CSIC)

Memoria de Tesis
presentada en la Universidad de Granada
para optar al grado de Doctor en Física

Directores de tesis:
Rosa González Delgado
Roberto Cid Fernandes

El doctorando, Rafael López Fernández, y los directores de la tesis, Rosa Mª González Delgado y Roberto Cid Fernandes, garantizamos, al firmar esta tesis doctoral, que el trabajo ha sido realizado por el doctorando bajo la dirección de los directores de la tesis y hasta donde nuestro conocimiento alcanza, en la realización del trabajo, se han respetado los derechos de otros autores a ser citados, cuando se han utilizado sus resultados o publicaciones.
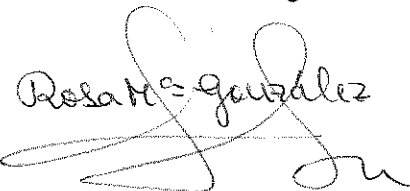
En Granada, a 8 de Junio de 2017

Director/es de la Tesis

Rosa Mª González Delgado   Roberto Cid Fernandes

Fdo.:   Fdo.:

Doctorando

Rafael López Fernández

Fdo.:

Agradecimientos

En primer lugar quiero agradecer a Rosa su confianza, ayuda y orientación durante estos años, sin la que este trabajo no sería posible. Gracias por lo que me has enseñado, por estar siempre dispuesta a escuchar y por ayudarme a resolver todas las innumerables dudas y problemas que han ido surgiendo. Además de su gran calidad científica he sido muy afortunado por tener una directora con tan enorme calidad humana, que me ha apoyado, comprendido y animado en todo este tiempo, tanto en lo relacionado con Astronomía como fuera de ella.

Gracias tambien a Roberto, mi segundo director, por tener la oportunidad de aprender algo nuevo cada vez que conversamos y por tu ayuda todos estos años, tanto a nivel científico como personal.

A todo el grupo de investigación, que me han hecho sentir como en casa. Gracias a Rubén, por su inestimable ayuda y paciencia en mis continuas visitas a su despacho para resolver todo tipo de dudas, y a Enrique, por sus enseñanzas, confianza y apoyo. A André, gran amigo y compañero de despacho durante su estancia en Granada, por todos sus consejos para que los scripts me funcionaran mejor. A Eduardo, por compartir alegrías, tristezas y los increibles desayunos al lado del IAA.

A Clara, quien me guió y ayudó a dar mis primeros pasos en el IAA, y que no ha dejado en todo este tiempo de ser un gran apoyo. Gracias por tantas conversaciones y que siempre acaben con una sonrisa.

A mi compañera Laura, a la que he seguido de despacho en despacho por su enorme apoyo, charlas, risas y cafés. A Miriam, por saber que puedo contar con una amiga más. A mis compañeros de tesis y de despacho: Zaira, Alex, Pablo, Sara y Jesus, con los que tantas horas de trabajo he compartido.

Por último, tengo que agradecer a William su ayuda en estos años. Dejo este agradecimiento para el final porque no se muy bien como expresarlo con palabras. Has sido mi compañero desde el principio de esta aventura y una guía constante en la que apoyarme. Me has resuelto tantos problemas y ensennñado tantas cosas que no hubiera sido capaz de realizar este trabajo sin ti. Muchas gracias además por tu ayuda fuera de la ciencia y del trabajo, siempre dispuesto a ponerme las cosas más fáciles.

Fuera del IAA quiero agradecer a mis compañeros de la Universidad, con los que se fue fraguando el gusto por la ciencia y el ineterés de realizar un doctorado. A Juan Pedro, Esperanza y Mario, por los buenos años estudiando Mateáticas.

Dejo para el final de los agradecimientos a mi familia, por ser el pilar fundamental de mi vida. A mi madre, sin la que no estaría escribiendo estas líneas, y a mi padre, por todo lo que me han ayudado, enseñado y apoyado desde que tengo uso de razón. Nunca podré agradeceros todo lo que me habéis dado. A mis hermanos, mis mejores amigos y con los que siempre puedo contar. A mi abuela Atá, a Ani, a Conchi y a Migue, que con su ayuda incondicional me han ayudado a crecer en todos los aspectos de mi vida. A toda mi familia por estar siempre pendiente de mi y apoyarme.

A Vero, por quererme tanto y ayudarme en estos años. Eres la mejor compañera que puedo tener. Gracias por sacarme siempre una sonrisa, por tu apoyo constante en los momentos difíciles y por hacerme siempre feliz. Te quiero.

Resumen

El estudio realizado en esta tesis se basa en el análisis estadístico de las propiedades de las poblaciones estelares en galaxias, combinando diferentes tipos de datos. Usamos espectroscopía de campo integral proporcionada por los datos de CALIFA e imágenes en el óptico y ultravioleta proporcionadas por SDSS y GALEX, respectivamente. El objetivo principal es obtener la evolución cósmica de la formación estelar y la historia de crecimiento en masa usando información integrada y espacialmente resuelta de galaxias en el Universo cercano.

Los objetos de este estudio es un conjunto de 366 galaxies para las que existen disponibles datos de CALIFA, GALEX y SDSS. Esta submuestra no está sesgada respecto de la muestra madre de CALIFA, incluyendo desde elípticas hasta galaxias espirales de tipo tardío y con $M_\star$ desde 10^9 hasta 8×10^{11} $M_\odot$. La muestra madre de CALIFA puede ser corregida en volumen, así como la submuestra, permitiendo con nuestros resultados estimar la evolución de la densidad de la tasa de formación estelar (ρ_{SFR}), la tasa específica de formación estelar ($sSFR$) y la densidad de masa estelar (ρ_{Mass}) hasta $z > 2$, y la contribución de las regiones centrales (<0.5 HLR) y más externas ($1 < R < 2$ HLR) a estos observables fundamentales en cosmología astrofísica en las galaxias cercanas .

Hemos desarrollado dos metodologías para analizar las propiedades de las poblaciones estalares. El primer método es una nueva versión del código de síntesis espectral STARLIGHT, que permite cualquier combinación de espectroscopía+fotometría, aunque en esta tesis nos centramos en datos de CALIFA+GALEX. El segundo método se basa en determinar las propiedades de las galaxias usando una librería de SFH paramétricas. Los parámetros de la SFH se obtienen ajustando una combinación de fotometría de GALEX+SDSS y los índices espectrales H_β, $[MgFe]'$ y D4000, medidos en los espectros de CALIFA. Los resultados son menos dependientes de la calibración en flujo de los espectros, que fija la forma del continuo óptico, ya que estamos ajustando las bandas de GALEX+SDSS.

Del análsis con STARLIGHT obtenemos que los ajustes puramente ópticos no predicen correctamenta las propiedades UV. Incluyendo fotometría UV en los ajustes, determinamos mejor la contribución de las poblaciones de menos de ~ 300 Myr. Sin embargo, las propiedades de las poblaciones estelares obtenidas con los ajustes ópticos son similares a las obtenidas con ajustes UV+ópticos dentro de las incertidumbres esperadas. Las diferencias se obtienen para las galaxias de baja masa y tipo tardío, aquellos sistemas con una importante presencia de poblaciones estelares de menos ≤ 300 Myr.

La comparación de ρ_{SFR}, ρ_{Mass} y $sSFR$ con estudios cosmológicos indica que un modelo que decae exponencialmente con un cierto retardo respecto al inicio de la formacin proporciona los mejores resultados. Éstos apuntan a un escenario de "downsizing" y sugieren un crecimiento de las galaxias de dentro hacia fuera. Los resultados de ρ_{SFR} indican que la formación estelar a $z = 0$ tiene lugar en las espirales tardías, fuera del las regiones centrales, mientras que para $z > 1$ está dominada por las actuales regiones internas. ρ_{Mass} aumenta desde $z = 5$ hasta $z = 0$, con las regiones externas acretando masa más lentamente que las regiones internas y a lo largo de un mayor período de tiempo. La $sSFR$ decrece conforme el universo evoluciona, estando nuestros resultados de acuerdo con estudios cosmológicos desde $z = 2$ hasta $z = 0$, los cuales indican que $sSFR$ evoluciona como $(1 + z)^2$. Sin embargo, para $z > 2$ nuestra $sSFR$ aumenta con una pendiente menor.

Summary

The study in this thesis is based on the statistical analysis of the stellar population properties of galaxies, combining different kinds of data. In particular we use Integral Field Spectroscopy (IFS) provided by CALIFA data and images in optical and UV range provided by SDSS and GALEX, respectively. The main goal is to obtain the cosmic evolution of the star formation and mass assembly history of galaxies using integrated and spatially resolved information of galaxies in the near Universe.

The objects in this study are those for which CALIFA+GALEX+SDSS data are available. This is a sub-sample of 366 galaxies which is unbiased with respect to the CALIFA mother sample, including from E to late type spirals and with $M_\star$ from 10^9 to 8×10^{11} $M_\odot$. The CALIFA mother sample is not a purely volume-limited sample, but can be "volume-corrected". As the sub-sample is representative of the CALIFA mother sample, our results can be used to estimate the star formation rate density (ρ_{SFR}), the specific SFR ($sSFR$) and the stellar mass density (ρ_{Mass}) up to $z > 2$, and the contribution of central (<0.5 HLR) and outermost regions ($1 < R < 2$ HLR) in nearby galaxies to these fundamental observables in astrophysical cosmology.

We have developed two different methodologies to analyse the stellar population properties of galaxies, which use different kinds of data. The first method is a new version of the full spectral fitting code STARLIGHT, which allows any combination of spectroscopy+photometry, but in this thesis we focus on CALIFA+GALEX data. The second one is based on parametric SFHs, which allows any kind of parametrization. In this thesis nine different models are used. The parameters of the SFH are obtained by fitting a combination of GALEX+SDSS photometry and the spectral indices H$_\beta$, [MgFe]$'$ and D4000, measured in the CALIFA spectra. One advantage of the second methodology with respect to the first one is that the results are less dependent on the spectroscopic flux calibration, which fixes the shape of the optical continuum, because instead we fit the GALEX+SDSS bands.

From the analysis with STARLIGHT we find that purely optical spectral fits are poor predictors of the UV properties. Including UV photometry in the fits, we better constrain the contribution of stellar populations younger than ~ 300 Myr. Despite their poor performance in predicting the UV fluxes, for nearly 90% of our sample the optical fits yield stellar population properties which agree with those obtained with UV+optical fits to within the expected uncertainties. The differences are found in low-mass, late-type galaxies, the systems where, because of their significant ≤ 300 Myr population, one would expect the addition of UV constraints to play a more relevant role.

The comparison of ρ_{SFR}, ρ_{Mass} and $sSFR$ with cosmological studies indicates that a "delayed-τ" model provides the best results. They agree with a "downsizing" scenario, in which massive galaxies form at higher redshift, and suggest an inside-out formation scenario of galaxies. The ρ_{SFR} results indicate that the majority of the star formation at $z = 0$ takes place in late type spirals, outside galaxy centres, while for $z > 1$ it is dominated by the actual inner regions. ρ_{Mass} increases from $z = 5$ to $z = 0$, with outermost regions assembling their mass more slowly than inner regions and over a more extended period of time. The $sSFR$ declines as the universe evolves, being our results in agreement with cosmological surveys from $z = 2$ to $z = 0$, which indicate that $sSFR$ evolves as $(1+z)^2$. However, for $z > 2$ our derived $sSFR$ increases with a lower slope.

Index

1

Introduction

Contents

The light emitted by stars is the best tool to investigate the formation and evolution of galaxies. The study of stellar populations in galaxies started with Baade (1944) identification of two populations of stars in M32 and NGC 205, but a rigorous study of the topic only commenced in the late 60's and early 70's (Tinsley, 1968; Faber, 1972; Searle et al., 1973) with Tinsley's *Fundamentals of Cosmic Physics* article (Tinsley 1980) being particularly influential. Since that time, the number of articles discussing stellar populations has risen rapidly.

This growth has been mainly possible through the development of models for the evolution of stellar populations that have found widespread use in a wide range of astronomical studies, from stellar clusters in the Milky Way to the most distant galaxies in the Universe. To obtain results about the physical properties of the stellar populations, these models are compared to observations using a number of different techniques.

In this chapter we present the astrophysical context for this thesis. In Section 1.1 describes the different galaxy formation scenarios. In Section 1.2 we summarize the stellar evolution processes and describe some features of the spectral energy distribution. Section 1.3 focuses on the method used to derive the stellar population properties of galaxies, the stellar population synthesis technique. Finally, in Section 1.4 we review the different tools that can be used to compare the stellar population models with the observed data.

The main goal of this thesis is to shed some light on the evolution of galaxies by using spatial resolved information that can account for the different galaxy components (disk and bulge) and for the total integrated light. Which models are better for describing the star formation history through the cosmic time? Using two different methods we analyse the star formation history of galaxies as a function of mass and morphological type. To better constrain the contribution of young stellar populations, both methods are able to combine optical data with UV photometry. Considering different models for the star formation history, we investigate which of them are consistent, comparing our results with other well-known observational relations.

1.1   Galaxies

Galaxies are complex systems where gas turns into stars, powered by nuclear reactions that also produce most of the chemical elements. Moreover, a galaxy consists mostly of dark matter, which we know about only by the pull of its gravity. The ages, chemical composition and motions of the stars we see today, and the shapes that they take, tell us about the past lives of galaxies. Thus, analysing the stellar populations we can obtain information about the physical processes that governed the formation and evolution of galaxies.

1.1.1   The Hubble sequence

Galaxies exhibit a wide variety of shapes and the most used morphological classification scheme is the *Hubble sequence* (Hubble 1926). In Figure 1.1 we observe Hubble's original tuning-fork diagram as published in 1936 in his *Realm of the Nebulae* (Hubble 1936). The Hubble sequence consists of four galaxy types: elliptical (E), lenticular (S0), spiral (S or SB), and irregular (Irr):

- Ellipticals: these galaxies are characterized by their ellipticity $e = (a - b/a)$, where a and b are respectively the major and minor axes of the ellipse formed by the projection of the galaxy on the sky plane. They also show a smooth light distribution and are classified as En, where n is a measure of ellipticity which varies between 0 (nearly circular) and 7 (very elongated), and is computed as $n = 10e$.

- Lenticulars: S0 galaxies represent the transition between elliptical and spiral galaxies. They present both an important bulge and a disc component. However, the disc of a lenticular galaxy is very different from that of a spiral galaxy. It presents little gas and almost no star formation occurring. Nevertheless, they don't present spiral arms.

- Spirals: they are composed of a central spherical bulge and a flat disk with spiral arms attached to the bulge. These galaxies can be divided into subclasses (Sa to Sd) with the spiral arms becoming more separated and an increase in the amount of dust in the interstellar medium (ISM). Also the number of young stars increases. Furthermore, these galaxies are divided into two types, depending on the existence of a central bar: normal spirals and barred spirals, which is indicated as SBa, for example.

- Irregulars: Morphologically, these objects are characterized by a lack of a clear nuclei or disc component and by a non-symmetric shape.

The main advantage of the Hubble sequence is that besides following a morphological sequence, galaxies also follow a sequence of physical properties, such as the integrated colour or the amount of gas, and kinematic properties. Furthermore, galaxy morphology is a consequence of the physical processes that govern their formation and evolution. Thus the properties of galaxies along the Hubble sequence can be explained by different histories of star formation.
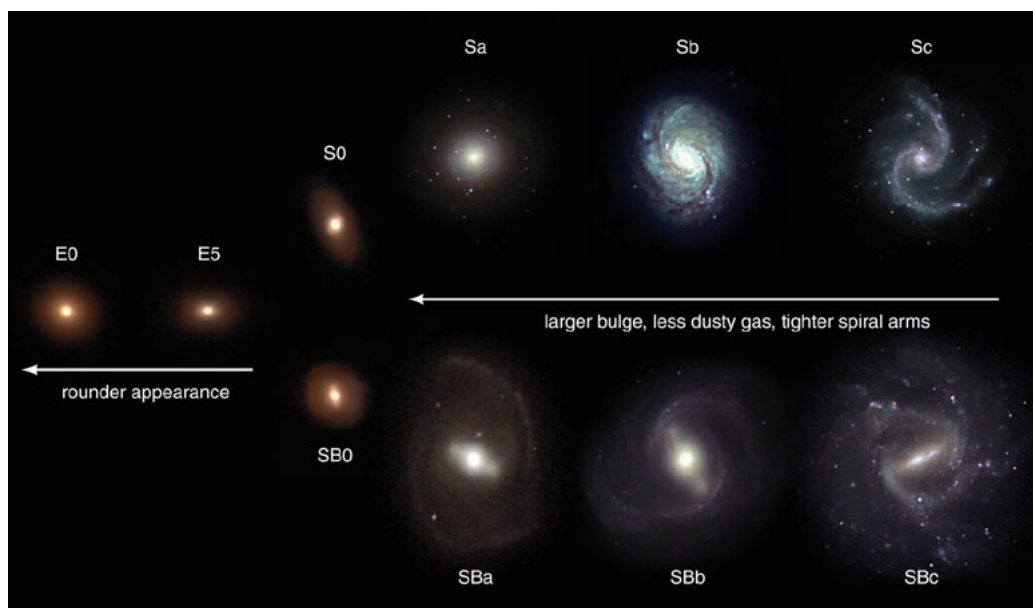
Figure 1.1 Diagram describing Hubble's morphological galaxy classification scheme.

The distinction between ellipticals and spiral galaxies is emphasized in Hubbles tuning-fork diagram, where early-type galaxies lie on the handle of the fork, well separated from spiral galaxies. A known issue of Hubble's classification, however, is that it mostly relies on optical images, from which it is nearly impossible to distinguish thin face-on disks of stars from much rounder edge-on spheroids. For this reason the fraction of disks-like systems hidden in the early-type category has been a matter of debate for decades. The results obtained from the ATLAS^{3D} team, analysing the stellar kinematics, show that the majority of the early-type galaxies in the nearby Universe do not consist of roundish spheroidal objects, but instead has disks, and mostly resemble spiral galaxies with the gas and dust removed. Only a tiny fraction of the early-type galaxies, the "slow rotators", are really spheroids (Cappellari et al., 2001; Krajnović et al., 2011; Emsellem et al., 2001). These results reveal a new paradigm for early-type galaxies which suggest a much closer connection between early-type and spiral galaxies than previously thought, and this will need to be considered in future models of how galaxies form.

1.1.2   The Colour-Magnitude Diagram

Besides the morphological type, galaxies exhibit bimodal distributions in a number of observed properties, such as colours: the blue cloud and the red sequence. This bimodality is seen in the optical colours (Strateva et al., 2001; Blanton et al., 2003), UV-optical colours (Wyder et al. 2007), the 4000 Å break (Dn4000; Kauffmann et al. 2003), and spectral type (Madgwick et al. 2002). The distribution of galaxies in the colour-magnitude diagram (CMD) provides a powerful tool for investigating the evolution of galaxy populations. In fact, morphology and colours are closely related: the blue cloud is mainly formed by late-type, spiral galaxies which are gas-rich and star forming, while the red sequence is formed by gas poor early-type galaxies (ETGs) with quenched star formation and formed by old stars (Trager et al. 2000). Between these two sequences, there is a region called the "green valley", which has been viewed as the crossroads of galaxy evolution. Baldry et al. (2004) explored the distribution of galaxies in the $(u - r)$ versus Mr diagram for low-redshift SDSS samples. Their galaxies separate into "blue cloud" and "red sequence", and the distribution of $(u - r)$ colour at each absolute magnitude bin fits well with the sum of two Gaussians. However, Wyder et al. (2007) showed that the $(NUV - r)$ colour distribution at each Mr can not be fitted well by the sum of two Gaussians due to an excess of galaxies between the blue and red sequences. In Figure 2.2 we observe the distribution of galaxies from a SDSS sample taken from Wyder et al. (2007). Schawinski et al. (2014) also shows that while the early- and late-type galaxies in the green valley exhibit (by selection) similar $u - r$ colours, they have significantly different $NUV - u$ colours. The early-type galaxies exhibit much redder $NUV - u$ colours at the same optical colour than the late types in the (optical) green valley. Thus, galaxies in the green valley region may not be a simple mixture of blue and red galaxies. The galaxies in the green valley were thought to represent the transition population between the blue cloud of star-forming galaxies and the red sequence of quenched, passively evolving galaxies (Bell et al., 2004; Faber et al., 2007; Martin et al., 2007; Schiminovich et al., 2007; Wyder et al., 2007; Mendez et al., 2011; Gonçalves et al., 2012) and the intermediate galaxy colours of green valley galaxies have been interpreted as evidence for the recent quenching of star formation (Salim

et al. 2007).

The CMD bimodality is already in place at z $\sim$ 1 (Cooper et al. 2006), with colour becoming bluer at higher redshift (Blanton, 2006; Willmer et al., 2006). Faber et al. (2007) argued that the number density of blue galaxies is more or less constant from z $\sim$ 1 to 0, while the number density of red galaxies increases. This work supports that the red sequence has grown in mass by a factor of 3 since z $\sim$ 1. A plausible scenario is that the growth of red galaxies was triggered by quenching star formation in blue galaxies, which caused them to migrate into the red sequence (Bell et al. 2004). In addition, galaxies may also be moving from the lower end of the red sequence to the blue cloud through accreting gas-rich dwarf galaxies (Faber et al. 2007). Blue galaxies with star formation being quenched will evolve from the blue cloud to the red sequence, passing through the green valley that thus represents an intermediate phase of this quenching process. Different mechanisms have been proposed for the cessation of star formation in blue galaxies, such as mergers (Bell et al., 2004; Hopkins et al., 2010), AGN feedback (Croton et al., 2006; Martin et al., 2007; Schawinski et al., 2010), morphological quenching (Martig et al. 2009, cold flows accretion and shock heating (Dekel & Birnboim, 2006; Cattaneo et al., 2006). In section 1.1.3 , different scenarios are described for the formation and evolution of galaxies.
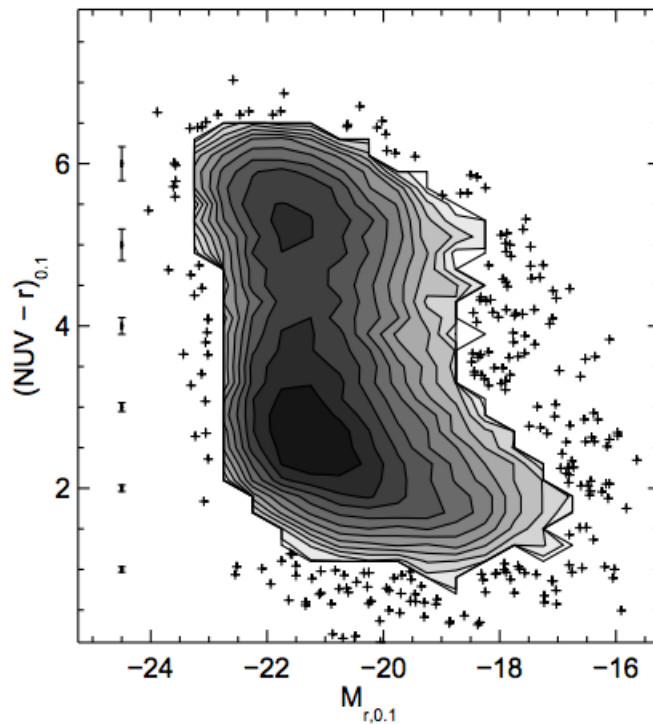
Figure 1.2 The distribution of galaxies from an SDSS sample in M_r vs. $(NUV - r)$. The figure is taken from Wyder et al. (2007).

1.1.3 Formation and evolution

Understanding the formation and evolution of galaxies is one of the most important challenges in Astrophysics. Although significant progress has been made in understanding galaxy evolution, it is

not well known what is the main driver for galaxy assembly. A complete understanding of galaxy evolution would describe the sequence of events that led from the formation of the first stars after the end of the cosmic dark ages to the present-day diversity of forms, sizes, masses, colours, luminosities, metallicities, and clustering properties of galaxies. In fact the balance of galaxies in the Hubble sequence that we observe at high redshift is different from those we observe today. Early observations using a mixture of spectroscopic and photometric redshifts showed that the Hubble sequence was not in place at high redshifts $z > 1$ (van den Bergh et al. 1996) when examined using WFC2 data. When we move to high z the irregular galaxies are more common than spirals and ellipticals. This suggests different processes that organize galaxy morphologies from high redshift toward morphologies we observe today. There are different proposed mechanisms, with merging and accretion being the most important.

Nowadays the most accepted cosmological model is the so called ΛCDM (Lambda-Cold Dark Matter) model. Following this model, primordial density fluctuations grow by gravitational instability, driven by cold, collisionless dark matter, leading to a "bottom-up" scenario of structure formation (Peebles 1982). According to this model, structures grow by the successive fusion of dark matter halos. These halos increase the baryonic matter overdensities, producing the first baryonic structures. In these halos the first stars are formed, which are metal-free and very massive ($> 100\ M_\odot$) (Abel et al., 2002; Bromm & Larson, 2004). These stars live for a short time and explode in very energetic supernova, which may destroy the halo and disperse their metals through the Universe. The next stars formed would be more metal rich and less massive. The death of these stars as a supernova would not destroy the halo, producing the formation of larger gravitational structures inside the halo.

On the other hand, Milky Way-like galaxies and galaxies of lower mass seem to have formed from streams of cold gas. In this contrasting picture, gas from cosmic web filaments flows directly onto galactic disks forming at the filamentary intersections. The narrow streams of cold gas deliver fuel for star formation.

The star-formation process within galaxies is critical, as galaxies do not exist without stars. Thus, there is a link between star formation and galaxy structure. In fact, the different galaxies along the Hubble sequence show different stellar population properties. So, investigating the star formation history of galaxies is fundamental for understanding the growth and evolution of galaxies. There are fundamental observational results related to the stellar mass assembly of galaxies:

1. The evolution of the star formation rate density ($SFRD$) is well known (Figure 1.3). There is a peak around $z \sim 2$ and from this peak to today the star formation rate density decreases by a factor 10 (Hopkins & Beacom, 2006; Fardal et al., 2007; Madau & Dickinson, 2014). Also it seems to be, but is less well documented, that from this peak towards the early epoch of the Universe the star formation rate density declines.

2. sSFR (sSFR $\equiv$ SFR/$M_\star$) describes the fractional growth rate of stellar mass in a galaxy or, equivalently, the ratio of current to past star formation. Figure 1.4 shows the evolution of sSFR (in Gyr^{-1}) with redshift. For $z \leq 2$ the globally averaged sSFR declines rapidly (Rodighiero et al., 2010; Oliver et al., 2010; Karim et al., 2011; Elbaz et al., 2011; Speagle et al., 2014), while it slowly increase at $z > 2$ (Magdis et al., 2010; Stark et al., 2013).
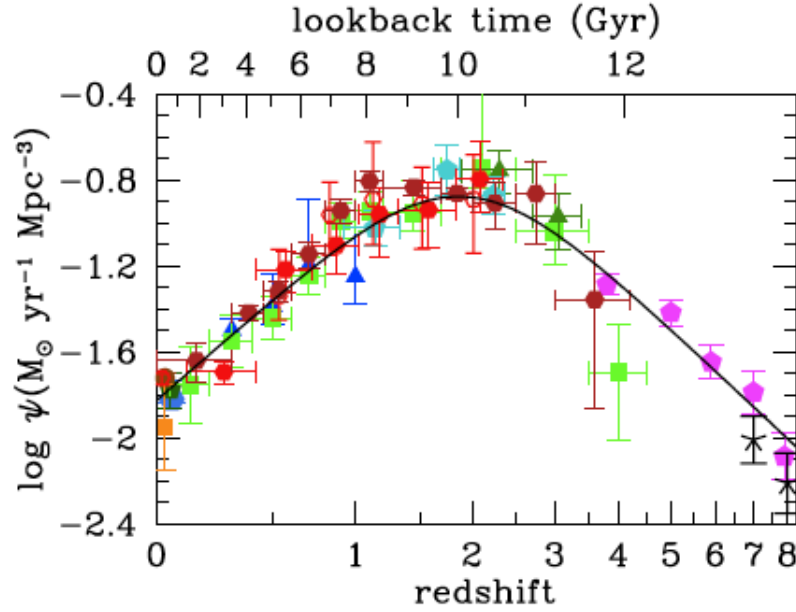
Figure 1.3 The history of cosmic star formation. This Figure is taken from Madau & Dickinson (2014).
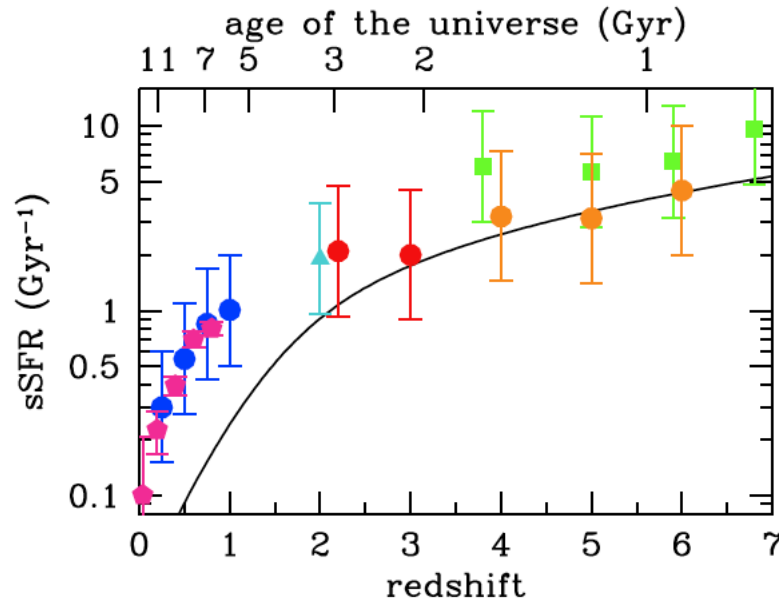
Figure 1.4 The evolution of specific star-formation rate (sSFR $\equiv$ SFR/$M_\star$). This Figure is taken from Madau & Dickinson (2014).

3. In Figure 1.5 we observe the evolution of stellar mass density ($\rho_\star$). There is a strong rise in the mass build-up between $z \sim 7$ and $z \sim 1$. However, from $z \sim 1$ to the present, the mass build-up is more moderate (Gallazzi et al., 2008; Li & White, 2009; Moustakas et al., 2013).

What produces the evolution in the SFRD, sSFR and $\rho_\star$? It seems that some physical processes are required to suppress star formation. There are different points of view. One of them is to assume that
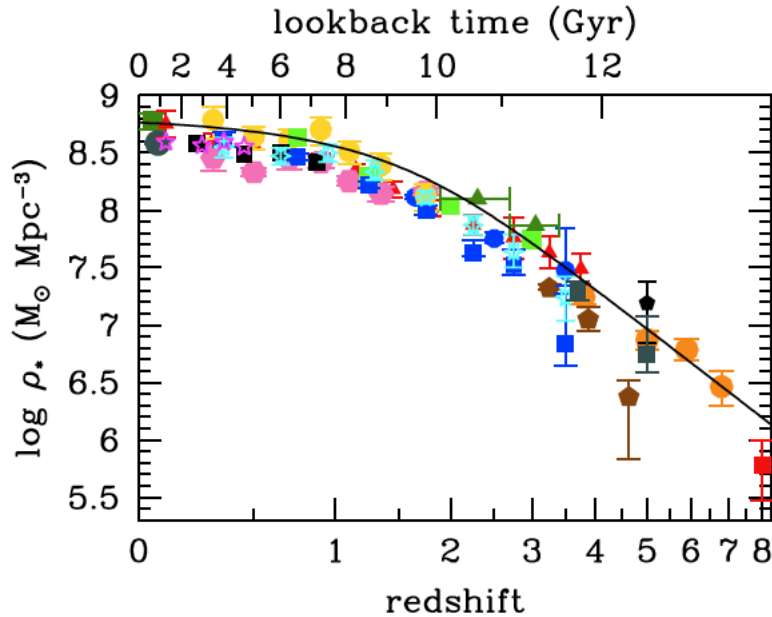
Figure 1.5 The evolution of the stellar mass density. This Figure is taken from Madau & Dickinson (2014).

the growth of galaxies is a uniform phenomenon that is interrupted by internal or external quenching processes. For example feedback from supernova (SN) or AGN can cause the suppression of gas accretion onto galaxies.

An alternative view is to consider that galaxy growth is a more heterogeneous phenomenon as suggested by the different star formation histories (SFH) obtained from different surveys (Gladders et al., 2013; Oemler et al., 2013; Dressler et al., 2016; Abramson et al., 2016).

The SFHs most commonly used in the literature are exponentially-decaying burst (Maraston et al. 2010), although these parametrizations are not able to explain the behaviour of the SFR for $z > 2$. There are, however, other declining SFHs or "delayed-τ" models (Sandage, 1986; Steinhardt et al., 2014; Moustakas et al., 2013) which allow early linear growth followed by a later exponential decline. Other studies at high redshift, have advocated rising SFHs as better functional fits, such as exponentially-rising SFHs (Maraston et al., 2010; González et al., 2012), power-law-rising SFHs (Papovich et al., 2011; Smit et al., 2012) and linearly-rising SFHs (Lee et al. 2010). Also a lognormal function has recently been proposed to fit the SFHs observed in galaxies (Gladders et al. 2013).

Besides high redshift studies, the SFH of the Universe can be inferred using the present day fossil record of galaxies. This is the approach used in this thesis, which is described in Section 1.3.

1.2   The light of stars

1.2.1   The spectral energy distribution

Galaxies emit radiation across the full electromagnetic spectrum and most of the energy is emitted in the ultraviolet, optical and infrared spectral ranges. This emission comes from stellar radiation, either

direct or reprocessed by gas and dust in the ISM.

In the past, when only ground-based telescopes were available, observations of galaxies were limited to optical and near-infrared wavelengths. But in the past few decades, thanks to improvements in observational technology and the launch of space telescopes, ultraviolet and infrared observations have become available. These observations have brought new insights into the physical processes occurring in galaxies. Nowadays, observations at ultraviolet, optical and infrared wavelengths are becoming available for large samples of galaxies (e.g., Galaxy Evolution Explorer (GALEX), Sloan Digital Sky Survey (SDSS), Calar Alto Legacy Integral Field Area Survey (CALIFA), Two Micron All Sky Survey (2MASS)).

To constrain the stellar populations and ISM of galaxies from these multi-wavelength observations requires a consistent modeling of the emission by stars, gas and dust. The stellar emission of galaxies dominates the galactic spectral energy distributions at ultraviolet, optical and near-infrared wavelengths. The total stellar spectrum of a galaxy is a result of the contribution by all the individual stars of which it is comprised. Therefore, to interpret observed galactic spectra, we need to understand the stellar population of a galaxy (composed of stars of different masses, chemical compositions and ages) and follow the evolution of the different stars over time.

Many of the fundamental properties of stellar populations are encoded in their spectral energy distributions (SEDs). These properties include the star-formation history (SFH), stellar metallicity and abundance pattern, stellar initial mass function (IMF), total mass in stars, and the content of dust and gas. Some of these properties are easier to measure than others, and each provides important clues concerning the formation and evolution of galaxies.

The Lick Indices

When high resolution spectra are available, it is possible to analyse the individual absorption lines. Fitting the stellar evolution models to the lines, it is possible to obtain the properties of the stellar populations of galaxies. A problem with this method is defining the continuum to measure the absorption of the lines. Burstein et al. (1984) and Faber et al. (1985) suggested that instead of attempting to estimate the true continuum, a pseudo-continuum should be established by taking regions of the spectrum from either side of the absorption line. The pseudo-continuum allows the strength of the feature to be studied independently of dust extinction or spectrophotometric calibration errors. This study was originally done for 21 absorption lines and are named the Lick indices, due to the Lick Observatory where they were observed. The problem with this technique is that it does not take into account the shape of the continuum, which provides a useful information about stellar properties.

The 4000Åbreak

It is a sharp discontinuity at 4000Å that can be produced by two sources: blanket absorption of high energy radiation from metals in the stellar atmospheres, and the lack of hot blue stars. The feature is known as the 4000Å break and was formalized as an index by Bruzual A. (1983). He found that the index was best estimated in a similar way to the Lick indices, by estimating the pseudo-continuum

level either side of the break. This formal determination of the break is known as $D4000$, and is used as an age indicator of the stellar population, although is affected by the presence of metals. This index, when combined with other indicators, is very useful for breaking the metallicity degeneracy (Kauffmann et al. 2003).

UV continuum

New stellar populations emit radiation over the broad spectrum. Low-mass stars dominate the mass integrated over the whole stellar population, but at young ages the luminosity is dominated by ultraviolet emission from massive stars. These stars have short lifetimes, so UV emission fades quickly. For this reason, UV luminosity is regarded as a good tracer of the formation rate of massive stars. On the other hand, the UV luminosity output by a stellar population also depends on its metallicity. In general, less-metal-rich stars producing more UV light and the amplitude of this effect is not insignificant.

The greatest drawback for UV measurements of star formation is the obscuring effect of dust. Extinction is strong in the UV, so even modest amounts of dust can dramatically suppress the emerging UV flux. Dust re-emits the absorbed energy in the IR. The UV measurements need to be corrected for the effects of dust absorption, or the absorbed energy can be measured directly through IR emission if a whole set of data is available.

There are some empirical relations to correct the UV luminosity from the extinction, which relate A_V with colour $FUV - NUV$ (Meurer et al., 1999; Calzetti et al., 2000; Seibert et al., 2005; Muñoz-Mateos et al., 2009; Overzier et al., 2011). When using only UV photometry, these relations are very useful for correcting the observed data, but in this thesis we follow a different technique. As a combined UV + optical analysis is developed, we introduce A_V as a free parameter in the code, which is fitted to match both the optical and UV data. Thus it is not necessary to perform any extinction correction on the data.

1.2.2 Stellar evolution

In this section we give a very brief summary of the main features of stellar evolution. The life time of a star depends mainly on its mass. The more massive a star is, the higher the energy production rate it requires to remain in equilibrium. These stars consume fuel for the production of energy quicker than lower-mass stars. Thus, the life time of low mass stars is longer than those for high mass stars. As the evolution of stars depends on their masses, here we summarize the different stages of the evolution of stars according to the initial masses. In Figure 1.6 we show the Hertzsprung-Russel (HR) diagram with the evolutionary tracks for stars with different masses. To interpret the total emission of galaxies it is crucial to understand the evolution of stars in the HR diagram.

- **Very low-mass stars** ($\leq 0.25\ M_\odot$): They have a very slow evolution; these stars have convective interiors and can reach lifetimes of 13 Gyr. Therefore, the core is continuously being recycled with hydrogen coming from the outer layers, and they can convert all the initial hydrogen into helium. When hydrogen is exhausted in the stars, they begin to contract. Due to the low stellar mass, the gravitational energy released during the contraction is not enough to make the

central temperature reach high enough values to start He-burning reactions. After the hydrogen burning these stars cool down and become white dwarfs. These stars radiate most of the energy at optical wavelengths.

- **Low-mass stars** ($\leq 2M_\odot$) A star with initial mass around 1 $M_\odot$ spends about 10 Gyr on the main sequence. When a star exhausts the hydrogen in its core, it leaves the main sequence and begins to fuse hydrogen in a shell outside the core. The core increases in mass as the shell produces more helium. The star expands and becomes a Red Giant, which is named the "red giant branch" (RGB). At this stage the star can be hundreds of times larger than it was when it first entered the main sequence. RGB stars have high luminosities and they radiate mainly at near-infrared wavelengths due to their cool temperatures. The helium core becomes more and more dense as material is added to it, and so the temperature increases, eventually reaching the minimum temperature to start burning He (i.e. about 10^8 K). The star migrates to the horizontal branch on the HR diagram, gradually shrinking in radius and increasing its surface temperature. After a star has consumed the helium at its core, hydrogen and helium fusion continues in shells around a hot core of carbon and oxygen. The star follows the asymptotic giant branch (AGB) on the HR diagram, paralleling the original red giant evolution, but with even faster energy generation (which lasts for a shorter time). Although the AGB phase is relatively short, it is crucial to understand this stage of stellar evolution in order to interpret the spectral energy distributions of star-forming galaxies, since AGB stars contribute significantly to the near-infrared emission of galaxies. Although helium is being burnt in a shell, the majority of the energy is produced by hydrogen burning in a shell further from the core of the star. When the He shell around the core runs out of fuel, the "thermally-pulsating AGB" (TP-AGB) phase begins. They are not sufficiently massive to start carbon fusion, so they contract again, going through a period of post-asymptotic-giant-branch superwind forming a planetary nebula. At the centre of this nebula remains the core of the star, which cools down to become a white dwarf. The nebula keeps expanding until it dissipates in the interstellar medium.

- **Intermediate-mass stars** ($\sim 2-7M_\odot$). In this range, a star needs to produce more energy than a solar-mass star while on the main sequence to remain in hydrostatic equilibrium. Therefore, it burns H in the centre at a faster rate and the effective temperature and luminosity are higher. These stars go through the RGB, horizontal branch, AGB and TP-AGB phases, but the processes occur faster than for low-mass stars. As in the case of solar-mass stars, thermal pulses cause strong stellar winds and the star loses a large part of its mass. During this time, the carbon core keeps contracting. If the temperature reaches high enough values to ignite carbon, the star will undergo a "carbon flash", leading to a supernova explosion. If the temperature is too low, the star loses its outer layers as a planetary nebula and the core cools down as a white dwarf. The initial mass and chemical composition of the star, and the total mass lost during its evolution, determine which of the two scenarios occurs. In either case, the star returns material to the interstellar medium at the end of its life.

- **High-mass stars** ($\geq 7M_\odot$). The evolution of the most massive stars is extremely rapid with

lifetimes of typically a few Myr. These very hot stars radiate huge amounts of energy particularly in the ultraviolet range. Due to their rapid evolution, theses stars are very complex to model.

Because of the high mass, the star can reach high enough temperatures for C-burning reactions. When the central C gets exhausted, the core contracts again and the next reactions, burning O, Mg and Ne all the way to Fe, occur very quickly until the star consists of a compact core of iron with surrounding shells burning lighter elements. The nucleus of the Fe atom has a much higher binding energy than lighter elements. Thus, the star is incapable of continuing to produce energy in the core, and the core collapses gravitationally to extremely high density and explodes violently as a supernova. The outer layers of the star are returned to the interstellar medium, and the core remains as a neutron star.

If the mass of the stellar remnant is high enough, the neutron degeneracy pressure will be insufficient to prevent collapse below the Schwarzschild radius. The stellar remnant thus becomes a black hole. The mass at which this occurs is not known with certainty, but is currently estimated at between 2 and 3 $M_\odot$.
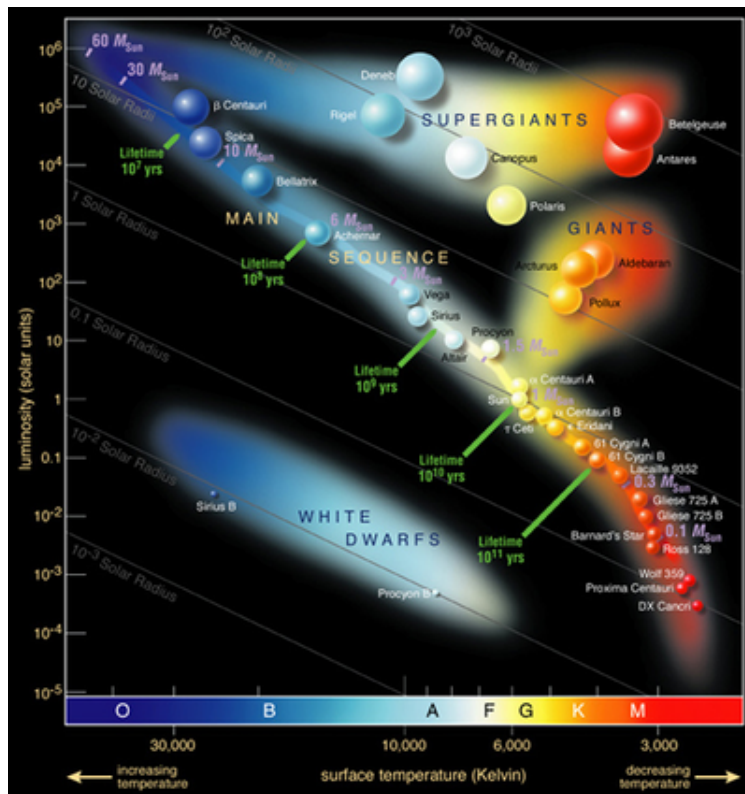
Figure 1.6 Evolutionary tracks in the HR diagram for three model stars with low (1 $M_\odot$), intermediate (5 $M_\odot$) and high (25 $M_\odot$) initial masses. The tracks start at the zero-age main sequence and end at the remnant stage. The heavy portions of each curve define locations where major nuclear burning phases occur. Figure created by the European Southern Observatory.

1.3 Stellar population synthesis

The stellar population synthesis technique is a powerful tool for interpreting the SEDs of galaxies and for extracting stellar population properties. A lot of work has been done to extract information from the SEDs of galaxies, exploiting information from the far-ultraviolet (FUV) to the far-infrared (FIR). The first attempts to interpret integrated galaxy spectra in terms of the stellar content of galaxies tried to reproduce the observed spectra using linear combinations of individual stellar spectra of different types (Faber, 1972; Turnrose, 1976). More recently, widely-used models have been based on the evolutionary synthesis technique (Tinsley, 1978; Bruzual A. & Charlot, 1993; Bressan et al., 1994; Worthey, 1994; Leitherer & Heckman, 1995; Maraston, 1998; Vazdekis, 1999; Bruzual & Charlot, 2003), which is the tool used in this thesis. Two different approaches can been used based on this technique which will be explained in the next sections.

Although a great effort has been made to extract information from the whole spectral range, the UV and IR spectral windows are rather more difficult to reproduce owing to the obscuring effects of the atmosphere. However, numerous balloon and space-based observatories have opened up the UV and IR to detailed investigations. In these spectral regions dust plays a major role; it absorbs and scatters much of the UV light emitted by stars and re-radiates that energy in the IR. In young stellar populations the UV is dominated by hot massive stars, whereas in old stellar populations the UV can be influenced by hot evolved stellar types (O'Connell 1999).

In this thesis UV and optical data are combined. Low level ongoing star formation may leave weak/undetectable imprints in the optical continuum of a galaxy while at the same time accounting for most of its UV flux. Clearly, a combined optical + UV analysis would lead to better estimates of a galaxy's star formation history (SFH).

1.3.1 Simple Stellar Population

A simple stellar population (SSP) describes the evolution in time of the SED of a single, coeval stellar population at a single metallicity and abundance pattern. Three basic inputs are required to make an SSP: isochrones, stellar spectral libraries, and an IMF. In Chapter 3 the different components are described. These components are combined in the following way:

$$f_{\mathrm{SSP}}(t, Z) = \int_{m_{\mathrm{low}}}^{m_{\mathrm{up}}} f_{\mathrm{star}}[T_{eff}(M), log\, g(M)|t, Z]\Phi(M)dM$$

where M is the initial stellar mass, $\Phi(M)$ is the IMF, f_{star} is a stellar spectrum, and f_{SSP} is the final SSP spectrum, which depends on the age and metallicity. m_{low} and m_{up} are the lower and upper limit of integration. The lower limit is usually taken to be the hydrogen burning limit (either 0.08 or $0.1 M_\odot$, depending on the models), and the upper limit is dictated by stellar evolution. The isochrones determine the relation between T_{eff} , $log\, g$, and M for a given t and Z.

1.3.2 Composite Stellar Populations

In this section the composite stellar populations (CSPs) are presented. They differ from simple ones in three respects: (a) they contain stars with a range of ages given by their SFH ; (b) they contain

stars with a range of metallicities as given by their time-dependent metallicity distribution function, P(Z, t); and (c) they contain dust. These components are combined in the following way:

$$f_{CSP}(t, Z) = \int_0^t \int_0^{Z_{max}} \text{SFR}(t') f_{\text{SSP}}(t', Z) e^{-\tau(t')} P(Z, t) \, dZ \, dt'$$

where the integration variables are the stellar population age, t', and metallicity, Z; and τ is the dust optical depth. Several SFHs are usually adopted: exponential decaying models, rising models, τ-delayed models, constant models or any combination of thereof. Although in the previous definition of a CSP metallicity was integrated, the treatment of metallicity in CSPs is usually more simplistic than the treatment of SFRs. Usually, the P(Z, t) function in the previous equation is replaced by a δ-function, which means using a single metallicity for the entire composite population. In Figure 1.7 we can observe the complete process to obtain an SSP and a CSP.

1.4 Fitting Models to Data

To measure the physical parameters of stellar populations using the stellar population synthesis technique, it is necessary to fit the models to data, either in the form of broadband SEDs, moderate-resolution optical/NIR spectra, or spectral indices. The fitting techniques are usually based on a $\chi 2$ minimization technique. As the number of parameters increases, Markov Chain Monte Carlo techniques become increasingly more efficient (Conroy et al., 2009; Acquaviva et al., 2011).

There are two different approaches to reproducing the observed data. The first one is assuming a prior about the shape of the star formation history (parametric method). Another approach is to find the best combination of SSPs which fit the observed data, without any assumption on the SFH (non-parametric method). In this thesis we explore both approximations.

This process works upon data that often consist of multi-band photometry, preferably covering as much of the spectral energy distribution as possible, for instance GALEX plus SDSS (Kaviraj et al., 2007b; Salim et al., 2007; Schiminovich et al., 2007; Schawinski et al., 2014) or 2MASS magnitudes (Barway et al. 2013). At other times the input is spectroscopic, such as optical spectra provided by the SDSS. Methods to analyse F_λ split into those which reduce F_λ to a set of spectral indices and those which attempt to fit it λ-by-λ (see Walcher et al. (2011) for a comprehensive review). Because of the informative nature of absorption and emission lines spectroscopy is in principle more powerful than photometry. Purely spectroscopic studies, however, are invariably limited in λ-coverage, and hence limited in the ability to exploit stellar population information encoded over long λ baselines more easily covered with multi-band photometry.

Tools for retrieving stellar population properties out of multi-band photometry are common in the literature (e.g. the CIGALE code of Noll et al. (2009)).

On the other hand, methods which mix photometric and spectroscopic information are less common in the literature. One of these works is presented by Schawinski et al. (2007), which fits a combination of UV to IR photometry with Lick indices derived from SDSS spectra. In this thesis we explore the combination of UV and optical data obtained from different surveys (GALEX, SDSS and CALIFA) to retrieve the SFH of galaxies.
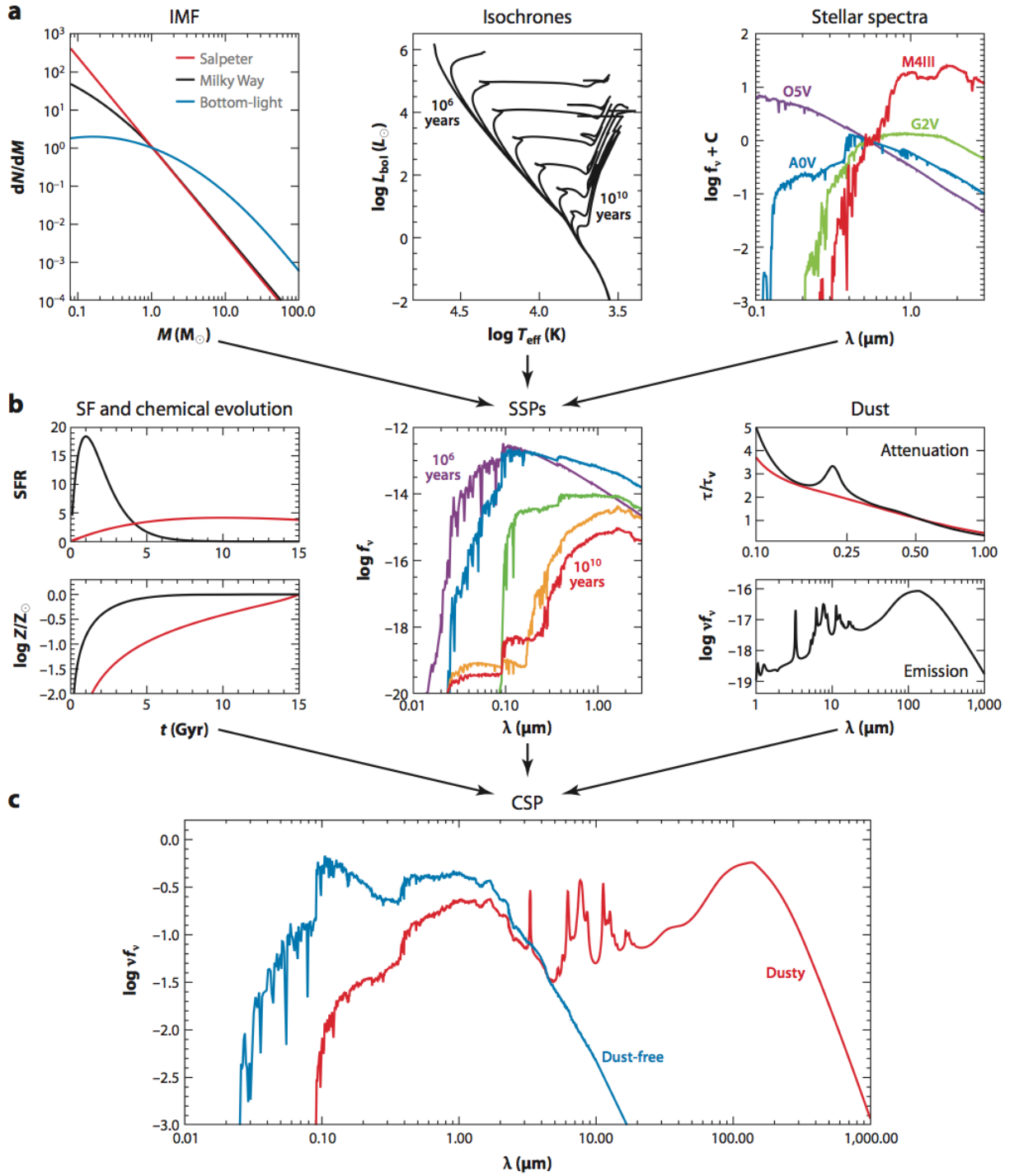
Figure 1.7 The complete process of constructing SSPs and CSPs. Figure taken from Conroy (2013).

1.4.1 Parametric SFH

This technique is based on the assumption of a prior about the parameters that define the SFH. Several studies have been done regarding the functional form one should adopt. Exponentially decaying models are the most commonly used in the literature, but also τ-delayed models or constant SFR. Recently, some studies have shown that for high redshift galaxies models with rising SFHs tend to provide a

better fit to observed high-redshift SEDs and produce SFRs in better agreement with other indicators (Lee et al., 2010; Maraston et al., 2010; Wuyts et al., 2011). Also the form of the rising SFHs has been discussed without any conclusion about the best choice. Pforr et al. (2012) advocated exponentially increasing SFHs, whereas Lee et al. (2010) advocated delayed τ models of the form SFR $\propto te^{-t}$.

A problem when analysing the SED is that the young stars, being so bright, tend to outshine the older, less luminous stars (Papovich et al. 2001). Some authors have found that this effect results in underestimated stellar masses when single-component SFH models are used (Daddi et al., 2004; Shapley et al., 2005; Lee et al., 2009; Pforr et al., 2012). In this thesis both single component models as well as more complex models that combine two components are explored. In both cases, when using a single or a more complex SFH, the results are sensitive to the influence of the prior.

Also, it is possible to use a technique that was introduced by Finlator et al. (2007), which consists of using a library of SFHs drawn from semianalytic or hydrodynamic models of galaxy formation. This technique has the advantage that the model SFH library is more likely to contain realistic SFHs (with rising and falling SFHs, multiple bursts, etc.). The results are also sensitive to the prior, which in this case is the reliability of the model in producing a realistic range of SFHs.

1.4.2 Nonparametric Star-Formation Histories

The codes based on nonparametric SFHs have the advantage of removing the systematic effects introduced by the assumption of the prior regarding the SFH. An example is STARLIGHT (Cid Fernandes et al. 2005), used in this thesis. Also, there are other groups that have used this approach for e.g.: MOPED by Heavens et al. (2000), STECMAP by Ocvirk et al. (2006), VESPA by Tojeiro et al. (2007), ULySS by Koleva et al. (2009). These methods have been tested and are capable of recovering complex SFHs ((Ocvirk et al., 2006; Tojeiro et al., 2007; Koleva et al., 2009; Cid Fernandes et al., 2014). But also the data quality has to be good: a wide wavelength coverage, high spectral resolution, and high S/N (typically > 20 Å^{-1}) are required in order to recover properly complex SFHs.

1.5 This work

In this thesis we present a new version of the STARLIGHT synthesis code, which combines photometry with a full λ-by-λ analysis. We focus on UV photometry from GALEX and optical spectra from CALIFA. This version is described in Chapter 4. Using SSPs, STARLIGHT combines the models to reproduce the observed data for deriving the stellar population properties. On the other hand, we use a parametric method based on CSPs to derive the stellar population properties, which is described in Chapter 5. We combine multi-band photometry (from GALEX and SDSS) with some spectral features from CALIFA data (H_β, $[MgFe]'$ and $D4000$).

Few comparisons have been made between different techniques, for instance nonparametric methods with more conventional techniques. Tojeiro et al. (2009) compared SFRs estimated with VESPA to emission line-based SFRs from Brinchmann et al. (2004). Also Sánchez et al. (2016b) compares different methods analysing CALIFA galaxies. We have analysed the same sample of galaxies using both methods which allow us a consistent comparison of the results, which is detailed in Chapter 6.

2

Sample and data processing

Contents

2.1 Introduction

The study in this thesis is based on the statistical analysis of the stellar populations properties of galaxies, combining different kinds of data. In particular we use Integral Field Spectroscopy (IFS) provided by CALIFA data and images in optical and UV range provided by SDSS and GALEX.

The IFS allows us to gather spectra of the sky over a two-dimensional field-of-view, obtaining a datacube with axes of x, y (the two spatial axes) and wavelength. IFS solves the main disadvantages of traditional long-slit and allows us to obtain high S/N spectra applying a suitable spatial binning. An integral field spectrograph consists of two components: the spectrograph, that separates light into different wavelengths, and an integral field unit (IFU), that divides the 2D spatial plane to obtain spectra from different spatial positions. The 2D spatial division can be done using lenslet array, fibres (with or without lenslets) and image-slicer. The elements of the IFU are often called 'spatial pixels' (or 'spaxel'). The IFS provides information to analyse the spatially resolved properties of galaxies, studying inner and outer parts, computing gradients, radial profiles and obtaining 2D images. Also we can analyse the integrated properties through a spectrum containing information from the whole galaxy.

The sample in this thesis contains 366 galaxies from the CALIFA (Sánchez et al. 2012 survey sample for which GALEX and SDSS images are available . Figure 2.1 shows the morphological distribution of our 366 galaxies (filled bars), as well as that of the mother sample (empty bars). Hubble types are labelled with a brown-to-blue (ellipticals to late type spirals) colour palette, which is used throughout this thesis. The similarity of the two distributions ensures that our subsample is a fair representation of the mother sample. This is an important aspect because it allows us to apply the volume corrections derived by Walcher et al. (2014) to extend the statistical results presented here to those of the galaxy population as a whole.

Figure 2.2 shows the $u - r$ versus Mr CMD, grey points represent the mother sample and colored points the galaxies in our sample. The figure shows that these 366 galaxies cover the whole CMD, ranging from early to late types galaxies, being a representative subset of the CALIFA sample as whole. In this chapter we describe the different data set used in this thesis and the methodology used to combine them.

2.2 CALIFA spectroscopy

The Calar Alto Legacy Integral Field Area (CALIFA) survey is a large project of the Centro Astronómico Hispano Alemán at the Calar Alto observatory to obtain spatially resolved spectra for 600 local ($0.005 < z < 0.03$) galaxies by means of IFS. CALIFA observations started in June 2010 with the Potsdam Multi Aperture Spectrograph (PMAS, Roth et al. 2005), mounted at the 3.5m telescope, employing the PPak wide-field IFU (Roth et al., 2005; Kelz et al., 2006). This project provides high quality spectra over a wide, hexagonal field of view of $72'' \times 64''$ (331 science fibres with a fibre size of $2.7''$), with a final sampling of 1 arcsec per pixel and PSF $\sim 2.5''$ (García-Benito et al. 2015). A diameter-selected sample of 939 galaxies were drawn from the 7th data release of the Sloan Digital Sky Survey (SDSS, Abazajian et al. 2009) which are described in Walcher et al. (2014). From this mother
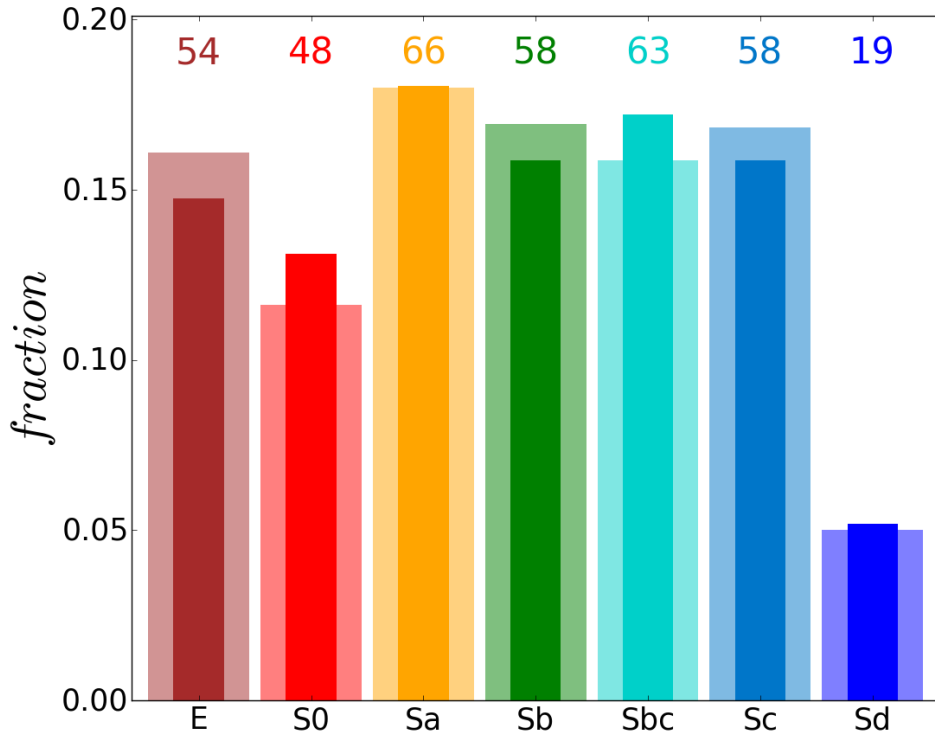
Figure 2.1 Comparison of the distribution of Hubble types in the CALIFA mother sample (939 galaxies, bars) and the 366 galaxies analysed here (narrow color bars). The histograms are normalized to unity, so that the two distributions are directly comparable. The number of galaxies in each morphology bin is labelled in colour with the same palette used throughout the paper.

sample the 667 target galaxies were randomly observed. The data are publicly available through three data releases (Husemann et al., 2013; García-Benito et al., 2015; Sánchez et al., 2016a). Every galaxy in the CALIFA sample is observed in the optical range using two different overlapping setups. The V500 low-resolution mode (R $\sim$ 850) covers the range 3745-7500 Å. The blue mid-resolution setup (V1200; R $\sim$ 1650) covers the range 3400-4840 Å. In order to reach a filling factor of 100% across the FoV, a 3-pointing dithering scheme is used for each object. The exposure time per pointing is fixed. V1200 observations are carried out during dark nights with total exposure time of 1800 s (split into 2 or 3 individual exposures) per galaxy. V500 observations are taken during grey nights with 900 s per pointing. To reduce the effects of vignetting on the data, we combine the observations from the V1200 and V500 setups. For a detailed description of the observing strategy and the pipeline reduction scheme we refer to the survey presentation (Sánchez et al. 2012), with improvements in the reduction presented in the three data releases (Husemann et al., 2013; García-Benito et al., 2015; Sánchez et al., 2016a).
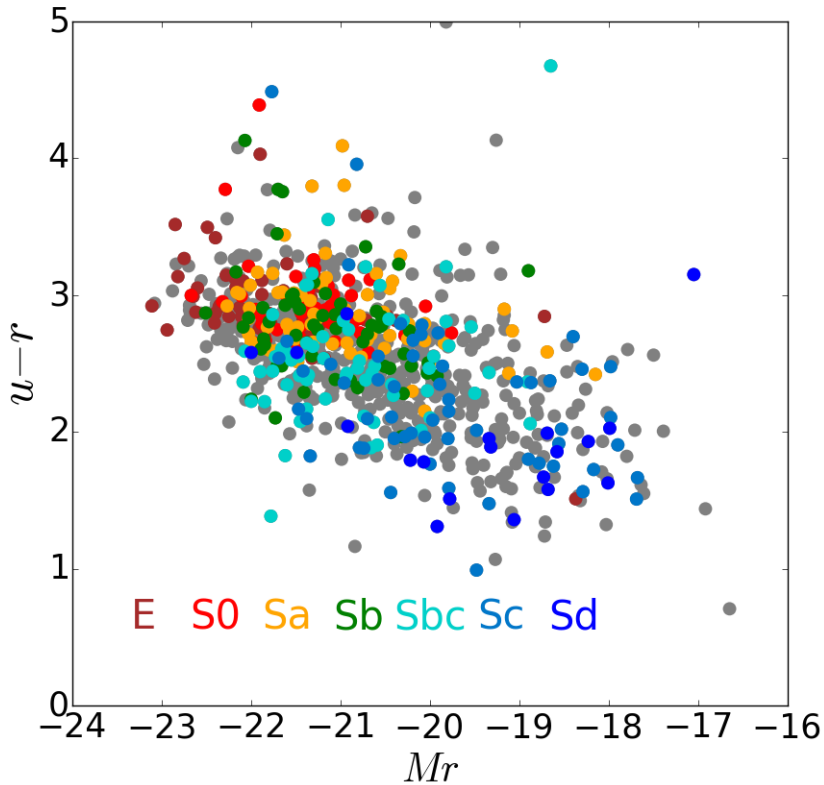
Figure 2.2 Colour-magnitude diagram. Mother sample galaxies are plotted in grey, while the 366 galaxies analysed in this thesis are marked as coloured points

2.3   GALEX photometry

The Galaxy Evolution Explorer (GALEX), a NASA Small Explorer mission, is an all-sky imaging and spectroscopic survey in the ultraviolet (Martin et al. 2005). GALEX is a space telescope that was launched on April 28 2003 with a 50 cm Ritchey-Chretien telescope with four channels: FUV and near-UV (NUV) imaging and FUV and NUV spectroscopy. In this thesis we use photometry from far-ultraviolet (FUV, effective wavelength $\lambda_{eff} \sim 1542$ Å) and near-ultraviolet (NUV, $\lambda_{eff} \sim 2274$ Å) bands. The data come from the GR6 data release. The GALEX archive provides simultaneous co-aligned FUV and NUV images with a FoV of 1.2 degrees wide, spatial scale of 1.5 arcsec per pixel and a spatial resolution of $\sim$4.5 arcsec (FWHM).

A full description of the calibration and data products of *GALEX* can be found in Morrissey et al. (2007). The intensity images (*int*) are in units of counts/second and they are not background subtracted. The photometric calibration is such that:

$$m_{FUV} = 18.82 - 2.5 \log{(\text{counts/s})}$$

$$m_{NUV} = 20.08 - 2.5 \log{(\text{counts/s})}$$

where both are AB magnitudes. The GALEX archive provides an estimation with SExtractor of the

sky background intensity, but we also measure sky directly in different regions on the intensity images and then compute the average values. Also a flag image is provided noting pixels potentially affected by bright star artifacts. The last data product that we use are the relative response images ($rrhr$) which contain the effective exposure time for each pixel in seconds.

Given int and $rrhr$ images we obtain that

$$counts = int * rrhr,$$

thus the photon noise is approximately

$$pho\_err = \frac{\sqrt{int * rrhr}}{rrhr},$$

in units of counts/second. To measure the error due to the sky background (sky_err) we compute the standard deviation of the sky values in each region with respect to the sky level estimation. Thus we obtain the error image in counts/second as

$$int\_err = \sqrt{pho\_err^2 + sky\_err^2}.$$

As we have the error (int_err) of the signal (int) in counts/second, the error on the magnitude would be obtained as

$$mag\_err = 2.5 * \log(e) * int\_err/int.$$

Galactic extinction corrections following Wyder et al. (2007) were applied to the data. For the FUV we assume the value $A_\lambda/E(B-V) = 8.24$ and for NUV we assume the ratio to be 8.2.

2.4   SDSS photometry

The goal of SDSS was to map one-quarter of the entire sky in detail. The photometric and spectroscopic data are provided by the 2.5 meter telescope located at Apache Point Observatory in Southern New Mexico. In this thesis we use the fully-calibrated, sky-subtracted data frames provided by the tenth data release (DR10, Ahn et al. 2014), which are in *nanomaggies*. A *maggie* is a linear measure of flux density; one *maggie* has an AB magnitude of 0, or a flux density of 3631 Jansky in any band. Thus , the *nanomaggie* is a linear unit of flux density equal to 10^{-9} *maggie*. We convert images in nanomaggies to AB magnitudes as follows

$$m = -2.5 * \log(\text{nanomaggies} * 1e^{-9}).$$

For a suitable synthesis analysis we need error images not provided directly by the reduction pipeline, but we can compute it as explained here. The frames provide calibration images ($cimg$) and sky images ($simg$) that can be used to return the product images (img) to the state it was in when input into the photometric pipeline, as follow

$$dn = img/cimg + simg.$$

These *dn* values are in the same units as the "data numbers" stored by the raw data files that come off the instrument. They are related to the detected number *nelec* of photo-electrons by

$$nelec = dn * gain,$$

where *gain* conversion factor is provided by the reduction pipeline. The *nelec* number is statistically Poisson distributed. In addition, there are other sources of noise, related to conventional CCD, that come from the readout-noise and the noise in the dark current. The readout-noise is the noise which is seen in the bias level and can be represented by one value which is an estimate of the standard deviation of the bias level values. The phenomenon of dark current is basically charge which accumulates in the CCD pixels due to thermal noise which produces an additive quantity to the electron count in each pixel. Both sources of noise are lump together as the "dark variance" in the reduction pipeline. With these values we compute the error in *dn* as

$$dn\_err = \sqrt{nelec/gain + darkVariance}.$$

The statistical errors in the sky (*sky_err*) are computed as the standard deviation of the sky values. Thus the final error images in nanomaggies are computed as

$$img\_err = \sqrt{(dn\_err * cimg)^2 + sky\_err^2}.$$

As we have the error (*img_err*) of the signal (*img*) in nanomaggies, the error in the magnitude would be obtained as

$$mag\_err = 2.5 * \log(e) * img\_err/img.$$

To correct from Galactic extinction we use the conversions from $E(B-V)$ to total extinction A_λ tabulated in Table 22 of Stoughton et al. (2002), which are $A_\lambda/E(B-V) = 5.155, 3.793, 2.751, 2.086, 1.479$ for filters u, g, r, i, z respectively.

2.5 Data processing

In this thesis we analyse the stellar population properties through the combination of the different data sets. Specifically, we apply STARLIGHT to analyse CALIFA spectra plus GALEX photometry and our parametric method to analyse a set of data obtained from CALIFA, GALEX and SDSS. In both cases, our aim is to study the integrated and also spatially resolved stellar population properties. For this purpose, we use different tools to obtain datacubes and images with the same spatial scale and extract information from the different kinds of data through a common segmentation spatial map. We take galaxy NGC0023 as an example to show the different steps in the data processing.

2.5.1 GALEX and SDSS: MONTAGE software

Montage is an open source toolkit designed to work with astronomical images in Flexible Image Transport System (FITS) format, comprised of several modules, rather than a single executable. This
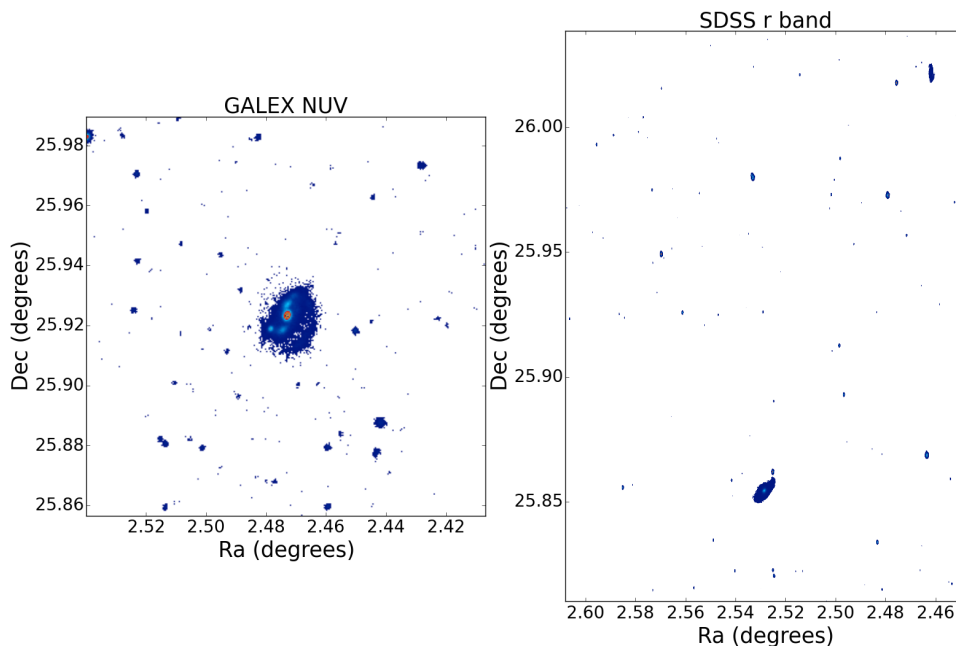
Figure 2.3 Left panel: GALEX NUV image for galaxy NGC0023 as provided by the GALEX pipeline. Right panel: SDSS r band image for the same galaxy, NGC0023, as provided by SDSS pipeline.

design has many benefits for users because they are able to adapt the code for their own purposes and use a specific module for the desired task. The complete documentation and description of modules is found on the Montage webpage (http://montage.ipac.caltech.edu/).

To combine our different kinds of data we use the **mGetHdr** and **mProject** tools of Montage. We use the first one to read the header from the FITS CALIFA datacube and extract it to a text file. The **mProject** reprojects a single image to the scale defined in a FITS header template file. The program provides the reprojected image and also en "area" image that contains the fraction of input pixel sky area that went into each output pixel. The program implements the Variable-Pixel Linear Reconstruction algorithm, or "Drizzle", (Fruchter & Hook 2002). The code maps and input pixel grid, into an output grid taking into account shift, rotation and geometric distortion, preserving the photometry and resolution. We use this tool to perform a resampling of the SDSS and GALEX images to the same spatial scale as CALIFA, which means 1 arcsec/pixel. Also the program aligns and cuts the GALEX images using WCS to obtain processed FUV and NUV images with the same FoV as our CALIFA datacubes.

Figure 2.3 shows the GALEX-NUV image and SDSS-r band image for galaxy NGC0023 as provided by the GALEX and SDSS pipelines, respectively. The FoV is different in both surveys and also much larger than CALIFA FoV. In Figure 2.4 we show the processed images with Montage software. The left panel shows the CALIFA image at 5635 Å. Middle and right panels show the GALEX NUV and SDSS r band images projected with Montage software. The white pixels in the three images represent pixels with no signal.
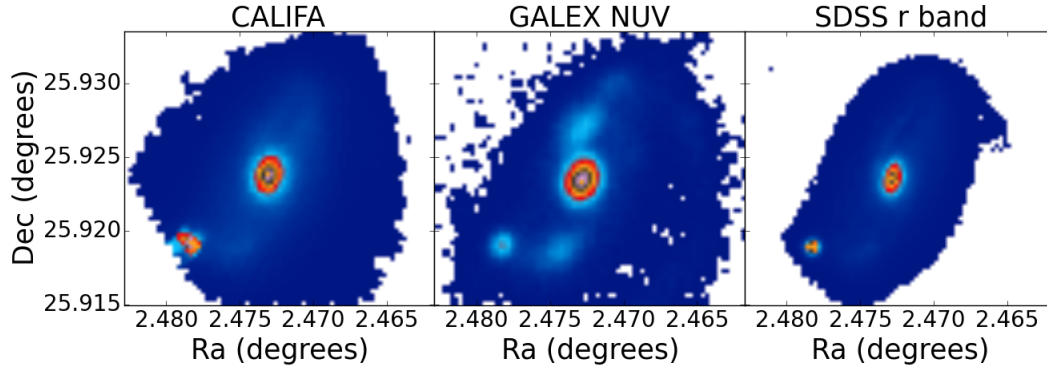
Figure 2.4 Left panel: CALIFA image for NGC0023 at 5635Å. Middle panel: GALEX NUV image for NGC0023 obtained with Montage software. Right panel: SDSS r band image for NGC0023 obtained by Montage software.

2.5.2   Spatial masks

We need to mask out foreground stars, artefacts and low S/N regions. The first candidates are identified by applying SExtractor (Bertin & Arnouts 1996) to the SDSS r-band image. For a better approximation, we perform a visual inspection of each galaxy, correcting its mask when necessary. Afterwards, we visually inspect the GALEX images together with flag images provided by the GALEX archive to mask some possible stars observed in the UV and correct their masks again. The final step in defining the spatial mask is to impose a a spectral quality threshold based on the S/N of the CALIFA data (we impose S/N > 3 Å for outskirts of galaxies).
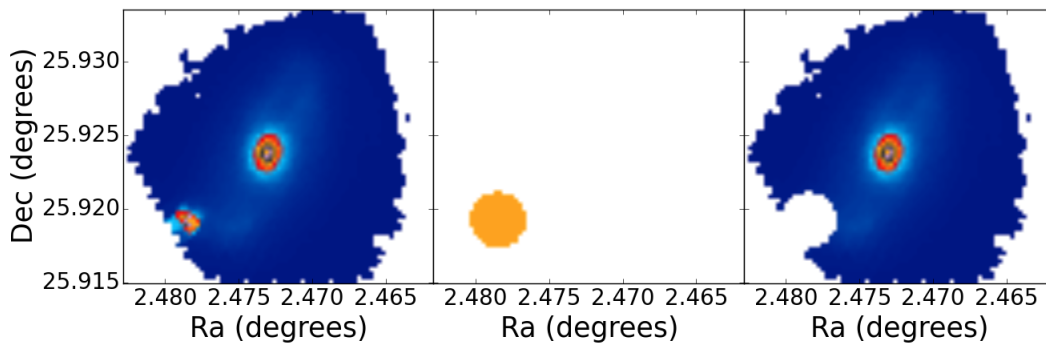
Figure 2.5 Left panel: CALIFA image for NGC0023 at 5635Å. Middle panel: spatial mask of NGC0023 for foreground stars. Right panel: The CALIFA image product after applying the spatial mask.

Figure 2.5 shows the mask applied to galaxy NGC0023 to foreground stars. In particular, we mask the bottom left region observed in the left panel of the image. The middle panel shows the masked pixels and the right panel the image product after applying the selected mask. We also mask this region in GALEX and SDSS images as Figure 2.6 shows.
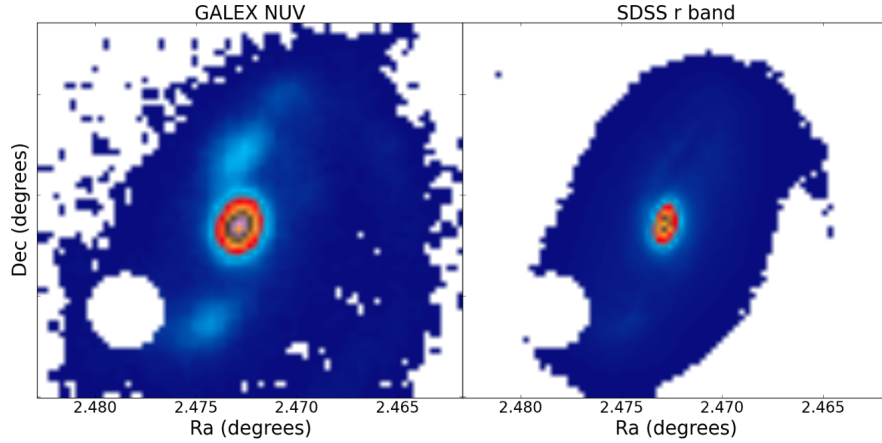
Figure 2.6 Left panel: GALEX NUV projected masked image for galaxy NGC0023. Right panel: SDSS r band projected masked image for galaxy NGC0023.

2.5.3 CALIFA: QBICK **pipeline**

To pre-process datacubes for a 3D spectral fitting analysis we use a fully automated package named QBICK. Here we describe the main steps packed in this tool, with a complete description available in Cid Fernandes et al. (2013).

1. Refinements of the b_λ (flag) and ϵ_λ (error) spectra: the pipeline reduction provides b_λ flags ($b_\lambda \equiv 0$ for good pixels and > 0 for flagged ones), but QBICK identifies some other problematic pixels. We flag pixels around the strongest sky lines seen in the CALIFA data: HgI 4358 Å, HgI 5461 Å, OI 5577 Å, NaI D (around 5890 Å), OI-OH (6300 Å), OI 6364 Å, and the B-band atmospheric absorption (Sánchez et al. 2012). We force $b_\lambda > 0$ when the error is large ($\epsilon_\lambda > 5F_\lambda$, where F_λ is the observed spectrum), but these pixels are not relevant for the spectral fits. Also pixels with very low values of ϵ_λ are flagged, because they can produce a very large weight on the analysis.

2. Rest-framing: the second step is to rest-frame all the spectra. We use the redshift derived from the reduction pipeline for the central 5″ spectrum (Sánchez et al. 2012).

3. Spatial binning: this step consists of applying a segmentation map to the data, grouping spaxels into spatial zones. In the next section we describe the two different maps used in this thesis. Besides the spectra for each zone, QBICK also produces the total spatially integrated spectrum.

4. Resampling in λ: to finish, all the spectra are resampled to 2 Å and the final zone spectra are stored in an ASCII file with flux, error ad flag columns necessary for the spectral analysis.

2.5.4 **Segmentation maps**

In this thesis we distinguish between two kinds of analysis. On the one hand, we combine optical data with UV photometry from GALEX images. The segmentation map defined for this analysis consists of four regions: $R < 0.5$, $R < 1$, $1 < R < 2$ y $R > 1$, where R denotes the radial distance to the

nucleus in units of the optical Half Light Radius (HLR), defined as the semi-major axis length of the elliptical aperture which contains half of the total light of the galaxy at the rest-frame wavelength 5635 Å (Cid Fernandes et al. 2013). None of our galaxies have a HLR smaller that the FWHM of the GALEX PSF, and most (338/366) have HLR larger than 8 arcsec, so these extractions are broad enough to avoid resolution issues and also let us analyse the inner and outer parts of galaxies, besides the integrated properties. These extractions are used to analyse the new version of STARLIGHT and also to fit the combination of GALEX+SDSS+CALIFA data with our parametric method. In Figure 2.7 we show an example of this kind of segmentation map for galaxy NGC0023. The left panel shows the regions $R < 0.5$ and $1 < R < 2$, while the right panel shows the regions $R < 1$ and $R > 1$. We obtain two inner regions, $R < 0.5$ and $R < 1$, and two outer regions, $1 < R < 2$ and $R > 1$, which overlap.
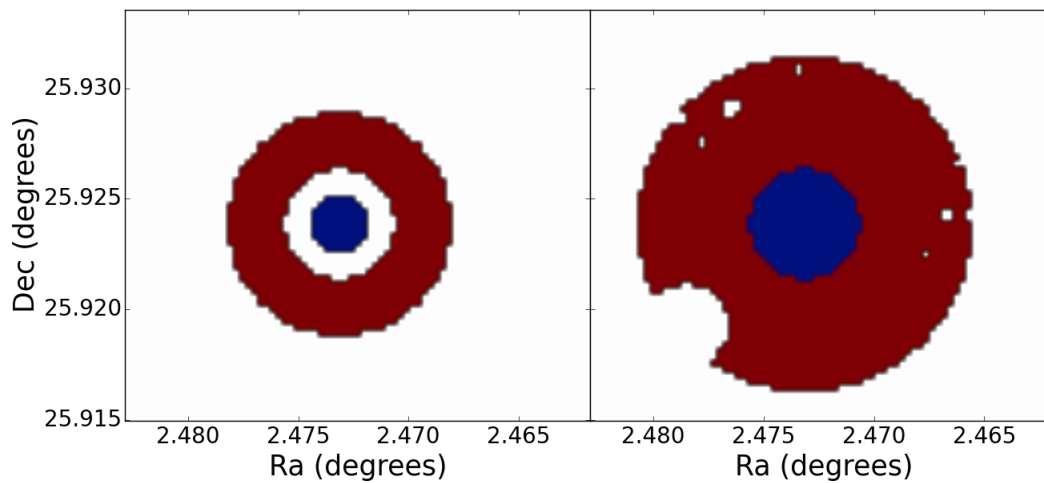
Figure 2.7 Left panel: segmentation map of NGC0023 for $R < 0.5$ and $1 < R < 2$, where R denotes distance in units of HLR. Right panel: segmentation map of NGC0023 for $R < 1$ and $R > 1$.

On the other hand, there are several works based on results of a STARLIGHT analysis of the CALIFA optical spectra (Pérez et al., 2013; Cid Fernandes et al., 2013, 2014; González Delgado et al., 2014b,a, 2015, 2016). In these works the segmentation structure is based on the Voronoi tessellation technique, as implemented by Cappellari & Copin (2003). The technique uses an adaptive binning scheme where the bin size depends on the local S/N: larger bins will be applied in the low S/N regions while smaller bins will be retained in high S/N regions. In our tessellation, the target for the minimum S/N is set to 20, obtaining on average of ∼ 1000 zones per galaxy. A complete description of the procedure is found in Cid Fernandes et al. (2013). We use this same segmentation map to fit SDSS+CALIFA data with our parametric method and compare with previous works based on STARLIGHT results. Figure 2.8 shows a Voronoi tesselation for NGC0023. In this case we obtain ∼ 1200 zones, which means ∼ 1200 spectra with S/N over 20. As we observe, the inner zones are single pixels, while for outer regions it is necessary to add more pixels to achieve spectra within the S/N threshold, so we obtain bigger zones.
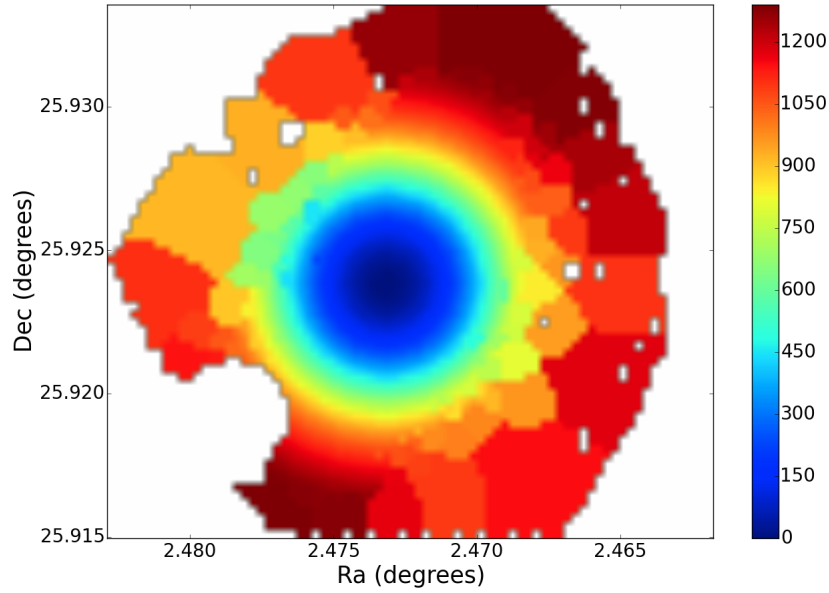
Figure 2.8 Voronoi zones for galaxy NGC0023. For this galaxy we obtain ~ 1200 spectra with S/N over 20. In this image we also mask pixels with S/N ≤ 3 Å.

2.5.5   Pycasso

The STARLIGHT results are stored in a plain ASCII file, one for each fitted spectrum. For the analysis of the integrated spectra or the segmentation maps based on the HLR, as explained in previous section, the stellar population properties can be directly post-processed from the output file to obtain SFHs, to compute the mass growth over time, to condense the results into first moments like the mean t and Z, etc. The results from the parametric method are stored in an hdf5 file and the stellar population properties can also be post-processed from the output hdf5 file.

However, when using the Voronoi scheme, the data require more organization, due to the huge number of output files. To handle datacubes we developed PYCASSO, the Python Califa Starlight Synthesis Organizer, which comprises three main parts:

1. A *writer* module, which stores the output of all STARLIGHT fits of the individual zones of a one galaxy into a single FITS file.

2. A *reader* module, which reads this file and structures the data in an easy to access and manipulate format.

3. A *post-processing* module, which performs a series of common operations such as mapping any property from zones to pixels, resampling and smoothing the population vectors, computing growth functions, averaging in spatial, time or metallicity dimensions, etc.

To deal with the parametric method results, we store the information for each galaxy in a single hdf5 file. This file contains information for all the zones of the same galaxy and through the *post-processing* PYCASSO module we map any property from zones to pixels or compute radial profiles, as we do with STARLIGHT.

3

Stellar population models

Contents

3.1 Introduction

The tool for interpreting the spectroscopy/photometry of galaxies and to infer their star formation histories and metallicity distributions are the simple stellar populations (SSPs) synthesis models.

An SSP model is an assembly of single stars with the same age and the same chemical composition. In nature, the best examples of SSPs are star clusters, which are groups of stars that were born at the same time from a molecular cloud. They have been used to test the models, finding that accuracies of about 0.1 dex in age and 0.3 dex in metallicity can be achieved (González Delgado & Cid Fernandes 2010).

In galaxies, their stars are born at different times and in different environments, so they are not SSPs, but such a complex population can be expanded in SSPs. Each SSP in a galaxy has particular features, according to its age and metallicity, which remains recorded in the whole galaxy spectrum. A galaxy spectrum can be seen as a fossil record of its history, allowing us to know how the galaxy formed and evolved.

Evolutionary synthesis models is a technique introduced by Tinsley (1968) that allows us to predict the synthetic spectrum of a stellar population through three ingredients: (1) the initial mass function, (2) the stellar evolutionary tracks, and (3) the stellar libraries.

In section 3.2 we summarise the main ingredients of the evolutionary synthesis models. In section 3.3 we present some different models and the degeneracies affecting the models. In section 3.4 we present the spectral synthesis methods that we use in this thesis.

3.2 Ingredients of the evolutionary synthesis models

3.2.1 Initial Mass Function

The Initial Mass Function (IMF) describes the number of stars per mass interval at the moment that the stars were born. It is an important ingredient in stellar population models because many galaxy properties depend on the IMF, including mass to- light ratios, derived galaxy masses and star formation rates, the rate of the luminosity evolution of the constituent stellar populations or the metal enrichment.

Salpeter (1955) first described the IMF as a power-law, $dN = \xi(m)dm = km^{-\alpha} = dN$, where dN is the number of stars in the mass interval $m, m + dm$ and k is the normalization constant. Salpeter arrived at the power-law index $\alpha = 2.35$ for $0.4 \lesssim m/M_\odot \lesssim 10$.

Above $1M_\odot$ there is very good agreement when assuming the IMF to be a power-law of Salpeter index. However, for masses below $1M_\odot$ the IMF is uncertain and there are other parametrization, like the log-normal of Chabrier (2003), or the shallower power-law of Kroupa (2001). Figure 3.1 (taken from
Bastian et al. 2010) shows the different behaviour of the IMF parametrized by the Γ index ($\alpha = \Gamma + 1$).

The shape and universality of the IMF is still under investigation. Studies of the field, young clusters and associations, and old globular clusters suggest that the vast majority were drawn from a universal IMF: a power law of Salpeter index ($\alpha = 2.35$) above a few solar masses, and a log normal (Chabrier 2003) or shallower power law (Kroupa 2001), with $\alpha \sim 1 - 1.25$, for lower mass stars.
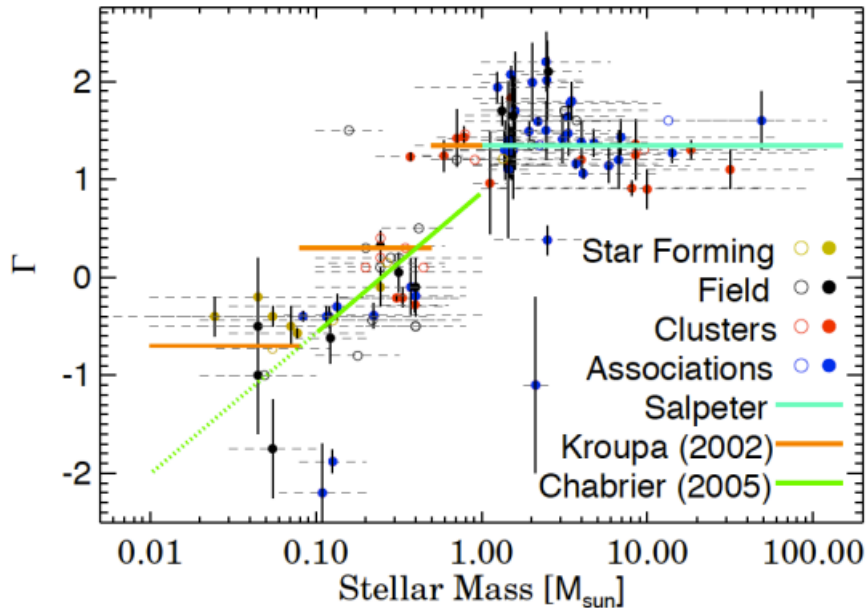
Figure 3.1 Derivative of the IMF-slope (Γ) according to stellar mass (from Bastian et al. 2010).

Observations of resolved stellar populations and the integrated properties of most galaxies are also consistent with a universal IMF, suggesting no gross variations over much of cosmic time (Bastian et al. 2010).

In this work we use SSPs with Chabrier IMF, defined as:

$$\xi(m) \propto \begin{cases} \frac{1}{m} e^{\frac{-(\log m - \log m_c)^2}{2\sigma^2}} & (m \leq 1 M_\odot) \\ m^{-2.3} & (m > 1 M_\odot) \end{cases},$$

with $m_c = 0.08 M_\odot$ and $\sigma = 0.69$.

3.2.2   Stellar tracks

The evolution of a star depends primarily on its mass. Stars greater than 1.4 times the mass of the Sun, consume their fuel and explode as a supernova casting off much of their mass. Stars near the sun's mass spend much more time on the main sequence, swell into a red-giant (RGB) and finally shed some of the outer layers into space as a planetary nebula.

Stellar tracks model the evolution of a star in brightness and temperature, according to its mass and metallicity. Some phases throughout stellar evolution are very fast or variable in time, so they are difficult to model due to, in practice, evolutionary tracks are discretely sampled. Also some aspects of stellar evolution including the treatment of convection, close binary evolution, rotation effects, and mass-loss, amongst many others, introduce uncertainties into the models.

A number of widely-used models exist in the literature. The most popular models are those from Padova and Geneva groups. Padova models span a wide range in ages (masses) and chemical compositions, and cover most relevant evolutionary phases. The Geneva models (Schaerer et al., 1993b,a; Charbonnel et al., 1993) are focused on following high-mass stars through advanced evolutionary

phases, including the Wolf-Rayet (WR) phase, but they do not model low mass stars. Other models have focused on the main sequence, red giant branch (RGB), and horizontal branch (HB) evolution of low-mass stars ($M < 3M_\odot$). Models computed by Schoenberner (1983), Vassiliadis & Wood (1994) and Bloecker (1995) are widely use to cover the post-AGB evolutionary phase. This phase is one of the most difficult evolutionary phases to model because of the combined effects of thermal pulses (i.e. helium shell flashes), changes in surface abundance caused by heavy-element dredge-up (e.g. carbon) and important mass-loss terminated by a superwind and the ejection of the stellar envelope (Habing 1995, 1996. The spectral signature of stars in the TP-AGB phase appears around ~ 1 Gyr, which is the time period when they are important contributors to the SSPs spectra. While the optical part of the spectra is not significantly affected by the TP-AGBs, their emission dominates the NIR bands, and produces a significant uncertainty in the K band luminosity and therefore, in the stellar masses derived from it.

In this thesis we use the isochrones from Padova group (Alongi et al., 1993; Bressan et al., 1993; Fagotto et al., 1994a,b; Girardi et al., 1996).

3.2.3 Stellar libraries

Stellar spectral libraries are another main ingredient in evolutionary synthesis models. They are required to convert the outputs of stellar evolution calculations − surface gravities, g, and effective temperatures, T_{eff} − according to metallicity, Z, into observable SEDs. The libraries can be theoretical or empirical.

Theoretical libraries offer the great advantage of covering parameter space more densely and homogeneously, including spectral resolution, and of producing spectra that are not subject to observational issues such as flux calibration and atmospheric absorption. However they are based on model atmospheres and, therefore, are limited to the approximations adopted in the computations. There are a number of decisions that must be made when computing synthetic spectral libraries including how to treat convection and the microturbulent velocity profile, and whether or not to model departures from local thermodynamic equilibrium (LTE) and plane-parallel geometries. Additional important limitations include the incomplete and often inaccurate atomic and molecular line lists.

A good parameter coverage is not trivial for empirical libraries, which are limited to whatever is possible to obtain given observational constraints. Empirical spectra, of course, do not suffer from issues with line lists, treatment of convection, etc., but they are plagued by standard observational constraints such as correction for atmospheric absorption, flux calibration, and limited wavelength coverage and spectral resolution.

There is, however, no single spectral library, whether theoretical or empirical, that covers the desired range of parameter space and the best approach is to join some of them. The SSP models used in this thesis are based on MILES (Sánchez-Blázquez et al. 2006, and GRANADA (Martins et al., 2005; González Delgado et al., 2005) libraries:

- MILES empirical library consists of 985 stars spanning a large range in atmospheric parameters. The spectra were obtained at the 2.5 m Isaac Newton Telescope and cover the range 3525 to 7500 Å at 2.3 Å (full width at half-maximum) spectral resolution. The spectral resolution,

spectral-type coverage, flux-calibration accuracy and number of stars represent a substantial improvement over previous libraries used in population-synthesis models.

- GRANADA synthetic library contains 1654 high-resolution stellar spectra, with a sampling of 0.3 Å and covering the wavelength range from 3000 to 7000 Å for a wide range of metallicities (twice solar, solar, half solar and 1/10 solar). The library was computed with the latest improvements in stellar atmospheres, incorporating non-local thermodynamic equilibrium (non-LTE) line-blanketed models for hot, massive ($T_{eff} \geq 27500$ K) and LTE line-blanketed models (Phoenix) for cool ($3000 \leq T_{eff} \leq 4500$ K) stars. The total coverage of the grid is 3000 K $\leq T_{eff} \leq 55000$ K and $-0.5 \leq \log g \leq 5.5$.

3.3 Evolutionary synthesis models

In this section we describe the characteristics of the base of stellar population synthesis models used in this thesis, the so called base *CBe*. It has previously been described and used in the stellar population analysis of the CALIFA sample (Cid Fernandes et al., 2014; González Delgado et al., 2014b,a, 2015, 2016).

Base *CBe* is built from an update of the Bruzual & Charlot (2003) models, replacing STELIB (Le Borgne et al. 2003) with a combination of the MILES (Sánchez-Blázquez et al., 2006; Falcón-Barroso et al., 2011) and GRANADA (Martins et al. 2005) spectral libraries. The evolutionary tracks are those collectively known as Padova 1994 and the IMF is that of Chabrier. This base contains six metallicities:

$$\log Z/Z_\odot = -2.3, -1.7, -0.7, -0.4, 0, \text{ and } + 0.4.$$

Base CBe contains $N_\star = 246$ elements (41 ages from 0.001 to 14 Gyr and the six metallicities above).

In Figure 3.2 we show the spectral evolution of *CBe* SSPs for solar metallicity and eight ages from top to bottom: 4 Myr, 10 Myr, 40 Myr, 160 Myr, 500 Myr, 1 Gyr, 3 Gyr and 10 Gyr. Right panel shows the spectra in units of $L_\odot \text{Å}^{-1} M_\odot^{-1}$. Left panel shows the spectra normalized in 5635Å, the normalisation wavelength used in this thesis. Regarding the normalised spectra we can observe the differences between the optical and UV range. Small differences in the optical range between two SSPs can account for large differences in the UV. This difference in the UV motivates the combination of optical and UV data in the work of this thesis, in order to obtain better estimation of ages and metallicities. In particular, to detect low level ongoing star formation and better constrain the star formation history.

3.3.1 Degeneracies

In the spectra of a SSP with a single age and metallicity, an age change can be countered by a metallicity change so that almost every colour and spectral index remains the same. A given SSP spectrum is redder due to being older or having a higher metallicity. On the other hand, a SSP is bluer if it is younger or has lower metallicities. Also extinction introduces a third variable into this problem, by increasing the extinction the spectrum become redder.
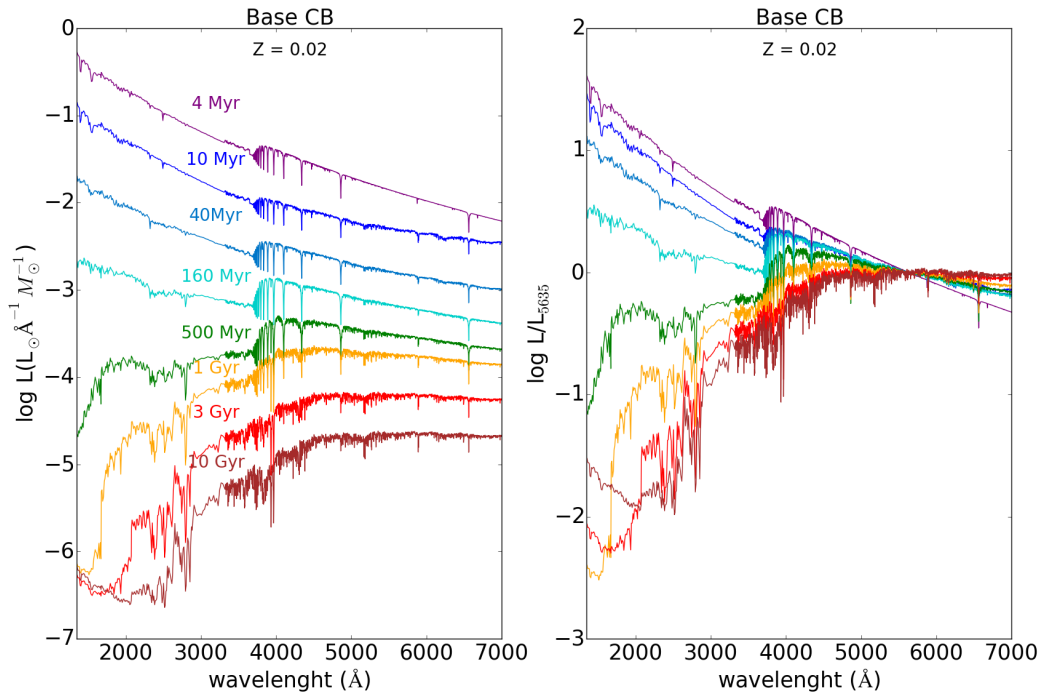
Figure 3.2 Left panel: Spectral evolution of base CB SSPs for solar metallicity and 8 ages from top to bottom 4 Myr, 10 Myr, 40 Myr, 160 Myr, 500 Myr, 1 Gyr, 3 Gyr and 10 Gyr. Right panel: same as left panel but with models normalized at 5635 Å.

In Figures 3.3 and 3.4 we show two extreme cases. Figure 3.3 shows the spectra of two SSPs with different ages, 13 Gyr and 2 Gyr, and different metallicities, 0.2 $Z_\odot$ and 2.5 $Z_\odot$. In the left panel we observe the optical range. A spectra become redder when increasing the metallicity, then the SSP of 2 Gyr and 2.5 $Z_\odot$ appears similar to that of 13 Gyr and 0.2 $Z_\odot$, which is older. In the right panel we observe the UV range, showing that the younger population emits lower UV flux than the older population due to the different metallicities. Figure 3.4 shows the spectra of two SSPs with different ages, 50 Myr and 300 Myr, and affected by different extincion magnitudes, both for solar metallicity. The young SSP, of 30 Myr, is affected by 0.5 mag of extinction following the law of Calzetti et al. (2000). The older population, of 300 Gyr, is not affected by extincion. In the left panel we observe the optical range and the right panel also shows the UV range. Although the ages are different, the effect of extinction causes the spectra to be similar in the shape of optical continuum. However, the spectra are quite different in terms of the stellar features and the 4000 Å break. The fluxes in the UV range are also quite different, higher for the SSP of 30 Myr. In both cases we observe that differences in UV fluxes are better appreciated than in the optical range, indicating that UV data can be useful to better constrain the stellar population properties. The best solution for breaking the degeneracy is the spectroscopy, through full spectral fitting, because we can observe all the spectral features.

A second approach is to use some spectral features and not the full spectrum. Worthey (1994) conducted a detailed analysis of optical features in the form of spectrocopic indices (the so-called Lick indices) and found that akin to the broad-band colours, the indices, while partially diminishing the
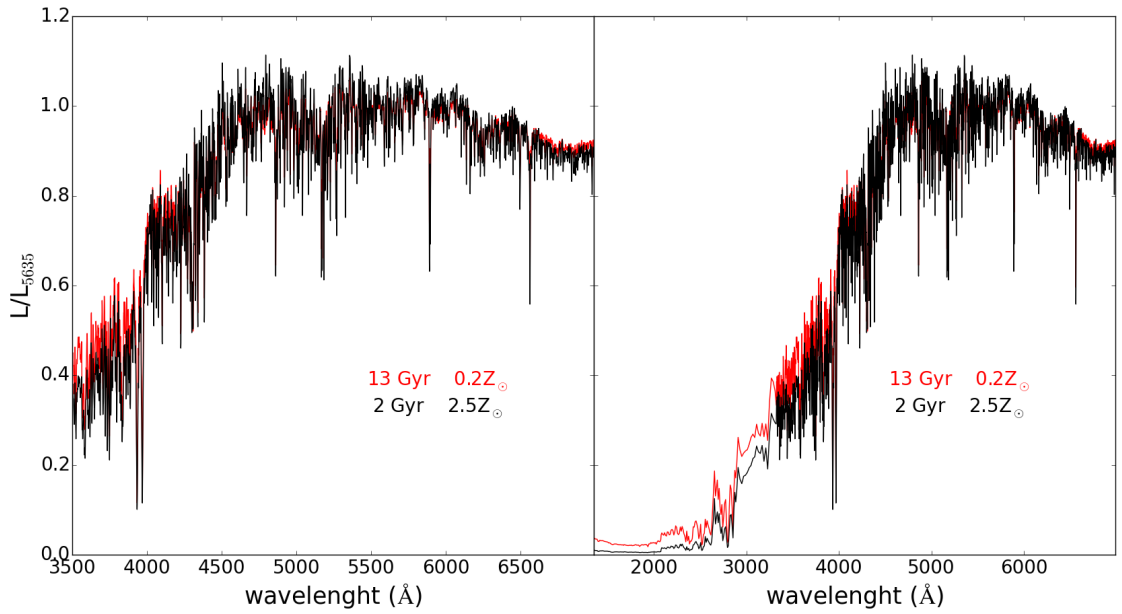
Figure 3.3 Left panel: Comparison between two SSPs from base CB affected by age-metallicity degeneracy. In red we show a SSP of 13 Gyr and 0.2 $Z_\odot$ while in black we show the SSP of 2 Gyr and 2.5 $Z_\odot$. Both are normalized at 5635 Å. Right panel: same as left panel but also covering the UV range.
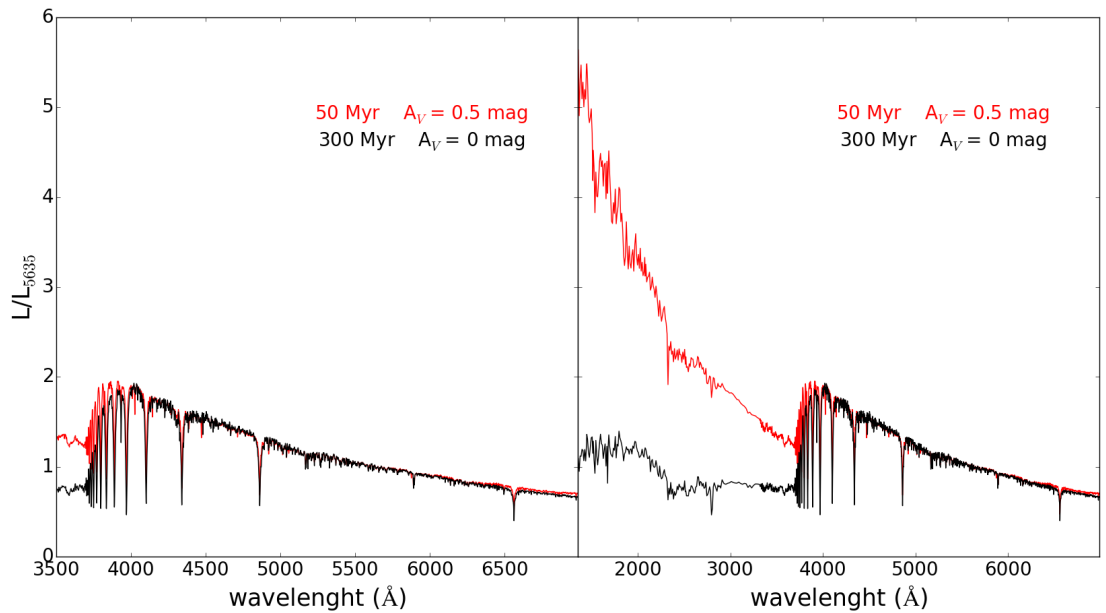
Figure 3.4 Left panel: Comparison between two SSPs from base CB affected by age-extinction degeneracy. In black we show a SSP of 300 Myr not affected by extinction and in red we show a SSP of 50 Myr and affected by 0.5 mag of extinction following the law of Calzetti et al. (2000). Both are normalized at 5635 Å. and in both the metallicity is fixed to solar. Right panel: same as left panel but also covering the UV range.

age-metallicity degeneracy, are also degenerate. Worthey (1994) identified a small number of spectral indices that were unusually sensitive to age, including the hydrogen Balmer lines, and several indices that were unusually sensitive to metallicity, including the Fe4668 and Fe5270 indices, so he concluded that the age-metallicity degeneracy could be broken by jointly considering a handful of carefully chosen indices. Broad band colours are also degenerate, but including very large spectral range it is possible to mitigate this effect.

Some works have investigated the effect of including other spectral windows that help to break the age-metallicity degeneracy. In particular, UV colours (Yi, 2003; Kaviraj et al., 2007b) have been investigated on the basis that UV properties are dominated by different stellar types at different evolutionary phases with respect to those dominating the optical. The overall results indicate that UV indeed helps to better constrain the age but the determination of chemical composition was still better determined by the more sensitive optical features.

3.4   The fossil method

In this thesis we use two different methods to derive the stellar population properties of galaxies, combining photometry and spectroscopy. While tools to retrieve stellar population properties out of multi-band photometry are common in the literature (e.g. the CIGALE code of Noll et al. 2009), methods which mix photometric and spectroscopic information are less common. An example is the work of Schawinski et al. (2007), who model UV to IR photometry in conjunction with Lick indices derived from SDSS spectra.

The strategy followed by both methods is to consider that the integrated light from a galaxy is the sum of single stellar populations, each with its ages and metallicities; thus, the best model of the galaxy luminosity is calculated as:

$$M_\lambda = \sum_{j=1}^{N^\star} p_j SSP_\lambda(t, Z) * 10^{-0.4A_V q_\lambda},$$

where p_j is the scaling factor that gives the fractional contribution to light or mass of each SSP, $q_\lambda = A_\lambda/A_V$ is the reddening curve and $SSP_\lambda(t, Z)$ gives the spectrum of an SSP of age t and metallicity Z. The technical details will be explained in the corresponding chapters 4 and 5.

3.4.1   Full spectral synthesis

The first method used in this thesis is the analysis of stellar populations properties through spectral synthesis, using the SSPs model to fit λ-by-λ the whole spectrum and UV photometry. We have developed a new version upon the full spectral fitting code STARLIGHT of Cid Fernandes et al. (2005). The method admits any combination of spectra and photometry, but we focus on the specific case of CALIFA optical spectroscopy (Sánchez et al. 2012) plus GALEX photometry (Martin et al. 2005), a combination which has the key advantage of allowing us to mitigate aperture effects, a serious source of concern in any experiment involving data gathered through different instruments. In chapter 4 we describe the new version of STARLIGHT code.
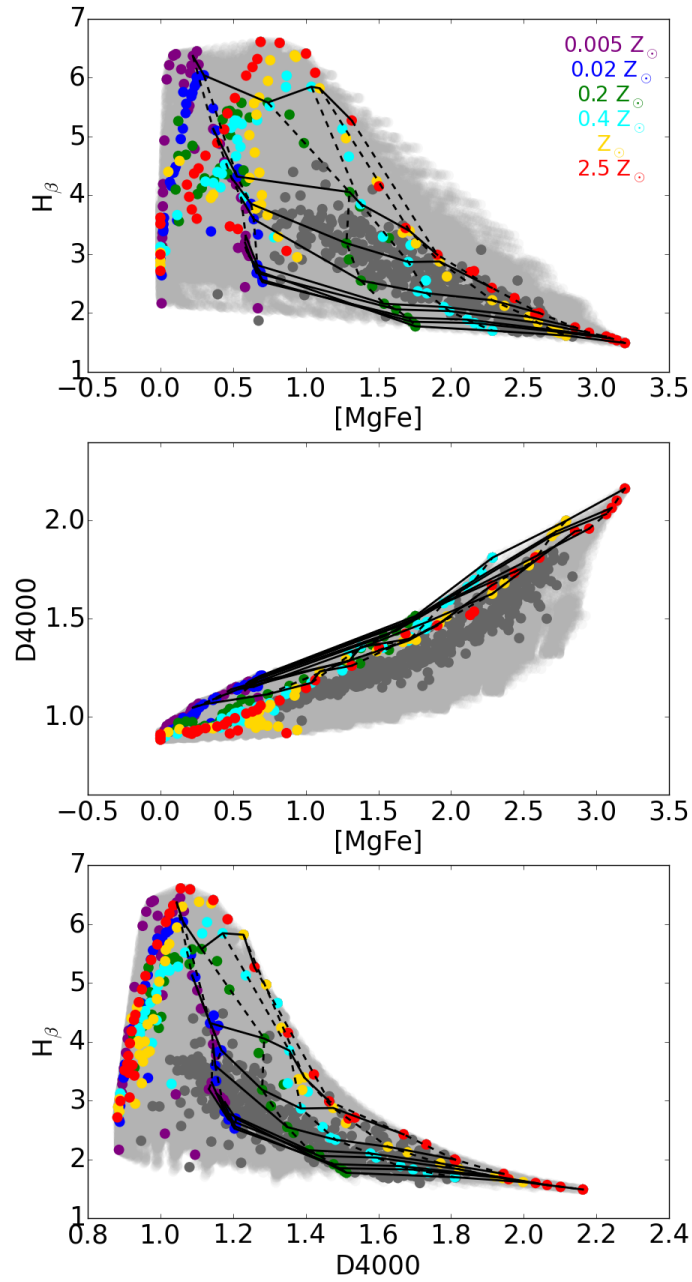
Figure 3.5 Top: [MgFe] versus Hβ. Middle: [MgFe] versus D4000. Bottom: D4000 versus Hβ. Dark grey points represent values measured in the integrated observed data. Coloured points are values measured in the Base CBe. Light grey points show the values obtained by running all the different combination of two SSPs in the Base CBe. Solid black lines indicate different ages: 500 Myr, 1Gyr, 2 Gyr, 3Gyr, 6 Gyr, 7Gyr, 10 Gyr, 11 Gyr and 14 Gyr. Dashed black lines draw different metallicities.

3.4.2 Line absorption fits

The second method is also through the combination of spectroscopy and photometry, but in this case we just take some spectral features and include GALEX+SDSS photometry. We combine a set of Lick indices with the 4000 Å break (D4000) as defined in Balogh et al. (1999), which is a strong age indicator. In the Lick system, Hβ index is the primary age-sensitive spectral indicator, whereas Mg and Fe are the primary metallicity indicators. In our analysis we use both D4000 and Hβ as age-sensitive lines. As metallicity indicator we use a combination of Mgb, Fe5270 and Fe5335 ([MgFe]$'$), defined in Thomas et al. (2003) as

$$[\text{MgFe}]' = \sqrt{\text{Mg}\,b(0.72 \times Fe5270 + 0.28 \times Fe5335)}\,.$$

The advantage of this index is that it is completely independent of α/Fe and can be used as a metallicity tracer. We measure the metallicity sensitive indices (Mgb, Fe5270 and Fe5335) and D4000 in the CALIFA optical spectra. Hβ may be affected by the emission of gas if any exists in the galaxy, thus we apply an emission line subtraction using a STARLIGHT fit and then we measure the index.

In Figure 3.5 we show Hβ, [MgFe]$'$ and D4000 measured in the integrated spectra and also in the SSPs of the Base CBe. Dark grey points represent the values of the CALIFA sample and the metallicity of the SSPs is colour-coded. Solid black lines indicate different ages: 500 Myr, 1Gyr, 2 Gyr, 3Gyr, 6 Gyr, 7Gyr, 10 Gyr, 11 Gyr and 14 Gyr. Dashed black lines indicate different metallicities. Light grey colours represent the results obtained by combining two different SSPs, running all possible combinations. For two SSPs we create 10 different models:

$$M_\lambda = f * SSP_\lambda(t_1, Z_1) + (1 - f) * SSP_\lambda(t_2, Z_2),$$

where $f = 0, 0.1, 0.2, 0.3, 0.4, 0.5, 0.6, 0.7, 0.8$ and 0.9. The top panel shows [MgFe]$'$ versus Hβ. The measured values in SSPs form an envelope of values obtained from observed spectra. This means that through a combination of the SSPs we can obtain synthetic spectra with the same index values of the observed ones. The middle panel shows [MgFe]$'$ versus D4000, obtaining a good correlation between these two indicators. [MgFe]$'$ is good tracer of metallicity, being not very dependent on age, and D4000 is a good age tracer, being not very dependent on metallicity. Thus, this panel shows the age-metallicity relation. This does not happen when one axis is Hβ because although it is a good age indicator, it also varies with metallicity. The bottom panel shows D4000 versus Hβ. Again the values measured in the base form an envelope of the obtained from the data, indicating that through a combination of SSPs we can obtain synthetic values that match the observed ones. This panel shows again the variation of Hβ with metallicity. If both D4000 and Hβ were pure age indicators, we would obtain a clear correlation between the two indicators, as in the middle panel, but this does not occur. Besides the input data, the main difference with STARLIGHT is that in this case we use a parametric SFH to fit the data. In chapter 5 the parametric method is described.

4

Simultaneous spectroscopic and photometric analysis of galaxies

Contents

4.1   Introduction

In this chapter we develop and test a combined spectroscopic + photometric analysis built upon the full spectral fitting code STARLIGHT of Cid Fernandes et al. (2005). The method admits any combination of spectra and photometry, but we focus on the specific case of CALIFA optical spectroscopy (Sánchez et al. 2012) plus GALEX photometry (Martin et al. 2005).

The chapter is organized as follows: Section 4.2 describes how to combine spectra and photometry into a single figure of merit to be optimized. Section 4.3 presents simulations designed to test the code under realistic circumstances. Section 4.4 explores an actual application based on a combination of optical spectra from CALIFA data and GALEX fluxes. Section 4.5 discusses how the addition of UV constraints improves the estimation of ages and metallicities, and the implications for the stellar mass-metallicity relation.

The results in this chapter are those published in López Fernández et al. (2016). On this work, were analysed 260 galaxies, which represent well the CALIFA mother sample. The 260 galaxies are a sub-sample of the 366 galaxies analysed in this thesis.

4.2   Method

The combined spectroscopic + photometric modelling can in principle be applied to any arbitrary combination of data, like a near-IR spectrum plus optical and/or UV photometry, an optical spectrum plus near-IR photometry, etc. For concreteness, the simulations and actual applications explored in later sections focus on the combined analysis of a 3700–7000 Å optical spectrum and NUV (~ 2274 Å) plus FUV (~ 1542 Å) photometry from GALEX.

4.2.1   Input data

We describe the spectroscopic data to be fitted in terms of the following elements:

[1.] The observed spectrum O_λ and its error $\sigma(O_\lambda)$. Mask ($mask_\lambda$) and flag ($flag_\lambda$) spectra to mark regions to be discarded from the analysis because of emission lines or artifacts (e.g. bad pixels and sky residuals). $w_\lambda = \sigma(O_\lambda)^{-1}$ is the weight given to pixel λ. Masked and flagged pixels have $w_\lambda = 0$. Discounting zero-weight entries one is left with N_λ^{eff} fluxes to be fitted. N_λ^{eff} is typically of the order of 10^3.

The photometric data, indexed with a subscript l running from $l = 1$ to N_l filters, consist of

[(a)] the apparent AB magnitude of the object m_l^{obs} and its error $\sigma(m_l^{\mathrm{obs}})$. the filter transmission curves $T_l(\lambda)$.

The input photometry is corrected for Galactic extinction, but K-corrections are not necessary since we will perform the synthetic photometry in the galaxy's redshift z.

4.2.2   The model

Model predictions for the observed spectroscopic and photometric fluxes are built by a linear combination of spectra from a base $B_{j,\lambda}$ ($j = 1 \ldots N_\star$), usually (but not necessarily) drawn from evolutionary

synthesis models for simple stellar populations (SSP) of different ages and metallicities. Each base spectrum is first normalized by its value at a chosen reference wavelength λ_0 (= 5635 Å in this thesis). The scaled base spectra are then combined in proportions x_j to build a model spectrum M_λ given by

$$M_\lambda = M_{\lambda_0} \left(\sum_{j=1}^{N_\star} x_j b_{j,\lambda} \right) r_\lambda \otimes G(v_\star, \sigma_\star) \tag{4.1}$$

where $b_{j,\lambda} \equiv B_{j,\lambda}/B_{j,\lambda_0}$, r_λ is a shorthand for the $e^{-\tau_V(q_\lambda - q_{\lambda_0})}$ reddening produced by a foreground screen of dust with an extinction curve $q_\lambda = \tau_\lambda/\tau_V$, and $G(v_\star, \sigma_\star)$ denotes a gaussian kinematical kernel centred at velocity $v_\star$ and with dispersion $\sigma_\star$.

Provided the base spectra cover the wavelengths of our N_l filters, Eq. (4.1) can be used to predict model magnitudes m_l

$$m_l = -2.5 \log \frac{\int M_{\lambda/(1+z)} T_l(\lambda) \lambda \, d\lambda}{\int T_l(\lambda) \lambda^{-1} \, d\lambda} - 2.41 \tag{4.2}$$

where the rest-frame model spectrum M_λ is shifted to the observed frame, thus circumventing the need for K-corrections.

4.2.3 Combining spectroscopic and photometric figures of merit

A purely spectroscopic analysis would consist of, for instance, estimating the model parameters by minimizing

$$\chi^2_{\text{SPEC}} = \sum_\lambda w_\lambda^2 (O_\lambda - M_\lambda)^2 \tag{4.3}$$

as in Cid Fernandes et al. (2005). The analogous photometric figure of merit is

$$\chi^2_{\text{PHO}} = \sum_{l=1}^{N_l} \left(\frac{m_l^{\text{obs}} - m_l}{\sigma_l} \right)^2 \tag{4.4}$$

which compares model and observed magnitudes. The total χ^2 to be considered in a joint analysis is then simply

$$\chi^2_{\text{TOT}} = \chi^2_{\text{SPEC}} + \chi^2_{\text{PHO}} \tag{4.5}$$

We have also experimented with other definitions of χ^2_{TOT}. One might, for instance, want to ensure that the spectroscopic and photometric data be given commensurable weights in the joint analysis. This can be implemented by scaling χ^2_{PHO} by a factor of $\sim N_\lambda^{\text{eff}}/N_l$ (or, equivalently, scaling the observational errors).

Throughout this thesis we adopt Eq. 4.5 in its original form. The simulations and real-data applications presented below produced good spectroscopic and photometric fits with no need for *ad*

hoc scaling factors. Such weighting schemes should be more relevant in cases where the observational errors are not well known.

4.2.4   Aperture mismatch: Implementation of photometric constraints as ranges

Another problem to consider when modelling spectra and photometry is that they are often collected through different apertures. The applications of the code in Section 4.4 are based on a combination of optical spectra from CALIFA data and GALEX fluxes, whereby the spectra are extracted from the projection of the GALEX aperture on the integral field data cube, thus mitigating aperture effects. Nonetheless, in the interest of completeness we discuss the 'range-fitting' scheme implemented in the new STARLIGHT to deal with aperture uncertainties.

Even disregarding spatial variations of the stellar populations, an aperture mismatch implies flux scale differences which make the simultaneous fit of O_λ and m_l meaningless. Aperture corrections are designed to fix this problem by scaling the input data to a same flux level, yet these are but approximate corrections, subject to systematic uncertainties.

To deal with this issue we introduce a modified version of $\chi^2_{\rm PHO} = \sum_l \chi^2_l$ where the $e^{-\chi^2_l/2}$ gaussian likelihood of each $m_l^{\rm obs}$ implicit in Eq. (4.4) is replaced by a flat top gaussian likelihood, where χ^2_l is given by

$$\chi^2_l = \begin{cases} \left(\frac{m_l - m_l^{\rm low}}{\sigma_l}\right)^2 & m_l \leq m_l^{\rm low} \\ 0 & m_l^{\rm low} < m_l < m_l^{\rm upp} \\ \left(\frac{m_l - m_l^{\rm upp}}{\sigma_l}\right)^2 & m_l \geq m_l^{\rm upp} \end{cases} \tag{4.6}$$

This modification acts in the sense that the model magnitude m_l no longer sees $m_l^{\rm obs}$ as a target to be matched within a $\sim \pm\sigma_l$ margin of error. Instead, the code will seek m_l values which do not depart by much more than $\sim \sigma_l$ from the $m_l^{\rm low} < m_l < m_l^{\rm upp}$ range. For $\sigma_l \ll (m_l^{\rm upp} - m_l^{\rm low})$ the likelihood effectively becomes a box car, which guarantees that the model m_l remains within the allowed range. Put another way, all solutions leading to m_l in the given $m_l^{\rm low}$–$m_l^{\rm upp}$ range are equally acceptable, contributing nothing to the global figure of merit.

A qualitatively similar effect could be obtained by exaggerating the uncertainty in m_l beyond its nominal value $\sigma(m_l)$. We nevertheless prefer the 'range-fitting' recipe outlined above, which has the advantage of expressing in an explicit way the systematic character of uncertainties in matching fluxes from different instruments/telescopes. An added benefit of our formulation is that it allows the incorporation of lower or upper limits in the analysis. Suppose that all we know about the FUV flux in a galaxy is that it is weaker than $m_{\rm FUV}^{\rm upp}$. One can couple this observational upper limit to an arbitrarily low lower limit and feed this information into our recipe to enforce that the resulting stellar populations will conform to the given upper limit. As shown in Section 4.3, purely optical studies can easily allow optically insignificant but UV-dominant populations, so that the use of UV limits can be useful.

As mentioned above, our data allow us to match the O_λ and m_l apertures, so that no range-fitting scheme is necessary. We thus set $m_l^{\rm low} = m_l^{\rm upp} = m_l^{\rm obs}$, so that the code tries to fit the observed magnitude within its observational error.

4.3 Simulations

As a first test of the new STARLIGHT outlined above we carried out a set of controlled experiments whereby the observables of a theoretical galaxy are fitted. The simulations are designed analogously to those in Cid Fernandes et al. (2005), where the original STARLIGHT was first tested. The goals here are twofold: *(i)* To gauge the performance of the code under different levels of signal-to-noise (S/N), and *(ii)* to evaluate the practical benefits of a joint UV photometry plus optical spectral analysis in comparison to a purely optical one.

4.3.1 Test galaxies

We generate test galaxies using the parameters (essentially $\vec{x}$ and τ) obtained from the analysis of 260 CALIFA galaxies ranging from early to late types. This strategy has the advantage of ensuring that our test galaxies are both diverse and realistic, while also saving us the trouble of inventing test galaxies with *ad hoc* descriptions of the SFH.

The observables for these test galaxies, namely the 3700–6800 Å optical spectrum O_λ and the m_l^{obs} (where l = NUV, FUV) magnitudes, were generated from their full synthetic spectra and then perturbed according to

$$O_\lambda = O_\lambda^0 \left(1 + \frac{\mathcal{N}(0,1)}{S/N} \right) \tag{4.7}$$

$$m_l^{\mathrm{obs}} = m_l^0 + (2.5 \log e) \frac{\mathcal{N}(0,1)}{S/N} \tag{4.8}$$

where O_λ^0 and m_l^0 are the original input spectrum and magnitudes, and $\mathcal{N}(0,1)$ is a gaussian deviate of zero mean and unit variance. Five levels of noise were considered: $S/N = 5, 10, 20, 50, 100$. (The corresponding errors in magnitudes are 0.217, 0.109, 0.054, 0.022 and 0.011, respectively.) Five realizations of the noise were made for each S/N. In total, the test sample consists of $260 \times 5 \times 5 = 6500$ galaxies.

To emulate actual fits inasmuch as possible we masked regions around the main emission lines, including the whole Balmer series up to Hϵ. As in actual spectral fits (González Delgado et al. 2015) the NaI D doublet was also masked because of its interstellar component.

Each version of each test galaxy was fitted twice: with and without the UV information. Fits considering only the optical spectrum are hereafter called OPT (for optical) fits, while those which also fit NUV and FUV data are called PHO (for photometry) fits.

4.3.2 Example fits

Fig. 4.1 shows an example. The black spectrum and black NUV and FUV points represent the input data for a test galaxy. The blue and red spectra are the results of PHO and OPT fits, respectively, and similarly for the filled blue and open red UV fluxes. Though the full λ-by-λ predicted UV spectrum is drawn, only the NUV and FUV fluxes are relevant in our analysis.

The OPT and PHO fits are so similar in the optical that they cannot be told apart in Fig. 4.1. Indeed their M_λ fluxes differ by less than 1% on average over the fitted range (3700–6800 Å). In the
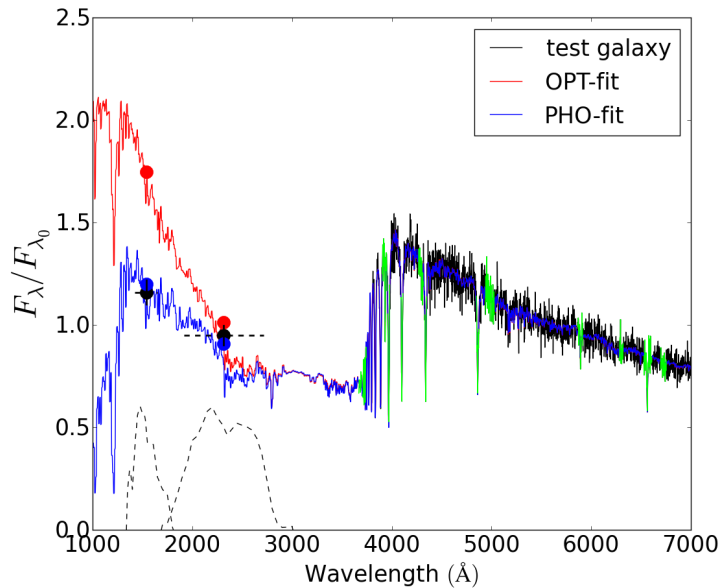
Figure 4.1 Example optical-only (OPT) and optical+UV (PHO) fits of a simulated galaxy. The black line shows the observed spectrum, with masked regions marked in green. Black diamonds and error bars show the NUV and FUV fluxes—the corresponding filter transmission curves are shown as dashed black lines. Red and blue lines show OPT and PHO fits, respectively. The two fits are indistinguishable in the optical, but diverge in the UV, where the lines are drawn as dashed to indicate that we do not have actual UV spectra, but only the photometry, indicated by filled circles. The OPT fit overpredicts the UV fluxes (especially FUV) because of optically-insignificant but UV-dominant young populations (see text).

UV, however, they diverge. While the PHO fit matches the UV data to within the errors, the OPT fit overpredicts the UV fluxes, specially in the FUV filter. That PHO fits perform better in the UV is of course not surprising, since they are designed to take the UV photometry into consideration, while OPT fits ignore it. What is perhaps unexpected is that the two fits so different in the UV yield nearly identical optical spectra.

This happens because the OPT fit ascribes 5% of the light at $\lambda_0 = 5635$ Å (our chosen reference wavelength) to populations of 30 Myr or younger. This small number reflects the insignificant contribution of these populations to the optical spectrum. Removing this component or replacing it by another one would make little difference for the optical fit. Yet, this same component overwhelms all the others at UV wavelengths (Kaviraj et al. 2007b). In the absence of UV constraints, STARLIGHT sees no harm in depositing some small amount of light in this population. Once it is informed about the UV fluxes, however, it realizes that some other combination of base elements must be sought to accommodate both the optical spectrum and the UV photometry. In the case at hand, the 1–30 Myr populations found in the OPT fit shrink to 2% in the PHO fit, being replaced by an increase in populations of 30–100 Myr. In rough terms, one can summarize the change as a shift from populations of O and B to one of B and A stars.

Fig. 4.2 shows three further examples. In all cases PHO fits do an excellent job in fitting both the optical spectrum and the UV photometry. The tendency of OPT fits to overshoot the UV fluxes
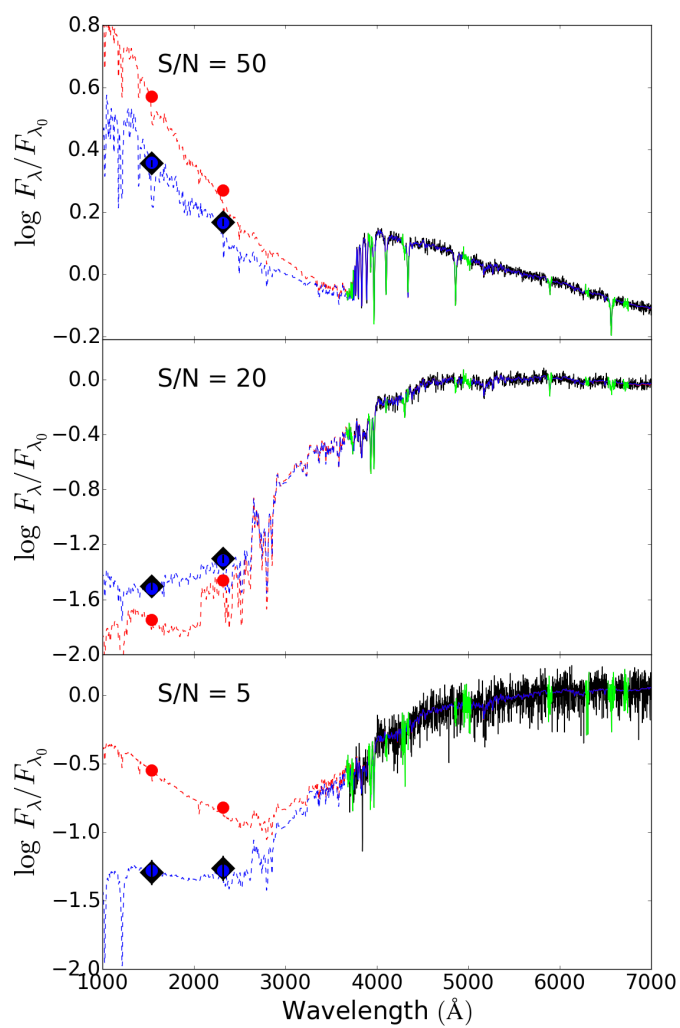
Figure 4.2 As Fig. 4.1 for three further examples of OPT and PHO fits to simulated galaxies. The three panels are representative of blue cloud (top panel), green valley (middle), and red sequence (bottom) galaxies. The labels indicate the S/N of the simulated data.
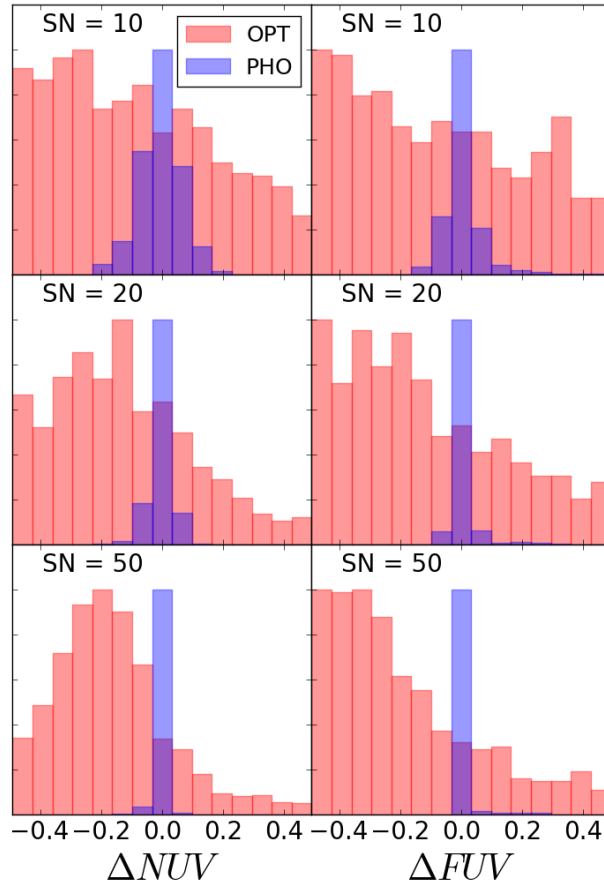
Figure 4.3 Comparison between observed and predicted NUV (left) and FUV (right) magnitudes for simulations with $S/N = 10$, 20 and 50 (from top to bottom). In all panels $\Delta = \text{Predicted} - \text{Observed}$. Histograms have been scaled to the same peak.

is illustrated by the top and bottom examples, but the middle one shows that the opposite can also happen. As observed in Fig. 4.1, the optical spectra are practically indistinguishable between PHO and OPT fits, indicating again that a small variation in the fraction of young stellar populations can be imperceptible in the optical spectra but produce an important change in the UV flux.

As a whole, these examples suggest that a simultaneous analysis of optical spectra and UV photometry should bring some improvement in the estimation of the strength of young stellar populations in a galaxy. For a more global mapping of what actually changes from OPT to PHO we examine the results of the full set of simulations.

4.3.3 Input versus output: UV fluxes

To quantify the performance of the fits we define Δ as the output $-$ input difference in some quantity (say, the NUV magnitude) and examine its statistics. Fig. 4.3 shows the histograms of Δ for both NUV and FUV magnitudes. Different panels are for different S/N values, and blue and red lines are

Summary of simulations: $\overline{\Delta} \pm \sigma_\Delta$

Property (OPT)	S/N = 5	S/N = 10	S/N = 20	S/N = 50	S/N = 100
NUV	-0.25 ± 0.64	-0.26 ± 0.47	-0.22 ± 0.35	-0.19 ± 0.23	-0.16 ± 0.18
FUV	-0.28 ± 1.23	-0.35 ± 0.95	-0.32 ± 0.75	-0.32 ± 0.56	-0.26 ± 0.47
$\chi^2_{\rm SPEC}/N_\lambda^{\rm eff}$	1.06 ± 0.04	1.06 ± 0.04	1.05 ± 0.04	1.05 ± 0.04	1.06 ± 0.05
Property (PHO)	S/N = 5	S/N = 10	S/N = 20	S/N = 50	S/N = 100
NUV	0.00 ± 0.14	0.00 ± 0.08	-0.00 ± 0.04	-0.00 ± 0.02	-0.00 ± 0.02
FUV	-0.00 ± 0.21	0.00 ± 0.12	0.01 ± 0.08	0.01 ± 0.06	0.01 ± 0.05
$\chi^2_{\rm SPEC}/N_\lambda^{\rm eff}$	1.06 ± 0.04	1.06 ± 0.04	1.06 ± 0.04	1.06 ± 0.05	1.07 ± 0.06

Table 4.1 Statistics of the simulations. For each of the NUV and FUV magnitudes the table lists the mean predicted minus observed difference ($\overline{\Delta}$) and its standard deviation (σ_Δ). Also listed is $\chi^2_{\rm SPEC}/N_\lambda^{\rm eff}$, a measure of the qualify of the fit of the optical spectrum. Columns are for the different levels of noise ($S/N = 5, 10, 20, 50, 100$).

for PHO and OPT fits, respectively.

Fig. 4.3 reinforces the conclusions that: (1) PHO fits do match the UV fluxes, as designed to, and (2) OPT fits are lousy predictors of UV fluxes, with large $\Delta m_{\rm NUV}$ and $\Delta m_{\rm FUV}$ even for high quality data. Table 4.1 summarizes these results by listing the mean ($\overline{\Delta}$) and standard deviation (σ_Δ) of Δ for $m_{\rm NUV}$ and $m_{\rm FUV}$ over all test galaxies. Δ and its dispersion behaves as expected for PHO fits, with $\overline{\Delta} \sim 0$ and σ close to the expected noise levels. OPT fits, on the other hand, have a tendency to overpredict the UV fluxes (= underpredict magnitudes, so $\Delta < 0$) by 0.1–0.3 mag, even for high quality data, and σ_Δ is well above the photometric errors.

Table 4.1 also lists the statistics of the $\chi2_{\rm SPEC}/N_\lambda^{\rm eff}$ figure of merit. The results show that the large differences in UV predictions between OPT and PHO fits occur for equivalent performances insofar as the optical spectrum is concerned, corroborating the visual impression drawn from the examples in Figs. 4.1 and 4.2.

4.3.4 Input versus output: Physical properties

The OPT $\times$ PHO comparisons above were carried out in a space of observable quantities (UV magnitudes and optical spectral residuals). We now compare OPT and PHO in terms of physical properties. Table 4.2 (built to be similar to Table 1 in Cid Fernandes et al. (2005)) lists the statistics of Δ as a function of S/N as obtained with these two approaches, and for the suite of properties discussed next.

Stellar mass and extinction

Stellar mass ($M_\star$) is not an explicit parameter in STARLIGHT, but a byproduct of the light fraction population vector ($\vec{x}$) translated to mass fractions ($\vec{\mu}$) through the known light-to-mass ratios of the $N_\star$ base populations. As widely known (Salim et al., 2007; Taylor et al., 2011), and foregoing IMF-related uncertainties, $M_\star$ is a relatively robust quantity in both photometric and spectroscopic analysis.

Table 4.2 shows that $\log M_\star$ is recovered very accurately in the simulations, with $\overline{\Delta} \sim 0$ for both PHO and OPT fits and any S/N. The dispersion (i.e. the uncertainty) in $\Delta \log M_\star$ for OPT fits ranges from $\sigma_\Delta = 0.16$ to 0.06 dex from S/N between 5 and 100, and very slightly smaller for PHO fits. UV info therefore does not help constrain $M_\star$ in any significant way.

<div align="center">Summary of simulations: $\overline{\Delta} \pm \sigma_\Delta$</div>

Property (OPT)	S/N = 5	S/N = 10	S/N = 20	S/N = 50	S/N = 100
$\log M$	-0.03 ± 0.16	-0.02 ± 0.12	-0.02 ± 0.09	-0.01 ± 0.07	-0.01 ± 0.06
τ_V	0.03 ± 0.16	0.02 ± 0.10	0.02 ± 0.06	0.01 ± 0.03	0.01 ± 0.02
$\langle \log t \rangle_L$	-0.11 ± 0.28	-0.08 ± 0.22	-0.06 ± 0.18	-0.06 ± 0.13	-0.04 ± 0.11
$\langle \log t \rangle_M$	-0.04 ± 0.25	-0.02 ± 0.18	0.00 ± 0.14	0.00 ± 0.11	0.00 ± 0.09
$\langle \log Z \rangle_L$	-0.06 ± 0.31	-0.05 ± 0.22	-0.05 ± 0.14	-0.04 ± 0.09	-0.04 ± 0.06
$\langle \log Z \rangle_M$	0.06 ± 0.43	0.04 ± 0.33	0.04 ± 0.22	0.03 ± 0.13	0.03 ± 0.09
x_Y	1.92 ± 8.09	1.38 ± 5.80	1.07 ± 5.16	0.73 ± 4.15	0.42 ± 3.52
x_I	3.56 ± 15.03	2.62 ± 11.65	1.47 ± 7.81	1.55 ± 5.34	1.4 ± 4.51
x_O	-4.47 ± 16.05	-3.16 ± 12.68	-1.71 ± 8.88	-1.46 ± 5.99	-1.04 ± 4.76
μ_Y	0.09 ± 2.88	-0.05 ± 0.74	-0.06 ± 0.44	-0.05 ± 0.47	-0.05 ± 0.39
μ_I	2.65 ± 12.84	1.61 ± 9.23	0.44 ± 5.40	0.43 ± 3.84	0.44 ± 3.03
μ_O	-2.74 ± 13.27	-1.56 ± 9.49	-0.37 ± 5.51	-0.38 ± 4.03	-0.38 ± 3.21
Property (PHO)	S/N = 5	S/N = 10	S/N = 20	S/N = 50	S/N = 100
$\log M$	0.00 ± 0.15	0.00 ± 0.11	0.01 ± 0.08	0.01 ± 0.06	0.01 ± 0.05
τ_V	0.03 ± 0.16	0.01 ± 0.10	0.01 ± 0.05	0.00 ± 0.03	0.00 ± 0.02
$\langle \log t \rangle_L$	-0.01 ± 0.23	0.01 ± 0.16	0.02 ± 0.10	0.02 ± 0.06	0.02 ± 0.05
$\langle \log t \rangle_M$	-0.01 ± 0.23	0.00 ± 0.17	0.02 ± 0.13	0.02 ± 0.10	0.03 ± 0.09
$\langle \log Z \rangle_L$	-0.05 ± 0.30	-0.05 ± 0.22	-0.03 ± 0.13	-0.03 ± 0.07	-0.01 ± 0.05
$\langle \log Z \rangle_M$	-0.05 ± 0.37	-0.03 ± 0.26	-0.03 ± 0.15	-0.02 ± 0.10	-0.01 ± 0.08
x_Y	-0.73 ± 5.48	-0.88 ± 3.98	-0.86 ± 2.98	-0.50 ± 2.08	-0.56 ± 1.75
x_I	3.92 ± 14.76	2.00 ± 10.37	0.69 ± 7.15	0.51 ± 4.45	0.59 ± 3.81
x_O	-2.16 ± 15.24	-0.29 ± 10.95	0.99 ± 7.24	0.79 ± 4.41	0.75 ± 3.53
μ_Y	0.08 ± 3.58	-0.06 ± 0.52	-0.08 ± 0.33	-0.05 ± 0.27	-0.06 ± 0.20
μ_I	1.67 ± 11.15	0.44 ± 7.32	-0.41 ± 4.50	-0.36 ± 3.00	-0.32 ± 2.43
μ_O	-1.74 ± 11.65	-0.38 ± 7.59	0.49 ± 4.59	0.41 ± 3.09	0.38 ± 2.44

Table 4.2 Statistics of the simulations. For each physical property the table lists the mean simulated minus original difference ($\overline{\Delta}$) and its standard deviation (σ_Δ) for S/N varying from 5 to 100. The age-grouped light (x) and mass (μ) fractions are given in percentage.

The same happens with the dust parameter τ_V. In this case, for $S/N = 20$ we have $\overline{\Delta} \pm \sigma_\Delta = 0.02 \pm 0.06$ for OPT-fits, and 0.01 ± 0.05 for PHO-fits. In both cases τ_V is recovered to a similar level of precision.

Mean stellar age and metallicity

Table 4.2 further lists the $\overline{\Delta} \pm \sigma_\Delta$ values for the luminosity weighted mean (log) age ($\langle \log t \rangle_L$) and metallicity ($\langle \log Z \rangle_L$). The first moment of the age distributions is given by $\langle \log t \rangle_L \equiv \sum_j x_j \times \log t_j$, and similarly for the metallicity. Mass weighted versions of these quantities are obtained replacing the light-fraction population vector $\vec{x}$ by its mass-fraction counterpart $\vec{\mu}$.

Examining the entries for these age and metallicity moments in Table 4.2 we see that σ_Δ decreases systematically from OPT to PHO fits, particularly for $\langle \log t \rangle_L$. For $S/N = 20$, for example, the addition of GALEX information to the optical spectrum brings the dispersion in $\Delta \langle \log t \rangle_L$ from 0.18 to 0.10 dex. OPT fits also tend to be slightly biased towards younger ages, by $\overline{\Delta} \langle \log t \rangle_L = -0.04$ to -0.11 dex as S/N decreases from 100 to 5, whereas PHO fits are not biased for any S/N. The bias

is smaller for the mass weighted mean age $\langle \log t \rangle_M$ than for $\langle \log t \rangle_L$, indicating that this difference derives from differences in the young populations, which contribute much more in light than in mass.

The simulations indicate that the GALEX input also improves the stellar metallicity estimates, e.g. from 0.04 ± 0.22 to -0.03 ± 0.15 dex in $\Delta\langle \log Z \rangle_M$ for OPT and PHO $S/N = 20$ fits respectively. As for the mean stellar age, this improvement reflects the enhancement in the ability to estimate the contribution of young stellar populations.

Star formation history: Condensed population vector

There are several ways to process STARLIGHT's output population vectors into quantities which describe a galaxy's SFH. One which has been widely explored in the past (González Delgado et al., 2004; Cid Fernandes et al., 2004, 2005) is to rebin $\vec{x}$ on to 'young' ($t_j < 10^8$ yr), 'intermediate-age' ($10^8 \leq t_j \leq 10^9$ yr), and 'old' ($t_j > 10^9$ yr) populations (x_Y, x_I and x_O, respectively).

Table 4.2 shows the statistics of Δx_Y, Δx_I, Δx_O. As expected, the σ_Δ dispersions decrease for increasing S/N. All components of this condensed population vector have smaller uncertainties when UV constraints are added, i.e. as one goes from OPT to PHO fits. The gain is markedly larger for the youngest components, as might be expected given that young populations, when present, have a dominant contribution in the UV. Focusing again on the $S/N = 20$ simulations, we obtain that $\sigma_{\Delta x_Y}$ decreasing by $\sim 42\%$ as UV constraints are incorporated, while $\sigma_{\Delta x_I}$ and $\sigma_{\Delta x_O}$ decrease by some 8 and 18% respectively. The same conclusion applies to the condensed mass-fractions population vector (μ_Y, μ_I, μ_O), also included in Table 4.2.

In line with the mean age and metallicity results reported just above, we conclude that the simulations corroborate the basic intuitive notion that the addition of UV information to an optical spectral analysis is specially helpful in constraining the properties of young stellar populations (up to ~ 300 Myr). It is therefore natural to expect our optical+UV STARLIGHT analysis to be particularly relevant for systems containing O, B and/or A stars, the UV-dominant component under most circumstances. This expectation is born out in the next Section.

4.4   Application to CALIFA+GALEX data

The experiments above served to validate the new capabilities of STARLIGHT, as well as to provide a general sense on the changes resulting from the addition of UV photometry to an optical spectrum as observables in the analysis. In this section we apply to real data, combining CALIFA spectra with GALEX magnitudes. Fig. 4.4 shows galaxies scattered from the blue cloud to the red-sequence in a UV-optical colour magnitude diagram (CMD).

All the analysis in this section is based on spatially integrated data. In Section 4.5 we further explore results obtained from four spatial extractions: $r <0.5$, $r < 1$, $1 < r < 2$, and $r > 1$, where r denotes the radial distance to the nucleus in units of the optical Half Light Radius (HLR).
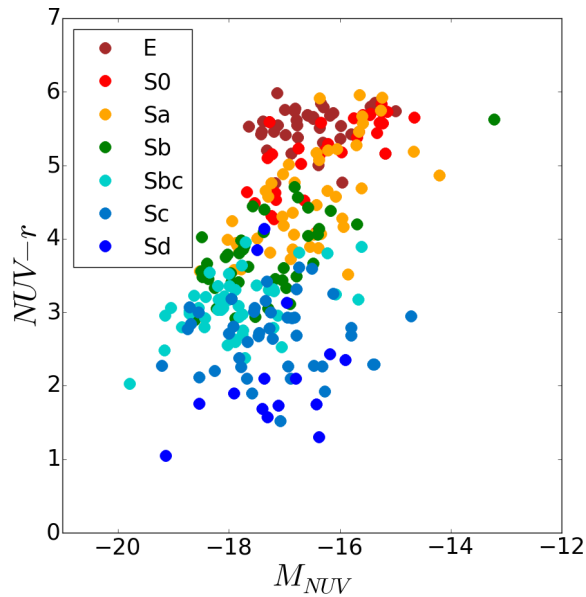
Figure 4.4 Distribution of the 260 galaxies in the colour magnitude diagram M_{NUV} vs $NUV - r$. Colour codes distinguish the morphological type, as labelled.

4.4.1 Results

In analogy with the sequence followed in Section 4.3, we first present the results regarding STARLIGHT's algorithmic goal, which is to fit the input observables (Sec. 4.4.1), and then in terms of the stellar population properties derived from the fits (Sec. 4.4.1). Except for the observational errors, which in this case come from the actual data, the STARLIGHT analysis was performed exactly as described in Section 4.3, with OPT fits analyzing only the 3700–6800 Å spectra, and PHO fits adding the NUV and FUV magnitudes to the fit.

STARLIGHT **fits**

Fig. 4.5 exemplifies the STARLIGHT fits with three galaxies: NGC 3057 (top), IC 4215 (middle), and UCG 05771 (bottom). As in Fig. 4.2, OPT fits are shown in red and PHO fits in blue. As in the simulations, the optical spectra are equally well fitted in both kinds of fits. For instance, the mean percent deviation between O_λ and M_λ (eq. 6 in Cid Fernandes et al. (2013)) are 2.8 and 3.1% in OPT and PHO fits. Also as in the simulations, differences emerge in the UV. Again, UV fluxes tend to be overpredicted in OPT fits (top and bottom panels), but this is just a tendency, not a general rule. Cases like IC 4215 (middle panel), where the OPT predictions fall short of the observed UV fluxes, also happen.

Fig. 4.6 shows the NUV versus $NUV - r$ CMD derived from the synthetic photometry over the fitted spectra. As expected, the PHO-based CMD (upper panel) matches the observed one (Fig. 4.4), with rms differences of just 0.025 mag in M_{NUV} and 0.044 in $NUV - r$. OPT fits, however, predict a wrongly shaped CMD. The incorrectly predicted NUV fluxes produce shifts in both M_{NUV} and $NUV - r$. The red sequence scatters towards both redder and bluer colours (as can be seen comparing
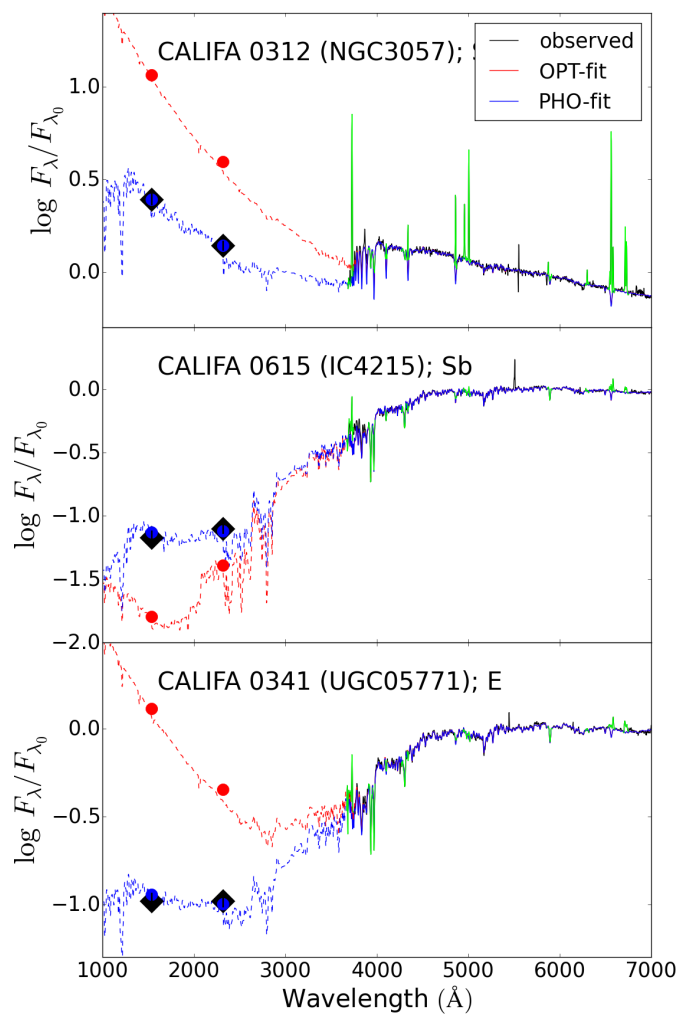
Figure 4.5 Example OPT and PHO fits for three galaxies of different morphological types: The Sd galaxy NGC 3057 (top), the Sb IC 4215 (middle), and the elliptical UCG05771 (bottom).
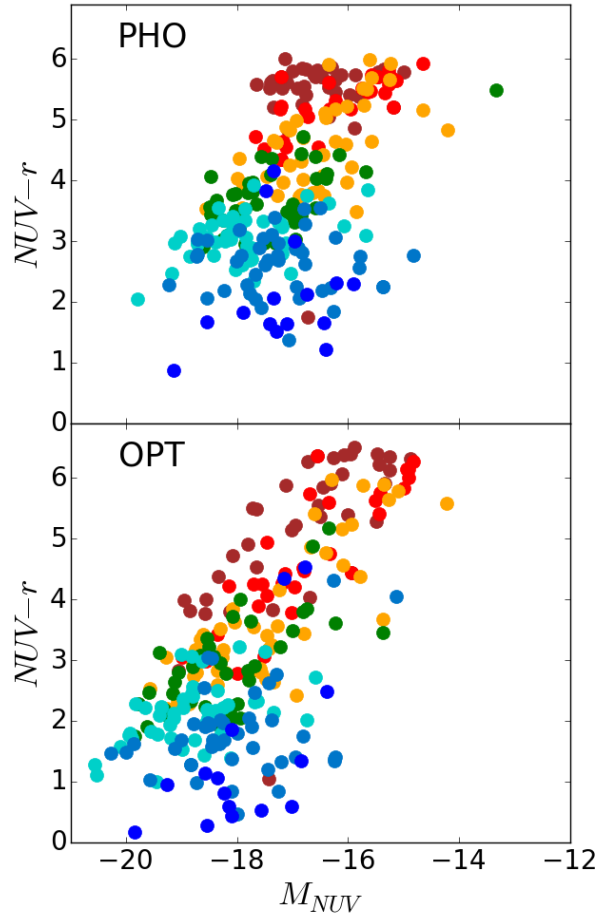
Figure 4.6 Synthetic magnitudes in the colour magnitude diagram M_{NUV} vs $NUV - r$ for PHO (top) and OPT (bottom) fits.

the location of E galaxies in the two panels), while late type systems become both bluer and more luminous. As found in the simulations, OPT fits are poor predictors of the UV properties, particularly for systems in the blue cloud.

Physical properties: Mass and dust attenuation

Now we turn the focus from the observables to the stellar population properties derived from the analysis. Fig. 4.7 compares PHO and OPT results for a series of properties, where points are colour coded by the Hubble type.

Stellar masses, shown in the top-left panel, are essentially the same in PHO and OPT fits. Defining Δ as the PHO $-$ OPT difference in the value of any given property, we find a mean value of $\overline{\Delta} = 0.04$ dex for $\log M_{\star}$, with a dispersion $\sigma_{\Delta} = 0.09$ dex. The scatter is somewhat larger for late type systems, but still very small. For instance, for Sc–Sd galaxies (blue points) we obtain $\overline{\Delta} = 0.05$ and $\sigma_{\Delta} = 0.1$ dex, whereas for E-S0-Sa we obtain $\overline{\Delta} = 0.01$ and $\sigma_{\Delta} = 0.05$ dex.
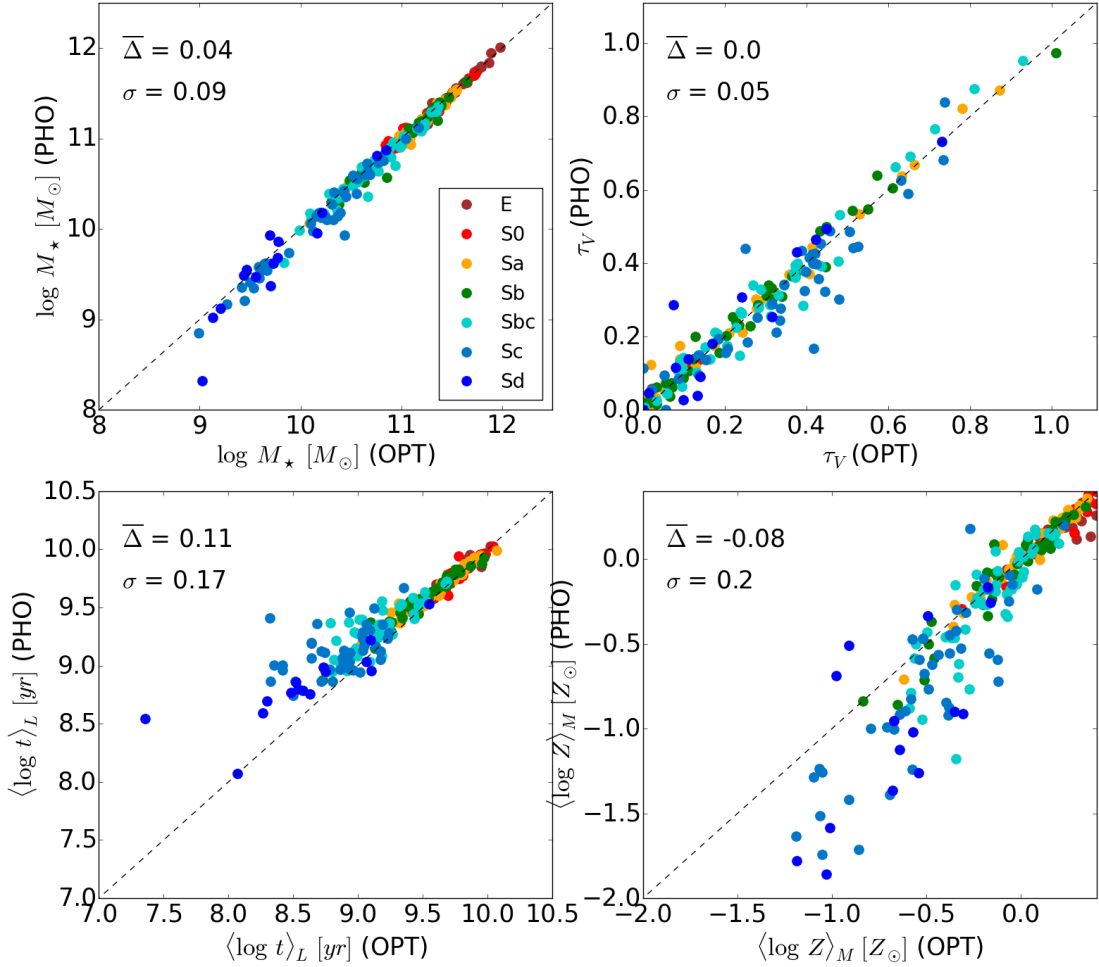
Figure 4.7 Comparison of physical properties obtained with OPT and PHO fits. Each panel lists the average of the $\Delta = \text{PHO} - \text{OPT}$ difference ($\overline{\Delta}$) and its standard deviation (σ_Δ).

Regarding the τ_V values, we again observe no significant differences between PHO and OPT results, as seen in the top-right panel of Fig. 4.7. In this case we obtain $\overline{\Delta} = 0.0$ and $\sigma = 0.05$. Late type systems (bluer points) are again the ones with a larger dispersion; $\sigma = 0.07$ if only Sc and Sd galaxies are considered. As a whole, however, and in agreement with the results of our simulations, neither $M_\star$ nor τ_V estimates gain much from the addition of UV constraints to a purely optical, conventional STARLIGHT spectral fit.

A note on why $\tau_V(\text{PHO}) \sim \tau_V(\text{OPT})$

The apparently negligible impact that UV information has upon our derived values of τ_V is perhaps surprising in light of the known sensitivity of UV fluxes to dust. Though subtle, the reasons for this somewhat counter intuitive result are easily understood. This section opens a parenthesis to explain

them.

First, recall that OPT fits over predict the UV flux, so that PHO fits must find solutions which produce less UV. At the same time, and this is the key constraint here, PHO fits must keep the predicted optical spectrum essentially unchanged, since they must (by design) match both UV and optical data. UV fluxes can be diminished by: (1) increasing τ_V, (2) decreasing the contribution of young stars (x_Y), and/or (3) increasing the age of the young population. The latter of these three (non-exclusive) alternatives is much more plausible than the others.

The first of these solutions is problematic. More dust may lead to the correct UV fluxes, but the larger reddening would then require increasing x_Y to bluen the optical colours back to the observed values. More x_Y would in turn imply more UV and require further increasing τ_V until an optimal balance is achieved. Note that even if this works in terms of colours, the increase in x_Y would dilute absorption lines and hence degrade the quality of the optical fit. Increasing the age and metallicity of the old populations could perhaps restore the observed strengths of absorption features, but at this point it is clear that this route is a highly contrived one. The second alternative suggested above, namely, decreasing x_Y, sounds less problematic, but it is not a complete solution per se since the missing light must be replaced by something else. This 'something else' should look like young stars in the optical but have a smaller UV per optical photon output.

This brings us to the third and more natural solution: Aging the young population. From the optical point of view, populations of a few Myr or a few tens of Myr are very similar. For instance, and fixing Z at $Z_\odot$ for convenience, populations of 3 and 50 Myr have $g - r$ colours of -0.5 and 0, and $D_n(4000)$ of 0.9, and 1.0, respectively. These relatively small differences contrast with the strong evolution of the UV, with $NUV - r$ changing from ~ -1.3 to $+0.5$ over the same time span. A change from populations of a few Myr to a few tens of Myr therefore produces the kind of result we need: less UV-per-optical emission at $\sim$ constant optical colours. As discussed later in Section 4.4.1, the retrieved SFHs of OPT and PHO fits confirm this interpretation.

Aging the youngest populations thus offers the best way of simultaneously satisfying optical and UV constraints, which explains why τ_V remains approximately unaltered between OPT and PHO fits. It is adequate to recall that this conclusion applies to the simple foreground dust screen scenario adopted in this thesis. Fits which allow for population-dependent τ_V-values will certainly be more sensitive to the addition UV information.

Physical properties: Mean stellar age and metallicity

The bottom panels of Fig. 4.7 compare mean age ($\langle \log t \rangle_L$) and metallicity ($\langle \log Z \rangle_M$) values as estimated from PHO and OPT fits. Here we see an effect which was also detected in the simulations: The difference in $\langle \log t \rangle_L$ is mainly due to the youngest systems, which are somewhat older in PHO than in OPT. By virtue of the inter relations between mass, age, metallicity, and morphology, these young galaxies are also late types (Sbc–Sd) of low mass and metallicity.

Metallicities, on the other hand, change in the opposite direction, decreasing from OPT to PHO (bottom right panel of Fig. 4.7). Again, the effect is negligible for most galaxies, but can be significant for late type ($M_\star \lesssim 5 \times 10^9 M_\odot$) systems. For these galaxies we obtain $\overline{\Delta} = -0.4$ and $\sigma = 0.26$ dex,
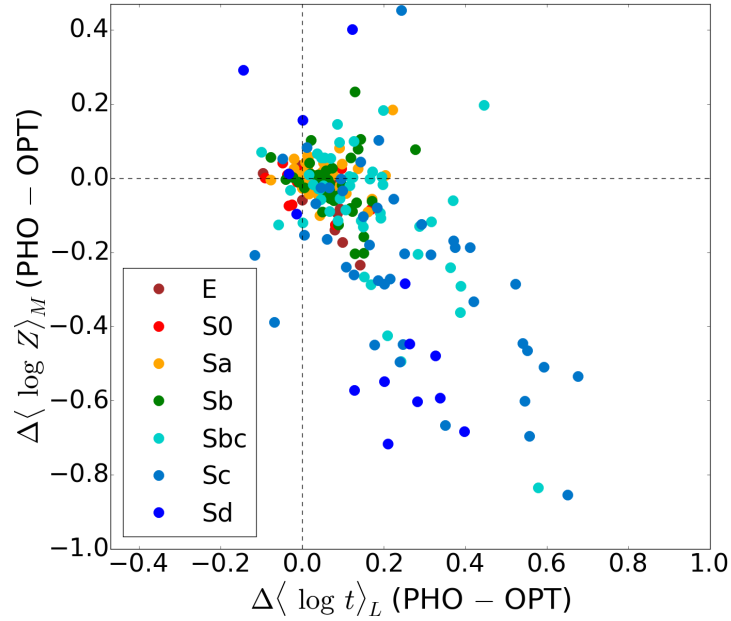
Figure 4.8 Comparison between age and metallicity variations obtained with OPT and PHO fits.

whereas for more massive systems the bias and dispersion are just $\overline{\Delta} = -0.04$ and $\sigma = 0.15$ dex.

Fig. 4.8 shows that the changes in age and metallicity are anti correlated, reflecting the well known age-metallicity degeneracy (Worthey 1994). Note, however, that this degeneracy is more frequently studied in the context of early type galaxies and their old stellar populations, while Figs. 4.7 and 4.8 show that it is late type systems which are affected the most. These are precisely the galaxies for which estimates of the stellar metallicity are harder to obtain, and our results indicate that the UV photometry brings in useful information to improve such estimates.

Finally, we emphasize that even though the anti-correlation stands out in Fig. 4.8, the majority of points cluster around $\Delta\langle\log t\rangle \sim \Delta\langle\log Z\rangle_M \sim 0$, with variations within the uncertainties expected from the simulations. Coupled to the negligible changes in $M_\star$ and τ_V, we conclude that for most galaxies the stellar population properties derived from OPT and PHO fits are consistent with one another.

Star Formation History

In STARLIGHT the SFH is encoded in the light ($\vec{x}$) or mass ($\vec{\mu}$) population-vectors. As documented elsewhere (Cid Fernandes et al., 2004, 2014), the individual components of these arrays are highly uncertain, but a coarser description in terms of broad age bins, or, equivalently, smoothed versions of $\vec{x}$ and $\vec{\mu}$, is robust.

In order to capture general trends in the SFH of our galaxies and how these change from OPT to PHO fits we first smooth the age distribution in $\vec{x}$ and $\vec{\mu}$ by a gaussian in $\log t$ with a FWHM of 0.7 dex, and average the results in three morphology-defined groups of galaxies: early (E, S0 and Sa), intermediate (Sb and Sbc), and late (Sc, Sd) types. These groups can be seen also as representative
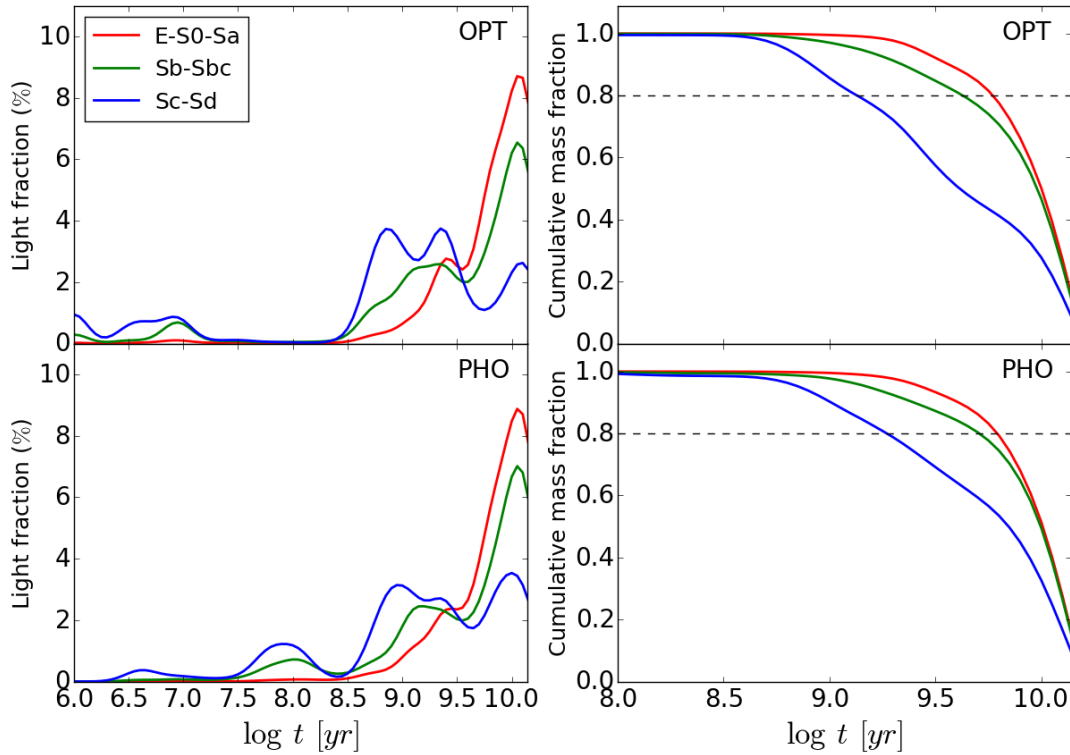
Figure 4.9 Mean star formation histories of early (red) intermediate (green) and late (blue) type galaxies, as derived from OPT (top panels) and PHO (bottom) fits. Left panels show smoothed versions of the light-fraction population vector ($\vec{x}$), plotted against the lookback time t. Right panels show the smoothed cumulative mass fraction functions, obtained by rescaling the mass converted into stars up to a lookback time t to a 0–1 scale. The 80 per cent line is drawn for reference.

of red, green and blue galaxies, respectively.

The results are shown in Fig. 4.9. Top panels are for OPT fits and bottom ones for PHO. The left plots show the smoothed age distribution in terms of their contribution to the flux at our chosen normalization wavelength $\lambda_0 = 5635$ Å, while the ones on the right present the cumulative contribution in terms of mass, re-scaling the mass turned into stars onto a 0–1 scale. Because of the highly non-linear mass-to-light relation of stars, these mathematically equivalent descriptions of the SFH highlight different aspects of the problem.

In terms of light fractions (left panels in Fig. 4.9), the more relevant differences between OPT and PHO fits are seen for ages < 300 Myr. In particular, the $t < 10$ Myr populations seen in OPT fits shift towards $t \sim 30$–300 Myr when UV constraints are included. This explains the excessive UV flux predicted in OPT fits and the systematically older mean ages obtained with PHO fits. Note, however, that this effect is basically restricted to blue and, to a lesser extent, green galaxies. The SFHs of red (early-type) galaxies do not change significantly from OPT to PHO fits. These results clarify the origin of the differences in luminosity weighted mean stellar ages seen in the bottom-left panel of Fig. 4.7, where late types stand out as the only ones with significant changes in $\langle \log t \rangle_L$.
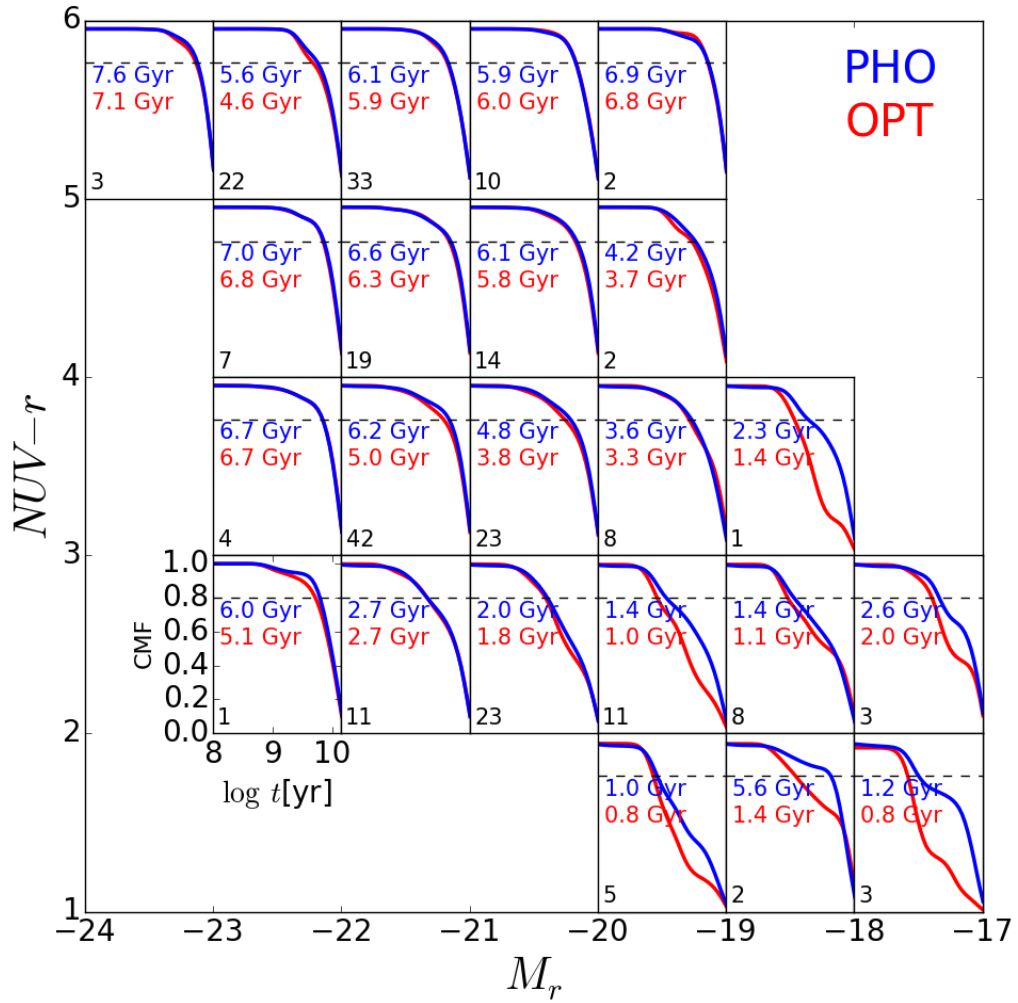
Figure 4.10 Cumulative mass fraction for galaxies in the $NUV - r$ versus M_r CMD. Dashed line indicates 80 per cent of the total mass. Blue profiles show the results with PHO fits and red profiles show the results with OPT fits. The number on bottom left of each panel shows the number of galaxies in the bin used to compute the mean curve. The age when 80 per cent of the mass is reached is listed in blue for PHO and red for OPT fits.

In contrast to left panels, the SFHs on the top and bottom right panels of Fig. 4.9 are hardly distinguishable. The only visible difference is for blue galaxies, and even then the cumulative mass fractions are very similar. To quantify the differences we compute the age at which the stellar mass has grown to 80 per cent of the total. OPT fits yield $t_{80\%} = 1.3$, 4.2, and 5.9 Gyr for blue, green and red galaxies respectively, while in PHO-fits these values become $t_{80\%} = 1.7$, 5.0, and 5.9 Gyr. This similarity is a consequence of the OPT-PHO changes occurring in relatively young stellar populations, that carry significant light but little mass.

In Fig. 4.10 we break up the mass assembly histories in boxes of 1×1 mag bins in the $NUV - r$ versus M_r CMD, first studied by Wyder et al. (2007). The gradual shift in SFHs towards more recent lookback times as one descends from red to blue bins reflects the strong relation between the $NUV - r$ colour and mean stellar age (further explored in Section 4.5), while the general aging as one moves towards more luminous (smaller M_r) bins reflects the well known cosmic downsizing (better appreciated by mentally collapsing the CMD along its y-axis). These general tendencies are seen in both OPT and PHO fits.

Regarding the differences in SFH between OPT and PHO fits, Fig. 4.10 reinforces the conclusion that they are essentially limited to low mass, blue galaxies, as further confirmed by comparing the values of $t_{80\%}$, listed in blue for PHO and red for OPT fits.

4.5   Discussion

The simulations and empirical results presented above showed that (1) the new code works, i.e. it simultaneously fits an optical spectrum and UV photometry, as designed to, and (2) OPT and PHO fits only differ relevantly for low-mass, late type-galaxies, whose mean ages become somewhat older while their mean metallicities tend to decrease.

In this section we discuss how the addition of UV constraints affects previously known results. We first examine empirical relations between mean stellar age and observables such as colours and the 4000 Å break (Section 4.5.1). The scatter in these relations provides an indirect way of assessing whether PHO fits are more reliable than OPT ones, as intuitively expected. We then revisit the relation between stellar metallicity and (a) mass, and (b) mass surface density, comparing with previous OPT-based CALIFA results with those obtained with our CALIFA + GALEX sample.

4.5.1   Empirical age indicators

Because PHO fits incorporate more constraints one tends to regard their output results as superior to those derived from OPT fits. Still, it would be nice to have some independent way of evaluating which approach produces better results.

We perform this judgement by comparing the scatter in empirical relations such as those shown in Fig. 4.11, where we relate our STARLIGHT-derived luminosity weighted mean (log) stellar age to observable properties. Top panels show the correlation between $\langle \log t \rangle_L$ and the $NUV - r$ colour, while in the middle and bottom panels the x-axis is replaced by $u - r$ and the 4000 Å break index, both purely optical properties. Left and right columns correspond to PHO and OPT fits, respectively. The data used in this figure come from the extended data set, containing both integrated properties and
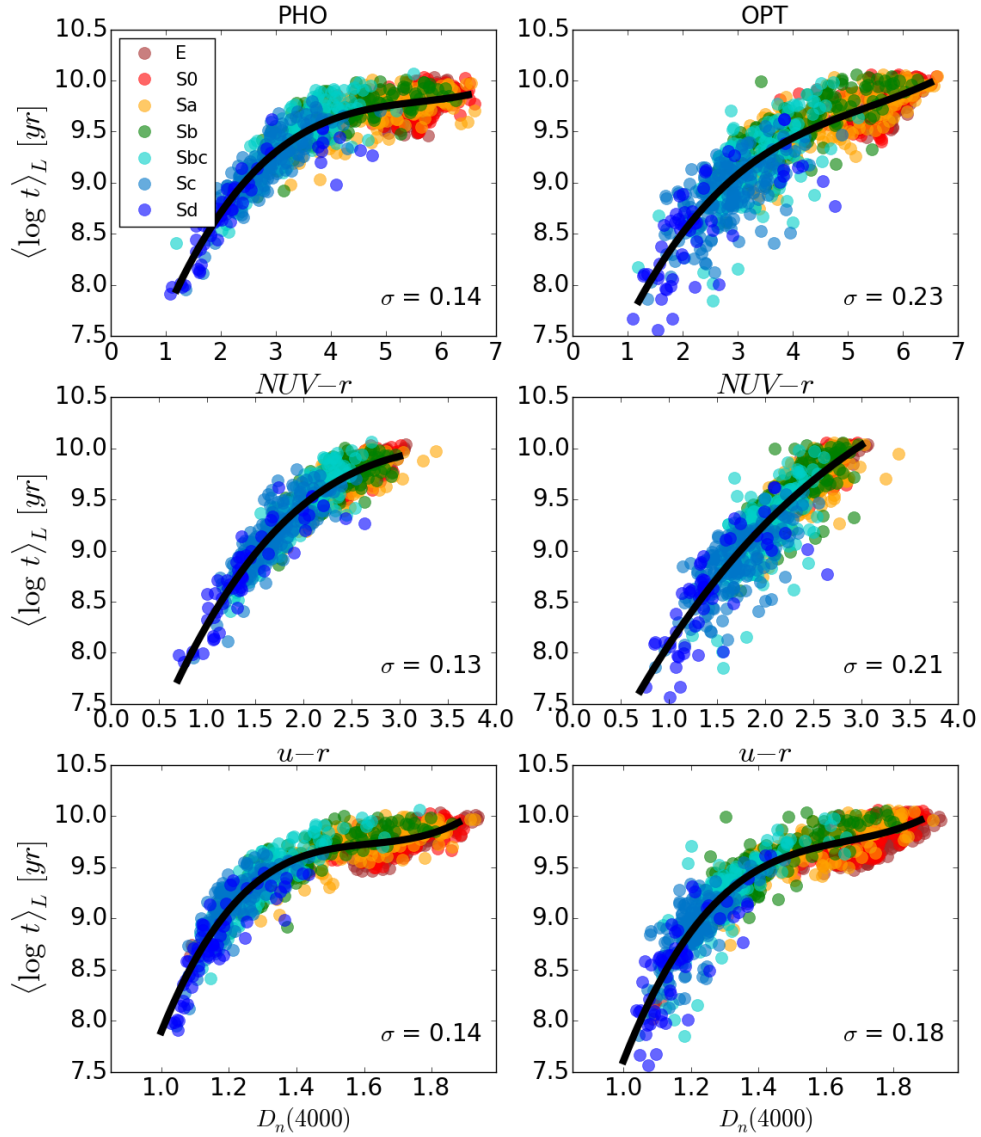
Figure 4.11 Empirical correlations between the STARLIGHT-derived luminosity weighted mean stellar age and the observed $NUV - r$ (top panels), $u - r$ (middle), and $D_n(4000)$ (bottom). Left panels are for PHO-fits and right ones for OPT fits. The black lines show polynomial fits to the points (see Table 4.3), and σ denotes the rms dispersion with respect to these lines. Points are coloured by morphological type following the palette in Fig. 4.4. The points in these diagrams come from four different radial extractions for each galaxy.

Empirical age indicators: Polynomial fits

Age indicator (x)	PHO	OPT
$NUV - r$	$0.0176x^3 - 0.2991x^2 + 1.7402x + 6.3182$	$0.0150x^3 - 0.2421x^2 + 1.4965x + 6.3654$
$u - r$	$0.0544x^3 - 0.6761x^2 + 2.8225x + 6.0703$	$0.0242x^3 - 0.3487x^2 + 2.0571x + 6.3474$
$D_n(4000)$	$6.86773x^3 - 33.3609x^2 + 54.3533x - 19.9681$	$5.9043x^3 - 29.4365x^2 + 49.5827x - 18.4440$

Table 4.3 Polynomial fits for empirical relations between mean (luminosity weighted) stellar age obtained with STARLIGHT and different observables (see Fig. 4.11): $\langle \log t/\mathrm{yr} \rangle_L = ax^3 + bx^2 + cx + d$, where $x = NUV - r$, $u - r$, or $D_n(4000)$.

values derived from four different spatial extractions. The improved statistics of this larger sample serves to better delineate the correlations.

A simple visual inspection suffices to conclude that the OPT-based relations are more dispersed than those based on PHO fits. This is not really unexpected in the case of the top panels, since OPT fits are completely oblivious of the $NUV - r$ colour, whereas PHO fits do take this information into account. In the middle and bottom panels, however, the x-axis represents properties which are known to both OPT and PHO fits. Still, the relations between $\langle \log t \rangle_L$ and $u - r$ and between $\langle \log t \rangle_L$ and $D_n(4000)$ are visibly better defined with PHO mean ages than with OPT ones. This improvement can be quantified by comparing the σ values given in each panel of Fig. 4.11, which represent the dispersion around the polynomial fits shown as solid lines and whose coefficients are given in Table 4.3. The scatter in OPT-based relations is almost twice as large as for PHO-based ones. As is evident from the cyan-blue colour of most outliers, this reduced scatter occurs because of late-type galaxies.

In short, besides taking more observational constraints into consideration, PHO fits produce better behaved mean stellar ages than OPT fits, in the sense that they correlate better (less scatter) with classical observable age indicators. PHO thus outplay OPT in this qualitative assessment.

4.5.2   Less age-metallicity-extinction degeneracies with UV data

Age and metallicity are more sensitive to UV than optical colours (Yi et al. 2004), and previous studies suggest that combining optical and UV provides better estimates of ages and can effectively break (or at least mitigate the effects of) the age-metallicity degeneracy (Yi, 2003; Kaviraj et al., 2007b). Indeed, we have just seen that a combined optical+UV analysis produces more accurate mean age estimates than a purely optical one for Sbc–Sd galaxies.

Because of the known covariances amongst stellar population properties, more accurate ages should also lead to more accurate metallicity and reddening estimates. Here we examine the origin of the dispersion in the empirical relations shown in Fig. 4.11.

In Fig. 4.12 we use the best fit $\langle \log t \rangle_L(NUV - r)$ relation given in Table 4.3 to investigate what third variable is responsible for the scatter in mean stellar age at fixed UV-optical colour. The figure shows the $\delta \langle \log t \rangle_L \equiv \langle \log t \rangle_L - \langle \log t \rangle_L(NUV - r)$ residual as a function of τ_V (top panels) and $\langle \log Z \rangle_M$ (bottom), for both PHO (left) and OPT fits (right). A strong anti correlation with τ_V is seen for both PHO and OPT fits, with $\delta \langle \log t \rangle_L$ becoming increasingly negative for increasing τ_V. This anti correlation is expected given the long wavelength baseline in the $NUV - r$ colour, which makes it susceptible to τ_V. The relation is steeper and visibly more dispersed for OPT fits.
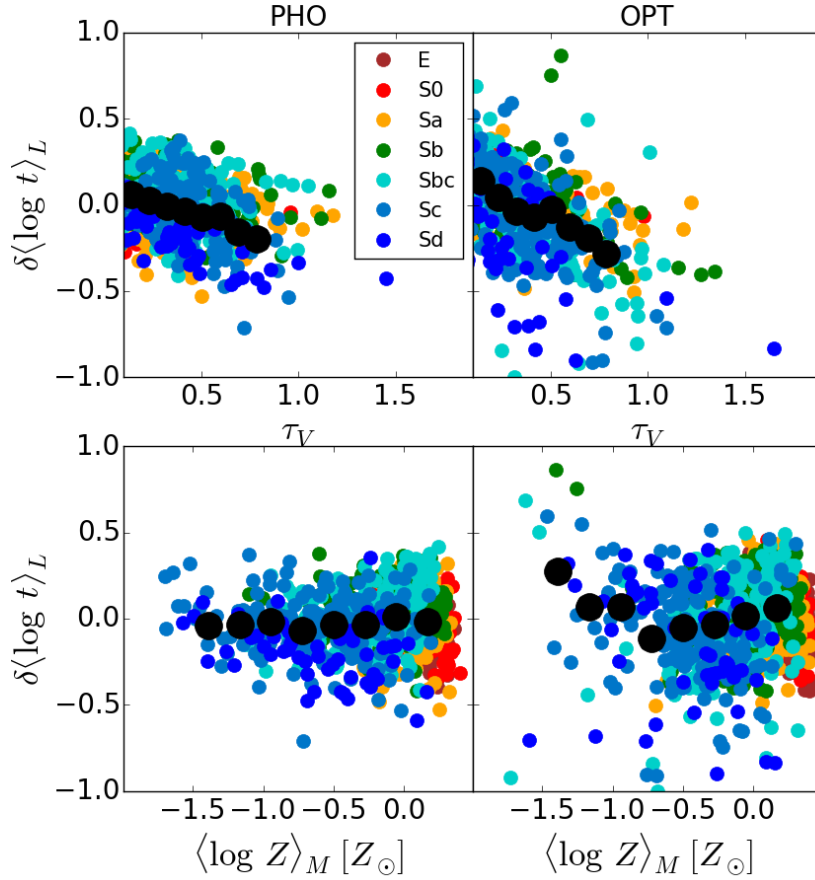
Figure 4.12 Residual from the $\langle \log t \rangle_L (NUV - r)$ relation (solid line in the top panels of Fig. 4.11) plotted against dust optical depth (top) and mean stellar metallicity (bottom), for both PHO (left) and OPT (right) fits. Black points trace the mean values for bins in the x-axis.

For OPT fits, metallicity also seems to play a role in the dispersion around the $\langle \log t \rangle_L (NUV - r)$ relation, as inferred from the bottom right panel of Fig. 4.12. Besides a significant dispersion, the trend of increasing $\delta \langle \log t \rangle_L$ for decreasing $\langle \log Z \rangle_M$ at low metallicities is qualitatively consistent with what one expects from the age-metallicity degeneracy. PHO fits, on the other hand, produce a $\sim$ flat relation between $\delta \langle \log t \rangle_L$ and $\langle \log Z \rangle_M$ (bottom left panel), indicating that the inclusion of UV data indeed minimizes the effect of the age-metallicity degeneracy with respect to fits considering only the optical spectrum. This qualitative assessment therefore reinforces our conclusion that PHO fits produce better constrained physical properties.

4.5.3   The stellar mass-metallicity relation

One of the most important correlations in galaxy evolution work is the one between mass and metallicity (Tremonti et al., 2004; Gallazzi et al., 2005). González Delgado et al. (2014a) have presented a STARLIGHT-based study on the relations between stellar metallicity and mass in CALIFA galaxies, both on global (i.e. galaxy-wide) and local (spatially resolved) scales. In this section we examine
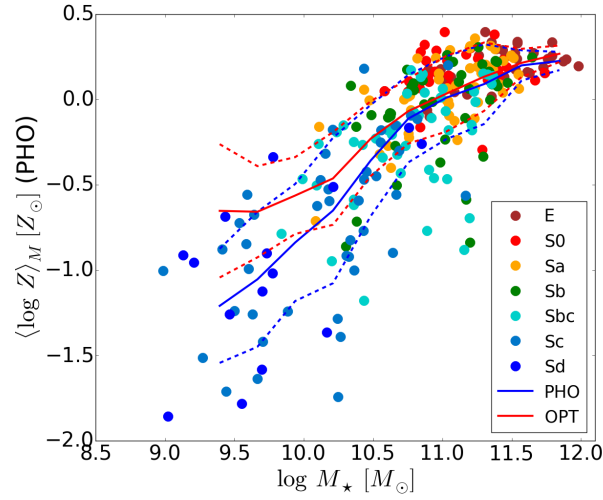
Figure 4.13 The mass-metallicity relation obtained with PHO fits. Blue lines indicate the mean profile with $\pm\sigma$ standard deviation (solid and dashed lines, respectively). Red lines show the mean mass-metallicity relation profile obtained with OPT fits with $\pm\sigma$ standard deviation (solid and dashed lines, respectively).
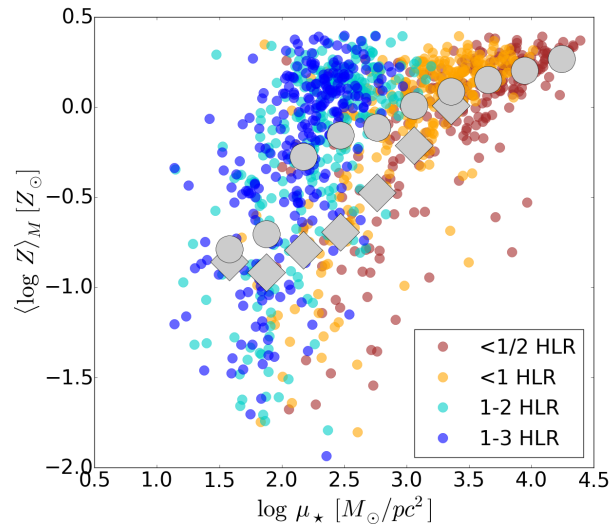
Figure 4.14 Local stellar metallicity versus the local stellar mass surface density obtained with PHO fits. Colours code results obtained for different radial extractions (in units of the optical Half Light Radius). Grey circles track the $\mu_\star$-binned average $Z_\star(\mu_\star)$ relation. Grey diamonds track the relation for Sc and Sd galaxies.

whether and how the mass-metallicity (MZR) and surface mass density-metallicity (μZR) relations change with the addition of UV data to spectroscopic data.

Our comparative analysis of PHO and OPT fits showed that changes in the mean stellar metallicity are only relevant and systematic for late type galaxies (Fig. 4.7), whose $\langle \log Z \rangle_M$ values decrease by ~ 0.4 dex on average. These presumably more accurate estimates are particularly welcome for these low-mass, star-forming galaxies, where the inherent difficulties in estimating stellar metallicities are aggravated by the almost featureless continuum of their hot stars, which heavily dilute the absorption lines carrying information on Z.

We can thus anticipate that changes in the MZR should be restricted to the low Z, low $M_\star$ end of the relation. This is confirmed in Fig. 4.13, where we show the PHO-based MZR. The blue lines show the smoothed mean relation (solid line) and the corresponding $\pm 1\sigma$ range (dashed). The OPT-based MZR for this sample is shown by the red line. As expected, the two are essentially identical at the high mass end, diverging towards low masses, with PHO fits reaching lower metallicities.

Fig. 4.14 presents the μZR as derived from our optical+UV STARLIGHT analysis. Small points are coloured according to the four spatial extractions. Despite the much coarser spatial resolution, the same dichotomy identified by González Delgado et al. (2014a) is seen in our PHO-version of the local μZR, with inner regions (brown and orange points) exhibiting a visibly flatter μZR than outer ones (cyan and blue). In fact, because of the stretched $\langle \log Z \rangle_M$ scale, this dichotomy becomes ever clearer than in a purely optical analysis. Reinforcing the results of González Delgado et al. (2014a), we find that the mean stellar metallicity is strongly related to the local density within galactic discs, while in spheroids $\mu_\star$ does not seem to play a major role in controlling chemical evolution.

The large grey circles in Fig. 4.14 show a smoothed mean μZR, obtained by averaging $\langle \log Z \rangle_M$-values in bins of $\mu_\star$. This mean μZR reflects the dual behaviour of the individual points, with an initially steep relation becoming weaker (flatter) above $\sim 10^{2.5} M_\odot \, \mathrm{pc}^{-2}$. Diamonds in Fig. 4.14 indicate the mean μZR obtained when restricting the sample to Sc and Sd galaxies. The metal poor, dense, inner (red and orange) zones of these late type galaxies account for nearly all of the outliers at $\mu_\star \gtrsim 10^3 M_\odot \, \mathrm{pc}^{-2}$. As suggested by González Delgado et al. (2014a), this may be related to the $\sim$ bulgelessness of these systems making their inner regions behave in a disc-like way in the stellar metallicity versus surface mass density space.

4.6 Conclusions

In this chapter we have presented a extended version of STARLIGHT by means a simulations an application to real data. The main results can be summarized as follows:

- By themselves, optical spectral fits are poor predictors of the UV properties, with errors of the order of 0.5 mag and a tendency to overpredict the fluxes, even for high signal-to-noise. This happens because optically insignificant young stellar populations can dominate the emission in the UV, so that even minor errors in the estimation of their optical contribution translate into large errors in the UV.

- Besides matching the input UV data to within the errors, the new optical+UV fits reduce the

uncertainties in the derived stellar properties.

- Applying the code to a combination of CALIFA+GALEX data we find that including UV photometry in the fits better constrains the contribution of stellar populations younger than ~ 300 Myr. PHO fits tend to replace $\lesssim 30$ Myr components by populations in the neighbourhood of 100 Myr (i.e. from O and B stars to B and A).

- Despite their poor performance in predicting the UV fluxes, for nearly 90% of our sample OPT fits yield stellar population properties which agree with those obtained with PHO fits to within the expected uncertainties. The differences are exclusively found in low-mass, late-type galaxies, precisely the systems where, because of their significant $\lesssim 300$ Myr population, one would expect the addition of UV constraints to play a more relevant role.

- For Sc and Sd galaxies with $M_\star < 5 \times 10^9 M_\odot$ we find that an optical+UV analysis yields older ages and lower metallicities than those derived with purely optical fits. These changes imply a steepening of the relations between stellar metallicity and mass (MZR) and surface density (μZR) at the low Z end, making the dual disc and spheroid behaviours even clearer than previously reported with OPT-based studies by our own group.

- Empirical relations between our (luminosity weighted) mean stellar age and observables such as the 4000 Å break, and UV and optical colours, are all less dispersed for PHO than for OPT fits, which indicates that the inclusion of UV constraints helps mitigating degeneracies between age, dust and metallicity.

5

Parametric SFHs

Contents

5.1   Introduction

In this chapter we present a different tool to derive the stellar population properties of galaxies, based on parametric SFHs. Unlike the stochastic SFH obtained with STARLIGHT, now we impose a particular parametric model. There are many examples in the literature where the stellar population properties have been derived using a parametric approach (Ganda et al., 2007; McArthur et al., 2004; Kauffmann et al., 2003) where a predefined shape for the star formation history and chemical enrichment is assumed. In this case, some parameters are fixed while others are fitted by comparing the observations with the predictions of the models. The main problem with this approach is that the results depend strongly on the priors. In this thesis we compare different models to analyse which could better represent the star formation history of galaxies.

To find the best parameters of the model we fit a combination of UV+optical photometry from GALEX and SDSS and spectral features from CALIFA data, Hβ and $D4000$ as age indicators and [MgFe]$'$ as a metallicity indicator. Our aim is to develop a tool that lets the space parameter and the input data used to run the fit be easily varied, with the final goal of obtaining a complete analysis of the stellar population properties (SFH, mass, age, metallicity, extinction, SFR...)

This chapter is organized as follow: In section 5.2 we describe the method in detail. In section 5.3 a set of simulations to test the capability of the code is presented. In section 5.4 we define the different models and summarize the quality of fits. Section 5.5 presents the stellar population properties obtained with this technique. Finally, in section 5.6 we compare the results obtained with the parametric method with STARLIGHT.

5.2   The method

In this section we describe the technical issues of the code. With the aim of obtaining a clear description we assume a generic SFH = SFH(t; Θ), where t is the time and Θ is the vector-parameters defining the SFH. For example, taking an exponentially-decaying burst with $\psi(t) = \psi_0 e^{-(t_0-t)/\tau}$, where t is lookback time, ψ_0 is the SFR at the onset of the burst, t_0 is the time since the onset of the burst, and τ is SFR e-folding time, we have $\Theta = (t_0, \tau, Z, A_V)$.

The goal is to sample the parameter space and find the best vector-parameters Θ that fit our data O (indices + photometry). At each point in the parameter space we follow the next steps:

- Given vector-parameters Θ we obtain SFH(t; Θ) and normalize to $1 M_\odot$.

- Secondly, we obtain the synthetic spectrum using SSPs:

$$F(\lambda; \Theta) = 10^{-0.4 q_\lambda A_V} * \int \mathrm{SFH}(t; \Theta) * SSP_{t, Z}(\lambda)\, dt,$$

  where Z and $A_V \in \Theta$.

- From $F(\lambda; \Theta)$ spectrum we compute the spectral indices and magnitudes, obtaining our model data M and comparing with observed data O.

We use Bayesian inference, in particular a Markov chain Monte Carlo (MCMC) method, to sample the parameter space from the posterior probability density function (PDF).

5.2.1   Bayesian inference

Given O a set of observations (in our case magnitudes and indices), the general goal of an MCMC algorithm is to draw a set of samples $\{\Theta_i\}$ in the parameter space from the posterior probability density

$$p(\Theta|O) = \frac{p(\Theta)p(O|\Theta)}{p(O)},$$

where $p(\Theta)$ is the prior distribution and $p(O|\Theta)$ is the likelihood function. The normalization $\dfrac{1}{p(O)}$ is independent of Θ once we have chosen the form of the generative model. So we can sample Θ from the posterior probability without computing $p(O)$, unless it was desirable to compare the validity of two different generative models. It is important because $p(O)$ is generally very expensive to compute.

The main advantage of the Bayesian analysis is that we can marginalize over the parameters. For example, if we want to marginalize over the parameter A_V, we can obtain the marginalized probability function $p(A_V, O)$. We can write $\Theta = (\beta, A_V)$, with β the other parameters. Then

$$p(A_V|O) = \int p(\beta, A_V|O)\, d\beta.$$

Once the sample produced by MCMC is available, we can also obtain the expected value of a function($f(\Theta)$), which in our case will represent a stellar property. For example, given Θ in the parameter space we can compute the mean stellar age (light or mass-weighted) $age(\Theta)$. Thus we can obtain the expected value of the age as

$$< age(\Theta) >= \int p(\Theta|O)age(\Theta)\, d\Theta$$

The prior distribution depends on the particular parametrisation we choose. For example, when using a single exponential decay model we set the range variation of parameter t_0, which is the time since the onset of the exponential, from 6 Myr to 14 Gyr. But when using two components SFH, both of them exponential, we have the parameter t_0^Y for the young component, varying from 6 Myr to 5 Gyr, and t_0^O for the old component, varying from 1 to 14 Gyr.

Likelihood function

As said previously, for an element in the parameter space Θ we can compute the synthetic spectrum $F(\lambda; \Theta)$ and measure the indices and magnitudes. Defining N_{Lick} as the number of Lick indices we use in the fit, we have:

$$\chi 2_{Lick} = \sum_{j=1}^{N_{Lick}} \left(\frac{L_j - I_j}{w_j} \right)^2,$$

where L_j is the observed index, I_j is the index measured in the synthetic spectrum $F(\lambda; \Theta)$ and w_j is the index error. On the other hand, defining N_{mag} as the number of magnitudes we use in the fit, we have

$$\chi2_{mag} = \sum_{j=1}^{N_{mag}} \left(\frac{O_j - M_j(M_\star)}{w_j} \right)^2, \tag{5.1}$$

where O_j is the observed magnitude, $M_j(M_\star)$ is the magnitude computed in the synthetic spectrum $F(\lambda; \Theta)$ scaled with a generic $M_\star$ mass and w_j is the magnitude error.

To compare the magnitudes measured in the synthetic spectrum with the observed one we would need the mass ($F(\lambda; \Theta)$ is scaled to $1 M_\odot$). In our models, the mass scales things up linearly in luminosity, so it adds a constant term to the M_j values,

$$M_j(M_\star) = M_j(1 M_\odot) - 2.5 \log \frac{M_\star}{M_\odot}, \tag{5.2}$$

where $M_j(1 M_\odot)$ is the magnitude compute on the $F(\lambda; \Theta)$ spectrum. Here it is not necessary to also set the mass as a free parameter in the code. Using the observed data we can derive $M_\star$, which minimizes $\chi2_{mag}$ for each element in the parameter space. Replacing (5.2) in (5.1) we obtain

$$\chi2_{mag} = \sum_{j=1}^{N_{mag}} \left(\frac{O_j - M_j(1 M_\odot) + 2.5 \log \frac{M_\star}{M_\odot}}{w_j} \right)^2.$$

Now we solve

$$\frac{\delta \chi2_{mag}}{\delta M_\star} = 0,$$

obtaining

$$2.5 \log M_\star = \frac{\sum (\frac{1}{w_j})^2 (M_j(1 M_\odot) - O_j)}{\sum (\frac{1}{w_j})^2}.$$

We define total $\chi2_{tot}$ as

$$\chi2_{tot} = \chi2_{mag} + \frac{N_{mag}}{N_{Lick}} * \chi2_{Lick}.$$

The factor $\frac{N_{mag}}{N_{Lick}}$ scales $\chi2_{Lick}$ to give the same weight to the magnitudes and indices.

As explained before, to compute the posterior probability function we need the likelihood function $p(O|\Theta)$. Assuming that the indices and magnitudes measurements are independent (not correlated) we obtain

$$p(O|\Theta) = \prod_{i}^{N} p(O_i|\Theta),$$

where O_i are the individual observables and $N = N_{Lick} + N_{mag}$. Then, assuming gaussian errors for O_i, we obtain that

$$p(O|\Theta) = \prod_i^N p(O_i|\Theta) = e^{-\frac{1}{2}\chi^2_{tot}}.$$

$\{\Theta_i\}$ sample

MCMC is a procedure for generating a random walk in the parameter space that, over time, draws a representative set of samples from the distribution $p(\Theta|O)$. Each point in a Markov Chain $X(t_i) = [\Theta_i]$ depends only on the position of the previous step $X(t_{i-1})$.

There are several MCMC algorithms. We use the **emcee** python-implementation of Goodman & Weare's Affine Invariant Markov chain Monte Carlo (MCMC) Ensemble sampler (Goodman & Weare 2010, GW10). The source code can be found here (http://dan.iel.fm/emcee)(Foreman-Mackey et al. 2013). Here we summarize the algorithm to generate a chain and refer to the original paper for more details. This method involves an ensemble of K chains $S = \{X_k\}$ where the proposal distribution of one chain k is based on the current positions of the $K - 1$ chains in the complementary ensemble $S_{[k]} = \{X_j, \forall j \neq k\}$,

$$S_{[k]}(t) = \{X_1(t+1), ..., X_{k-1}(t+1), X_{k+1}(t), ..., X_K(t)\}.$$

To update the position of a chain at position X_k, we take X_j randomly from the remaining chains $S_{[}k]$ and a new position is proposed

$$X_k(t) \rightarrow Y = X_j + Z(X_k(t) - X_j), \tag{5.3}$$

where Z is a random variable. If the density function g of the variable Z satisfies the symmetry condition

$$g(\frac{1}{z}) = zg(z)$$

then the Equation (5.3) is symmetric in the sense that

$$p(X_k(t) \rightarrow Y) = p(Y \rightarrow X_k(t)).$$

In this case, the chain will satisfy detailed balance if the proposal is accepted with probability

$$q = min\left(1, Z^{N-1}\frac{p(Y|D)}{p(X_k(t)|D)}\right), \tag{5.4}$$

where N is the dimension of the parameter space. GW10 advocates a particular form of $g(z)$, namely

$$g(z) \propto \begin{cases} \dfrac{1}{\sqrt{z}} & \text{if } z \in \left[\dfrac{1}{a}, a\right] \\ 0 & \text{otherwise} \end{cases} \tag{5.5}$$

where a is an adjustable scale parameter which GW10 set to 2. This procedure is repeated for each chain in the ensemble following **Algorithm GW10**.

Algorithm GW10

1: **for** k in $\{1, ..., K\}$:

2:    Use a random X_j from the complementary ensemble $S_{[k]}(t)$

3:    $Z \sim g(z) \rightarrow z$ (Eq.(5.5))

4:    $Y = X_j + z(X_k(t) - X_j)$

5:    $q = z^{N-1} p(Y|D)/p(X_k(t)|D)$

6:    $R \sim [0, 1] \rightarrow r$

7:    **if** $r \leq q$ (Eq. (5.4)):

8:       $X_k(t+1) = Y$

9:    **else**:

10:       $X_k(t+1) = X_k(t)$

5.2.2   Computing indices and magnitudes

Through the MCMC we sample the parameter space. Thus we need to compute the Lick indices and magnitudes at any point along the chains. It means that we would need to obtain our synthetic spectrum $F(\lambda; \Theta)$ at each step, but this takes a lot of computational time. A shorter path is to obtain the Lick indices and magnitudes from $\text{SFH}(t; \Theta)$, without computing the synthetic spectrum.

Lick indices

Suppose that the λ-range of an index I goes from λ_1 to λ_2. Given Θ in the parameter space we can write

$$F(\lambda; \Theta) = \int \text{SFH}(t; \Theta) * SSP_{t, Z}(\lambda)\, dt,$$

where $Z \in \Theta$. We can omit the extinction term because the indices are not affected by it. We could try to measure the indices in the SSPs ($I^{SSP_{t,Z}}$) and obtain the index in $F(\lambda; \Theta)$ ($I^{F(\lambda; \Theta)}$) from these computations, but

$$I^{F(\lambda; \Theta)} \neq \int \text{SFH}(t; \Theta) * I^{SSP_{t,Z}}\, dt.$$

With an example it can be observed clearly. From the definition of the index,

$$I = \int_{\lambda_1}^{\lambda_2} \frac{f(\lambda) - c(\lambda)}{c(\lambda)}\, d_\lambda, \tag{5.6}$$

and taking two spectra, f^1 and f^2, we observe that measuring the index I in $f^1 + f^2$ (I^{1+2}) is not the same as measuring I in f^1 (I^1), measuring I in f^2 (I^2) and then computing the sum of them:

$$I^{1+2} = \int_{\lambda_1}^{\lambda_2} \frac{f^1(\lambda) + f^2(\lambda) - c^1(\lambda) - c^2(\lambda)}{c^1(\lambda) + c^2(\lambda)} \, d_\lambda$$

and

$$I^1 + I^2 = \int_{\lambda_1}^{\lambda_2} \frac{c^2(\lambda) * (f^1(\lambda) - c^1(\lambda)) + c^1(\lambda) * (f^2(\lambda) - c^2(\lambda))}{c^1(\lambda) * c^2(\lambda)},$$

so

$$I^{1+2} \neq I^1 + I^2.$$

To obtain the index I without recovering $F(\lambda; \Theta)$ we need the flux and the continuum for each SSP ($f_I^{SSP_{t,z}}(\lambda)$ and $c_I^{SSP_{t,z}}(\lambda)$, respectively, for $\lambda_1 \leq \lambda \leq \lambda_2$). Then we obtain

$$I^{F(\lambda;\Theta)} = \int_{\lambda_1}^{\lambda_2} \frac{\int \text{SFH}(t; \Theta) * \left(f_I^{SSP_{t,z}}(\lambda) - c_I^{SSP_{t,z}}(\lambda) \right) dt}{\int \text{SFH}(t; \Theta) * c_I^{SSP_{t,z}}(\lambda) \, dt} \, d\lambda. \qquad (5.7)$$

Thus, we run a pre-processing step in which we create a grid with the flux and continuum for each SSP and each index we are going to measure. In this way we can compute the indices as eq. (5.7) without recovering the spectrum $F(\lambda; \Theta)$.

The definition of $D4000$ is different from the Lick indices, so we have to modify eq. (5.7). Balogh et al. (1999) defines $D4000$ as follows:

$$D4000 = \frac{\int_{4000}^{4100} f(\lambda) \, d\lambda}{\int_{3850}^{3950} f(\lambda) \, d\lambda}.$$

Again, we create a grid with the flux for $3850 \leq \lambda \leq 3950$ and flux for $4000 \leq \lambda \leq 4100$ for each SSP (f_b and f_r, respectively). In this case, we have to take into account the extinction, so at any point of the parameter space we can compute $D4000$ as

$$D4000^{F(\lambda;\Theta)} = \frac{\int_{4000}^{4100} 10^{-0.4 q_\lambda A_V} \left(\int \text{SFH}(t; \Theta) * f_r^{SSP(t,Z)}(\lambda) \, dt \right) d\lambda}{\int_{3850}^{3950} 10^{-0.4 q_\lambda A_V} \left(\int \text{SFH}(t; \Theta) * f_b^{SSP(t,Z)}(\lambda) \, dt \right) d\lambda}.$$

Another point to take into account measuring Lick indices is the resolution of the spectra. Our observed data are indices measured in the CALIFA spectra with different velocity dispersion for each galaxy. As proposed by Vazdekis et al. (2010) we define a common frame to measure the indices. We set a resolution of FWHM = 14Å (this corresponds to $\sigma = 357$ km/s at 5000 Å), as proposed by Vazdekis et al. (2010). With this resolution we can study both low and intermediate-mass galaxies, with velocity dispersion not much higher than 214 km/s, and massive galaxies. We broaden all the spectra by an amount such that the total resolution is FWHM = 14Å, before measuring the indices,

$$\sigma_{tot} = \sqrt{\sigma_{inst} + \sigma_{gal} + \sigma_{broad}},$$

where σ_{inst} is the instrumental resolution (6Å in CALIFA spectra) and σ_{gal} is the velocity dispersion of the galaxy.

Our SSPs have a 3Å and previous to the computation of the grid with the flux and continuum for each SSPs and index, we broaden the models to obtain FWHM = 14Å. First, we broaden the models to obtain spectra with 6Å resolution in λ, the same instrumental resolution as the CALIFA spectra. Second, through a velocity convolution we obtain final spectra with FWHM = 14 Å (357 km/s at 5000 Å).

Magnitudes

Similarly, we obtain the magnitudes at any point in the parameter space without recovering the synthetic spectrum. Writing again the expression for $F(\lambda; \Theta)$, but taking into account the extinction term, we have:

$$F(\lambda; \Theta) = 10^{-0.4q_\lambda A_V} * \int \mathrm{SFH(t; \Theta)} * SSP_{t, Z}(\lambda) \, dt. \tag{5.8}$$

The AB magnitude over a filter T is defined as

$$m_{AB}(T) = -2.5 \log \frac{\displaystyle\int_{\lambda_T} \lambda F(\lambda; \Theta) T(\lambda) \, d\lambda}{\displaystyle\int_{\lambda_T} \lambda^{-1} T(\lambda) \, d\lambda} - 2.41, \tag{5.9}$$

where λ_T is the λ-range of filter T and $T(\lambda)$ is the filter transmission curve. Replacing $F(\lambda; \Theta)$ by eq. 5.8 we obtain

$$\int_{\lambda_T} \lambda 10^{-0.4q_\lambda A_V} \left(\int \mathrm{SFH(t; \Theta)} * SSP_{t, Z}(\lambda) \, dt \right) T(\lambda) \, d\lambda =$$

$$= \int \mathrm{SFH(t; \Theta)} \left(\int_{\lambda_T} \lambda 10^{-0.4q_\lambda A_V} SSP_{t, Z}(\lambda) T(\lambda) \, d\lambda \right) dt. \tag{5.10}$$

We would like to compute the term between brackets for each SSP but it depends on the position in the parameter space due to A_V. Our aim is to remove A_V from the integral in λ. We define:

$$R(q) = 10^{-0.4q A_V}.$$

Supposeing T with a λ-range between λ_1 and λ_2, we compute the mean lambda T-weighted as:

$$\lambda_T^0 = \frac{\displaystyle\int_{\lambda_1}^{\lambda_2} \lambda T(\lambda) \, d\lambda}{\displaystyle\int_{\lambda_1}^{\lambda_2} T(\lambda) \, d\lambda}.$$

Then, running a Taylor expansion of $R(q)$ on q_T^0 ($= q_{\lambda_T^0}$) we obtain

$$S_T(q) = \sum_{i=0}^{\infty} \frac{R^{i)}(q_T^0)}{i!} (q - q_T^0)^i. \tag{5.11}$$

Deriving $R(q)$ we have

$$R^{i)}(q) = 10^{-0.4qA_V} * (-0.4A_V \ln 10)^i.$$

Computing the Taylor expansion until $i = 5$ we obtain a very good approximation for the extinction term, with $|S_T(q_\lambda) - R(q_\lambda)| < 10^{-5}$ for $\lambda \in \lambda_T$. This approximation is valid only for filter T, so we have to repeat the process for each filter involved in the fit. Replacing (5.11) in (5.10) we obtain

$$\int \text{SFH(t;}\Theta) \left(\int_{\lambda_T} \lambda \left(\sum_{i=0}^{5} \frac{10^{-0.4q_T^0 A_V} * (-0.4A_V \ln 10)^i}{i!} (q_\lambda - q_T^0)^i \right) SSP_{\text{t, z}}(\lambda)T(\lambda) \, d\lambda \right) dt =$$

$$= \int \text{SFH(t;}\Theta) * 10^{-0.4q_T^0 A_V} \left(\sum_{i=0}^{5} \frac{(-0.4A_V \ln 10)^i}{i!} \int_{\lambda_T} \lambda(q_\lambda - q_T^0)^i SSP_{\text{t, z}}(\lambda)T(\lambda) \, d\lambda \right) dt.$$

For every i and SSP we define

$$m_T^{SSP_{\text{t,z}}}(i) = \int_{\lambda_T} \lambda(q_\lambda - q_T^0)^i SSP_{\text{t, z}}(\lambda)T(\lambda) \, d\lambda.$$

and also

$$a_T = \int_{\lambda_T} \lambda^{-1} T(\lambda) \, d\lambda.$$

Replacing in eq. 5.9 we obtain

$$m_{AB}(T) = -2.5 \log \frac{\int \text{SFH(t;}\Theta) * 10^{-0.4q_T^0 A_V} \left(\sum_{i=0}^{5} \frac{(-0.4A_V \ln 10)^i}{i!} m_T^{SSP_{\text{t,z}}}(i) \right) dt}{a_F} - 2.41. \quad (5.12)$$

A pre-processing grid is also created with the values of $m_T^{SSP_{\text{t,z}}}(i)$ for each i, each SSP and each filter involved in the fit. Also, the q_T^0 and a_T values for each filter are stored during the pre-processing step. In this way we compute the magnitudes at any point in the parameter space without recovering $F(\lambda; \Theta)$, as shown in eq. 5.12.

To avoid any redshift correction we compute the $m_F^{SSP_{t,Z}}(i)$ matrix over the models at different redshift, from $z = 0.005$ to $z = 0.03$ in steps of 0.001, to cover the CALIFA galaxies redshift. To fit the observed data we obtain the value in our redshift grid nearest to the galaxy redshift and then the corresponding $m_T^{SSP_{\text{t,z}}}(i)$ matrix is taken.

5.3 Simulations

Before applying the models to the CALIFA sample, we will run a set of simulations to test the code. The model used in the simulations (which will be **M1** in the next section) is defined by three different parameters and the expression for the SFR is:

$$\psi(t) = \frac{A}{\tau^2}(t_0 - t)e^{-(t_0-t)/\tau},$$

where t_0 represents the onset of the burst, τ is SFR e-folding time and A is a normalization constant that depends on the mass of the galaxy. Another parameter of the model, which is not appreciated in last equation, is the metallicity. The A constant is not a free parameter of the model, because for each (t_0, τ, Z) we compute the constant that minimizes $\chi2$. So we have a three-dimension parameter space.

The goal of the simulations is to measure how the code can recover the parameters of the model, the observed magnitudes and indices and also the uncertainties in the stellar population properties.

5.3.1 Test galaxies

We generate 100 test galaxies using random choice parameters. The observables for these test galaxies, UV + optical magnitudes (namely m_l^{obs}) and H$_\beta$, [MgFe]$'$ and D4000 (namely I_l^{obs}), were generated from their full synthetic spectra and then perturbed according to

$$O_\lambda = O_\lambda^0 \left(1 + \frac{\mathcal{N}(0,1)}{S/N}\right) \tag{5.13}$$

$$m_l^{\mathrm{obs}} = m_l^0 + (2.5\log e)\frac{\mathcal{N}(0,1)}{S/N} \tag{5.14}$$

where O_λ^0 and m_l^0 are the original input spectrum and magnitudes, and $\mathcal{N}(0,1)$ is a gaussian deviate of zero mean and unit variance. The spectral features I_l^{obs} are computed from O_λ^0. Three levels of noise were considered: $S/N = 20$, 50, 100 (the corresponding errors in magnitudes are 0.054, 0.022 and 0.011, respectively). Five realizations were made for each S/N. In total, the test sample consists of $100 \times 3 \times 5 = 1500$ galaxies. We choose S/N larger than 20 because the stellar indices are very sensitive to the signal to noise.

5.3.2 Input versus output: Observables and physical properties

Magnitudes and stellar indices

Table 5.1 quantifies the results of fits. We define Δ as the output $-$ input difference in a certain quantity and examine its statistics. The table lists the mean ($\overline{\Delta}$) and standard deviation (σ_Δ) of Δ for the different quantities over all test galaxies. The first section in the table shows the observables involved in the fits: FUV, NUV, u, g, r, i, z, H$_\beta$, [MgFe]$'$ and D4000.

As we observe, Δ and its dispersion decreases when increasing the S/N, with σ_Δ close to the expected noise levels. For H$_\beta$ the uncertainties decrease from $S/N = 20$, to $S/N = 100$, but we recover it with lower precision than for the other observables, particularly for $S/N = 20$.

Stellar mass and extinction

In the second part of table 5.1 we begin by listing the mean ($\overline{\Delta}$) and standard deviation (σ_Δ) for the stellar mass and attenuation. It is well known that $M_\star$ is a very robust quantity in the photometric

Summary of simulations: $\overline{\Delta} \pm \sigma_\Delta$

Property	S/N = 20	S/N = 50	S/N = 100
FUV	0.03 ± 0.12	0.01 ± 0.04	0.01 ± 0.02
NUV	-0.02 ± 0.07	-0.01 ± 0.03	0.00 ± 0.01
u	-0.02 ± 0.07	-0.01 ± 0.02	-0.01 ± 0.01
g	0.01 ± 0.04	-0.01 ± 0.02	-0.01 ± 0.02
r	0.00 ± 0.05	0.00 ± 0.01	0.00 ± 0.01
i	0.00 ± 0.05	0.00 ± 0.01	0.01 ± 0.01
z	-0.01 ± 0.06	0.00 ± 0.02	0.00 ± 0.01
H_β	0.00 ± 0.19	-0.02 ± 0.13	-0.05 ± 0.08
$[MgFe]'$	-0.01 ± 0.05	-0.01 ± 0.03	-0.01 ± 0.02
D4000	0.00 ± 0.03	0.00 ± 0.01	0.00 ± 0.01
$\log M$	-0.02 ± 0.15	-0.03 ± 0.09	-0.02 ± 0.06
τ_V	0.12 ± 0.22	0.01 ± 0.14	-0.03 ± 0.08
$\langle \log t \rangle_L$	-0.15 ± 0.29	-0.04 ± 0.17	0.01 ± 0.09
$\langle \log Z \rangle_M$	0.07 ± 0.27	0.12 ± 0.17	0.09 ± 0.15
t_0	-0.02 ± 0.15	-0.03 ± 0.09	-0.02 ± 0.05
τ	0.12 ± 0.35	0.01 ± 0.15	-0.04 ± 0.09

Table 5.1 Statistics of the simulations. For each observable and physical property, the table lists the mean simulated minus original difference ($\overline{\Delta}$) and its standard deviation (σ_Δ) for S/N varying from 20 to 100.

analysis and it is observed in the simulations. This quantity shows lower uncertainties than the other stellar parameters. The dispersion in $\Delta \log M_\star$ ranges from $\sigma_\Delta = 0.15$ to 0.06 dex from S/N between 20 and 100.

The dust parameter τ_V is not as well recovered as the stellar mass. The uncertainties decrease when increasing S/N, but in this case, σ_Δ varies from 0.32 to 0.08.

Mean stellar age and metallicity

Table 5.1 also lists the $\overline{\Delta} \pm \sigma_\Delta$ values for the luminosity-weighted mean (log) age ($\langle \log t \rangle_L$) and mass-weighted mean (log) metallicity ($\langle \log Z \rangle_M$).

We obtain that σ_Δ also decreases when increasing S/N. The uncertainties for $\langle \log t \rangle_L$ are similar to those found for the attenuation. On the other hand, we obtain that the metallicity is not recovered as well. We find a slight bias towards younger ages and larger metallicities, mainly for $S/N = 20$, which is compensated with the bias found towards larger attenuation values.

Star formation history: Parameters of the model

The t_0 and τ values define the parametric model used in the simulation (and also the metallicity). The last part of table 5.1 shows the statistics for these parameters. The σ_Δ decreases in both cases when increasing the S/N, but we obtain larger values for the τ parameter. A bias towards larger τ values is observed, which means including younger stellar population in the model. It is reflected in the bias towards younger ages. On the other hand, the contribution of the young components would increase the flux in the different band, and it is compensated increasing the extinction values, and also

the metallicity.

5.4 The models

The most commonly SFHs used in the literature are declining (D), taken from an exponentially-decaying burst with $\psi(t) = \psi_0 e^{-(t_0-t)/\tau}$, where t is lookback time, ψ_0 is the SFR at the onset of the burst, t_0 is the time since the onset of the burst, and τ is SFR e-folding time (e.g. Maraston et al. 2010). There are, however, another declining SFHs or "delayed-τ" models (Sandage, 1986; Steinhardt et al., 2014; Moustakas et al., 2013) which allow linear growth at early times followed by an exponential decline at late times. Other studies at high redshift have advocated rising SFHs as better functional fits. These have taken several forms: that of exponentially-rising SFHs, with $\psi(t) = \psi_0 e^{(t_0-t)/\tau}$ (Maraston et al., 2010; González et al., 2012); power-law-rising SFHs, with $\psi(t) = \psi_0 (t_0 - t)^\alpha$ (Papovich et al., 2011; Smit et al., 2012); and linearly-rising SFHs, with $\psi(t) = \psi_0 + \frac{d\psi}{dt}(t_0 - t)$ (Lee et al. 2012). Frequently, constant SFHs are also used as a go-between for the two options, with $\psi(t) = \psi_0$ (Lee et al. 2012).

The derived stellar population properties are entirely dependent on the particular parametric model used in the analysis. In this thesis we use our code to analyse different models. We also include the rising models for a complete analysis, although they are commonly used for high redshift galaxies. In this thesis we explore two different regimes: one and two component SFHs.

We begin by presenting the different models and showing the quality fits using them when fitting information of the whole galaxy, which means the integrated magnitudes in the optical and UV and the spectral indices measured in CALIFA integrated spectra. To check the quality of fits is the first indicator of whether a model is suitable or otherwise becomes poor when describing the star formation history of a galaxy. A good quality fits does not mean that the parametrisation is realistic, and a further stellar population properties analysis is necessary, but a bad quality fit tells us that we can discard such a model as representative of the star formation history of a galaxy.

All models presented in this thesis are based on three different profiles, which are shown in figure 5.1. The curves are computed using the same parameters ($t_0 = 12$ Gyr, $\tau = 3$ Gyr) and are normalised to 1 $M_\odot$. Red and green curves are delayed-τ models. The second one will be named as "Sandage" profile due to it was first parametrised by Sandage (1986). The blue curve is an exponential profile.

The next paragraphs describe the different models and the quality of fits obtained with all of them. Table 5.2 summarizes the acronyms used for the models and the equations used to define them. Figure 5.2 shows the quality of fits, indicating $\overline{\Delta} \pm \sigma$ for the different observables, where $\Delta = \frac{Synthetic - Observed}{Error}$, and also the reduced $\chi2$, which is defined as $\sqrt{\frac{\chi2}{N}}$.
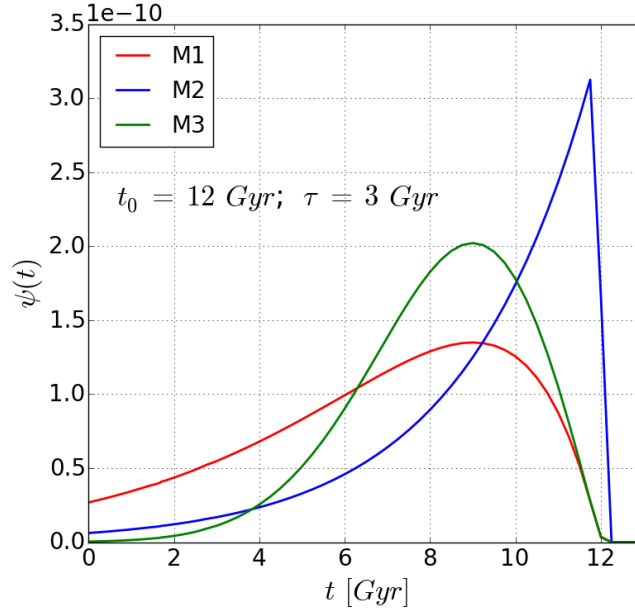
Figure 5.1 Parametric models **M1**, **M2** and **M3**. The parameters used in the example are $t_0 = 12$ Gyr and $\tau = 3$ Gyr. The curves have been scaled to $1\ M_\odot$.

One component SFHs

"Delayed-τ" model (M1)

The first model used in this thesis is a delayed-τ model, which was used in the simulations:

$$\psi(t) = \frac{A}{\tau^2}(t_0 - t)e^{-(t_0-t)/\tau},$$

where t_0 is the time since the onset of the burst, τ is SFR e-folding time and A is a normalization constant. This model allows the construction of decaying SFHs ($t/\tau \gg 1$) and rising SFHs ($t/\tau \ll 1$). With this model we have a four-dimension parameter space (t_0, τ, Z, A_V).

Figure 5.3 shows the fitting of indices and magnitudes using this model. Each panel shows [*Synthetic - Observed*]/*Error*. In the bottom row we also show the reduced $\chi2$, which is a measure of the whole quality fit. In the panels we also indicate μ and σ. A very good quality fit means values of reduced $\chi2 \sim 1$ and lower. In this case we obtain values around 1.19. Thus with this parametrisation we can adjust the observed data inside the expected uncertainties. Regarding the observables individually we realise that larger uncertainties appear for FUV and NUV. For FUV we obtain lower values ($\mu = -1.36$) than those expected, which means higher FUV fluxes, while obtaining larger values for NUV ($\mu = 1.84$), which means lower fluxes than expected. In both cases we obtain $\sigma \sim 1$. For Hβ, D4000 and [MgFe]$'$ we obtain $\mu = 0.66$, 0.56 and -0.38, respectively.

Exponentially-decaying burst (M2)

The following is the most widely used SFH in the literature:

$$\psi(t) = \psi_0 e^{-(t_0-t)/\tau},$$

where ψ_0 is the SFR at the onset of the burst, t_0 is the time since the onset of the burst, and τ is SFR e-folding time. As explained in section 5.2.1 we normalize the SFH, so ψ_0 is not a free parameter in the code. Again, we have a four dimension parameter space (t_0, τ, Z, A_V).

In figure 5.4 we observe the quality of the fits. Again we obtain a bias toward lower FUV and larger NUV values ($\mu_{FUV} = -1.36$, $\mu_{NUV} = 1.86$). Regarding Hβ, D4000 and [MgFe]$'$ we find $\mu = 0.76$, -0.44 and 0.5 showing larger values for Hβ, D4000 and lower values for [MgFe]$'$. The global fits are very similar to in previous case with reduced $\chi2 \sim 1.2 \pm 0.5$.

Summary of models

M1	Delayed-τ model	$\psi(t) = \frac{A}{\tau^2}(t_0 - t)e^{-(t_0-t)/\tau}$
M2	Exponentially-decaying burst	$\psi(t) = \psi_0 e^{-(t_0-t)/\tau}$
M3	"Sandage" profile	$\psi(t) = \frac{A}{\tau^2}(t_0 - t)e^{-(t_0-t)^2/2\tau^2}$
M4	Linearly-rising model	$\psi(t) = \psi_0 - \frac{d\psi}{dt}(t_0 - t)$
M5	Power-law-rising model	$\psi(t) = \psi_0(t_0 - t)^\alpha$
M6	Two exponential components	$\psi_{old}(t) = \psi_0 e^{-(t_0^{old}-t)/\tau^{old}}$ $\psi_{young}(t) = \psi_0 e^{-(t_0^{young}-t)/\tau^{young}}$
M7	Fixing old component	$\psi_{old}(t) = \psi_0 e^{-(14e9-t)/\tau^{old}}$ $\psi_{young}(t) = \psi_0 e^{-(t_0^{young}-t)/\tau^{young}}$
M8	"Sandage" young component	$\psi_{old}(t) = \psi_0 e^{-(t_0^{old}-t)/\tau^{old}}$ $\psi_{young}(t) = \frac{A}{[\tau^{young}]^2}(t_0^{young} - t)e^{-(t_0^{young}-t)^2/2[\tau^{young}]^2}$
M9	Constant SFR + exponentially declining	$\psi_{old}(t) = \psi_0$ $\psi_{young}(t) = \psi_0 e^{-(t_0-t)/\tau}$

Table 5.2 The table summarises the acronym used for the different models throughout this thesis as well as the parametrisation used for each model.

"Sandage" profile (M3)

The "Sandage" profile, first parametrised by Sandage (1986), is also a delayed-τ model with

$$\psi(t) = \frac{A}{\tau^2}(t_0 - t)e^{-(t_0-t)^2/2\tau^2},$$

which combines decaying SFHs ($t/\tau \gg 1$) and rising SFHs ($t/\tau \ll 1$). The difference is that the rising

and decaying occur faster in the "Sandage" profile than in the "delayed-τ" model for the same τ value. Again we obtain a four dimension parameter space (t_0, τ, Z, A_V).

Figure 5.5 shows the indices and magnitudes fitting using the "Sandage" profile. The same bias towards lower FUV magnitude and larger NUV magnitude is observed with this model, obtaining $\mu_{FUV} = -1.32$ and $\mu_{NUV} = 1.8$. The uncertainties in the estimation of stellar indices follow the same trend as in previous cases, with μ = 0.77, 0.53 and -0.36, for Hβ, D4000 and [MgFe]$'$, respectively. The global fits are again very similar to in previous cases with reduced $\chi2 \sim 1.23 \pm 0.52$.

Rising SFH

In a rising SFH model, a galaxy is actually forming mass at a larger rate than at any other time in the past. Studying local galaxies we know that SFR is lower than in the past, at least for Sb galaxies and earlier morphological types (González Delgado et al. 2016), so it seems that a global rising SFH doesn't have to work appropriately. Rising SFHs are used for high redshift studies but, in any case, we are going to fit the data using rising SFHs to analyse the results. We consider two different rising SFH models:

- Linearly-rising (RL) model **(M4)** with

$$\psi(t) = \psi_0 - \frac{d\psi}{dt}(t_0 - t).$$

- Power-law-rising (RP) model **(M5)** with

$$\psi(t) = \psi_0(t_0 - t)^\alpha.$$

Figures 5.6 and 5.7 show the indices and magnitudes fitting using the rising models. From both figures we observe that using the rising models we cannot fit the observed indices and magnitudes. It indicates that these models are not useful for deriving the SFHs of nearby galaxies, and we are not able to recover the stellar population properties with any reliability.

Two components SFHs

We introduce now more complex histories, with a larger parameter space dimension, composed of two events. Others works use this approach by modeling two instantaneous starbursts (e.g. Kaviraj et al. 2007a), representing an old and a young component, or modelling the young component with an exponentially declining profile (Schawinski et al. 2007). In this thesis we analyses more general versions of models used in these works, representing both components with exponentially declining profiles. Also, we fit a model representing the young component with the "Sandage profile" and review the model used by Schawinski et al. (2013). A new parameter appears in the models to account for the mass fraction of each component to the total mass.

Two exponential components (M6)

This model introduces an exponentially-decaying profile to represent both an old and a young component. In the prior distribution we define a range of variation of t_0 parameter for the old

component from 1 to 14 Gyr while for the young component t_0 can take values from 6 Myr to 5 Gyr. Also we vary the metallicity of both components. For the old component the metallicity Z_O can be any of the base, but for young component the metallicity Z_Y can be the same as or larger than Z_O. We assume these metallicity values because the evolution of stars that compose the old component of the galaxy produce the chemical enrichment of the interstellar medium. Thus, the stars which form the young component born from the enriched material. With this model we have an eight dimension parameter space.

In figure 5.8 we show the uncertainties obtained using this model. We achieve better results fitting the observables when introducing a second component in the model, with lower values of μ and σ. Values of reduced $\chi 2$ are lower than 0.79, indicating good quality fits. This model fits all the observables well, with $|\mu \pm \sigma| \lesssim 1$. For NUV we obtain the largest dispersion, with $\mu_{NUV} = 0.62$ and $\sigma_{NUV} = 0.64$.

Fixing old component (M7)

This model is a restriction of the two exponentially-decaying components model presented before. The difference is that we now fix the t_0 parameter to 14 Gyr. The t_0 for the young component moves again from 6 Myr to 5 Gyr. We assume the metallicity variation of both components as explained for the previous model. In this case we have a seven dimension parameter space. Using this model, we assume that all galaxies have experienced an initial star formation event at the beginning of cosmic time, superimposed by a recent event in the last 5 Gyr.

Figure 5.9 shows again the indices and magnitudes fitting. The results are very similar to in the previous case, both for reduced $\chi 2$ values and individual observables. We find reduced $\chi 2$ values lower than 0.82 and $|\mu \pm \sigma| \lesssim 1$ for all the observables, obtaining larger uncertainties for FUV and NUV (-0.52 ± 0.56 and 0.67 ± 0.68, respectively).

"Sandage" young component (M8)

This two components model has the same parameters as the two exponential components model (**M6**), but in this case we replace the young exponentially-decaying component with the "Sandage" profile.

The quality of fits is observed in figure 5.10 and is again very similar to those obtained using model **M6**. The reduced $\chi 2$ values are lower than 0.88 showing again good quality fits. For all the observables we obtain $|\mu \pm \sigma| \lesssim 1$. The largest differences appear for FUV and NUV with -0.39 ± 0.53 and 0.57 ± 0.69 respectively.

Constant SFR + exponentially declining (M9)

The model presented in this section is motivated by the analysis of Schawinski et al. (2014). In this work, they assume a constant star formation rate for 9 Gyr followed by a transition to an exponentially declining star formation rate with variable time scale, τ, representing the quenching time scale. In the model, they fix the time of the quenching at 9 Gyr, but in this thesis we set the t_0 value as a free parameter in the model. We now obtain a four dimension parameter space (t_0, τ, Z, A_V). This model works to fit UV and optical colours and analyse the shutdown of the star formation, as shown by Schawinski et al. (2014), but in this thesis we try to apply the model to fit a wider set of observables.

Figure 5.11 shows that the quality of fits is worse than those obtained with the previous two component models. None of the observables is fitted below the expected error, with σ values much larger than 1, and the reduced $\chi 2$ takes values lower than 1.85, while in the previous two component models they were not larger than 1.

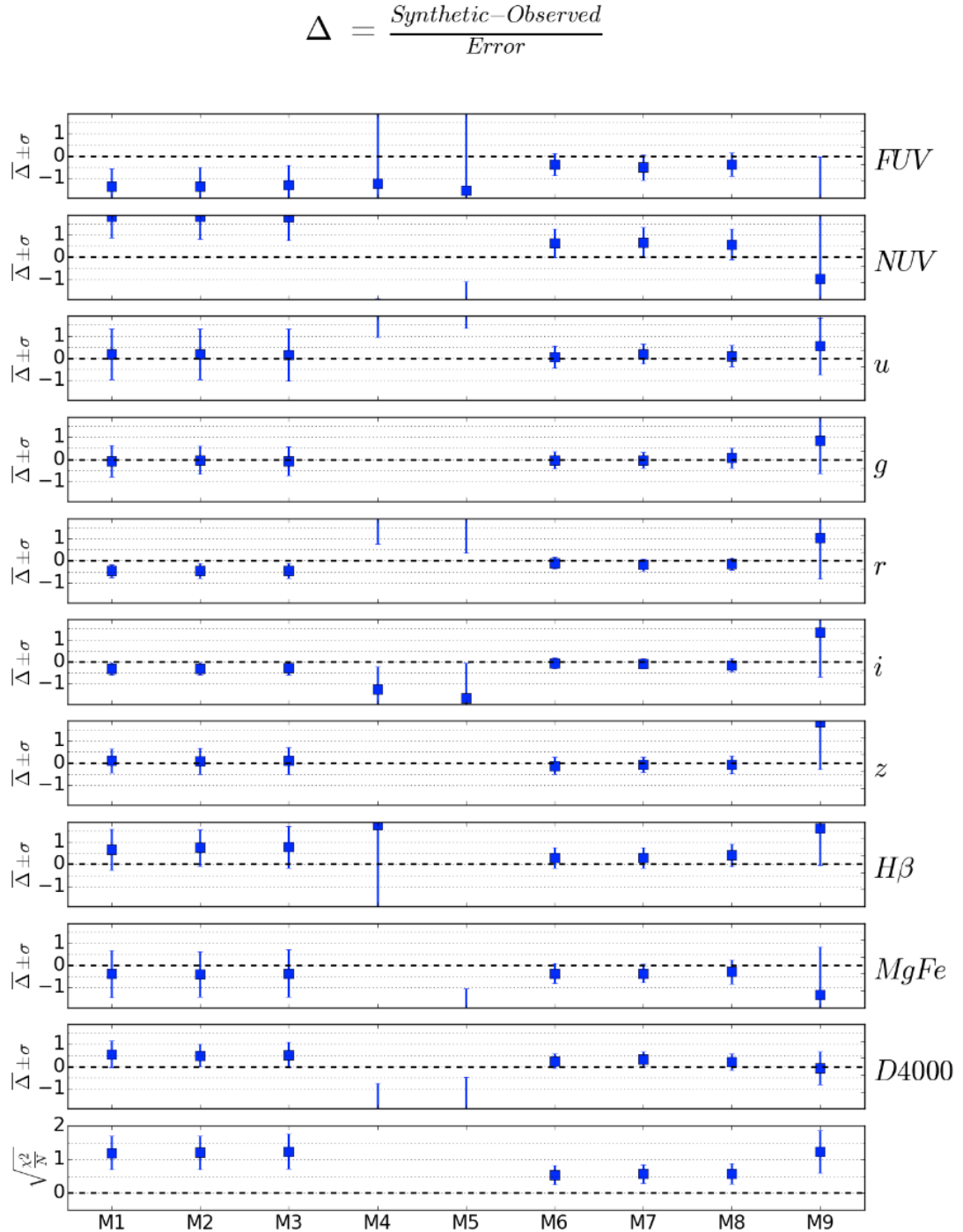$$\Delta = \frac{Synthetic - Observed}{Error}$$

Figure 5.2 Quality of fits using the different models. Each panel shows $\overline{\Delta} \pm \sigma$ for an observable and the different models, where $\Delta = \frac{Synthetic - Observed}{Error}$.
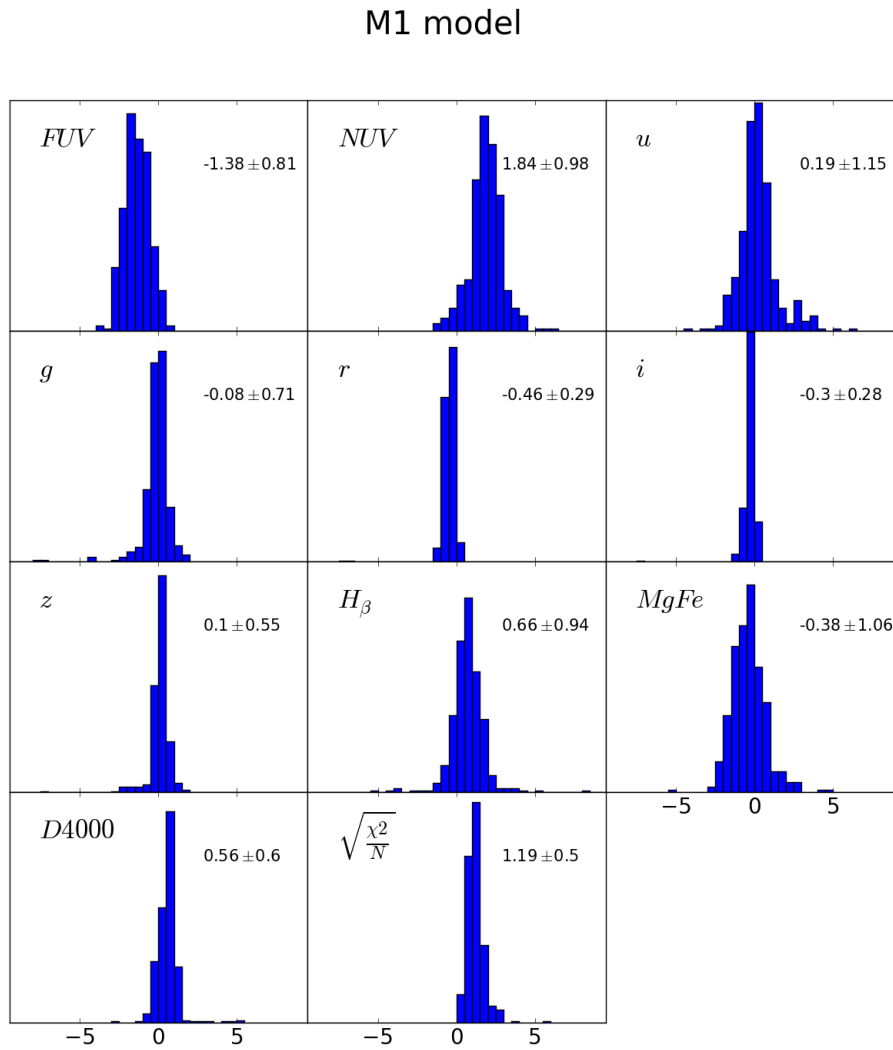
M1 model

Figure 5.3 Each panel represents $\frac{\text{Synthetic} - \text{Observed}}{\text{Error}}$ using the model **M1**. In the bottom row we also show the reduced $\chi 2$. The mean and the standard deviation of the distribution are shown in each panel.
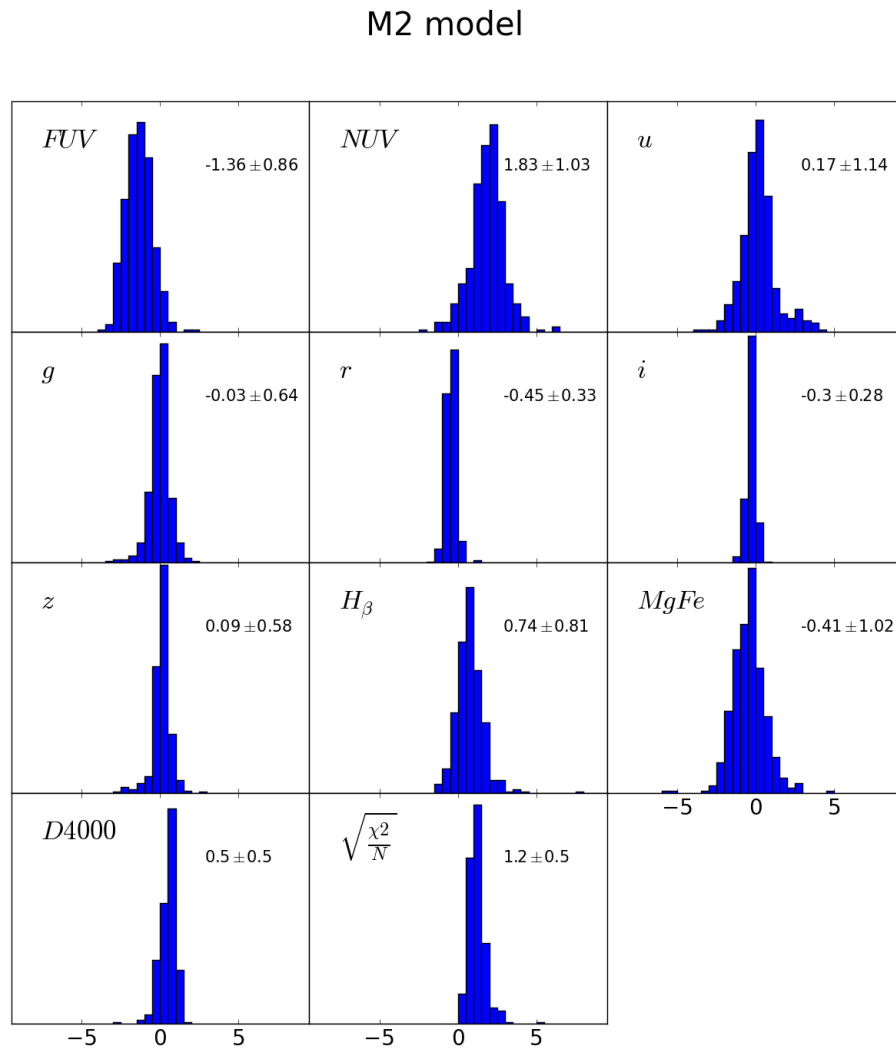
Figure 5.4 Same as Figure 5.3 using the model **M2**.

M3 model

Figure 5.5 Same as Figure 5.3 using the model **M3**.

Figure 5.6 Same as Figure 5.3 using the model **M4**.
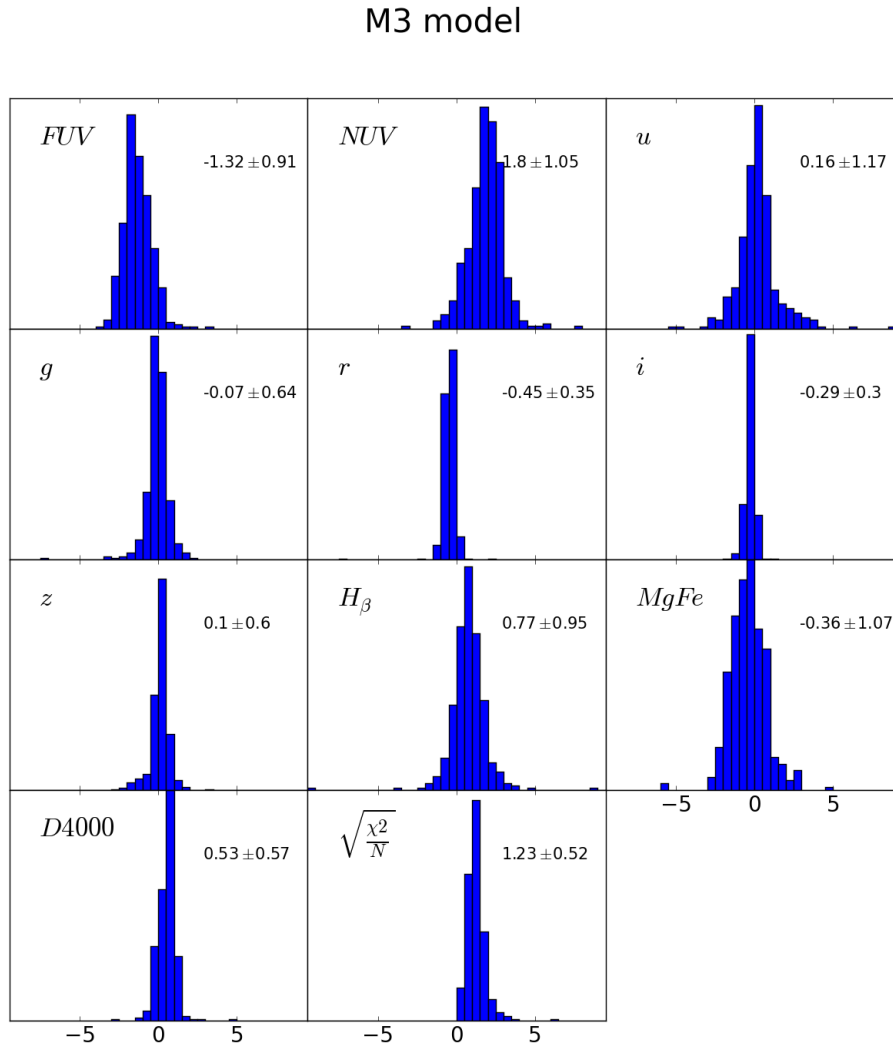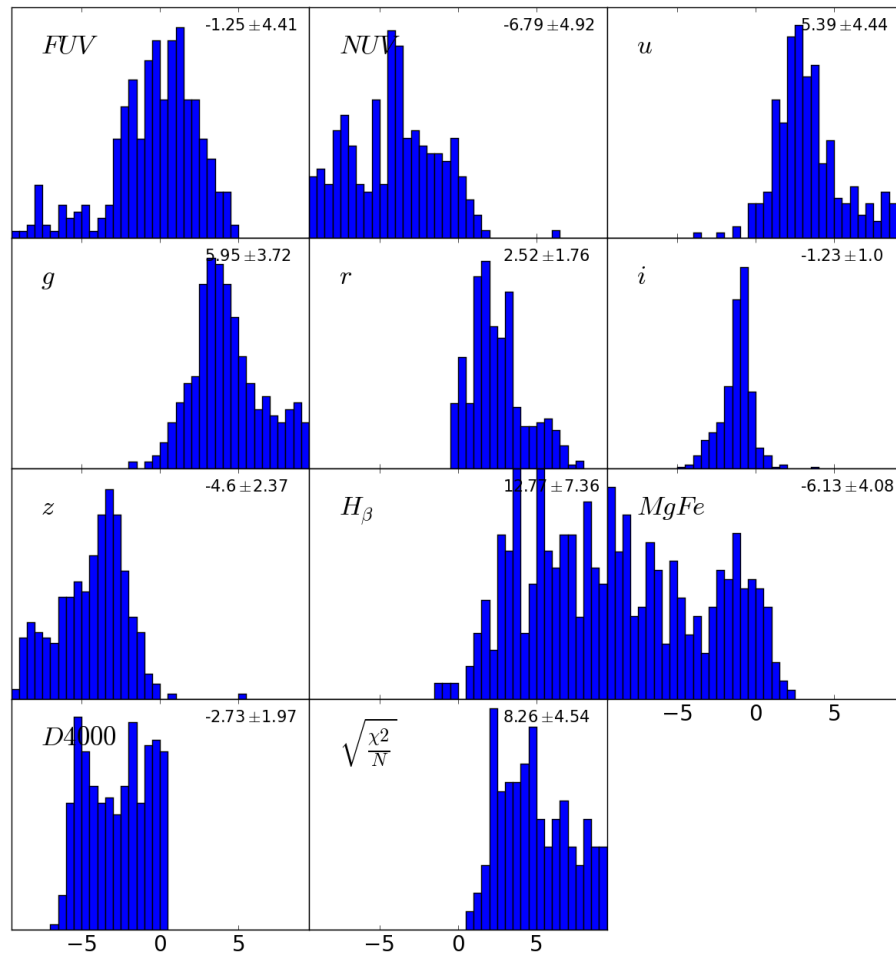
Figure 5.7 Same as Figure 5.3 using the model **M5**.

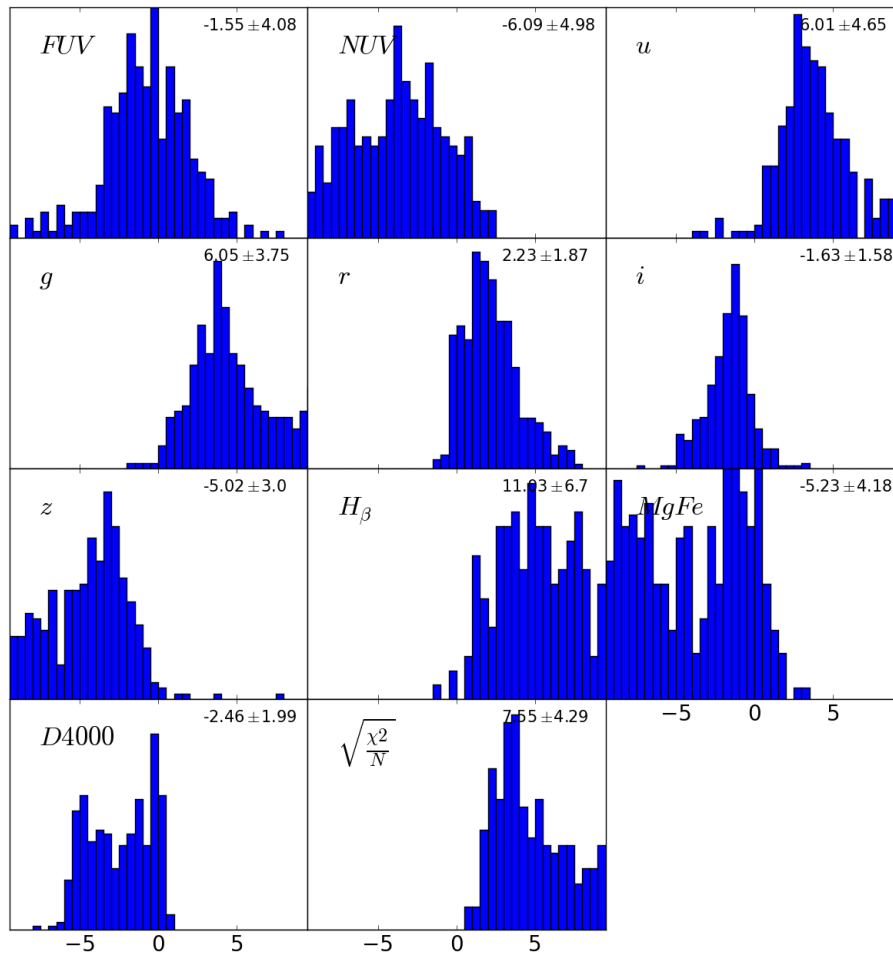## M6 model

Figure 5.8 Same as Figure 5.3 using the model **M6**.

Figure 5.9 Same as Figure 5.3 using the model **M7**.
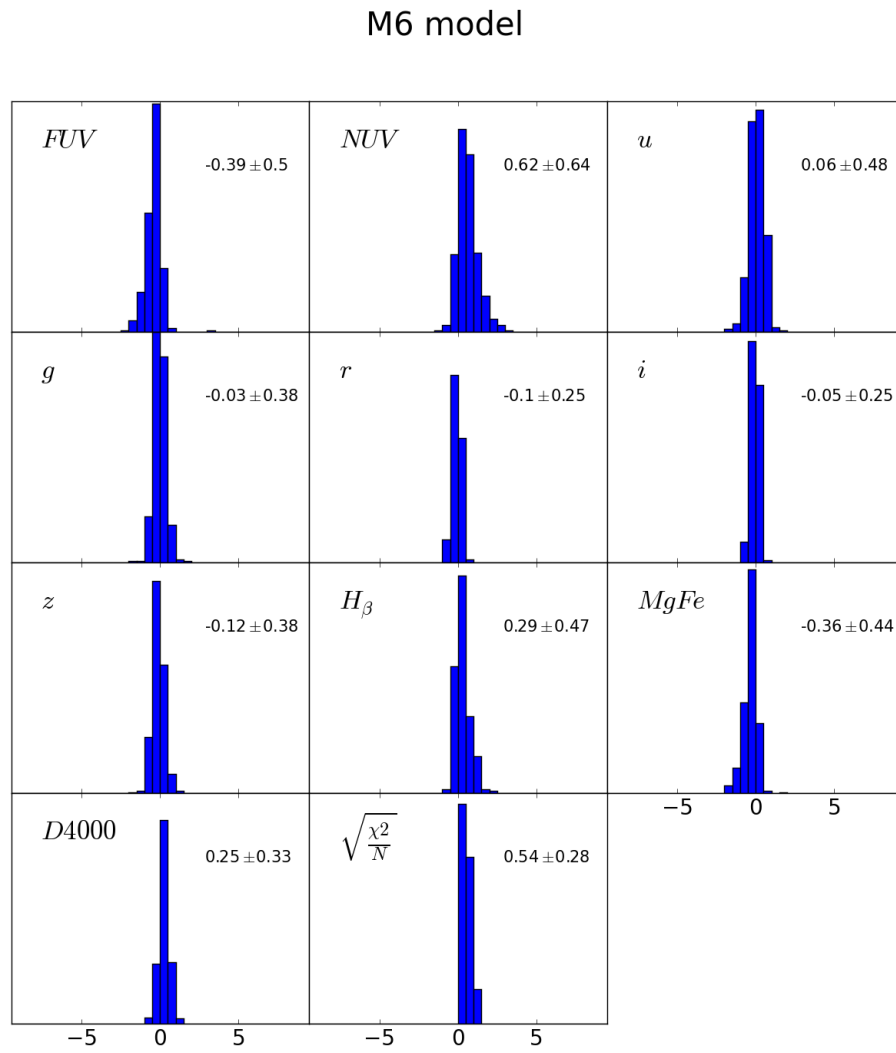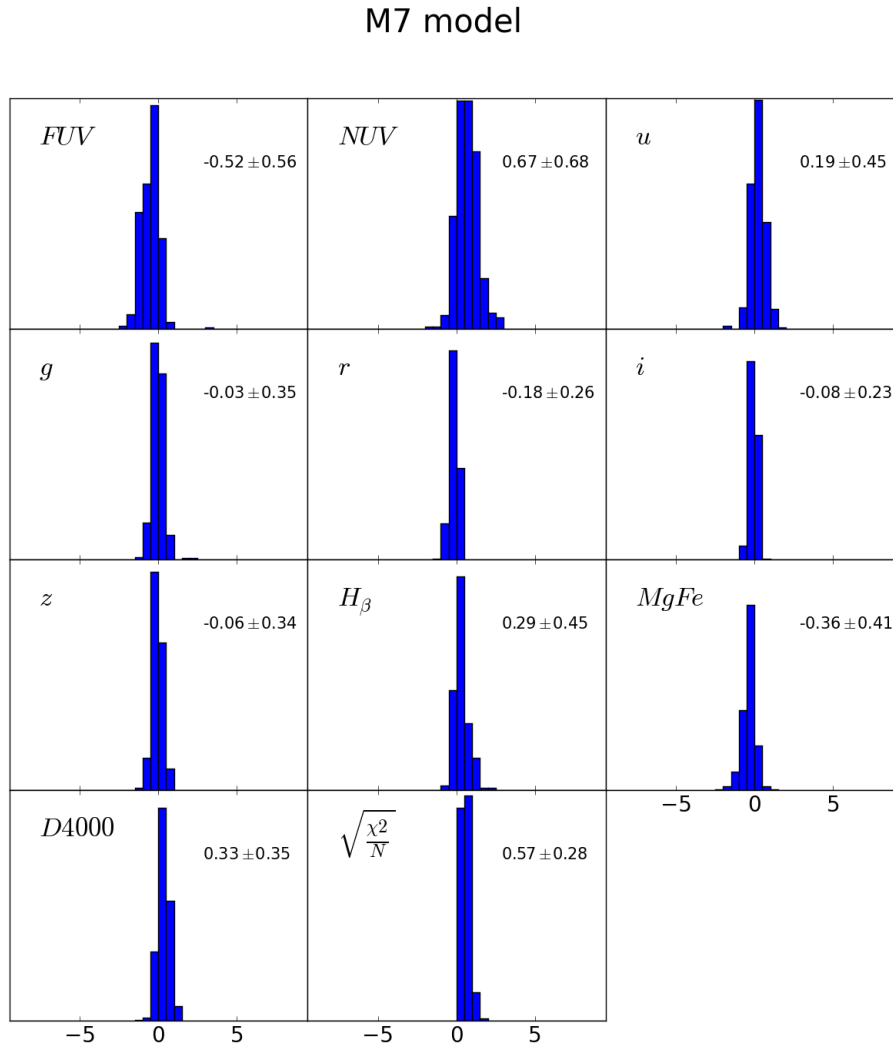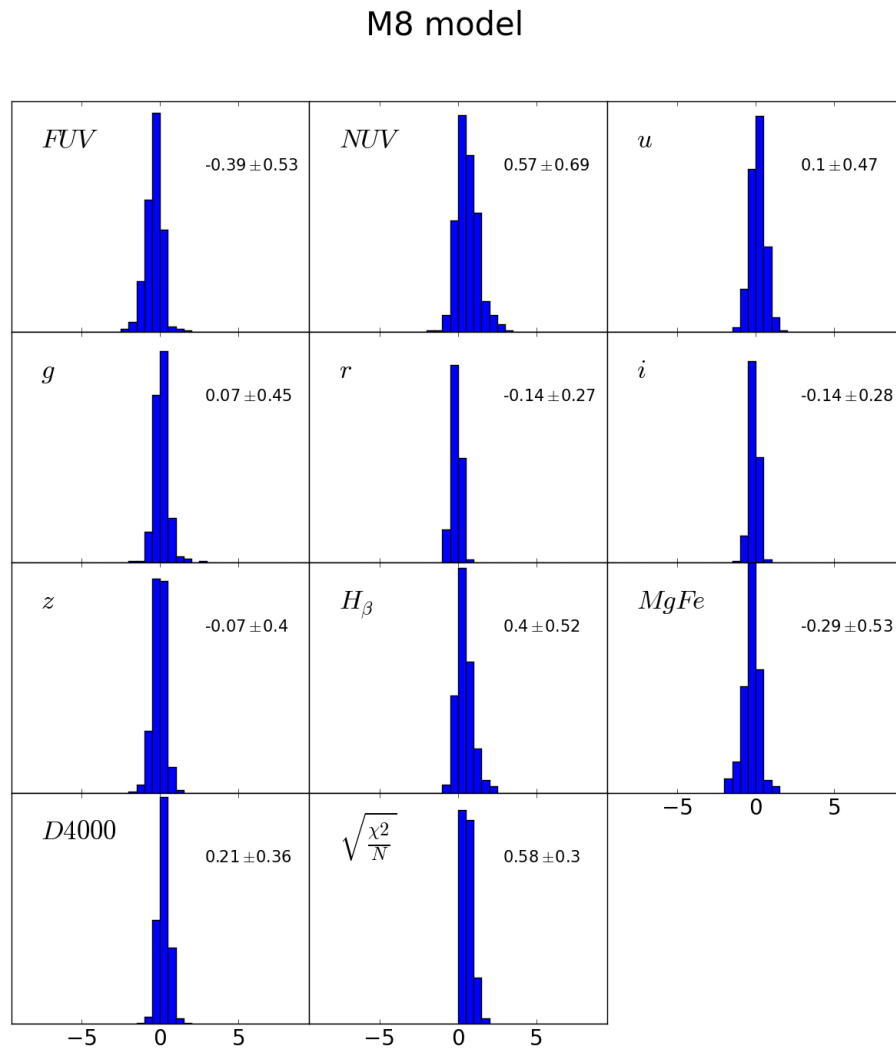
M8 model

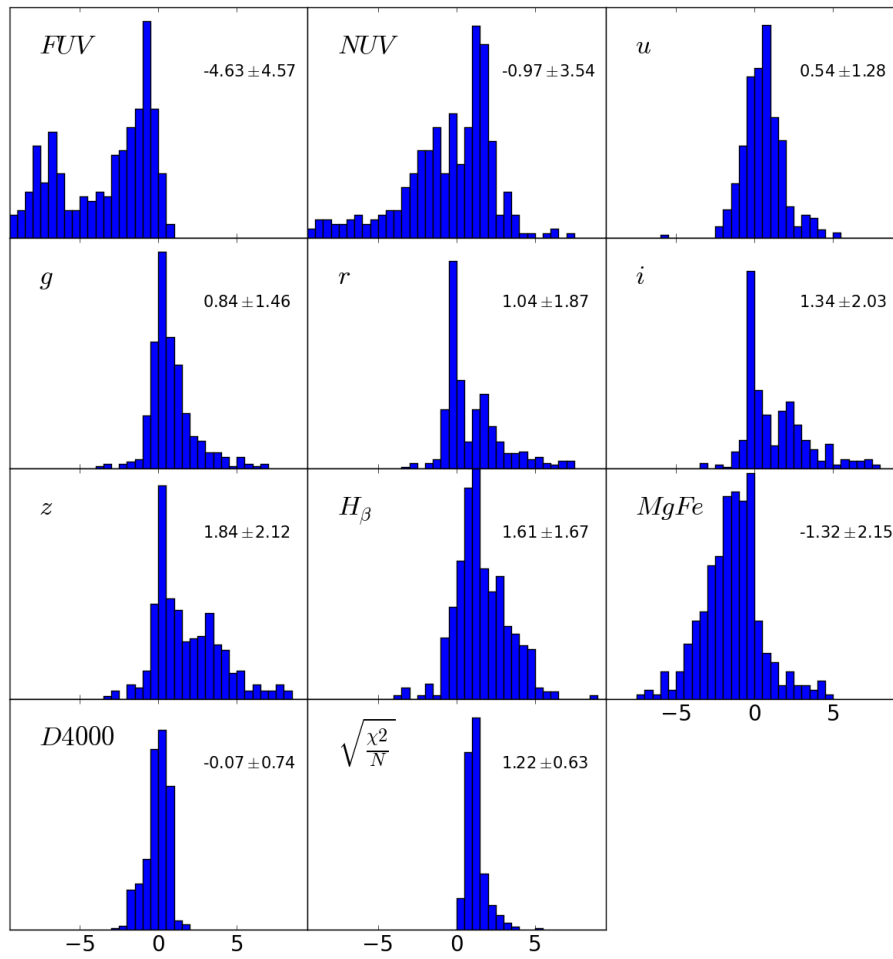Figure 5.10 Same as Figure 5.3 using the model **M8**.

Figure 5.11 Same as Figure 5.3 using the model **M9**.

5.5   Stellar population properties

In this section we present the integrated stellar population properties derived using the different models. As a reference model we choose **M1** and compare the other ones with it. Because we will discuss the SFH by stacking galaxies according to the Hubble type, it is important to know how the properties of galaxies relate to morphology. In Figure 5.12 we show the distribution of stellar population properties according to the Hubble type. From top to bottom we show the total stellar mass in galaxies, the attenuation values, the light-weighted mean stellar age and the mass-weighted mean metallicity. In the top panel we observe that mass is well correlated with the Hubble type, decreasing from early to late types. The second row shows the stellar extinction according to morphology. E and S0 have low extinction while Sa and later types have larger values. The third row shows how the mean age of the stellar populations changes along the Hubble sequence. The stellar age scales with Hubble type, decreasing from Sa to Sd. S0 and ellipticals have stellar populations of similar mean age, and they are older than spirals. In the bottom row we observe how stellar metallicity changes with the Hubble type. Metallicity increases from late to early type galaxies, although we find similar values for Sc and Sd, the galaxies with the lowest metallicities, and also between E and S0, those with larger metallicities.
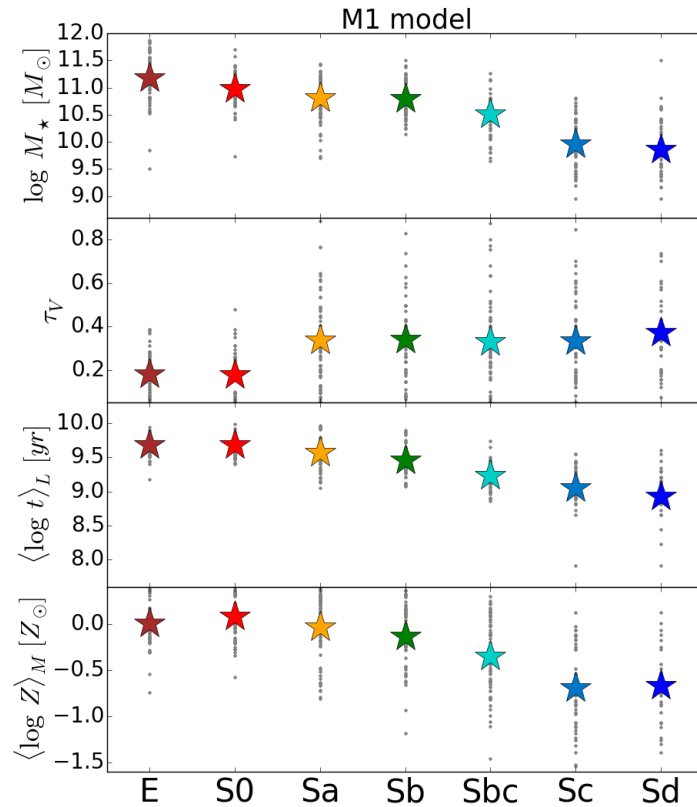

Figure 5.12 The properties of galaxies according to morphological type using **M1**. From top to bottom we show the stellar mass, attenuation value, mean stellar age and mean stellar metallicity.

Table 5.3 shows for the stellar population properties the differences between **M1** and the other models. For each property we indicate the mean ($\overline{\Delta}$) and standard deviation (σ) of the Δ ($= \mathbf{M1} - \mathbf{M}$) distribution, where **M** indicates a different model to **M1**.

Comparison with **M1** model: $\overline{\Delta} \pm \sigma_{\Delta}$

Model	$\log M_{\star}$	τ_V	$\langle \log t \rangle_L$	$\langle \log Z \rangle_M$
M2	0.01 ± 0.06	-0.01 ± 0.07	0.01 ± 0.09	0.02 ± 0.16
M3	-0.01 ± 0.11	0.01 ± 0.07	0.00 ± 0.09	0.04 ± 0.20
M4	-0.26 ± 0.20	-1.56 ± 0.76	0.68 ± 0.25	0.38 ± 0.41
M5	-0.32 ± 0.28	-1.47 ± 0.76	0.61 ± 0.27	0.49 ± 0.39
M6	-0.10 ± 0.14	0.05 ± 0.12	-0.13 ± 0.17	0.04 ± 0.31
M7	-0.14 ± 0.16	0.06 ± 0.12	-0.12 ± 0.15	0.21 ± 0.32
M8	-0.06 ± 0.15	0.03 ± 0.11	-0.04 ± 0.14	0.09 ± 0.31
M9	-0.11 ± 0.13	0.04 ± 0.08	-0.09 ± 0.18	0.14 ± 0.34

Table 5.3 Statistics of the comparison. For each model and physical property the table lists the mean **M1** minus **M** difference ($\overline{\Delta}$) and its standard deviation (σ_{Δ}), where **M** varies from **M2** to **M9**.

Model **M2** provides similar results to **M1**. Both models are very similar. The difference comes from the location of the peak of the SFR, which is delayed in comparison to t_0 in the model **M1**. This similarity is observed when computing the stellar population properties. For stellar mass and the light-weighted mean age we obtain $\overline{\Delta} = 0.01$ in both cases and $\sigma = 0.06$ and 0.09, respectively. Also the extinction values are very similar, with $\overline{\Delta} \pm \sigma = -0.01 \pm 0.07$. The derived metallicities show larger differences than the other parameters, with $\overline{\Delta} \pm \sigma = 0.02 \pm 0.16$. On the other hand, the larger uncertainties in the determination of metallicities is expected given the results of the simulations.

The **M3** model, using a "Sandage" profile, is again very similar to the **M1** model. In fact it is also a delayed τ-model, where the peak of the SFR occurs more recently than the onset of the burst, but the functional form of the model is different, as shown in the previous section. As is expected, we again obtain good agreement when comparing the derived properties, although the dispersion is slightly larger than in the previous case. The metallicity is again the property which shows more discrepancies, obtaining $\overline{\Delta} \pm \sigma = 0.04 \pm 0.2$.

The rising models imply a different view of the formation of galaxies. In this case, we assume that the SFR increases continuously from the beginning of the star formation history. For our sample of galaxies, it is expected that this kind of SFR is not representative of the formation history. As in the previous cases, the stellar mass is the most robust property, although we obtain a systematic deviation to larger values. Comparing with the **M4** model, the linear rising model, we obtain $\overline{\Delta} \pm \sigma = -0.26 \pm 0.2$ and comparing with **M5**, the power rising model, $\overline{\Delta} \pm \sigma = -0.32 \pm 0.28$. For the attenuation, the rising models provide larger values than the **M1** model. This is expected due to the high contribution of young stellar populations introduced by these models. For the mean stellar age and metallicity we obtain large discrepancies when comparing with **M1**.

Comparing with the **M6** model, two exponential components, we again obtain consistent values for the stellar mass between both methods. The dispersion is $\sigma = 0.14$ and the deviation $\overline{\Delta} = -0.1$. This means that with the **M6** model we derive larger masses than with the **M1** model. We will find the same feature comparing with the next models. As other works show (Wuyts et al. 2009; Sobral

et al. 2014), this is a systematic effect when using a single component SFH. Similarly, Michalowski et al. (2014) found that when a single-burst SFH is assumed, the stellar masses are systematically underestimated by 0.2 dex. For the other parameters we obtain good agreement between both models, although the uncertainties are larger than when comparing with **M2** and **M3**. Particularly, for the extinction $\overline{\Delta} \pm \sigma = 0.05 \pm 0.12$. For the stellar metallicity, the deviation is not significant between both models but the dispersion is large, $\sigma = 0.31$. The dispersion for the mean stellar age is $\sigma = 0.17$ and the offset is $\overline{\Delta} = -0.13$. For E and S0 galaxies the deviation is lower than for later types. The systematic difference in the stellar age comes from the assumed history. Focusing on late type galaxies, the star formation history is a combination of stellar populations of different ages, old, young and intermediate. Using two component models it is possible to reproduce the observed flux that comes from young stellar population by varying the young stellar component of the model. With the single component model we have two possibilities, the first one is to move the t_0 value, but it is a problem if older stellar populations are present in the star formation history. The second possibility is to increase the τ value, but this means adding the contribution of all young stellar populations, which results in younger ages.

Model **M7** is similar to **M6**, but in the case we fix the t_0 parameter in the old component to 14 Gyr. Again, the mass is the most robust parameter, obtaining $\sigma_\Delta = 0.16$, but the same offset is observed, with $\overline{\Delta} = -0.14$. For the attenuation we obtain $\overline{\Delta} = 0.06$ and $\sigma_\Delta = 0.12$, while for the mean stellar age, $\overline{\Delta} = -0.12$ and $\sigma_\Delta = 0.15$. In this case we observe more discrepancies in the metallicity values. The dispersion, $\sigma = 32$, is the same as we observed comparing with the model **M6**, but in this case we obtain a larger deviation ($\overline{\Delta} = 0.21$). Thus the model **M1** provides larger metallicities than **M7**. In the construction of two component models, we assume that the young component has equal or larger metallicity than the old component. As we are fixing the t_0 parameter of the old component, the contribution of this component to the total mass is larger than the contribution of the old component when using the model **M6**. It means that the mass-weighted mean metallicity would be lower using **M7**.

Models **M6** and **M8** have the same parametrisation as the old component but differ in the young component, which is represented by a "Sandage" profile in **M8**. We find similar results to those obtained with **M6**. For mass and attenuation we obtain $\overline{\Delta} \pm \sigma = -0.06 \pm 0.15$ and $\overline{\Delta} \pm \sigma = 0.03 \pm 0.11$, respectively. Comparing with the age values, the dispersion is similar to that obtained with **M6**, $\sigma = 0.14$, but in this case, introducing a delayed τ model in the young component, the offset with **M1** is reduced, $\overline{\Delta} = -0.04$. The metallicity is the parameter which shows larger dispersion, $\sigma = 0.31$, and the deviation is slightly larger than using **M6**, $\overline{\Delta} = 0.09$.

Comparing with **M9** we obtain good agreement for the other parameters, except for the metallicity. Particularly, for the stellar mass we have $\overline{\Delta} \pm \sigma = -0.11 \pm 0.13$. In the case of the extinction parameter we have, $\overline{\Delta} \pm \sigma = 0.04 \pm 0.08$, while for mean stellar age we have $\overline{\Delta} \pm \sigma = -0.09 \pm 0.18$. For the metallicity we obtain $\overline{\Delta} \pm \sigma = 0.14 \pm 0.34$.

5.6   Comparing Parametric method with STARLIGHT: Integrated properties

We have presented two different tools with the aim of recovering the stellar population properties using different data sets. With STARLIGHT we fit the optical spectra of galaxies plus UV photometry without imposing any restriction on the shape of the SFH. With the parametric method we fit optical and UV photometry plus spectral indices with the assumption on the shape of the SFH. The codes have different structures but both of them use a similar minimization technique to explore the parameter space, the Markov Chain Montecarlo Method. In this section we explore how the recovered properties are compared by using both methods.

5.6.1   Integrated properties: Star Formation History

We begin by analysing the star formation history recovered using the two methods. We are going to compare the SFHs according the Hubble type, but the results of the parametric method can be interpreted in two different ways. The first one is averaging the parameters on the model and then computing the mean SFH from the mean parameters. The second one is averaging the SFHs for the different morphological types. With STARLIGHT we average the mass fraction for the different ages in the spectral base:

$$\overline{SFH}(t) = \frac{1}{N} \sum_{gal \in C} SFH_{gal}(t), \tag{5.15}$$

where $SFH_{gal}(\log t)$ is the star formation history for an individual galaxy as a function of time, C is a morphological type and N is the number of galaxies that belong to C. In order to make a consistent comparison we compute the mean star formation history with the Parametric method in the same way.

Figures 5.13 to 5.22 show the mean star formation history of galaxies (left panel) and the cumulative mass fraction profiles for the different Hubble types obtained with STARLIGHT and for the different parametric models. The dashed black line in the right panels indicates the 80% of the total mass. In order to capture similar trends we resample the SFHs to similar ages with a constant step size of 0.2 dex.

On average, all galaxies have their peak of star formation at the earliest times (figure 5.13). Sb and earlier type galaxies show a very rapid decline in comparison with later morphological types, which show a more extended period of star formation (left panel). Rejuvenation is also observed for Sd galaxies in the last 2 Gyr. From the cumulative mass fraction profiles, we obtain that earlier types galaxies reach 80% of the total mass earlier in the past, with a rapid mass accretion. On the other hand, for later types the stellar mass has grown slower reaching 80% of the total mass more recently. This is in agreement with the "downsizing" observed in other surveys.

The results with **M1**, **M2** and **M3** follow a similar trend (figures 5.14, 5.15 and 5.16), with an extended period of star formation for Sbc and later morphological types and rapid mass accretion for earlier types. Models **M1** and **M3** are delayed-τ models and the derived star formation histories are very similar. The main difference is the location of the peak of star formation which occurs more recently using **M3**.
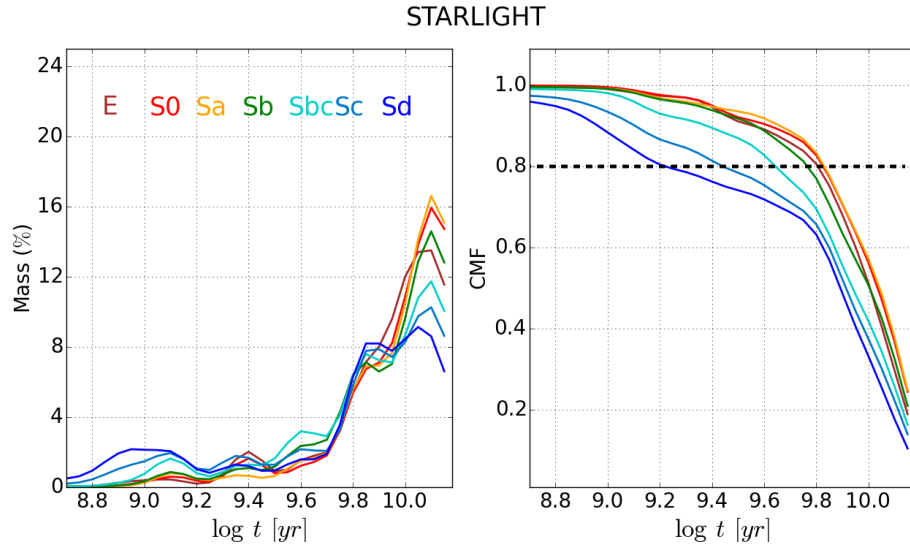
Figure 5.13 Mass fraction profiles (left) and cumulative mass fraction profiles (right) obtained with STARLIGHT. The colours indicate the different morphological types.

In the previous section we presented the rising models, commonly used in high redshift studies. From the previous analysis, we concluded that these models are not well representative of the star formation history of low redshift galaxies. Figures 5.17 and 5.18 show the mass fraction profiles and the cumulative mass fraction profiles obtained with linear and power rising models (**M4** and **M5**). From the assumption of a rising model, the peak in the star formation occurs at present. Thus it is expected that the mass has been formed more slowly than when using a decaying model, as we observe from the cumulative mass fraction profiles. In both cases, $t_{80} < 2.5$ Gyr, a lower value than in the previous models and STARLIGHT. Comparing linear with power rising models, we observe that in the first case (figure 5.17) the mass grows more slowly than when using the power rising model (figure 5.18).
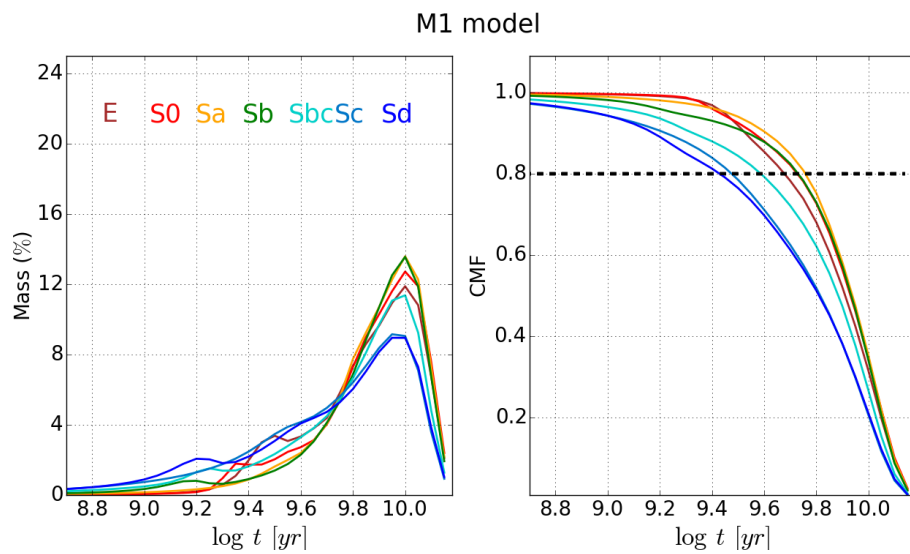

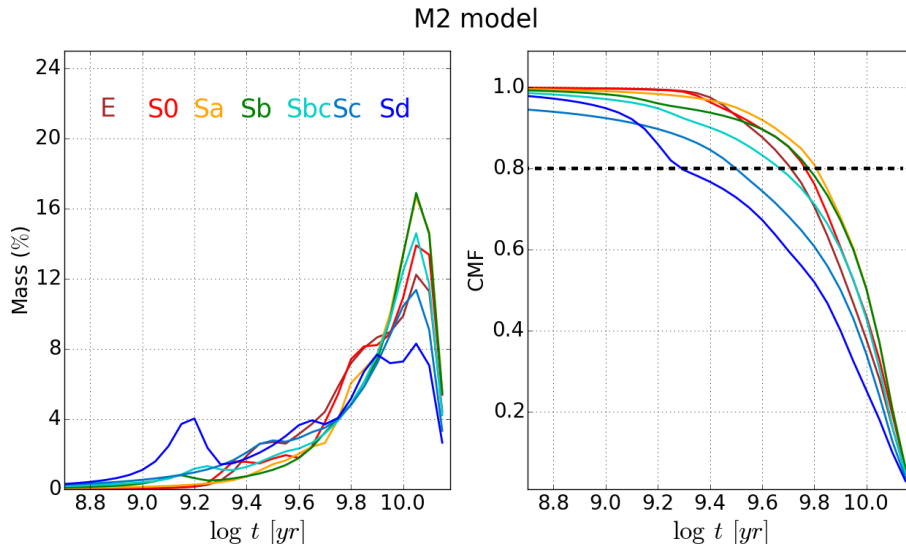Figure 5.14 Same as figure 5.13 using model **M1**.

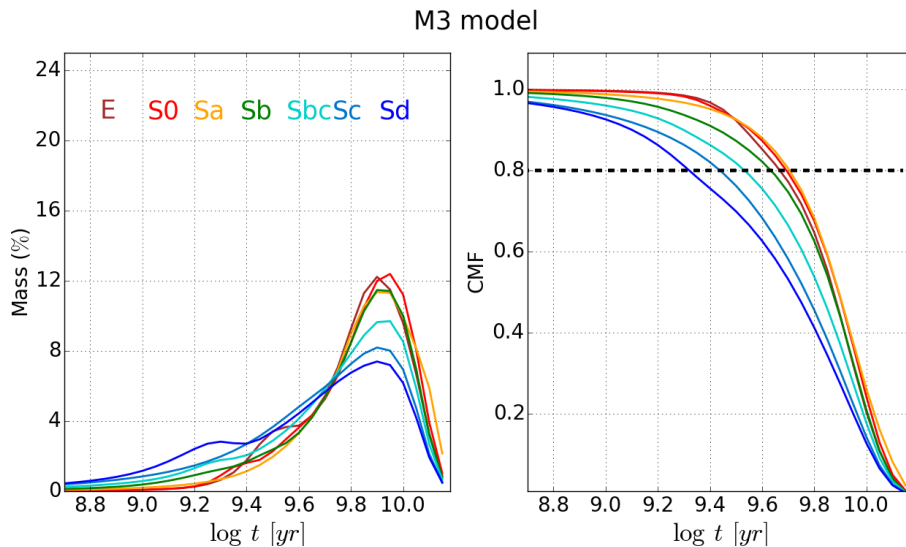Figure 5.15 Same as figure 5.13 using model **M2**.

Figure 5.16 Same as figure 5.13 using model **M3**.

Figure 5.19 shows the results with the **M6** model. The peak of star formation occur early in the past, but it correlates with the Hubble type. The peak for E and S0 galaxies occur earlier and with larger intensity than for later types. The cumulative mass fraction profiles show that E and S0 formed 80% of the total mass earlier in the past.

The mass profiles obtained with **M7** show the initial peak at 14 Gyr (figure 5.20). In this case we observe that almost the total mass has been formed in the first Gyrs of the formation of galaxies. This model shows a very fast galaxy growth, reaching 80% of the total mass in a few Gyr, although the accretion of mass occurs more rapidly in Sb and earlier types than in later type galaxies.

Model **M8** is similar to **M6**, varying the parametrisation of the young component, and the averaged profiles show similar features (figure 5.21). The mass profiles for E and S0 galaxies decrease rapidly and the beginning of the star formation occurs at the earliest times in comparison with later morphological
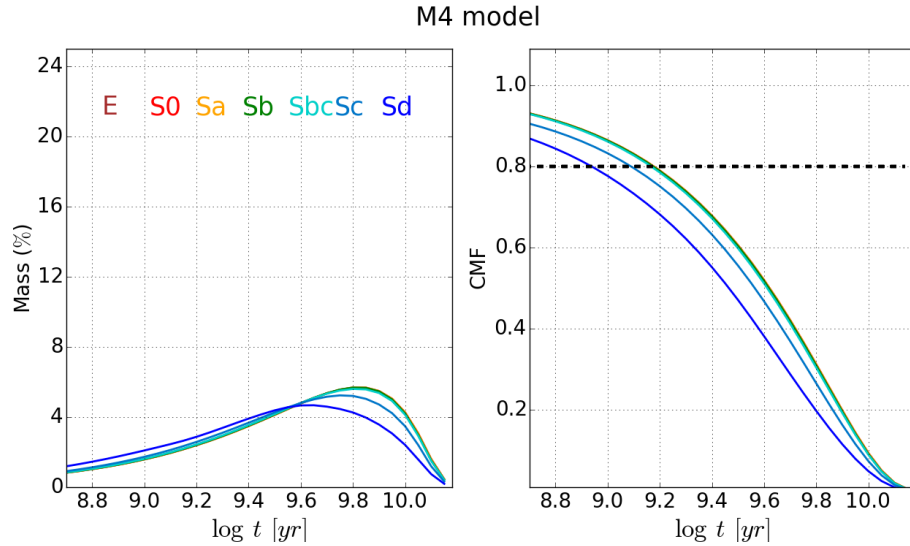
Figure 5.17 Same as figure 5.13 using model **M4**.
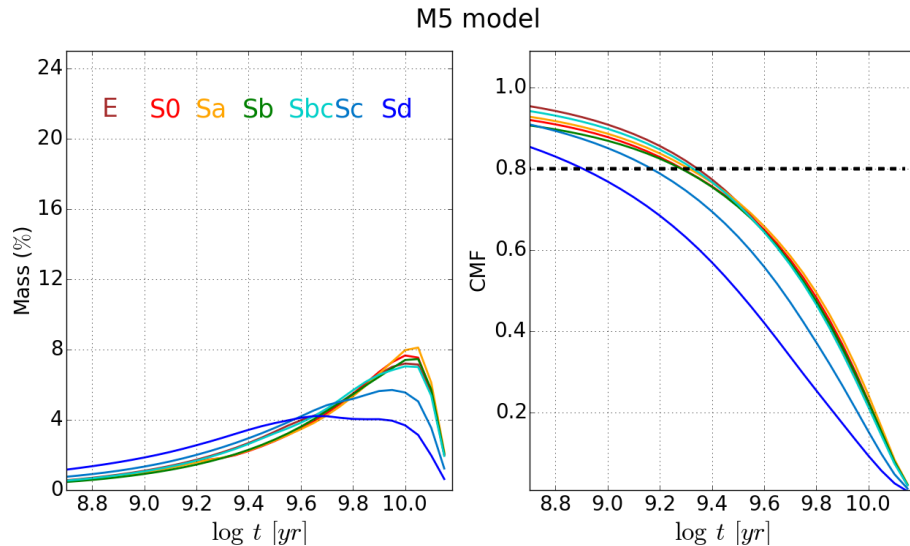
Figure 5.18 Same as figure 5.13 using model **M5**.

types. On the other hand, the period of star formation is more extended for later types. Regarding the right panel we find that t_{80} increase from Sd to E galaxies.

Figure 5.22 shows the results using **M9**. This model combines an initial constant SFR followed by a declined exponential profile. The decay of the star formation begins between 6 and 8 Gyr in the past, and the period to shut down the star formation correlates with the Hubble type, being more extended for late type galaxies.

From figure 5.23 to 5.31 we compare the star formation histories (left column) and the cumulative mass fraction profiles (right column) derived with STARLIGHT with those derived with the parametric models, according to the different morphological types. The solid lines show the results using parametric models, while dashed lines represent the results with STARLIGHT. The dashed black line in the cumulative mass fraction profile indicates 80% of the total mass.

M6 model

Figure 5.19 Same as figure 5.13 using model **M6**.

M7 model

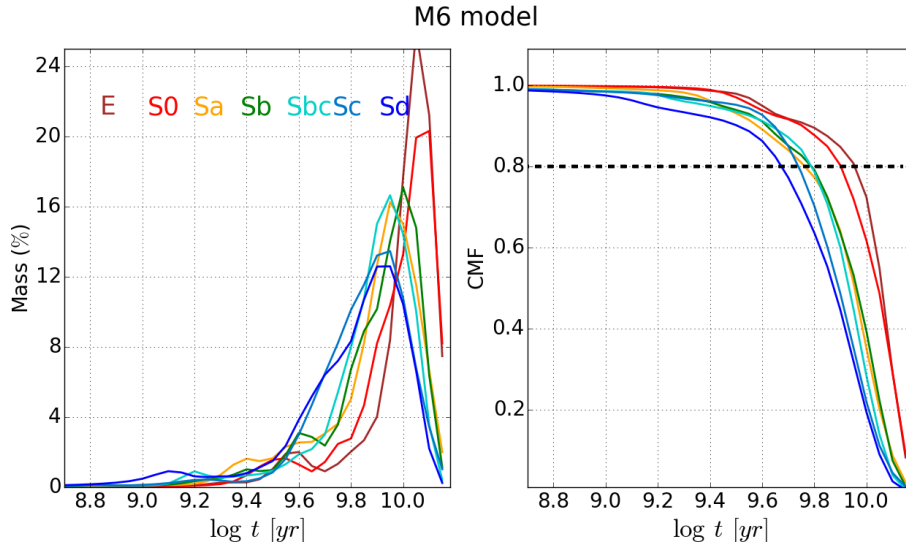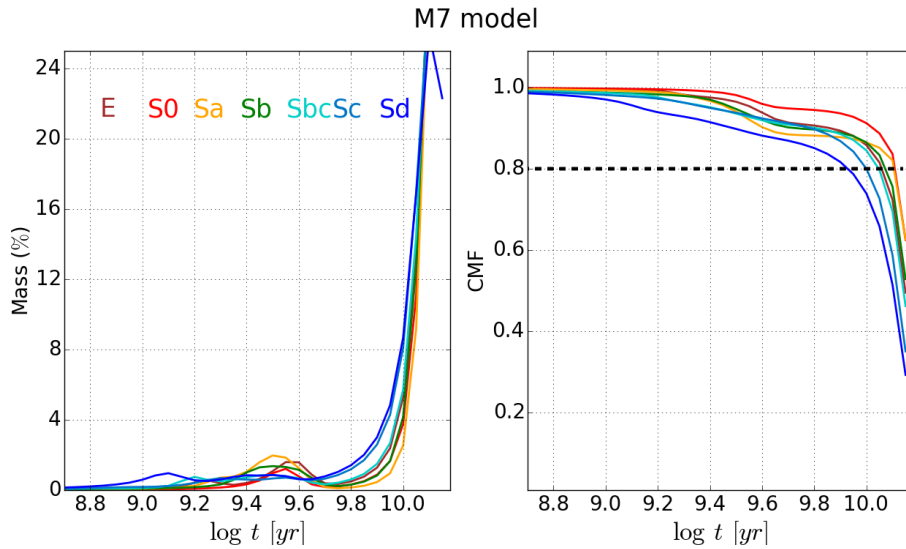Figure 5.20 Same as figure 5.13 using model **M7**.

M1, **M2** and **M3** provide similar trends in the star formation histories. Comparing with STARLIGHT (figures 5.23, 5.24 and 5.25), the peak of star formation occurs more recently for models **M1** and **M3**, which are delayed-τ models, and is located in the same epoch as with **M2**. On the other hand, from the cumulative mass fraction profiles we obtain a faster growth of galaxies using STARLIGHT for early type and similar t_{80} values for later type galaxies.

Figures 5.26 and 5.27 compare rising models with STARLIGHT. The period of star formation is more extended using rising models and t_{80} values are much lower than those obtained with STARLIGHT.

Comparing STARLIGHT with **M6** and **M8** models (figures 5.28 and 5.30) we obtain a similar location of the peak of star formation for E and S0 galaxies and a more recent location for later types using the parametric models. Using these models, a faster accretion of mass is obtained, with larger values for t_{80}. Figure 5.29 shows the mass fraction profiles and the cumulative mass fraction profiles
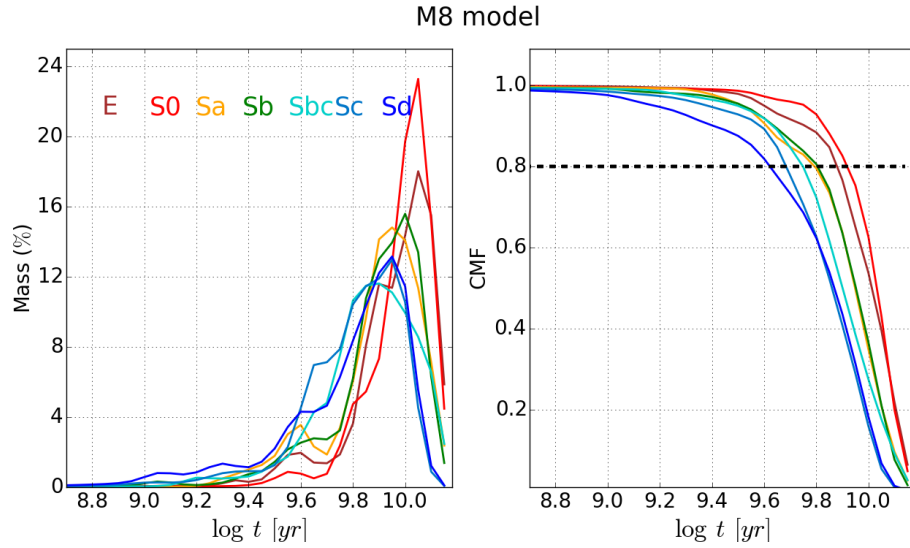
Figure 5.21 Same as figure 5.13 using model **M8**.
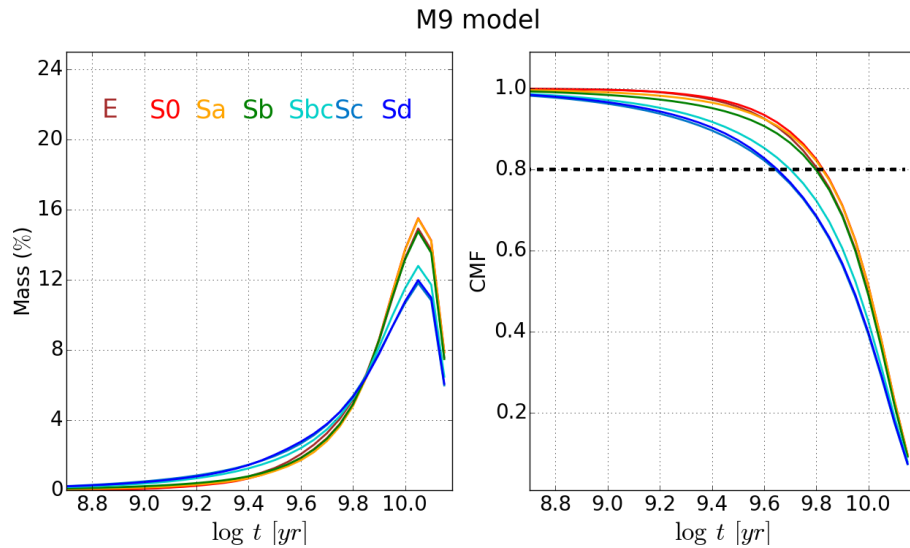
Figure 5.22 Same as figure 5.13 using model **M9**.

for the different morphological types using the **M7** model, fixing the t_0 value for the old component to 14 Gyr. The intensity of the peak of star formation is much larger using **M7** rather than STARLIGHT and the period of star formation is shorter, reaching 80% of the total mass in few Gyr.

The mass profiles obtained with **M9** are similar to those derived with STARLIGHT (figure 5.31). The peak of star formation is located during the same epoch using both methods and the star formation occurs along a similar period. Sc and Sd galaxies show larger t_{80} values using **M9**, which indicates a faster galaxy growth.
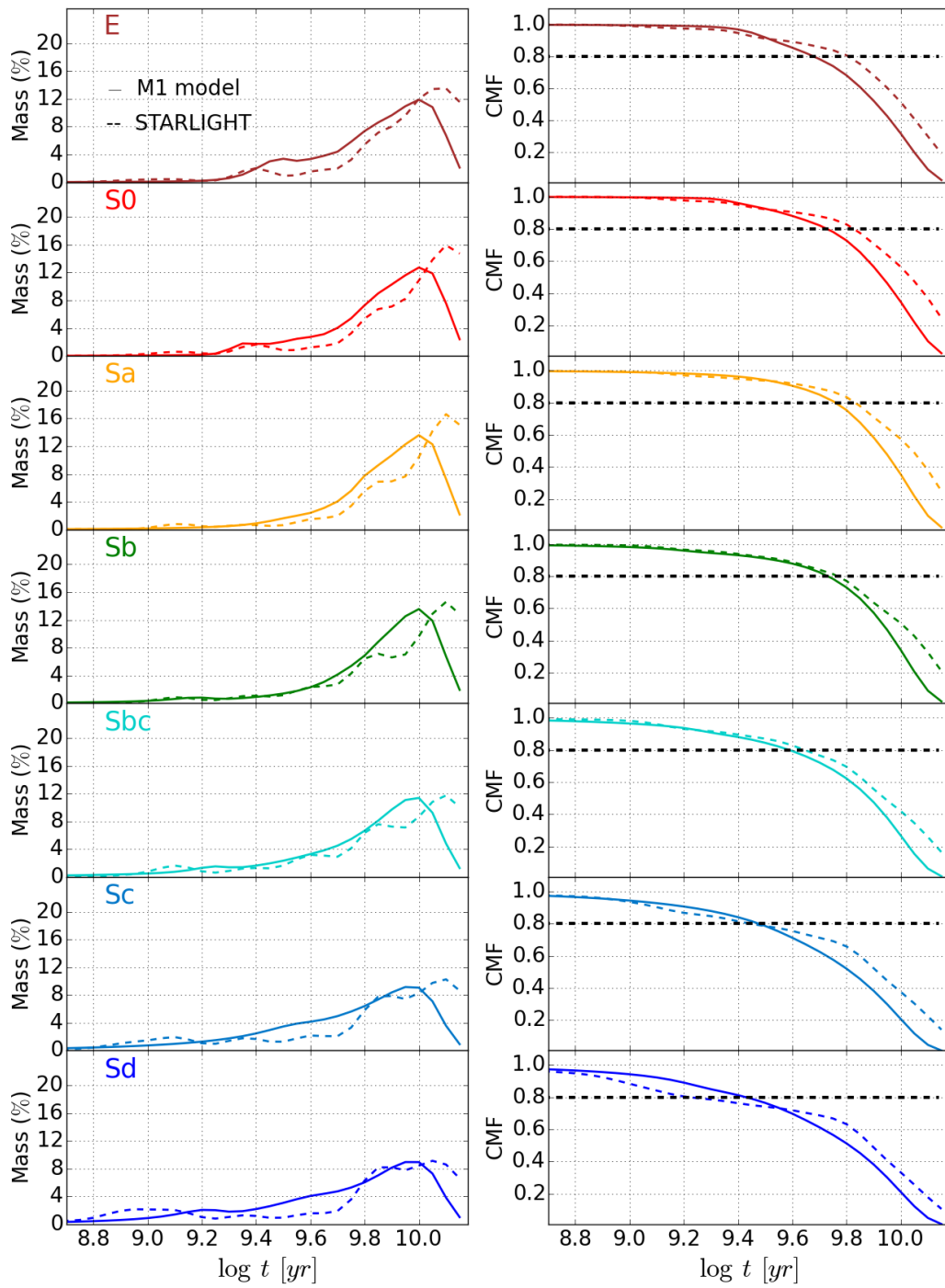
Figure 5.23 Mass fraction profiles (left column) and cumulative mass fraction profiles (right column). The solid lines show the results derived with the **M1** model. Dashed lines represent the results with STARLIGHT. The different morphological types are colour-coded.
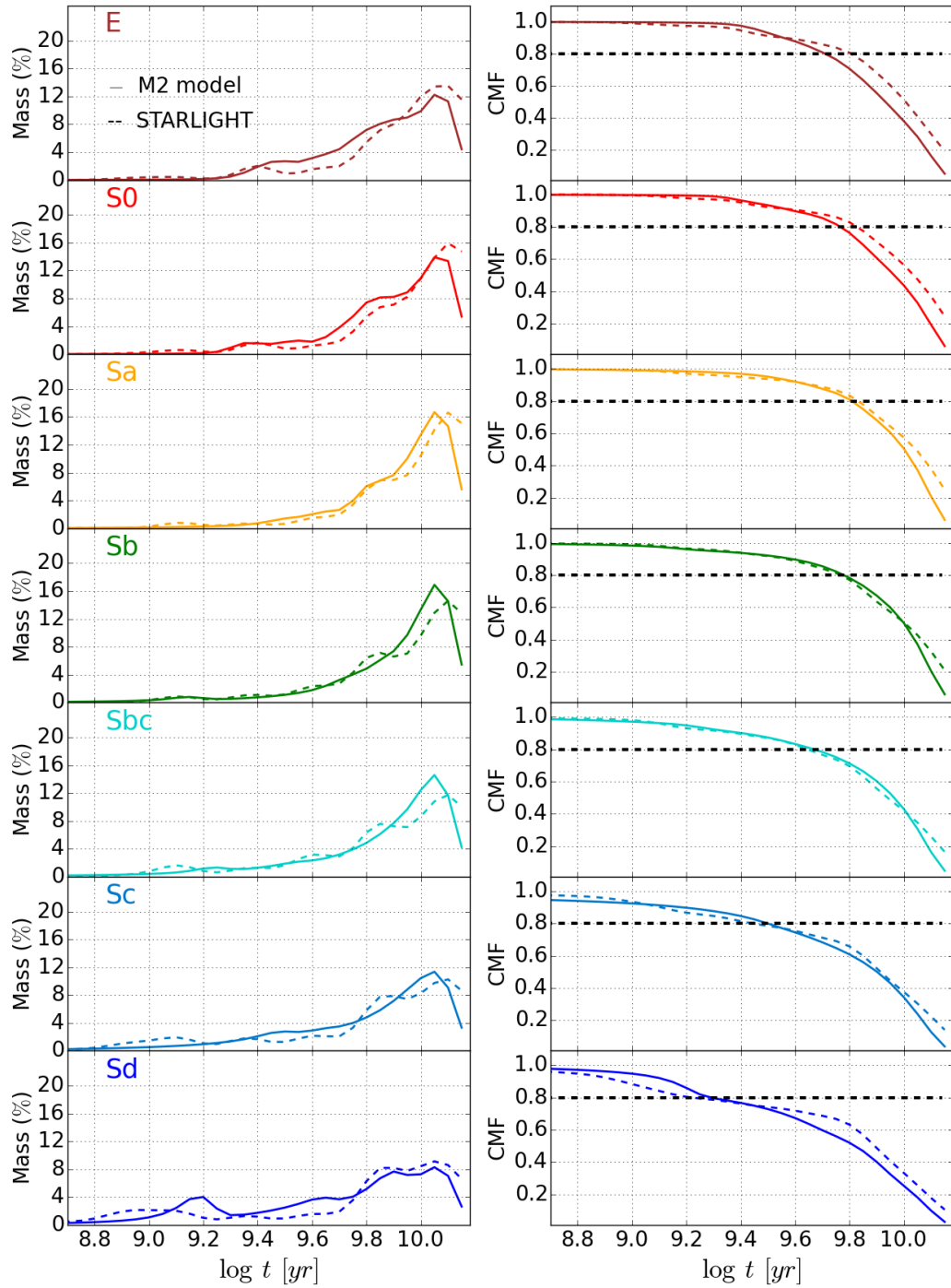
Figure 5.24 Same as figure 5.23 using the **M2** model.
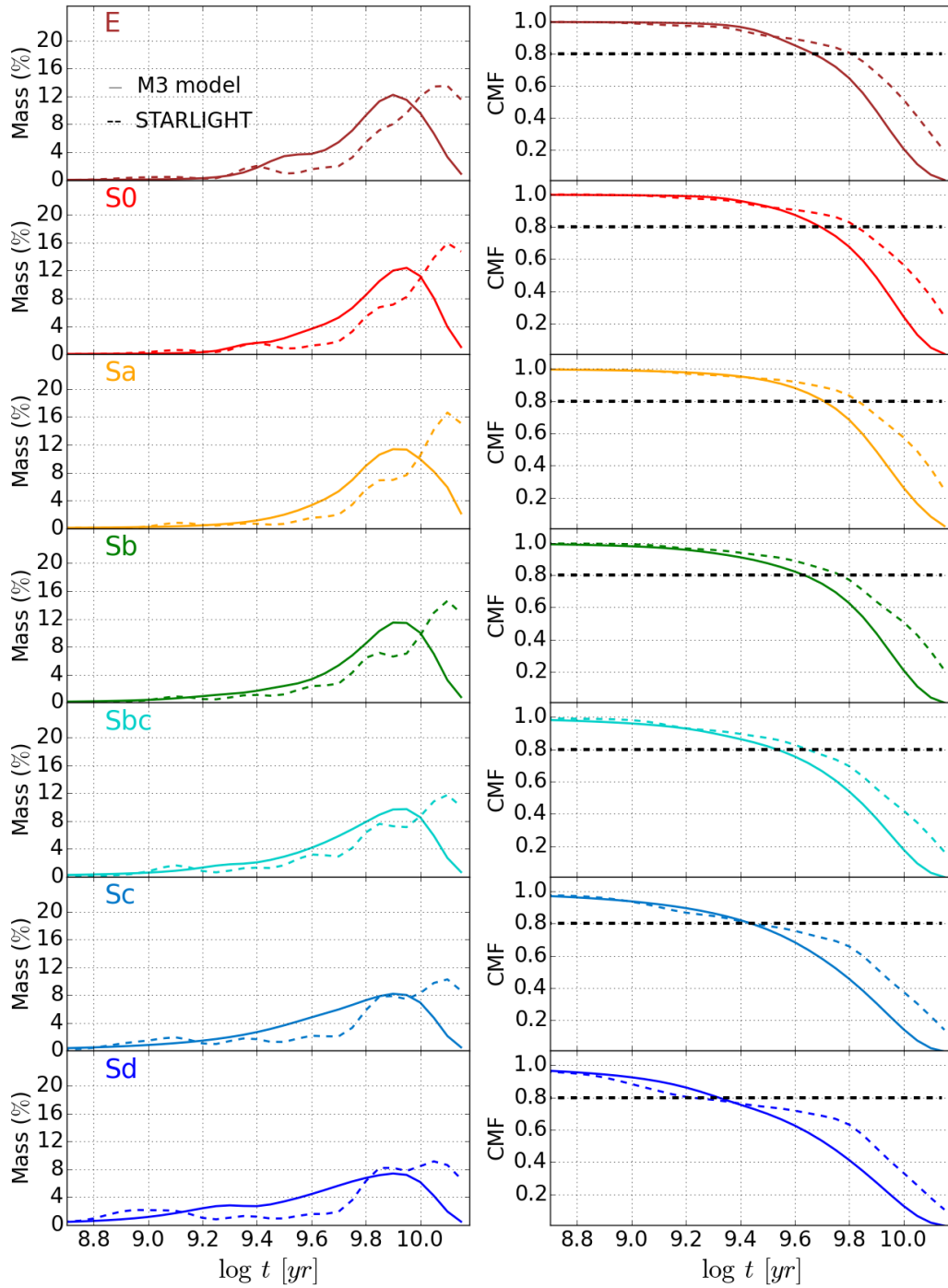
Figure 5.25 Same as figure 5.23 using the **M3** model.
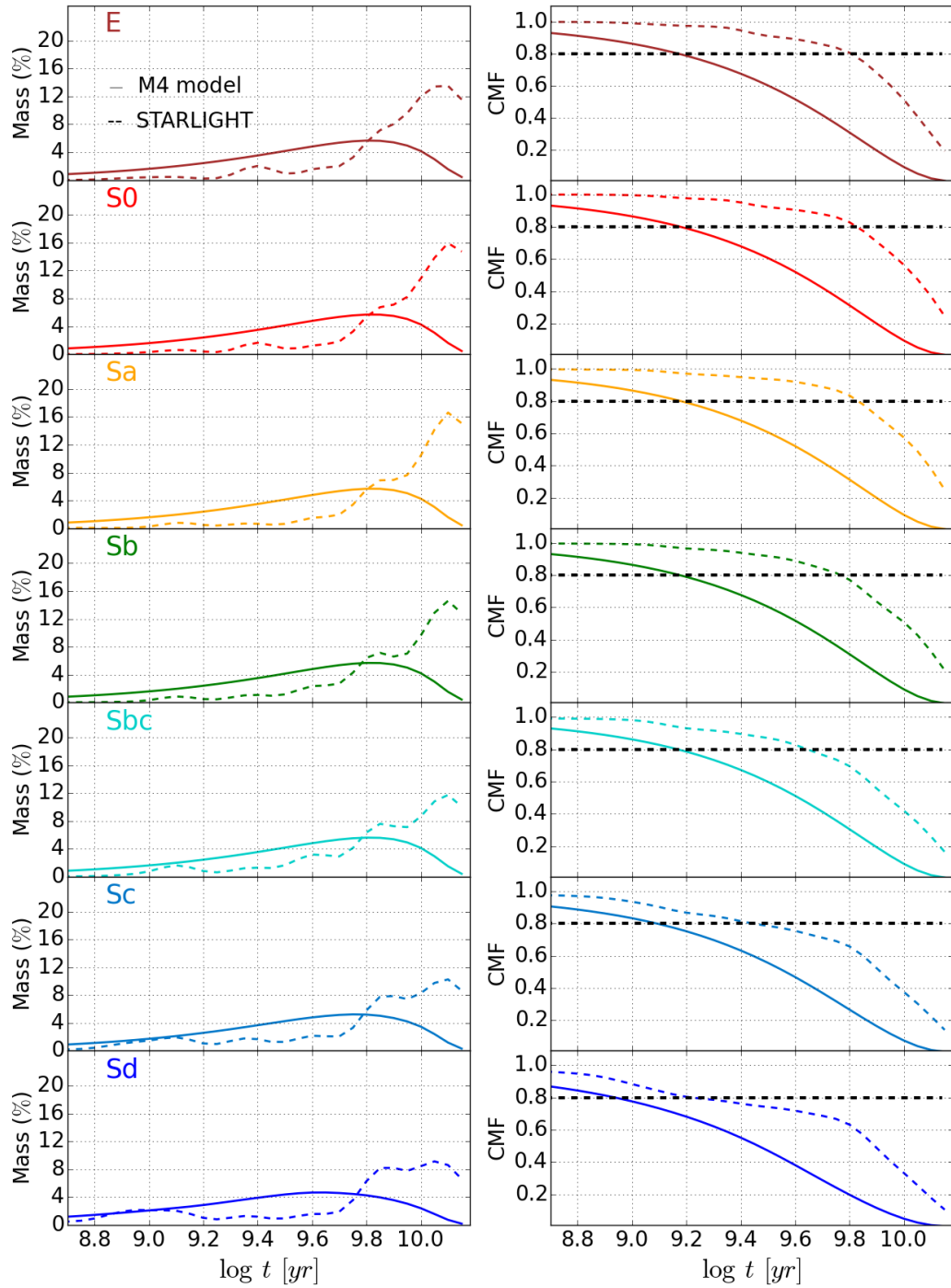
Figure 5.26 Same as figure 5.23 using the **M4** model.
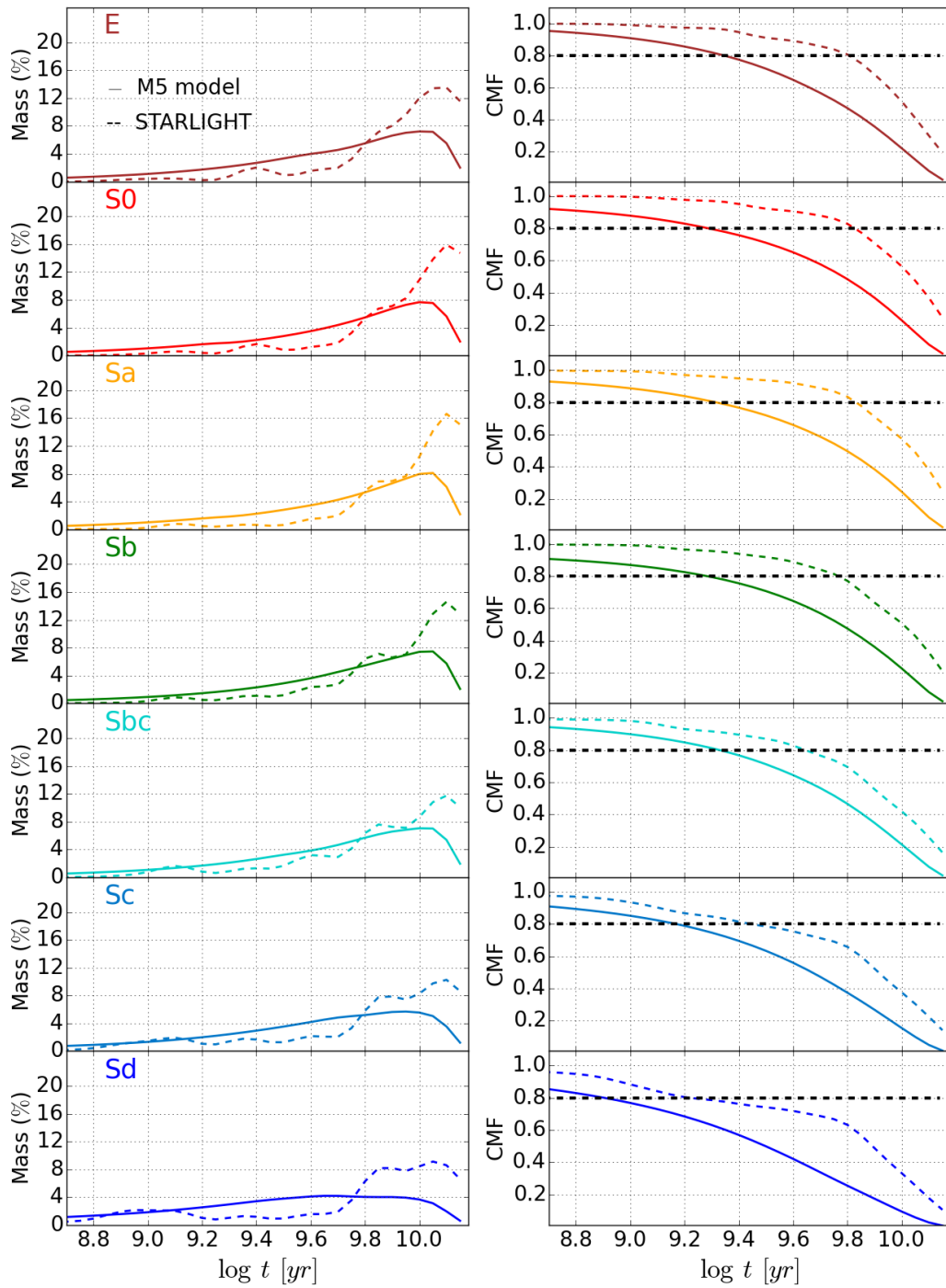
Figure 5.27 Same as figure 5.23 using the **M5** model.
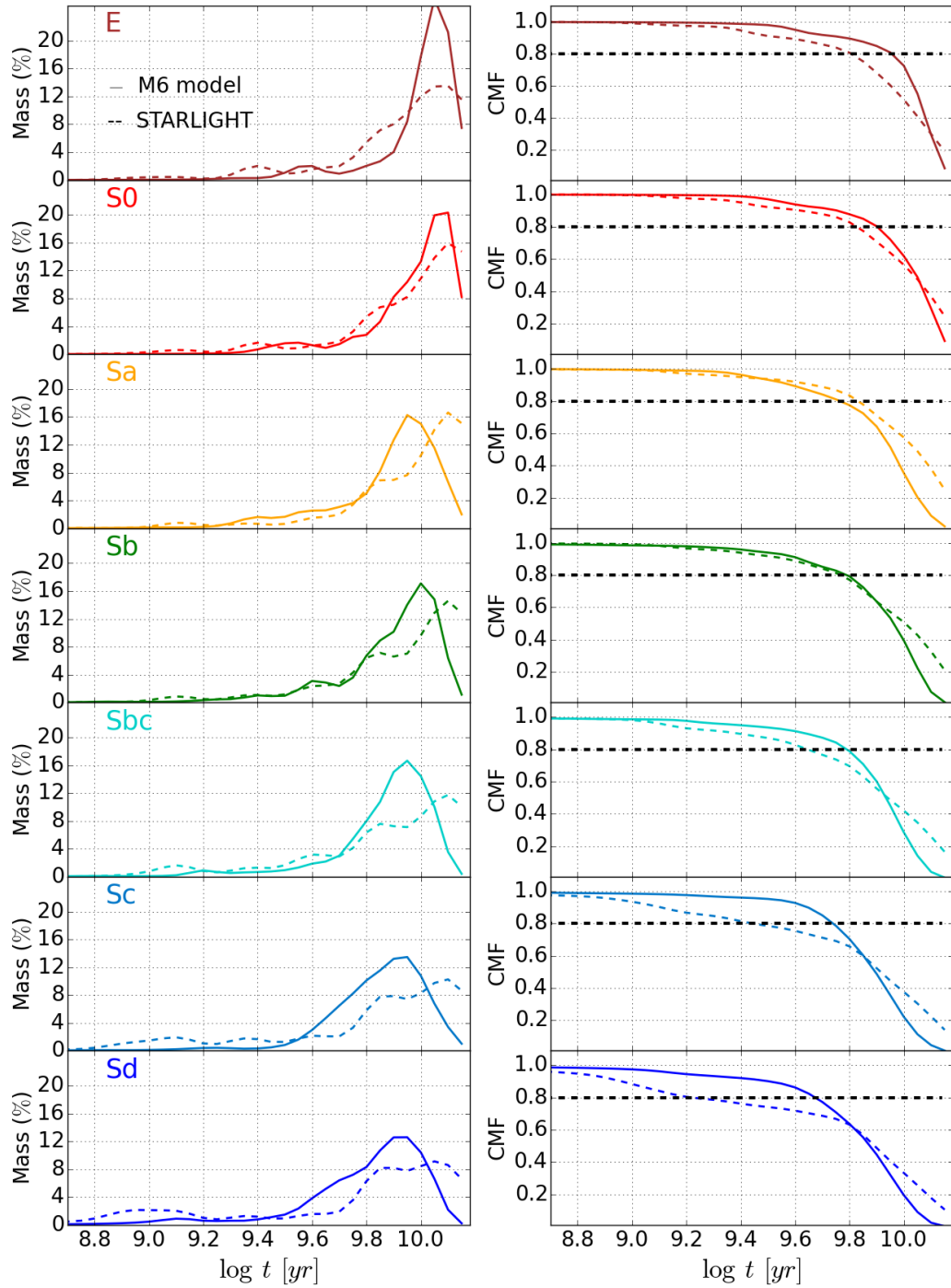
Figure 5.28 Same as figure 5.23 using the **M6** model.
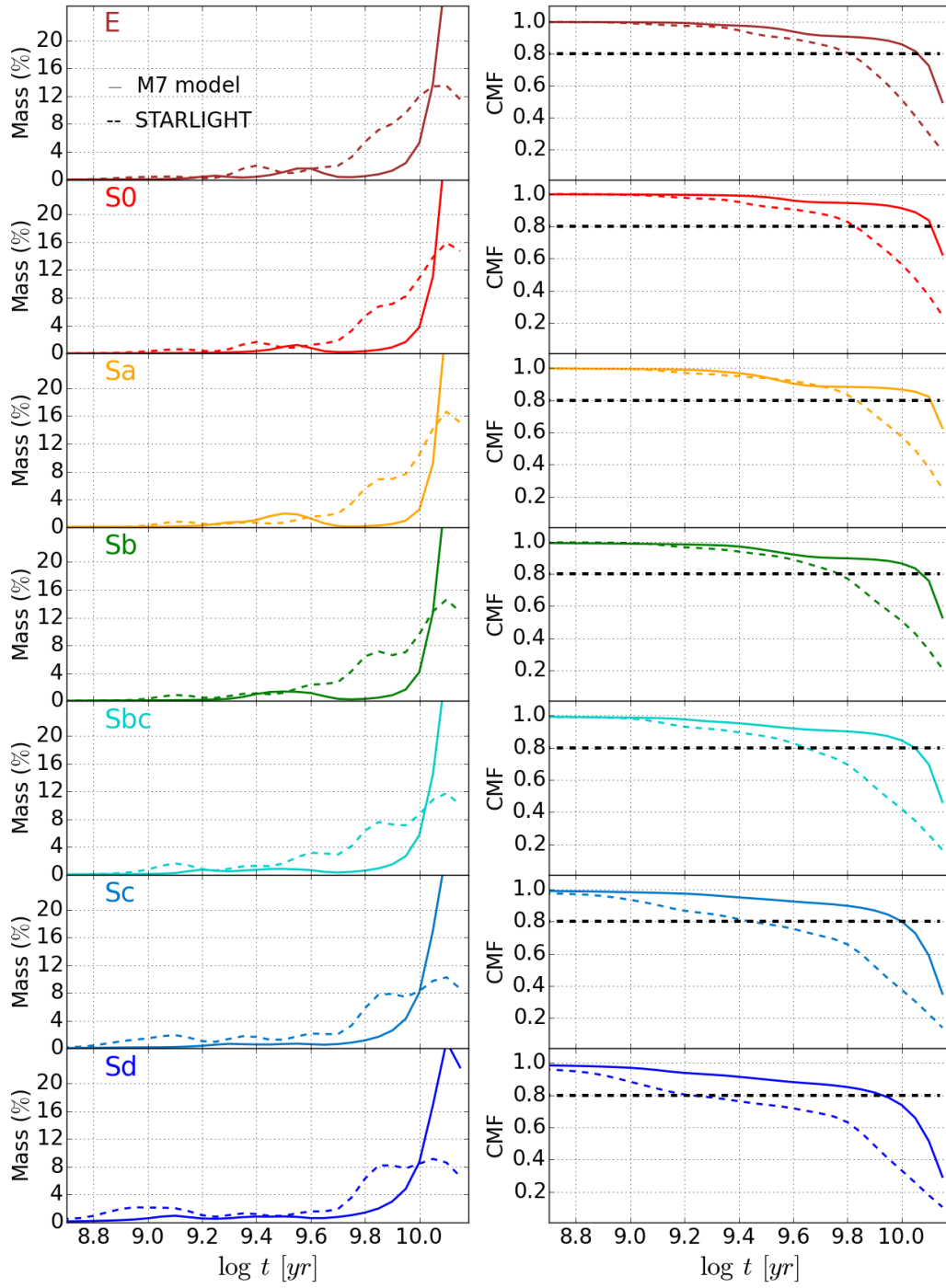
Figure 5.29 Same as figure 5.23 using the **M7** model.
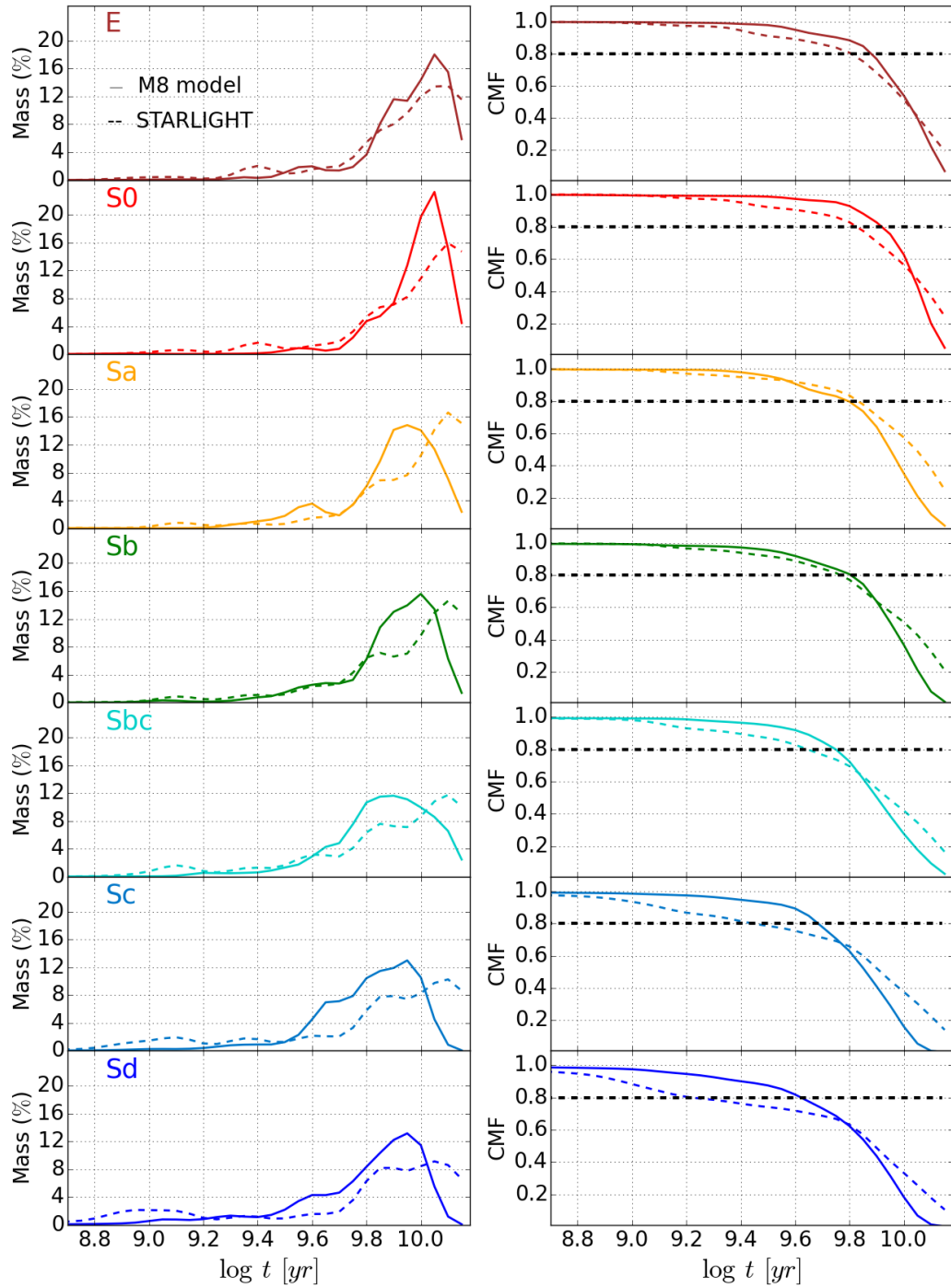
Figure 5.30 Same as figure 5.23 using the **M8** model.
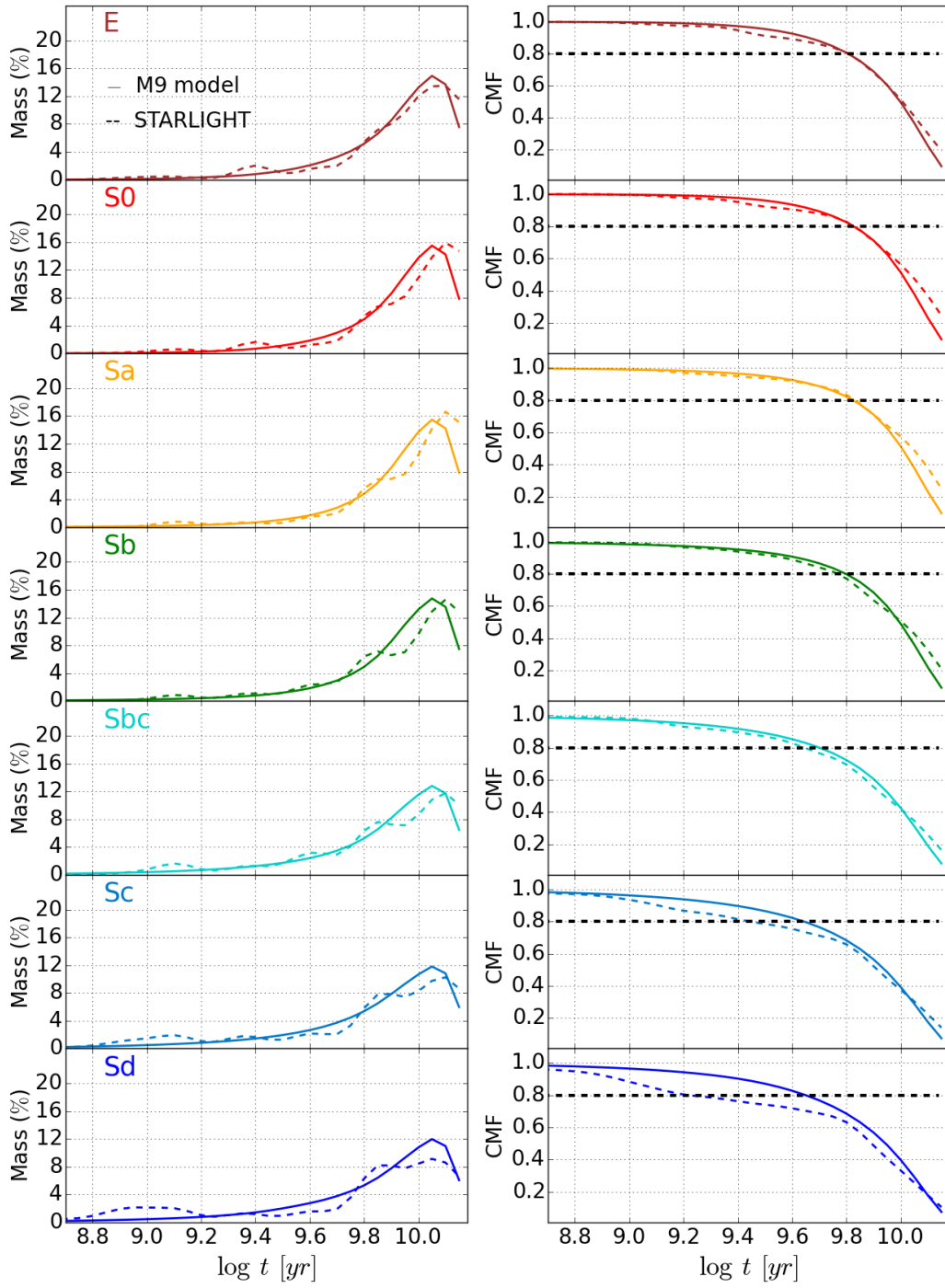
Figure 5.31 Same as figure 5.23 using the **M9** model.

5.6.2   Integrated properties: Stellar population properties

In this section we analyse the following stellar population properties: stellar mass, attenuation, mean stellar age and mean stellar metallicity. The different figures in this section compare the STARLIGHT results with those obtained with the different models. Table 5.4 summarizes the statistics of this comparison. For each property we indicate the mean ($\overline{\Delta}$) and standard deviation (σ) of the Δ (= STARLIGHT$-$**M**) distribution.

<div align="center">

Comparison with STARLIGHT: $\overline{\Delta} \pm \sigma_\Delta$

| Model	$\log M_\star$	τ_V	$\langle \log t \rangle_L$	$\langle \log Z \rangle_M$
M1	0.16 ± 0.17	-0.12 ± 0.12	0.12 ± 0.20	-0.07 ± 0.37
M2	0.18 ± 0.16	-0.12 ± 0.12	0.14 ± 0.18	-0.05 ± 0.37
M3	0.15 ± 0.20	-0.11 ± 0.12	0.12 ± 0.21	-0.01 ± 0.38
M4	-0.08 ± 0.21	-1.67 ± 0.79	0.99 ± 0.33	0.37 ± 0.52
M5	-0.15 ± 0.28	-1.58 ± 0.79	0.84 ± 0.35	0.59 ± 0.54
M6	0.07 ± 0.10	-0.07 ± 0.11	-0.01 ± 0.14	-0.02 ± 0.20
M7	0.02 ± 0.13	-0.05 ± 0.10	0.01 ± 0.15	0.17 ± 0.22
M8	0.10 ± 0.09	-0.08 ± 0.10	0.09 ± 0.13	0.03 ± 0.19
M9	0.05 ± 0.10	-0.07 ± 0.13	0.02 ± 0.17	0.08 ± 0.24

</div>

Table 5.4 Statistics of the comparison. For each model and physical property the table lists the mean STARLIGHT minus **M** difference ($\overline{\Delta}$) and its standard deviation (σ_Δ), where **M** varies from **M1** to **M9**.

"Delayed-τ" model (M1)

In figure 5.32 we compare the stellar population properties obtained with STARLIGHT and using the **M1** model. In the top row we observe the stellar mass ($M_\star$) and attenuation (τ_V), in the second row the mean stellar age ($\langle \log t \rangle_L$) and mean stellar metallicity ($\langle \log Z \rangle_M$). The parametric method results are shown on the x-axis and the STARLIGHT ones on the y-axis. Each panel shows $\overline{\Delta}$ with Δ defined as STARLIGHT $-$ Parametric, with the corresponding dispersion σ_Δ.

Regarding the stellar mass we obtain $\overline{\Delta} \pm \sigma = 0.16 \pm 0.16$. As we commented in the previous section, the observed offset is a systematic effect when using a single component SFH.

For the attenuation we found that the Parametric method provides larger values of τ_V ($\overline{\Delta} \sim -0.12$), but, on the other hand, we found the opposite effect for the mean stellar age, with $\overline{\Delta} \sim 0.12$. As we will show later we found the same effect when using the others single component models. As occurred with mass, the dispersion values are not too large, with σ_Δ=0.12 and 0.2, respectively.

For E and S0 galaxies, we obtain that the attenuation values are nearly zero with STARLIGHT, but not with the Parametric method. With STARLIGHT we can add some light fraction in a single population or change the extinction value to achieve the best spectral fitting, but using a single model, as we do here, and assuming that for E and S0 galaxies t_0 will be large, we can only change τ and τ_V to achieve the fit of the observables. Instead of adding some light fraction in a single component, if needed, we have to increase the τ value, which means to adding some light fraction to many young stellar populations, not only one. As is expected, a larger τ_V is obtained compared to with STARLIGHT.

The derived metallicities show larger discrepancies, with $\overline{\Delta} \sim -0.07$ and $\overline{\Delta} \sim 0.37$, which also happen also with the other single component models. Only when introducing a second component

in the model, we find more agreement in the derived metallicity values. We observe clearly larger metallicity derived with the Parametric for Sd galaxies, which is also found when using two component models, although with lower dispersion.

Exponentially-decaying burst (M2)

Figure 5.33 shows the stellar population properties obtained with both methods, using in this case the **M2** model. Regarding the stellar mass we obtain an offset of $\overline{\Delta} \sim 0.18$, practically the same as when using the **M1** model. On the other hand the dispersion value is also very similar to that obtained using the **M1** model, $\sigma_\Delta = 0.16$. Using the **M2** model we obtain larger values of τ_V ($\overline{\Delta} \sim -0.12$), but we found the opposite effect for the mean stellar age, with $\overline{\Delta} \sim 0.14$. As occurs with the mass, the dispersion values are not too large, with $\sigma_\Delta = 0.12$ and 0.18, respectively. The derived metallicities show again large differences, with $\overline{\Delta} \sim -0.05$ and $\overline{\Delta} \sim 0.37$.

"Sandage" profile (M3)

In figure 5.34 we compare the stellar population properties obtained with STARLIGHT and using the **M3** model. The offset in the stellar mass is very similar to in previous cases, $\overline{\Delta} \sim 0.15$, with a slightly larger dispersion, $\sigma_\Delta = 0.2$. **M3** is also a single component model, so this offset is expected as found for previous cases. Lower ages and larger attenuation values are also found. For τ_V we obtain $\overline{\Delta} \sim -0.11$ and $\sigma_\Delta = 0.12$, while for the mean stellar age $\overline{\Delta} \sim 0.12$ and $\sigma_\Delta = 0.21$. The values for the $\overline{\Delta}$ and σ are very similar to those obtained using the previous two models. Again, the offset for the attenuation values is larger for E and S0 galaxies than for later types. The derived metallicities again show large differences, with $\overline{\Delta} \sim -0.01$ and $\overline{\Delta} \sim 0.38$, as with other models. However in this case we observe that besides the worse agreement for Sd galaxies, we also found worst agreement for E and S0 galaxies, obtaining lower metallicity values when using the **M3** model.

Rising SFH

Analysing the stellar properties we also find discrepancies using the rising models. Figures 5.35 and 5.36 show the stellar mass, attenuation, mean stellar age and metallicity and the mass-metallicity relation. The mass is the most robust parameter and, although more in agreement with the previous models, we obtain $\overline{\Delta} \sim -0.08$ and $\sigma_\Delta = 0.21$ for linear model, and $\overline{\Delta} \sim -0.15$ and $\sigma_\Delta = 0.28$ for power rising model.

The attenuation is larger with the rising models than with STARLIGHT, obtaining $\overline{\Delta} \sim -1.67$ and $\sigma_\Delta = 0.79$ for the linear rising model, and $\overline{\Delta} \sim -1.58$ and $\sigma_\Delta = 0.79$ for the power model. This is expected because the rising models produce blue spectra by construction and to compensate this effect the τ_V has to be large.

On the other hand, we obtain ages with the linear rising model that remain in a narrow band. This is due to the fact that we are averaging the ages values weighted by a straight line (figure 5.35) and the slope and t_0 for the different profiles don't vary notably. The attenuation is the parameter which compensates for the excess flux produced by the young stellar population. Using the power rising model we obtain a more wider range of values, but also around the centre of the age range (figure 5.36).

Concerning the metallicity, we also find that the values are concentrated around the centre of

the metallicity range covered by the stellar populations. We observed in the previous section that these models are not able to reproduce the observables, both magnitudes and indices. That means very large values of $\chi2$. The best way to reduce the $\chi2$ values using these models is by changing the slope of the straight line (or the exponent in the power model) and changing the t_0 values. Thus, the metallicity values do not have much effect on the fits using these models. It means that the PDF for the metallicity will be very wide and centered around the mean value in the metallicity range.

The discrete values obtained for age and metallicity imply that the global relations are not reproduced as we observe in figures figure 5.45 and 5.46.

Two exponential components (M6)

Figure 5.37 shows the comparison with the **M6** model. Regarding the stellar mass we now obtain a very good agreement using both methods. In particular, $\overline{\Delta} = 0.07$ and $\sigma_\Delta = 0.1$. Introducing the second component in the histories we avoid the observed offset when deriving masses using the single component models.

A visually inspection of the τ_V values shows a good correlation between STARLIGHT and the Parametric method. Numerically, we obtain $\overline{\Delta} = -0.07$ and $\sigma_\Delta = 0.11$, which suggests an offset between the τ_V. The cause of this difference is mainly the values obtained for E and S0 galaxies. As explained before, with the parametric models we change the t_0 and τ values, but we cannot add any fraction to a single stellar population. However, if a young component is needed for a better spectral fitting, STARLIGHT can add light fraction in just one or several populations. For E and S0 galaxies, the Parametric method adds a young exponential component which accounts for many young populations. To compensate for this effect the attenuation value needs to be larger.

We also observe very good agreement in the mean stellar age, better than with one component models, obtaining $\overline{\Delta} = -0.01$ and $\sigma_\Delta = 0.14$, although for late type galaxies the ages obtained with the **M6** model are slightly larger than with STARLIGHT.

The derived metallicities values now show fewer discrepancies between both methods. In particular, $\overline{\Delta} = -0.02$ and $\sigma_\Delta = 0.2$. We observe good correlation for all galaxies except for Sd types, which show larger metallicites with the Parametric method than with STARLIGHT. We obtain very low metallicities when using STARLIGHT for Sd galaxies, but such low values are difficult to reach using the Parametric method. We assume that the metallicity for the young component is the same or larger than for the old component, and particularly for these galaxies the mass fraction for the young component is more important than for earlier types. Mathematically, it is possible to reach points in the parameter space to derive the same low metallicities that we obtain with STARLIGHT, but a better solution is found with larger metallicities but also slightly lower τ_V values.

Fixing old component (M7)

As previously said, figure 5.38 shows that mass is the most robust parameter and we obtain very good agreement using **M7**. In particular, $\overline{\Delta} = 0.02$ and $\sigma_\Delta = 0.13$. We note that, although we reduce the dimensions of the parameter space by fixing t_0 for the old component, we are using two components, and avoid the offset observed when using simple component models.

Regarding attenuation and mean stellar age, we obtain very similar results. For τ_V we have $\overline{\Delta} = -0.05$ and $\sigma_\Delta = 0.1$, while for the mean stellar age, $\overline{\Delta} = 0.01$ and $\sigma_\Delta = 0.15$. As with the previous

model, we obtain more agreement with STARLIGHT than using the single component models, reducing both $\overline{\Delta}$ (in absolute value) and σ_Δ.

For the metallicity we observe an offset with respect to the **M6** model. In particular $\overline{\Delta} = 0.17$ and $\sigma_\Delta = 0.22$. The lower metallicity values obtained with the Parametric method are due to the assumption on the model. When fixing t_0 for the old component we obtain that the mass fraction for the young component (f_Y) is very low. In our models, the old component is the "low" metallicity component, so such small values of f_Y produce a shift toward younger metallicities. On the other hand we include in the model a large contribution of old stellar population, with the peak of the SFR at 14 Gyr. Lower metallicity values are expected due to this restriction.

"Sandage" young component (M8)

In figure 5.39 we compare STARLIGHT with the **M8** model. Again, we find good agreement in the derived stellar mass ($\overline{\Delta} = 0.1$ and $\sigma_\Delta = 0.09$), although the offset is slightly larger than when using models **M6** and **M7**.

Concerning the attenuation we also obtain similar results to with previous models, obtaining $\overline{\Delta} = -0.08$ and $\sigma_\Delta = 0.1$ and again larger discrepancies for E and S0 galaxies. The mean stellar age values are also well estimated with this model but obtaining a slightly larger offset toward younger ages with the with **M8**, $\overline{\Delta} = 0.09$ and $\sigma_\Delta = 0.13$.

With respect to the metallicity, again we obtain more discrepancies with STARLIGHT. Summarising the differences in $\overline{\Delta} = 0.02$ and $\sigma_\Delta = 0.25$ we obtain basically the same results as when using **M6**. Visually, we clearly observe that differences for Sd galaxies remain using this model, but we also derive lower metallicities for Sb and earlier morphological types. Models **M6** and **M8** are very similar, modifying the shape of the young component, an exponential in the first case and the "Sandage" profile in the second. This means that with the same t_0 value for the young component, the peak of the star formation occurs earlier when using the "Sandage" profile and over a longer period of time. Compared to **M6**, a lower fraction for the young component would be needed to reproduce a similar result. This could explain the observed offset toward lower metallicity values for Sb and earlier morphological types. For Sd galaxies the fraction of young component is larger than for the other morphological types and our assumption of larger metallicities for the young component could be the reason for the discrepancies, as happened with model**M6**.

Constant SFR + exponentially declining (M9)

Using **M9**, the agreement in the stellar masses is clearly observed with $\overline{\Delta} = 0.05$ and $\sigma_\Delta = 0.1$ (figure 5.40). Although this model is not exactly composed by two components, the observed offset when using only a single component does not remains here.

When comparing the attenuation values, we find larger discrepancies, particularly for some Sd and E galaxies, but on average the values are not so different, with $\overline{\Delta} = -0.07$ and $\sigma_\Delta = 0.13$. For the mean stellar ages we also observe good agreement, obtaining $\overline{\Delta} = 0.02$ and $\sigma_\Delta = 0.17$. Some Sd galaxies are older when using the Parametric method, which are the same with lower τ_V values.

We can summarize the results for metallicity as $\overline{\Delta} = 0.08$ and $\sigma_\Delta = 0.24$, but observing the figure we see that we are obtaining almost discrete values. As explained when comparing this model with **M1** model in the previous section, this model is built combining a constant SFR for a period, determined

by parameter t_0, followed by an exponential decay, determined by the τ parameter. When analysing the parameter space we find that the PDF for both parameters, t_0 and τ of the exponential, are very narrow. As we assume a constant metallicity throughout the star formation history, the narrow PDFs imply the need obtain discrete metallicities, thus in our spectral base.
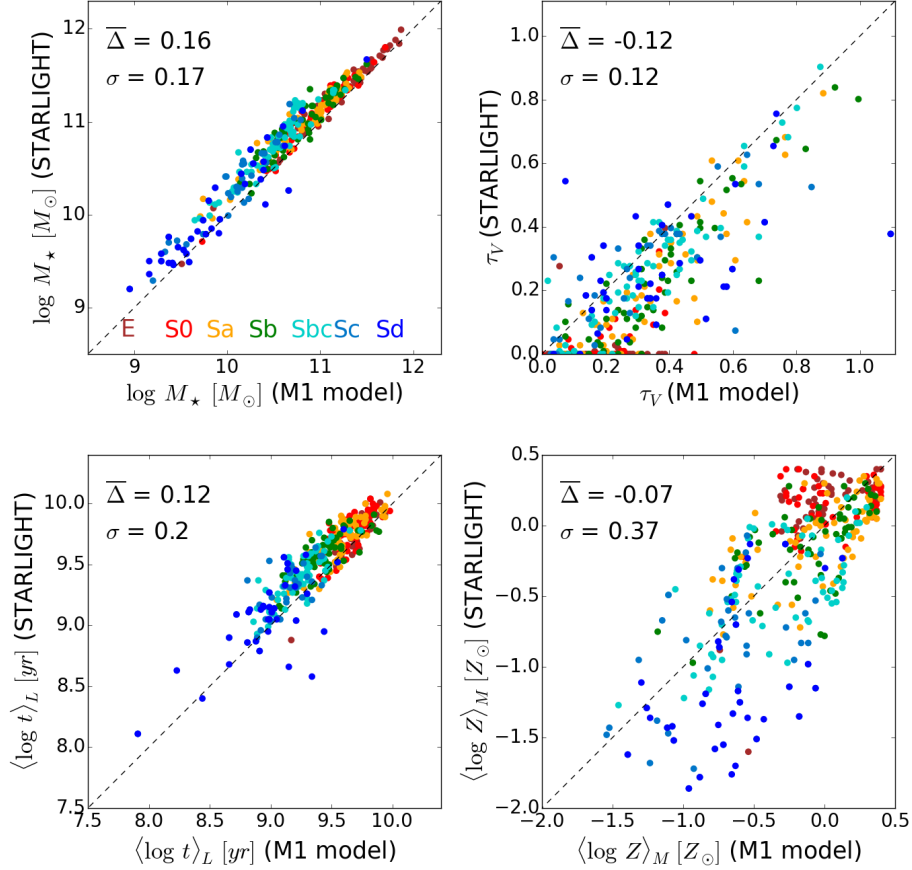
Figure 5.32 Each panel shows the comparison of a stellar population property between STARLIGHT (y-axis) and **M1** model (x-axis): stellar mass ($M_\star$, top left), attenuation (τ_V, top right), light-weighted mean stellar age ($\langle \log age \rangle_L$, bottom left) and mass-weighted mean stellar metallicity ($\langle \log Z \rangle_M$, bottom right). The morphological types are colour-coded. Each panel also indicates $\overline{\Delta}$ and σ, where Δ represents STARLIGHT $-$ **M1** for the different properties.
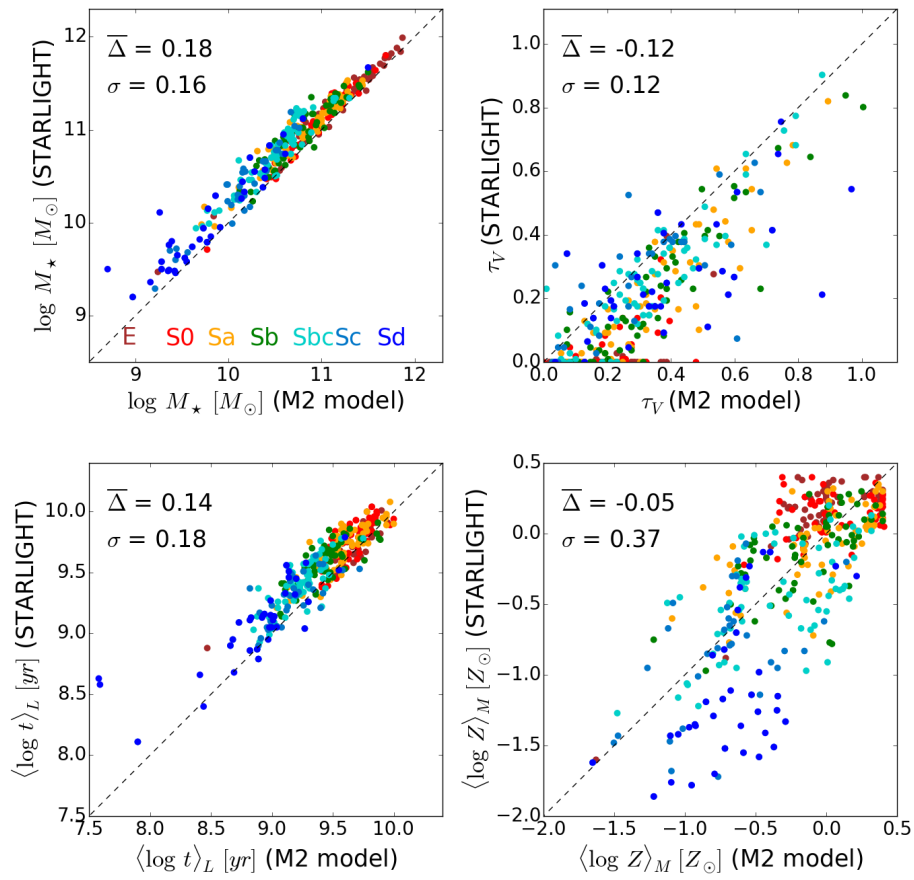
Figure 5.33 Same as figure 5.32 using model model **M2**.
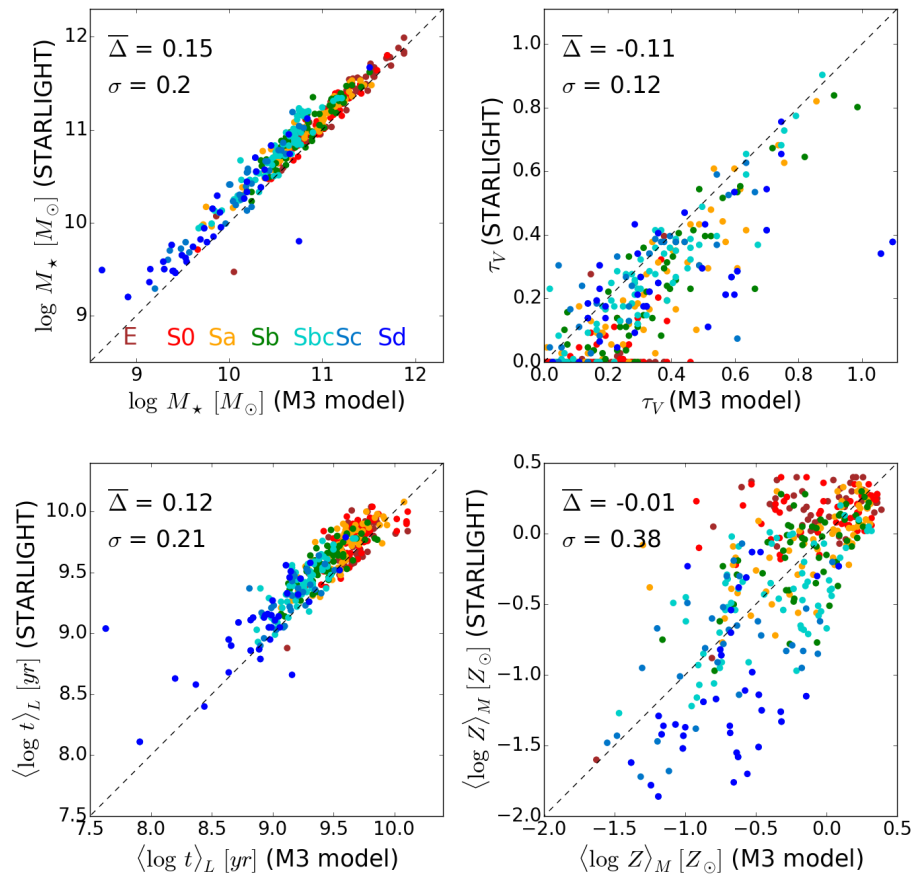
Figure 5.34 Same as figure 5.32 using model **M3**.
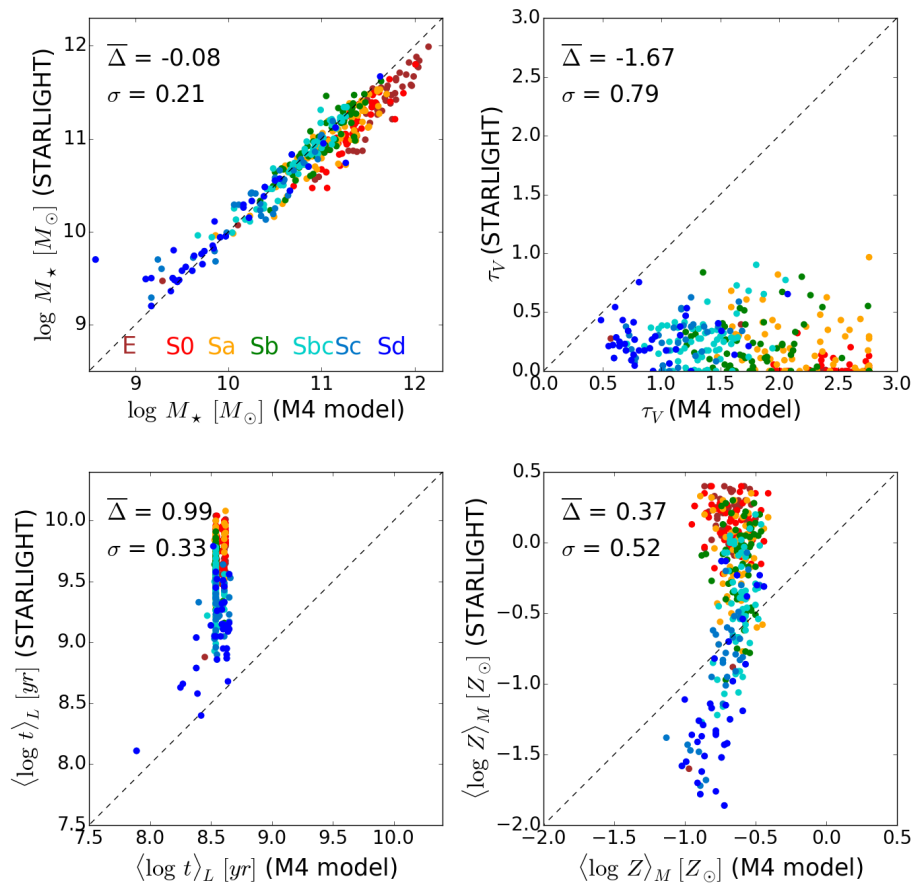
Figure 5.35 Same as figure 5.32 using model **M4**.
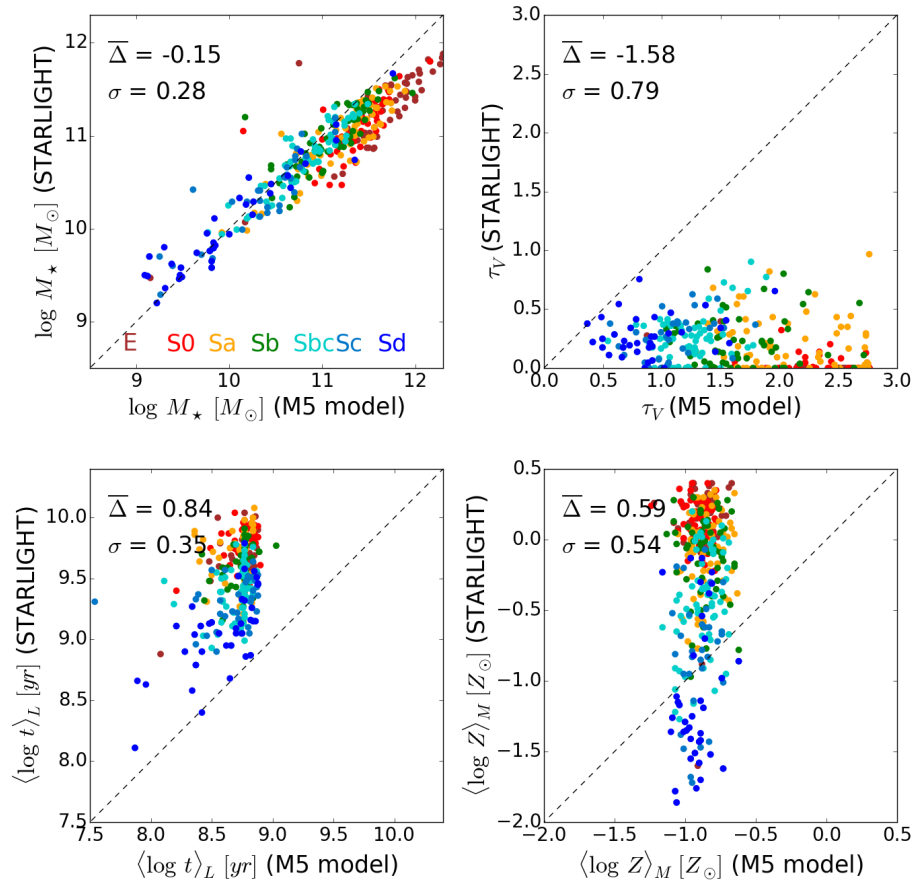
Figure 5.36 Same as figure 5.33 using model **M5**.
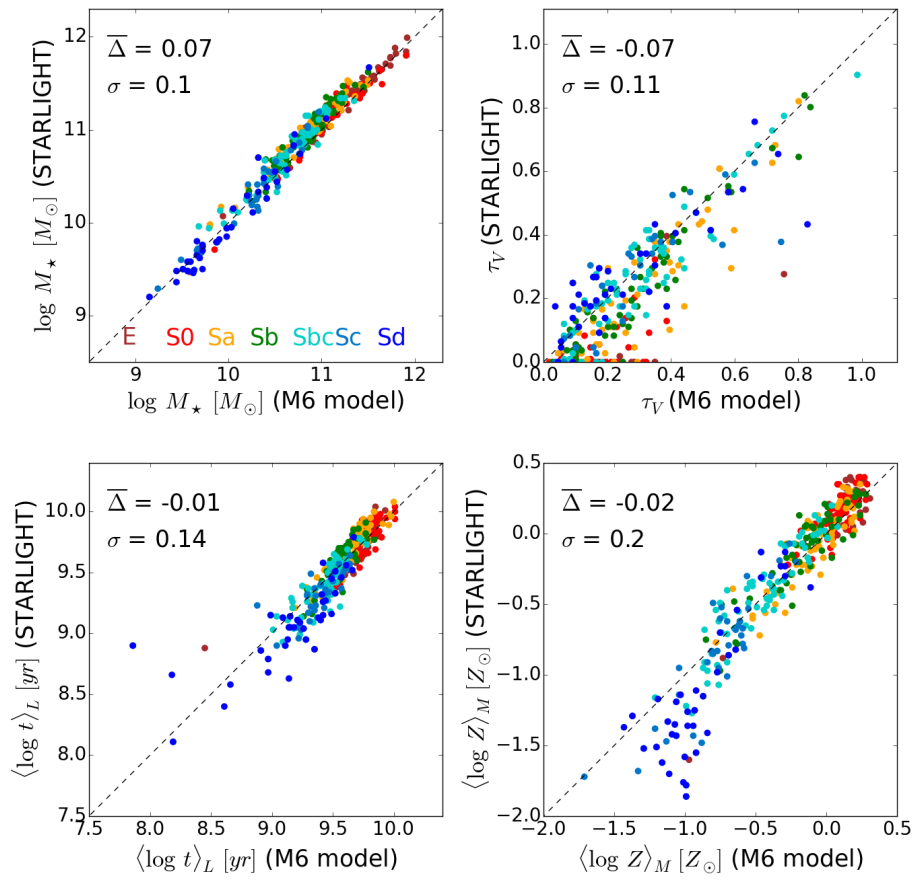
Figure 5.37 Same as figure 5.32 using model **M6**.
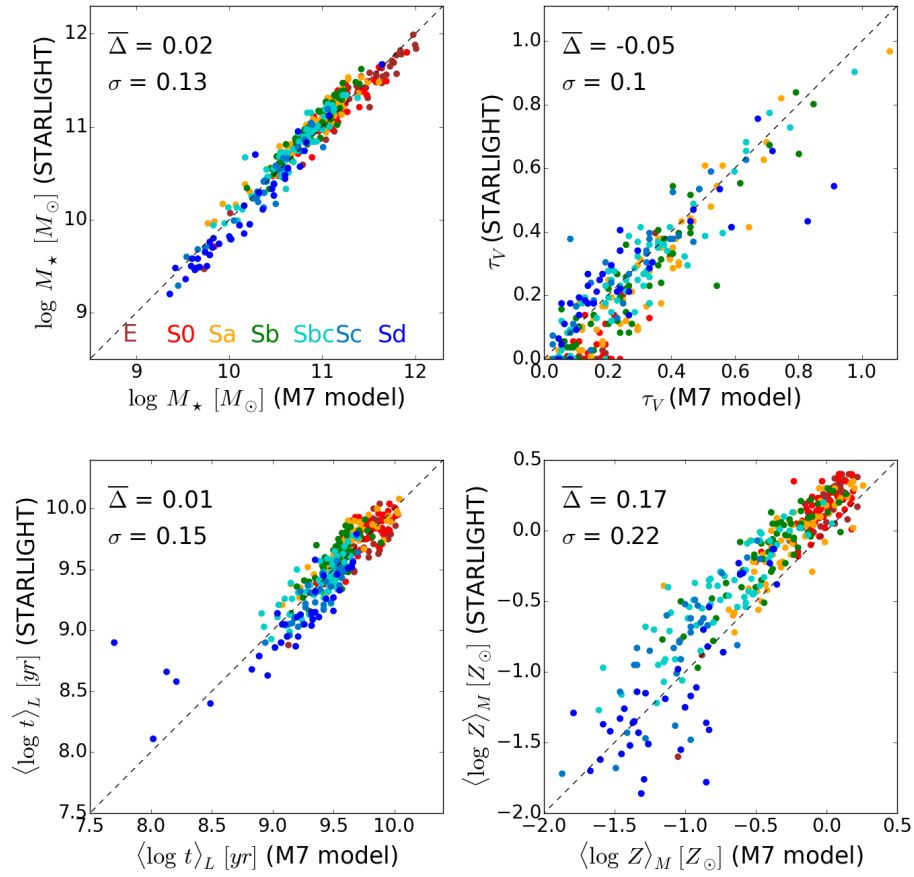
Figure 5.38 Same as figure 5.32 using model **M7**.
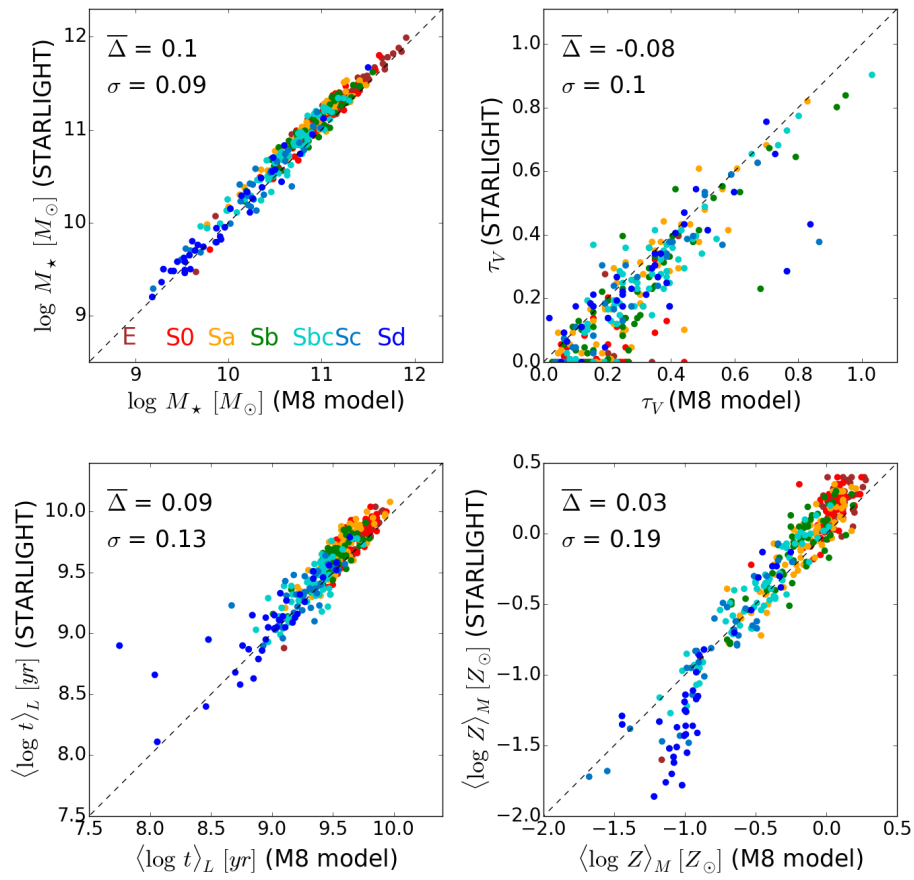
Figure 5.39 Same as figure 5.32 using model **M8**.
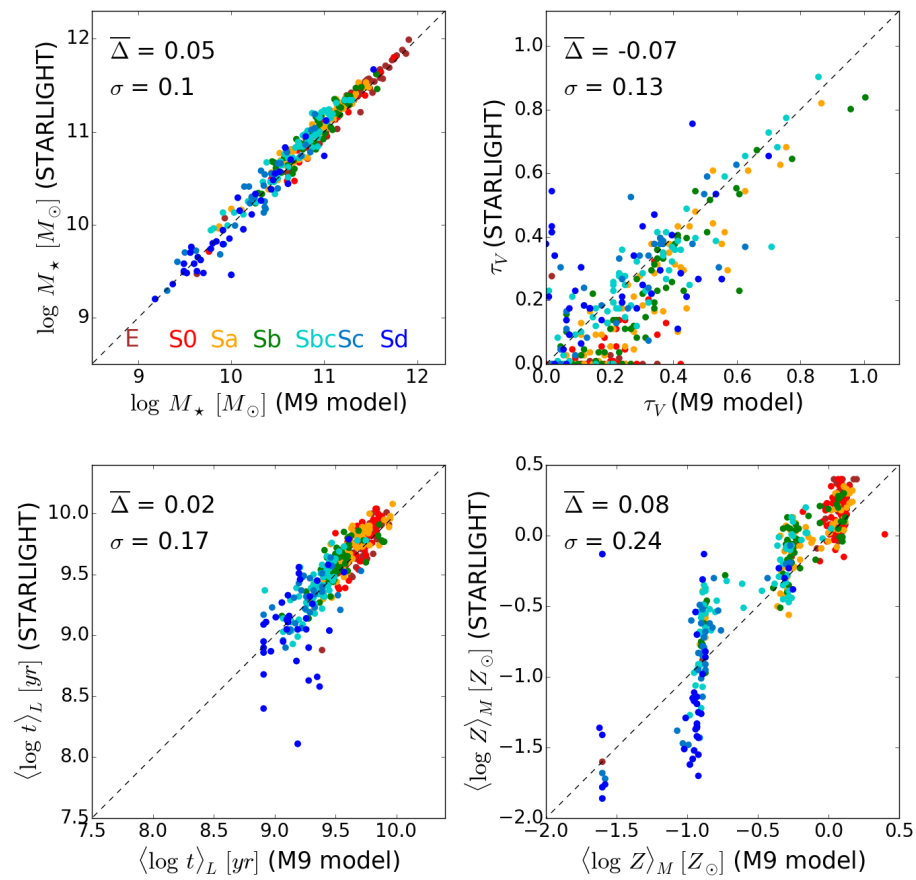
Figure 5.40 Same as figure 5.32 using model **M9**.

5.6.3 Integrated properties: Global relations

Figure 5.41 shows the $M_\star - Z$, $M_\star - \langle \log t \rangle$ and $\mu_\star - M_\star$ global relations obtained with STARLIGHT. The solid line in each plot indicates the mean profile and dashed lines represent $\pm 1\sigma$. The left panel in figure 5.41 shows how the global stellar metallicity changes with the galaxy stellar mass. Indeed a clear correlation and how stellar metallicities grow with $M_\star$ is observed. This relation has been presented in the previous chapter analysing the new version of STARLIGHT. The middle panel in figure 5.41 shows the age-mass relation. Mean ages increase with the galaxy mass, a "downsizing" behaviour that has been widely confirmed with different samples and methods. For example,)Gallazzi2005, found a similar relation using SDSS galaxies. They found that there is a transition at $M_\star \sim 3 \times 10^{10}\, M_\odot$, below which galaxies are typically young and above which they are old. The right panel shows the stellar mass surface density versus the total mass. The relation is almost linear, indicating that more massive galaxies are also denser than lower mass galaxies. We are going to analyse the same relations derived through the different parametric models. The mean profiles obtained with STARLIGHT are shown for reference in the different figures.
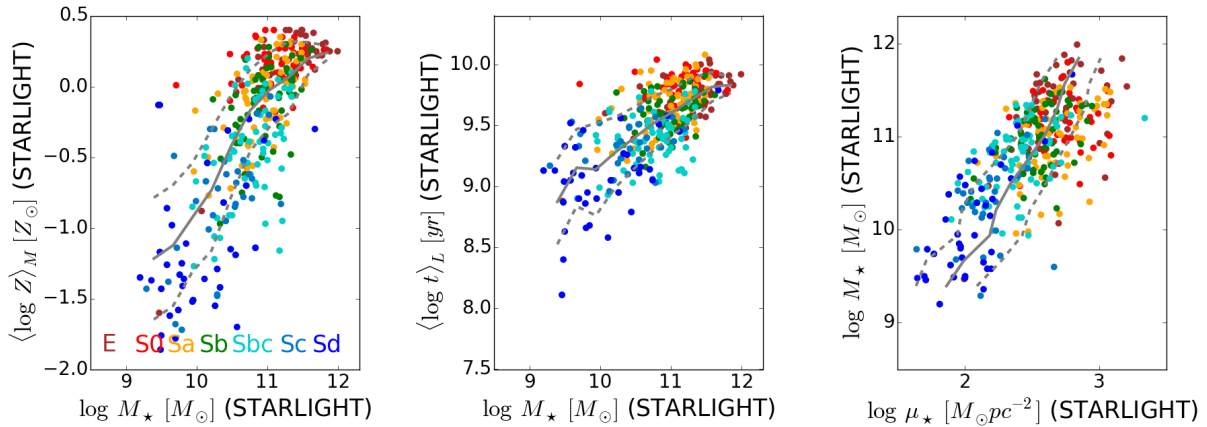
Figure 5.41 Left: The $M_\star - Z$ relation. Right: The $M_\star - \langle \log t \rangle$ relation. In both cases the results are derived with STARLIGHT. The solid line in each plot indicates the mean profile and dashed lines represent $\pm 1\sigma$.

Figure 5.42 shows the global relations obtained with **M1**. The black lines show the mean relation (solid line) and the corresponding $\pm 1\sigma$ (dashed) obtained with **M1**. The grey lines show the results with STARLIGHT, the mean relation (solid line) and the corresponding $\pm 1\sigma$ (dashed). The mean profiles for the mass-metallicity relation are similar to those obtained with STARLIGHT, except for young galaxies. The black and grey lines are similar for galaxies with masses over $10^{10.2}\, M_\odot$, while for low mass galaxies the black profile flattens, showing higher metallicities than those derived with STARLIGHT. Due to the good agreement for the age values, we obtain similar mean profiles for the age-mass relation. The $\mu_\star - M_\star$ relation is also linear, as obtained with STARLIGHT, although a shift among the mean profiles is observed, due to the lower masses derived with one component models. Similar relations are found using **M2** and **M3**, as can be observed in figures 5.43 and 5.44.

Figures 5.45 and 5.46 show the relations using the rising models. Only the $\mu_\star - M_\star$ relation is well recovered using **M4** and **M5** due to the sturdiness of the stellar mass.
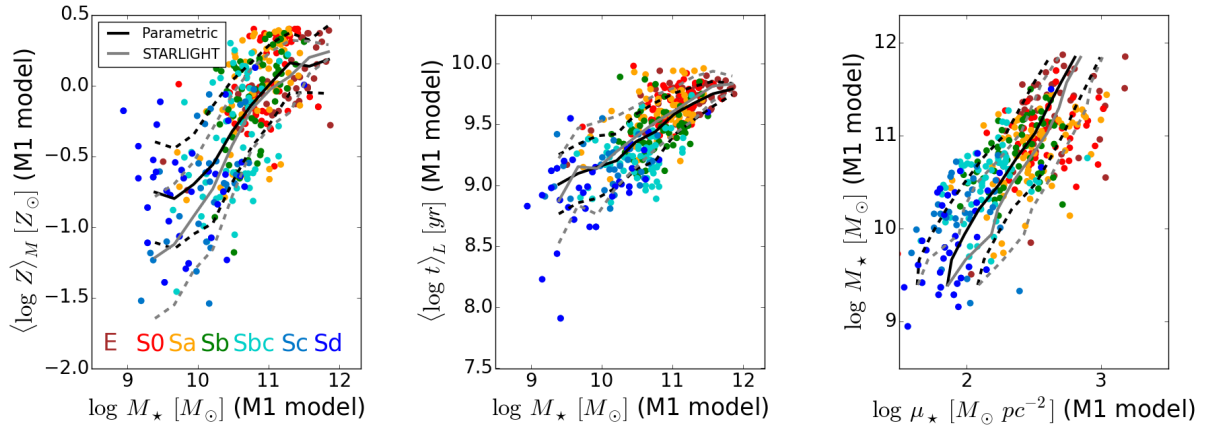
Figure 5.42 Left: The $M_\star - Z$ relation. Right: The $M_\star - \langle \log t \rangle$ relation. The results are derived using **M1**. The solid black lines represent the mean profile using **M1** and black dashed lines show $\pm 1\sigma$. The purple lines in both plots are the results obtained with STARLIGHT in figure 5.41.
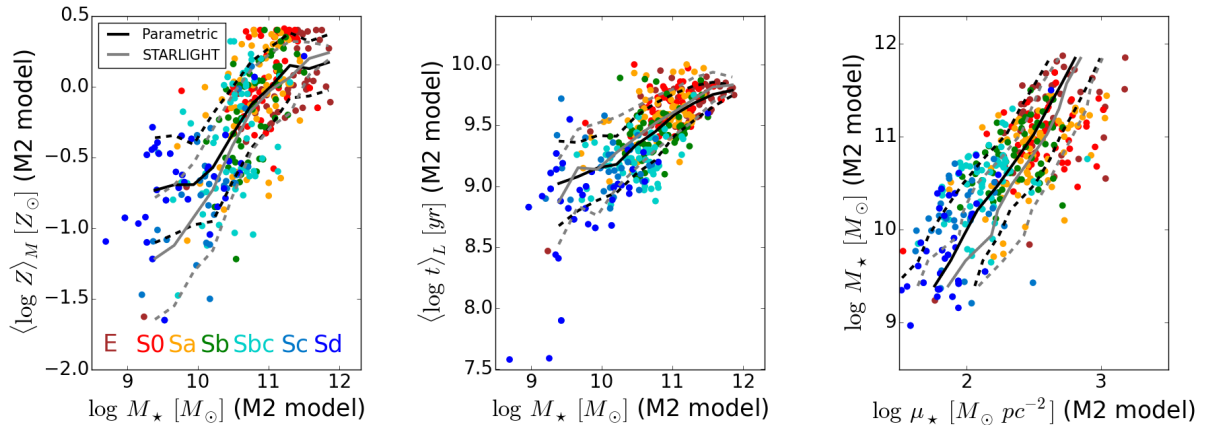
Figure 5.43 Same as figure 5.42 using model **M2**.

The better agreement in the metallicity values obtained with model **M6** produces a more similar mass-metallicity relation compared to STARLIGHT than in previous cases (figure 5.47). We obtain very similar mean profiles, although with the black profile being above the grey one for galaxies with masses below $10^{10.2} M_\odot$. The age-mass relation is similar to that derived with STARLIGHT, although the mean profile is above the grey for low mass galaxies due to the difference in ages for late type galaxies. Introducing a second component we obtain better agreement in the stellar mass, which is reflected in the $\mu_\star - M_\star$ relation. Models **M7** and **M8** draw similar global relations (figures 5.48 and 5.49). Particularly, the mean profile in the mass-age relation is almost the same as that obtained with STARLIGHT when using model **M8**. Also we obtain very good agreement in the $\mu_\star - M_\star$ relation. Some
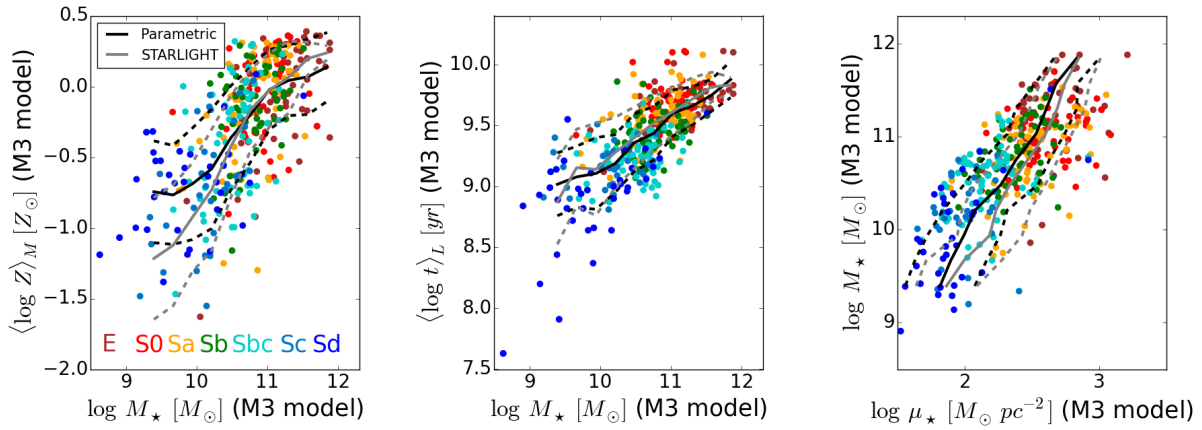
Figure 5.44 Same as figure 5.42 using model **M3**.
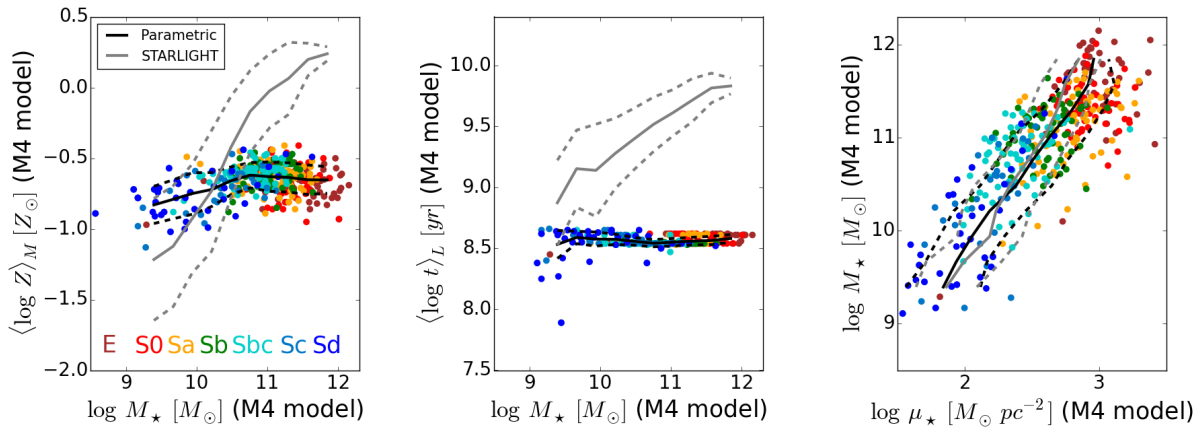
Figure 5.45 Same as figure 5.42 using model **M4**.

differences are found in the mass-metallicity relation when using **M7** and **M8**. In the first case (figure 5.48), the discrepancies observed in the metallicity are reflected in the mass-metallicity relation, with the grey profile above the black one, but being in agreement below $10^{10} M_\odot$. The mean profile in the mass-metallicity relation obtained with **M8** is similar to that obtained with **M6**, although lower metallicities for galaxies with masses above $10^{10.6} M_\odot$ are derived in the first case. Thus, comparing with STARLIGHT we find that the black curve remains below the grey for $\log M_{\star>10.6}$ (figure 5.49).

Figure 5.50 shows the global relations obtained with **M9**. With the discrete values obtained for the metallicity, it is not possible do derive the mass-metallicity relation as well as with other models, although in the bottom panel we compute the mean profile (black) for the derived values. We can only observe a general picture in which metallicity correlates with mass but without determining a continuous relation. On the other hand, we obtain again $M_\star - \langle \log t \rangle$ and $\mu_\star - M_\star$ relations in agreement with STARLIGHT.
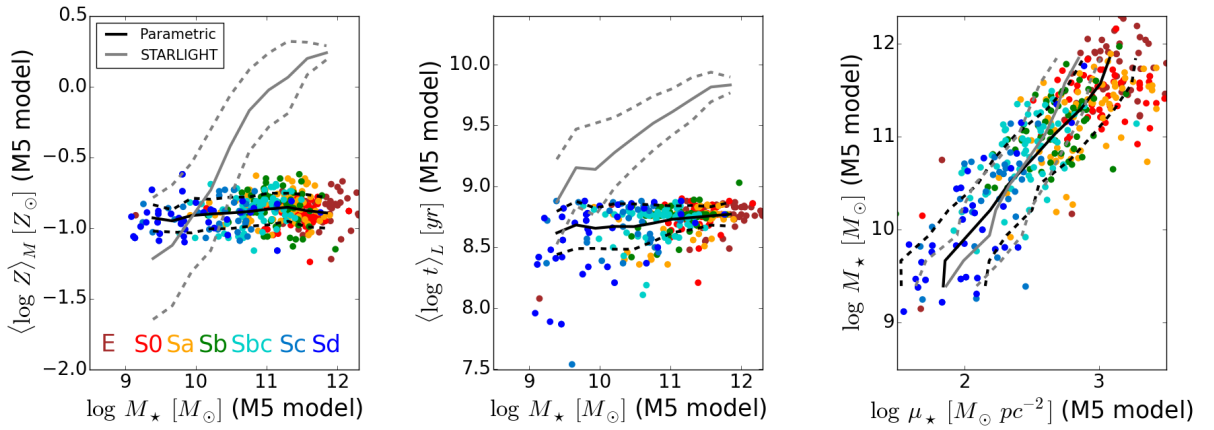
Figure 5.46 Same as figure 5.42 using model **M5**.
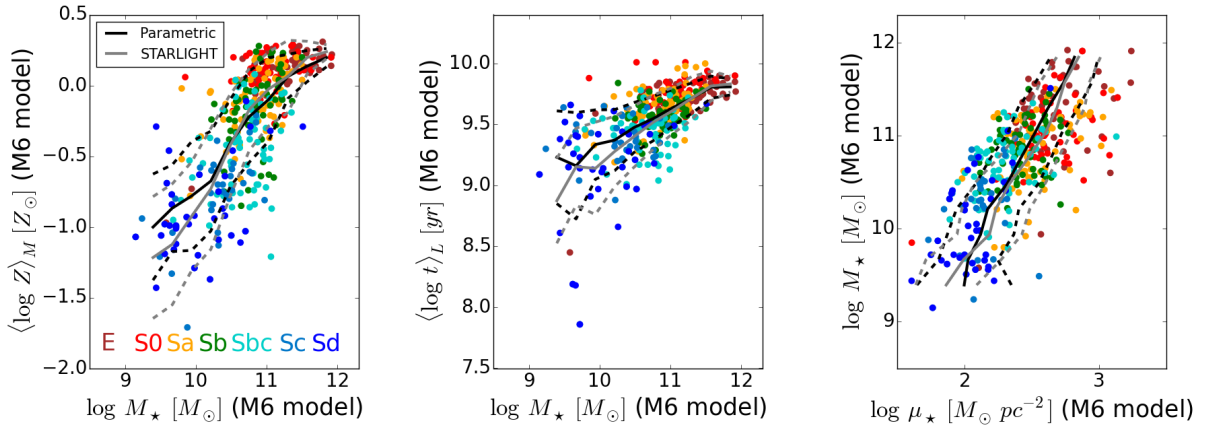
Figure 5.47 Same as figure 5.42 using model **M6**.
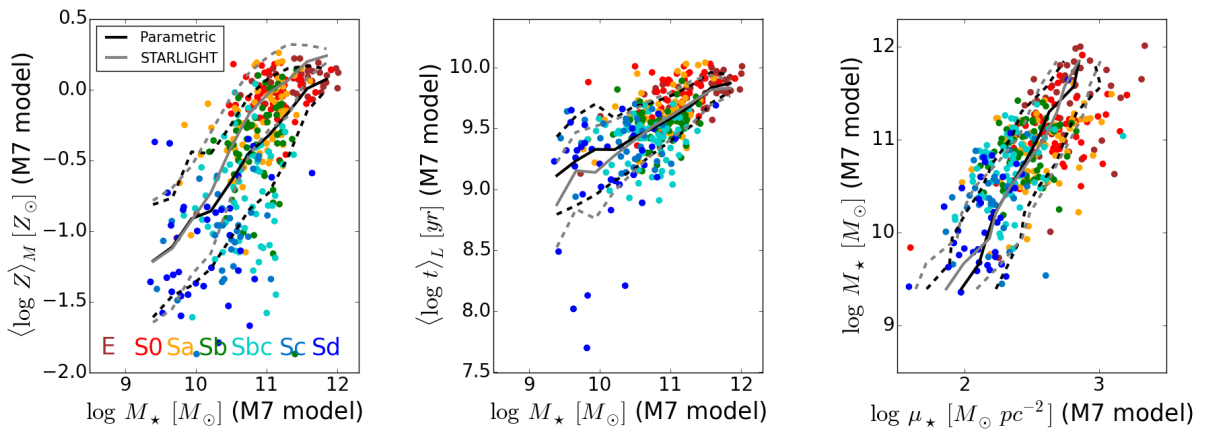
Figure 5.48 Same as figure 5.42 using model **M7**.
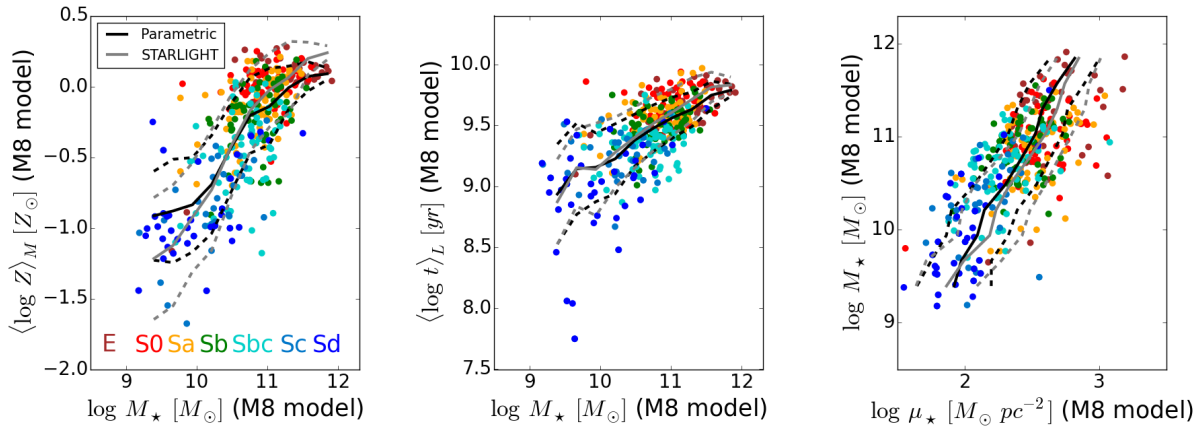
Figure 5.49 Same as figure 5.42 using model **M8**.
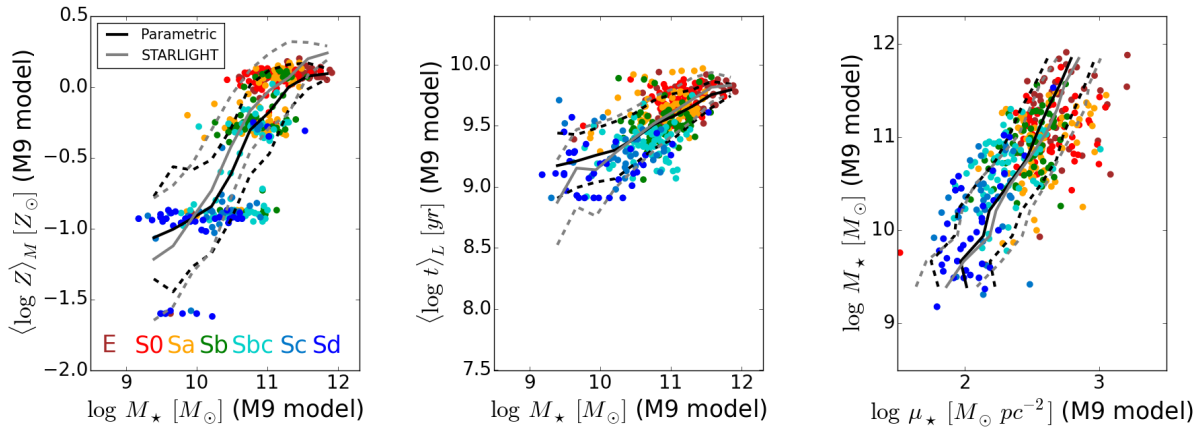
Figure 5.50 Same as figure 5.42 using model **M9**.

5.7   Conclusions

In this chapter we have presented a parametric method to derive the stellar population properties of galaxies, based on a combination of photometry + stellar indices. The photometric data are a combination of $GALEX + SDSS$ data, while the stellar indices are measured from the CALIFA spectra. To better constrain the age and metallicity we choose spectral features sensitives to these properties: H_β and D4000 more sensitive to age, and [MgFe]', more sensitive to metallicity. Through a set of simulations we have tested the consistency of the code, finding that both the parameters of the model and the stellar properties are well recovered.

Different models have been tested, both the capability of models to fit the observed data and the derived stellar population properties. All models produce reasonably good values for $\chi 2$, except the rising models, which are not representative of the whole star formation history of nearby galaxies.

However, the observed data are better recovered when increasing the dimension of the parameter space, obtaining lower $\chi 2$ values for **M6**, **M7** and **M8**.

On the other hand, comparing the derived stellar population properties with those derived with STARLIGHT, on average, we obtain consistent values, except for the rising models. With **M9** we obtain results that are in agreement with STARLIGHT for the age, attenuation and mass, but we are not able to recover the stellar metallicity as well as with other models.

5.7.1 Stellar population components

We have analysed the star formation history of galaxies for the different morphological types obtained with STARLIGHT and the parametric models. Tables 5.5 and 5.6, with Figures 5.51 and 5.52 summarize the star formation history by grouping the stellar populations into four age rages: $t \leq 9$ Gyr (red), $4 < t < 9$ Gry (orange), $1 < t < 4$ Gyr (green), and $t \leq 1$ Gry (blue), which allow us to extract information about the different epochs of the star formation history. Figure 5.51 and table 5.5 track

		E	S0	Sa	Sb	Sbc	Sc	Sd
ST	$x_{t<1\,Gyr}$	7 ± 11	4 ± 6	8 ± 8	11 ± 7	18 ± 9	30 ± 15	41 ± 21
	$x_{1<t<4\,Gyr}$	23 ± 17	21 ± 20	20 ± 13	26 ± 15	29 ± 15	26 ± 15	20 ± 14
	$x_{4<t<9\,Gyr}$	30 ± 19	31 ± 17	30 ± 14	31 ± 15	29 ± 12	25 ± 13	22 ± 11
	$x_{t>9\,Gyr}$	40 ± 22	44 ± 22	42 ± 19	33 ± 18	23 ± 14	19 ± 12	17 ± 12
M1	$x_{t<1\,Gyr}$	6 ± 9	7 ± 5	15 ± 9	22 ± 9	34 ± 10	40 ± 13	37 ± 15
	$x_{1<t<4\,Gyr}$	21 ± 29	19 ± 26	18 ± 13	20 ± 9	26 ± 11	28 ± 12	29 ± 14
	$x_{4<t<9\,Gyr}$	49 ± 28	49 ± 26	45 ± 18	39 ± 14	29 ± 8	23 ± 9	25 ± 14
	$x_{t>9\,Gyr}$	24 ± 22	25 ± 20	22 ± 15	19 ± 11	11 ± 7	8 ± 8	10 ± 11
M2	$x_{t<1\,Gyr}$	5 ± 5	7 ± 5	15 ± 9	22 ± 10	32 ± 10	39 ± 15	34 ± 13
	$x_{1<t<4\,Gyr}$	20 ± 29	16 ± 25	16 ± 14	18 ± 10	24 ± 13	26 ± 13	31 ± 19
	$x_{4<t<9\,Gyr}$	46 ± 23	44 ± 21	36 ± 21	30 ± 14	24 ± 7	21 ± 8	23 ± 17
	$x_{t>9\,Gyr}$	29 ± 30	33 ± 26	33 ± 19	30 ± 15	20 ± 10	15 ± 9	11 ± 12
M3	$x_{t<1\,Gyr}$	5 ± 5	7 ± 6	16 ± 9	23 ± 9	34 ± 10	42 ± 11	43 ± 13
	$x_{1<t<4\,Gyr}$	24 ± 26	23 ± 22	23 ± 11	27 ± 13	30 ± 10	30 ± 8	32 ± 12
	$x_{4<t<9\,Gyr}$	56 ± 25	55 ± 19	48 ± 17	41 ± 14	30 ± 9	23 ± 8	21 ± 12
	$x_{t>9\,Gyr}$	14 ± 16	15 ± 10	13 ± 13	10 ± 5	6 ± 3	5 ± 3	4 ± 3
M4	$x_{t<1\,Gyr}$	62 ± 2	62 ± 2	64 ± 2	65 ± 1	65 ± 2	66 ± 6	69 ± 9
	$x_{1<t<4\,Gyr}$	27 ± 1	26 ± 1	25 ± 1	25 ± 1	25 ± 1	25 ± 4	24 ± 6
	$x_{4<t<9\,Gyr}$	10 ± 1	10 ± 1	10 ± 1	9 ± 1	9 ± 1	9 ± 3	7 ± 4
	$x_{t>9\,Gyr}$	2 ± 1	2 ± 1	1 ± 1	1 ± 1	1 ± 1	1 ± 1	1 ± 1
M5	$x_{t<1\,Gyr}$	52 ± 5	54 ± 11	55 ± 10	56 ± 11	56 ± 7	59 ± 11	66 ± 14
	$x_{1<t<4\,Gyr}$	27 ± 2	25 ± 5	24 ± 5	24 ± 6	25 ± 4	25 ± 5	23 ± 7
	$x_{4<t<9\,Gyr}$	15 ± 4	15 ± 4	15 ± 4	14 ± 4	14 ± 4	12 ± 5	9 ± 6
	$x_{t>9\,Gyr}$	6 ± 3	6 ± 3	6 ± 2	6 ± 3	5 ± 3	4 ± 3	2 ± 3
M6	$x_{t<1\,Gyr}$	9 ± 12	8 ± 9	15 ± 16	21 ± 18	29 ± 13	35 ± 12	38 ± 13
	$x_{1<t<4\,Gyr}$	17 ± 16	15 ± 16	16 ± 23	13 ± 23	8 ± 20	7 ± 14	12 ± 18
	$x_{4<t<9\,Gyr}$	17 ± 16	31 ± 29	43 ± 25	37 ± 24	43 ± 30	46 ± 24	40 ± 23
	$x_{t>9\,Gyr}$	57 ± 28	45 ± 23	27 ± 23	29 ± 21	19 ± 28	13 ± 24	11 ± 22
M7	$x_{t<1\,Gyr}$	9 ± 11	8 ± 6	14 ± 13	21 ± 15	30 ± 11	40 ± 11	43 ± 12
	$x_{1<t<4\,Gyr}$	18 ± 15	12 ± 15	17 ± 25	11 ± 19	9 ± 18	6 ± 14	9 ± 15
	$x_{4<t<9\,Gyr}$	6 ± 6	5 ± 7	2 ± 4	3 ± 5	5 ± 6	7 ± 6	8 ± 6
	$x_{t>9\,Gyr}$	67 ± 16	76 ± 16	66 ± 24	64 ± 22	57 ± 20	47 ± 19	41 ± 20
M8	$x_{t<1\,Gyr}$	9 ± 12	13 ± 21	15 ± 17	21 ± 17	26 ± 11	333 ± 10	37 ± 13
	$x_{1<t<4\,Gyr}$	13 ± 13	6 ± 10	14 ± 26	10 ± 20	9 ± 21	10 ± 19	16 ± 24
	$x_{4<t<9\,Gyr}$	35 ± 20	31 ± 22	39 ± 22	41 ± 26	47 ± 30	47 ± 25	36 ± 24
	$x_{t>9\,Gyr}$	43 ± 22	49 ± 26	32 ± 27	29 ± 24	18 ± 29	10 ± 21	11 ± 22
M9	$x_{t<1\,Gyr}$	6 ± 5	7 ± 5	16 ± 9	22 ± 10	33 ± 9	35 ± 7	32 ± 9
	$x_{1<t<4\,Gyr}$	19 ± 15	17 ± 12	17 ± 8	18 ± 5	22 ± 4	24 ± 3	25 ± 5
	$x_{4<t<9\,Gyr}$	41 ± 9	40 ± 8	36 ± 8	32 ± 7	26 ± 4	24 ± 4	26 ± 5
	$x_{t>9\,Gyr}$	35 ± 13	36 ± 11	32 ± 9	27 ± 8	19 ± 6	16 ± 5	17 ± 6

Table 5.5 Average light fraction due to stars in different age ranges according the Hubble type, obtained with STARLIGHT and the parametric models.

		E	S0	Sa	Sb	Sbc	Sc	Sd
ST	$\mu_{t<1\,Gyr}$	1 ± 3	1 ± 1	1 ± 1	1 ± 1	2 ± 2	7 ± 14	13 ± 18
	$\mu_{1<t<4\,Gyr}$	11 ± 11	10 ± 14	9 ± 8	12 ± 10	18 ± 14	19 ± 16	16 ± 14
	$\mu_{4<t<9\,Gyr}$	30 ± 21	28 ± 18	29 ± 16	32 ± 17	35 ± 12	33 ± 15	34 ± 15
	$\mu_{t>9\,Gyr}$	58 ± 25	61 ± 23	61 ± 20	54 ± 22	45 ± 19	40 ± 20	36 ± 19
M1	$\mu_{t<1\,Gyr}$	1 ± 1	1 ± 1	1 ± 1	2 ± 2	4 ± 2	6 ± 3	7 ± 4
	$\mu_{1<t<4\,Gyr}$	17 ± 31	14 ± 27	10 ± 13	12 ± 11	20 ± 14	26 ± 17	28 ± 21
	$\mu_{4<t<9\,Gyr}$	51 ± 30	51 ± 28	53 ± 20	51 ± 16	49 ± 10	46 ± 10	45 ± 15
	$\mu_{t>9\,Gyr}$	32 ± 28	35 ± 27	36 ± 21	34 ± 17	27 ± 11	21 ± 12	21 ± 17
M2	$\mu_{t<1\,Gyr}$	1 ± 1	1 ± 1	1 ± 1	2 ± 2	3 ± 1	8 ± 18	6 ± 4
	$\mu_{1<t<4\,Gyr}$	16 ± 20	11 ± 26	9 ± 14	10 ± 12	16 ± 16	20 ± 19	30 ± 27
	$\mu_{4<t<9\,Gyr}$	47 ± 26	44 ± 24	39 ± 23	37 ± 16	37 ± 10	37 ± 13	39 ± 23
	$\mu_{t>9\,Gyr}$	37 ± 27	44 ± 25	51 ± 26	51 ± 20	48 ± 14	35 ± 17	25 ± 24
M3	$\mu_{t<1\,Gyr}$	1 ± 1	1 ± 1	1 ± 1	2 ± 2	5 ± 2	7 ± 3	8 ± 4
	$\mu_{1<t<4\,Gyr}$	18 ± 28	15 ± 23	14 ± 11	18 ± 15	24 ± 12	29 ± 11	33 ± 17
	$\mu_{4<t<9\,Gyr}$	61 ± 27	60 ± 20	62 ± 15	59 ± 14	54 ± 9	50 ± 8	46 ± 14
	$\mu_{t>9\,Gyr}$	21 ± 20	24 ± 16	23 ± 16	21 ± 9	17 ± 6	14 ± 6	12 ± 7
M4	$\mu_{t<1\,Gyr}$	15 ± 1	15 ± 1	15 ± 1	15 ± 1	15 ± 2	18 ± 12	24 ± 19
	$\mu_{1<t<4\,Gyr}$	38 ± 2	38 ± 1	38 ± 1	38 ± 1	38 ± 3	40 ± 8	42 ± 12
	$\mu_{4<t<9\,Gyr}$	38 ± 2	38 ± 1	38 ± 1	38 ± 1	38 ± 3	35 ± 9	29 ± 14
	$\mu_{t>9\,Gyr}$	9 ± 1	9 ± 1	9 ± 1	9 ± 1	9 ± 1	7 ± 3	5 ± 4
M5	$\mu_{t<1\,Gyr}$	10 ± 5	14 ± 20	13 ± 18	14 ± 21	11 ± 12	16 ± 18	25 ± 24
	$\mu_{1<t<4\,Gyr}$	29 ± 11	25 ± 7	25 ± 8	25 ± 8	28 ± 10	32 ± 12	379 ± 16
	$\mu_{4<t<9\,Gyr}$	39 ± 10	38 ± 11	38 ± 10	38 ± 10	39 ± 10	36 ± 11	29 ± 16
	$\mu_{t>9\,Gyr}$	22 ± 11	23 ± 10	25 ± 8	23 ± 10	21 ± 11	15 ± 12	9 ± 11
M6	$\mu_{t<1\,Gyr}$	1 ± 1	1 ± 1	1 ± 4	2 ± 5	2 ± 3	2 ± 3	3 ± 7
	$\mu_{1<t<4\,Gyr}$	11 ± 17	9 ± 12	14 ± 22	11 ± 21	8 ± 21	8 ± 20	14 ± 23
	$\mu_{4<t<9\,Gyr}$	20 ± 21	35 ± 26	49 ± 20	47 ± 20	62 ± 21	71 ± 25	67 ± 26
	$\mu_{t>9\,Gyr}$	69 ± 30	55 ± 28	36 ± 21	40 ± 21	28 ± 20	19 ± 24	16 ± 22
M7	$\mu_{t<1\,Gyr}$	1 ± 1	1 ± 1	1 ± 2	1 ± 4	1 ± 3	2 ± 4	3 ± 8
	$\mu_{1<t<4\,Gyr}$	8 ± 8	5 ± 9	12 ± 20	8 ± 15	7 ± 16	6 ± 14	8 ± 16
	$\mu_{4<t<9\,Gyr}$	5 ± 7	4 ± 6	2 ± 4	4 ± 6	6 ± 7	10 ± 10	12 ± 10
	$\mu_{t>9\,Gyr}$	86 ± 11	90 ± 10	85 ± 21	87 ± 19	86 ± 20	82 ± 21	76 ± 24
M8	$\mu_{t<1\,Gyr}$	1 ± 1	2 ± 6	1 ± 3	1 ± 3	1 ± 2	2 ± 3	3 ± 7
	$\mu_{1<t<4\,Gyr}$	7 ± 8	3 ± 7	13 ± 25	9 ± 20	9 ± 22	12 ± 25	20 ± 22
	$\mu_{4<t<9\,Gyr}$	39 ± 25	36 ± 27	48 ± 29	50 ± 23	65 ± 30	70 ± 25	60 ± 28
	$\mu_{t>9\,Gyr}$	53 ± 26	59 ± 28	38 ± 23	39 ± 25	25 ± 29	16 ± 21	17 ± 22
M9	$\mu_{t<1\,Gyr}$	1 ± 1	1 ± 1	1 ± 1	2 ± 1	3 ± 1	4 ± 1	4 ± 2
	$\mu_{1<t<4\,Gyr}$	9 ± 8	8 ± 7	8 ± 5	9 ± 4	14 ± 4	16 ± 4	16 ± 5
	$\mu_{4<t<9\,Gyr}$	40 ± 7	39 ± 7	39 ± 5	39 ± 4	40 ± 1	40 ± 1	40 ± 2
	$\mu_{t>9\,Gyr}$	50 ± 12	52 ± 11	52 ± 9	50 ± 7	43 ± 6	40 ± 5	40 ± 7

Table 5.6 Average mass fraction due to stars in different age ranges according the Hubble type, obtained with STARLIGHT and the parametric models.

the percentage of contributions in light; figure 5.52 and table 5.52 show the percentage of contributions in mass. In both figures, the columns show the results with the parametric models and STARLIGHT. As have been showed, the results with models **M4** and **M5** are not agreement with the other models and are not representative of galaxies in the local Universe. Thus we focus hereafter in the results obtained with STARLIGHT and the other models.

Light fraction, x:

- $x_{t\leq1\,Gyr}$: the evolution of the young component with the Hubble type, obtained with STARLIGHT, is similar to those obtained with models **M1**, **M2**, **M3**, **M6**, **M8** and **M9**: in these cases, $x_{t\leq1\,Gyr}$ increases from E to Sd. For STARLIGHT and **M1**, $x_{t\leq1\,Gyr} \sim 7$ % and 6 % for E galaxies, respectively; and for Sd galaxies $x_{t\leq1\,Gyr} \sim 41$ % and 37 %.

- $x_{1\,Gyr<t\leq4\,Gyr}$: for all the models, this component remains almost constant for all the Hubble types. For STARLIGHT, 9 % $\leq x_{1<t\leq4\,Gyr} \leq 19$ %. For **M1**, **M2** and **M3**, $x_{1<t\leq4\,Gyr} \leq 20$ % for Sbc and earlier types. Only for Sbc galaxies, with **M2**, and Sc and Sd galaxies with the

three models, $x_{1<t\leq4\,Gyr} > 20$ %. For **M9** we obtain similar results to STARLIGHT, with 8 % $\leq x_{1<t\leq4\,Gyr} \leq 16$ %, and lower values are obtained with **M6**, **M7** and **M8**.

- $x_{4\,Gyr<t\leq9\,Gyr}$: On average, this component decreases from E to Sd galaxies for **M1**, **M2**, **M3**, **M9** and STARLIGHT, although larger range of variation is obtained with **M1** and **M3**. For **M1**, $x_{4<t\leq9\,Gyr}$ decreases from 49 % in E galaxies to 23 % in Sd, while using STARLIGHT $x_{4<t\leq9\,Gyr}$ decreases from 30 % to 25 %. For **M6** we obtain the opposite behaviour, with $x_{4<t\leq9\,Gyr}$ increasing from 17 % in E galaxies to $x_{4<t\leq9\,Gyr} \geq 40$ % in later spirals. For **M8**, 31 % $\leq x_{4<t\leq9\,Gyr} \leq 47$ %, and very low values are obtained with **M7**, $x_{4<t\leq9\,Gyr} \leq 8$ % for all the Hubble types.

- $x_{t>9\,Gyr}$: The light fraction of the old component decreases from E to Sd galaxies for all the Hubble types, but larger range of variation is obtained with **M6** and **M8**. For STARLIGHT, $x_{t>9\,Gyr} \sim 40$ % and 19 % for E and Sd galaxies, respectively, which are very similar to **M2** and **M9**. For **M1** we obtain $x_{t>9\,Gyr} \sim 24$ % and 8 % for E and Sd galaxies, larger values than those obtained with **M3**. For **M6** and **M8** we obtain for E galaxies $x_{t>9\,Gyr} \sim 57$ % and 43 %, respectively, and for Sd galaxies, $x_{t>9\,Gyr} \sim 13$ % and 10 %. The values obtained with **M7** are larger for all the Hubble types, decreasing $x_{t>9\,Gyr}$ from 67 % in E galaxies to 47 % in Sd.

Mass fraction, μ:

- $\mu_{t\leq1\,Gyr}$: the mass fraction of the young component increases from E to Sd galaxies for all the Hubble types, although larger range of variation is obtained with STARLIGHT, from $\mu_{t\leq1\,Gyr} \sim 1$ % in E galaxies to 13 % in Sd.

- $\mu_{1\,Gyr<t\leq4\,Gyr}$: for **M1** and **M2**, 9 % $\leq \mu_{1<t\leq4\,Gyr} \leq 30$ %, increasing from E to Sd galaxies, while larger values are obtained for **M3**, with 14 % $\leq \mu_{1<t\leq4\,Gyr} \leq 33$ %. For **M8**, **M9** and STARLIGHT $\mu_{1<t\leq4\,Gyr}$ also increases from E to Sd, although the mass fraction is lower than with the previous models. In particular, for STARLIGHT $\mu_{1<t\leq4\,Gyr} \leq 12$ % for Sb and earlier types and $\mu_{1<t\leq4\,Gyr} \geq 16$ % for late type spirals. With **M6** and **M7**, $\mu_{1<t\leq4\,Gyr}$ does not correlate with the Hubble types, obtaining 8 % $\leq \mu_{1<t\leq4\,Gyr} \leq 14$ % with the first one, and 5 % $\leq \mu_{1<t\leq4\,Gyr} \leq 12$ % with the second one.

- $\mu_{4\,Gyr<t\leq9\,Gyr}$: the mass fraction of this component varies for the different models. With STARLIGHT and **M9** $\mu_{1<t\leq4\,Gyr}$ remains almost constant for all the Hubble types. With STARLIGHT, $28\,\% \leq \mu_{4<t\leq9\,Gyr} \leq 35\,\%$ and for **M9**, $\mu_{4<t\leq9\,Gyr} \sim 39\text{-}40$ %. For **M1**, **M2** and **M3**, this component decreases from E to Sd galaxies. Larger values are obtained with **M3**, with $\mu_{1<t\leq4\,Gyr} \sim 61$ % and 46 % for E and Sd galaxies, respectively. Lower values are obtained with **M2**, $\mu_{1<t\leq4\,Gyr} \sim 47$ % and 39 % , respectively. On the other hand, the mass fraction increases with **M6** and **M8**. For E galaxies, $\mu_{1<t\leq4\,Gyr} \sim 20$ % and 39 %, while for Sd, $\mu_{1<t\leq4\,Gyr} \sim 67$ % and 60 %. The lowest values are obtained for **M7**, with $\mu_{4<t\leq9\,Gyr} \leq 6$ % for Sbc and earlier types, and $\mu_{4<t\leq9\,Gyr} \sim,$ 10 % and 12 % for Sc and Sd galaxies.
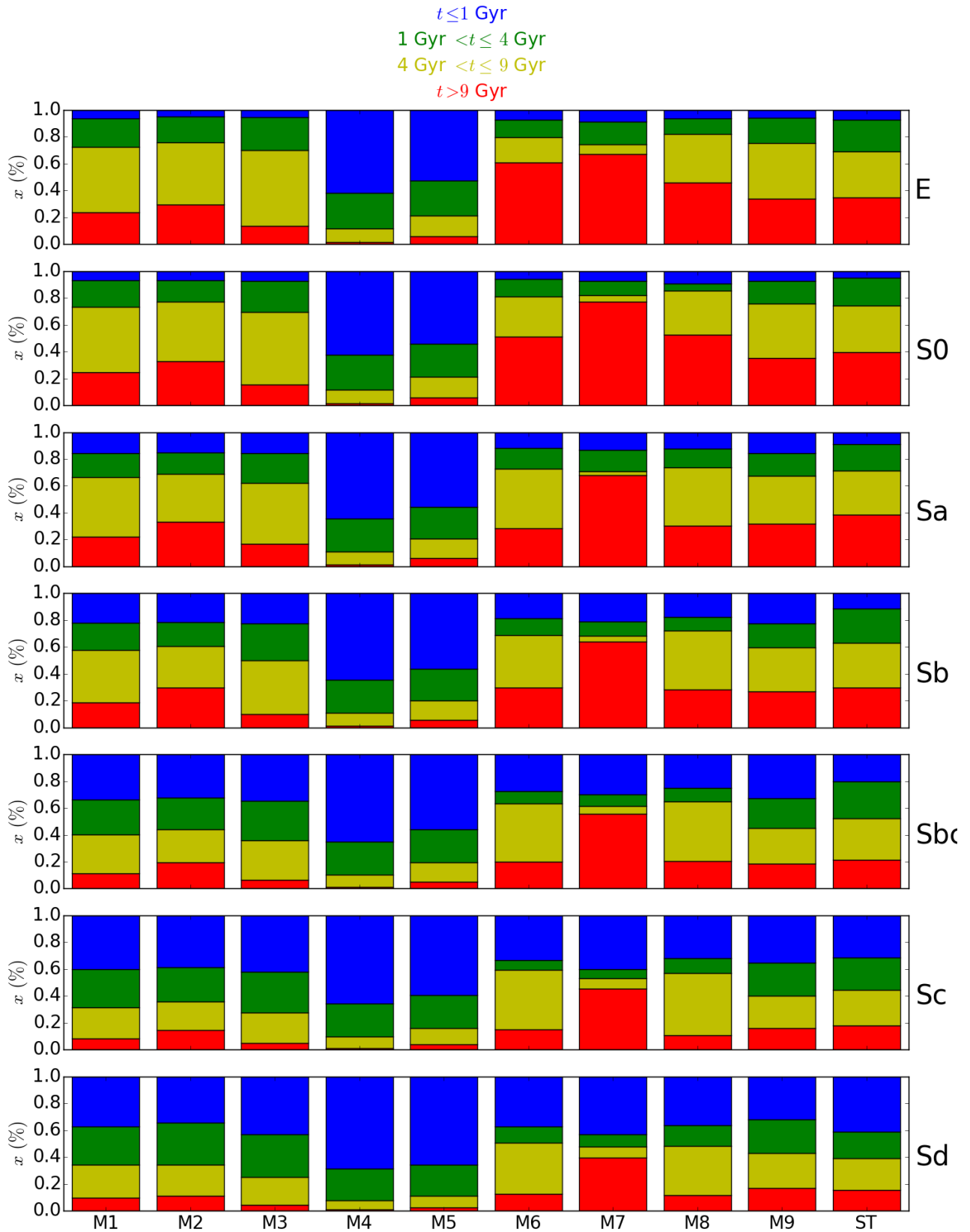
Figure 5.51 Average light fractions due to stars in different age ranges according to the Hubble type. Age (lookback time) ranges are colour-coded: old, intermediate and young populations are defined as those with $age \geq 9$ Gyr (red), 4 Gyr $< age < 9$ Gyr (yellow), 1 Gyr $< age < 4$ Gyr (green), and $age \leq 1$ Gyr (blue), respectively. The columns represent the results for the parametric models and STARLIGHT.
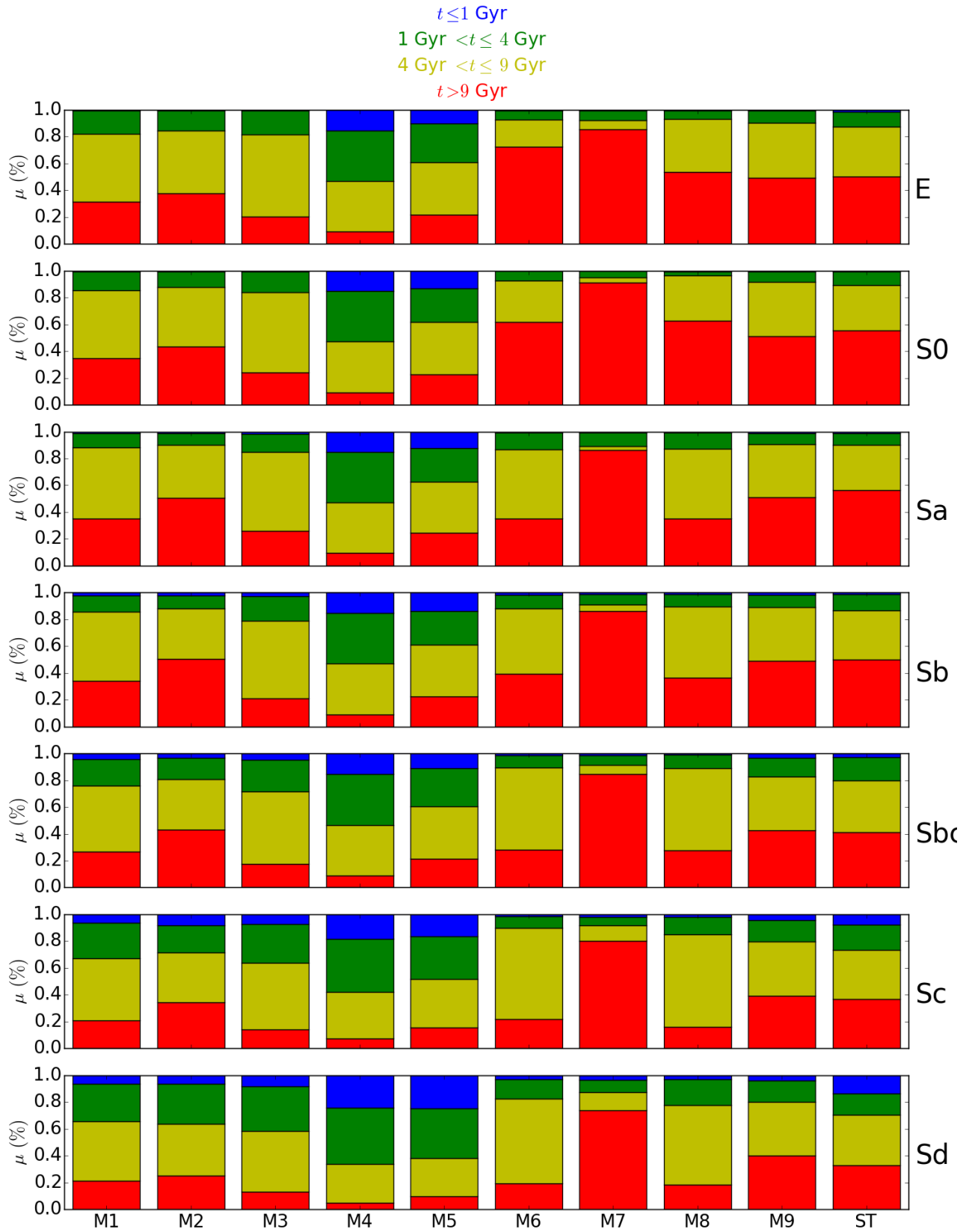
Figure 5.52 Same as figure 5.51 for the mass fraction.

- $\mu_{t>9\,Gyr}$: for all the models, $\mu_{t>9\,Gyr}$ decreases from E to Sd galaxies. For **M7** the mass fraction is larger than for the other models for all the Hubble types and also very large for Sd galaxies. For E galaxies $\mu_{t>9\,Gyr} \sim 86$ % and for Sd $\mu_{t>9\,Gyr} \sim 76$ %. The largest range of variation is obtained with **M6**, from 69 % in E galaxies to 16 % in Sd, and the results are similar to **M8** except for E galaxies. For **M2**, **M9** and STARLIGHT the evolution of mass fraction for this component is also quite similar. In particular, for STARLIGHT, $\mu_{t>9\,Gyr} \sim 58$ % for E galaxies and $\mu_{t>9\,Gyr} \sim 36$ % for Sd. For **M1** and **M2** we obtain in E galaxies $\mu_{t>9\,Gyr} \sim 32$ % and 37 %, respectively, and for Sd galaxies $\mu_{t>9\,Gyr} \sim 21$ % and 25 %.

5.7.2 Parameters of the models

In this chapter we have presented the star formation histories for the different Hubble types by averaging the individual star formation histories. In this section we compare the mean parameters obtained with the different models for the different Hubble types. Figures 5.53 and 5.54 show the mean parameters for the one component models as a function of Hubble type and different mass bins. The first row shows t_0 and the second row τ, with the error bars. Although **M9** is classified as being two component, really it is defined by two parameters, t_0 and τ, both referred to the exponential component. In **M1**, **M2** and **M3**, t_0 refers to the time where the galaxy starts to form stars. In **M9**, composed of a constant SFR plus an exponential decay, t_0 refers the time when the shut down of star formation begins.
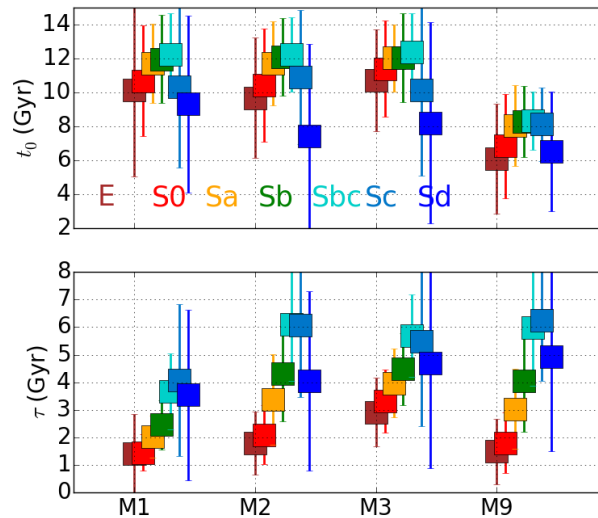

Figure 5.53 Mean parameters for models **M1**, **M2**, **M3** and **M4**: t_0 and τ. The different Hubble types are colour-coded.

- Sa, Sb and Sbc start to form earlier than E and S0. With **M1**, **M2** and **M3**, we obtain for these galaxies $t_0 \sim 12$ Gyr.

- With **M1** and **M2**, $t_0 \sim 10$ Gyr for E and S0 galaxies, while using **M3**, 10 Gyr $< t_0 <$ 12 Gyr.
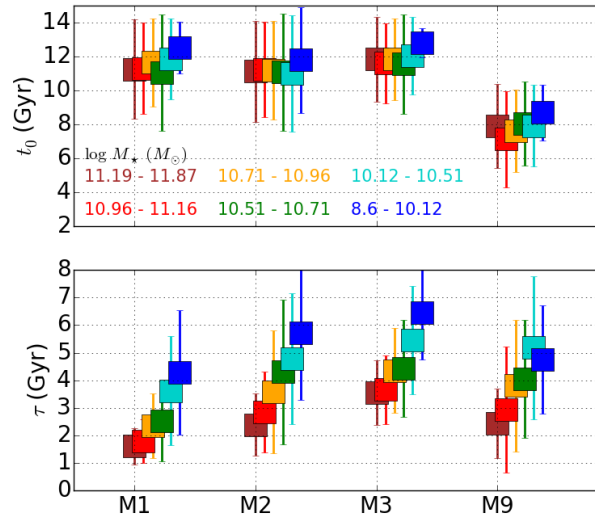
Figure 5.54 Mean parameters for models **M1**, **M2**, **M3** and **M4**: t_0 and τ. Mass bins are colour-coded.

- For Sc galaxies, we obtain $t_0 \sim 10$ Gyr with **M1** and **M3**, similar to E galaxies. On the other hand, higher value is obtained with **M2**, $t_0 \sim 11$ Gyr.

- Sd galaxies starts to form later on.

- $t_0 \sim 8$ Gyr for Sa, Sb, Sbc and Sc with **M9**, and 6 Gyr $< t_0 < 7$ Gyr for E, S0 and Sd galaxies. Thus, E, S0 and Sd galaxies begin the shut down of star formation later on.

- With **M1**, **M2** and **M3**, τ increases with the Hubble type, with more extended period of star formation in late type spirals than early on. The larger range of variation is obtained with **M2**, $\tau \sim 2$ Gyr for E and S0, and $\tau \sim 6$ Gyr for Sbc and Sd galaxies.

- With **M9**, τ also increases with the Hubble types. For E and S0 a faster shut down of star formation is obtained, with $\tau \sim 1$-2 Gyr. Larger values are obtained for Sbc and Sc galaxies, with $\tau \sim 6$ Gyr.

- Stacking galaxies as a function of mass, similar t_0 is obtained for all the Hubble types with **M1**, **M2** and **M3**, and slight larger for Sd galaxies. τ increases with galaxy mass, indicating a more extended period of star formation in low mass galaxies than in massive ones.

- With **M9**, t_0 is similar for all the Hubble type and τ correlates with the mass, which indicates that the shut down of star formation begin at the same epoch but occurs faster in massive galaxies.

Figures 5.55 and 5.56 show the mean parameters for **M6**, **M7** and **M8**, stacking galaxies as a function of Hubble type and mass bins. The first and second panels show the parameters of the old component, while third and fourth show the parameters of the young component, t_0 and τ, respectively. The last panel indicates the mass fraction of the old component.
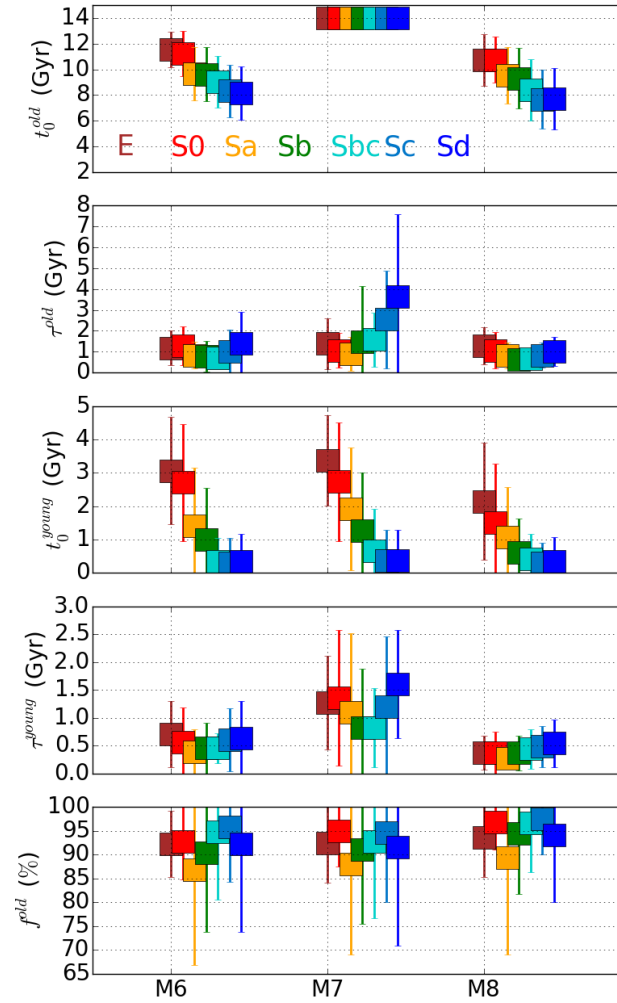
Figure 5.55 Mean parameters for models **M6**, **M7** and **M8**: t_0^{old}, τ^{old}, t_0^{young}, τ^{young} and f^{old}. The Hubble types are colour-coded.

- With **M6** and **M8**, t_0^{old} decreases with the Hubble type, from $t_0^{old} \sim$ 10-12 Gyr for E and S0 galaxies, to $t_0^{old} \sim$ 8 Gyr for late type spirals. Thus, late type galaxies started to form later on. For the model **M7**, t_0^{old} is fixed to 14 Gyr.

- τ^{old} remains almost constant for all the Hubble types with **M6** and **M8**, $\tau^{old} \sim$ 0.5-1.5 Gyr, indicating a rapid growth of the stellar mass. On the contrary, τ^{old} increases with the Hubble type with **M7**, obtaining for Sd galaxies $\tau^{old} \sim$ 3.5 Gyr.

- Thus, with the three models an earlier growth of early type galaxies is obtained.

- t_0^{young} decreases from E to Sd galaxies with all the models. For **M6** and **M7**, $t_0^{young} \sim$ 3-3.5 Gyr
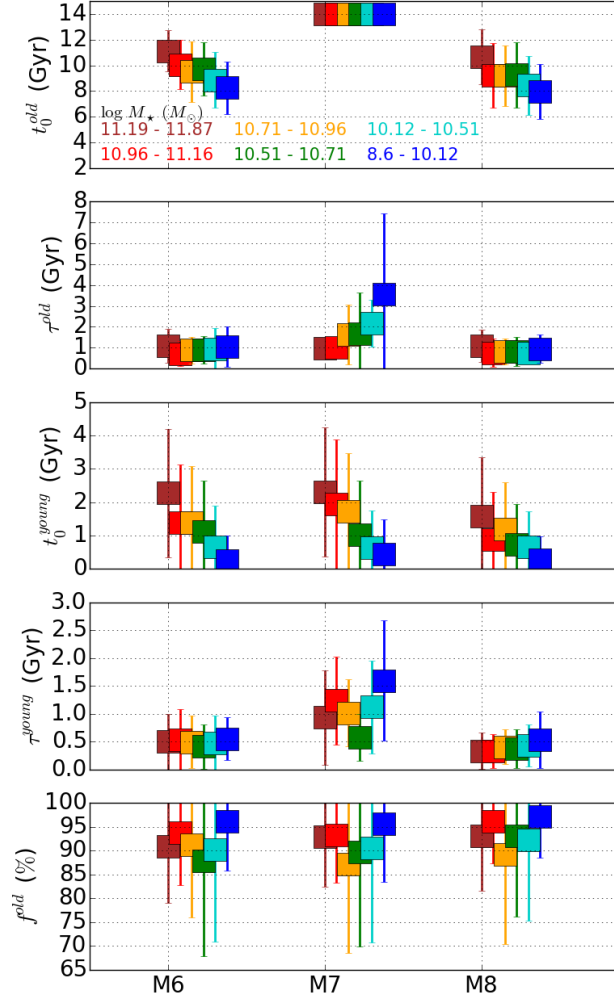
Figure 5.56 Mean parameters for models **M6**, **M7** and **M8**: t_0^{old}, τ^{old}, t_0^{young}, τ^{young} and f^{old}. Mass bins are colour-coded.

for E galaxies, and $t_0^{young} \sim 0.5$ Gyr for Sc and Sd. The range of variation of t_0^{young} with **M8** is smaller, with $t_0^{young} \sim 2$ Gyr for E galaxies, and $t_0^{young} \sim 0.5$ Gyr for Sc and Sd.

- $\tau^{young} < 1$ Gyr with **M6** and **M8** for all the Hubble types. For **M7**, 0.5 Gyr $< \tau^{young} < 2$ Gyr obtaining the lower values for Sb and Sbc and larger for Sd galaxies.

- The young component simulates a rejuvenation of galaxies but with a low contribution to the total mass of galaxies, obtaining for all the Hubble types $f^{old} > 80$ %.

- Stacking galaxies as a function of mass, we obtain with **M6** and **M8** that massive galaxies start to form stars earlier ($t_0^{old} \sim 11$ Gyr) than low mass galaxies ($t_0^{old} \sim 8$ Gyr). For both models

$\tau^{old} \sim 1$ Gyr for all the Hubble types.

- With **M7**, $t_0^{old} = 14$ Gyr and τ^{old} increase from $\tau^{old} \sim 1$ Gyr in massive galaxies to $\tau^{old} \sim 3.5$ in low mass galaxies.

- The results indicate an earlier formation of massive galaxies with the three models.

- t_0^{young} correlates with the mass, decreasing from massive to low mass galaxies. A larger range of variation is obtained with **M6** and **M8**, $t_0^{young} \sim 2.5$ Gyr for massive galaxies and $t_0^{young} \sim 0.5$ Gyr for low mass galaxies.

- $\tau^{young} \sim 0.5$ Gyr with **M6** and **M8** for galaxies in all the mass bins, while 0.5 Gyr $< \tau^{young} < 2$ Gyr with **M7**.

- $f^{old} > 80$ % for galaxies in all the mass bins.

5.7.3   The growth of galaxies

In the context of galaxy evolution, there is clear evidence for "downsizing (see Cowie et al. 1996 for its first definition) where massive galaxies formed earlier and faster than lower mass systems. The term of "downsizing" has been extended to different observational trends, such as age-downsizing, with more massive galaxies hosting older stellar populations than lower mass galaxies. The downsizing scenario has been supported by a lot of works from literature (Cimatti et al., 2006; Pozzetti et al., 2007; Pérez-González et al., 2008; González Delgado et al., 2015). The physical interpretation of this evolutionary picture is not trivial in the hierarchical merging scenario of ΛCDM cosmology because the mass-downsizing evolution seems anti-hierarchical. However, much progresses has been made in the last decades. For example, De Lucia et al. (2006) were able to reproduce the age-downsizing of elliptical galaxies by invoking AGN feedback to quench the star formation earlier in more massive systems with respect to less massive ones within the standard framework of the hierarchical assembly for stellar mass. The role of AGNs in influencing galaxy evolution and quenching star formation is supported by several observations (Fabian, 2012; Cimatti et al., 2013; Cicone et al., 2014); however, other models are capable of rapidly forming early type galaxies without considering the AGN feedback (Naab et al., 2006; Khochfar & Silk, 2006; Johansson et al., 2012).

This scenario for galaxies is also supported by our results. The previous analysis shows that the contribution of old stellar populations is more important in E and S0 galaxies. On the other hand, younger stellar populations contribute to account for the total mass for later morphological types. The period to form the total mass varies for the different galaxies, obtaining with **M1**, **M2**, **M3**, **M7** and **M9** a correlation between τ and the Hubble type. Using **M6** and **M8** we do not find evidence that early type galaxies were grow faster than later types, although it is clear that they formed earlier in the past.

Figures 5.57 and 5.58 show t_{80}, defined as the age at which 80% of the total mass is reached, for the different Hubble types and mass bins.

- For all the models t_{80} decreases with Hubble type, which is a manifestation of the "downizing" scenario.
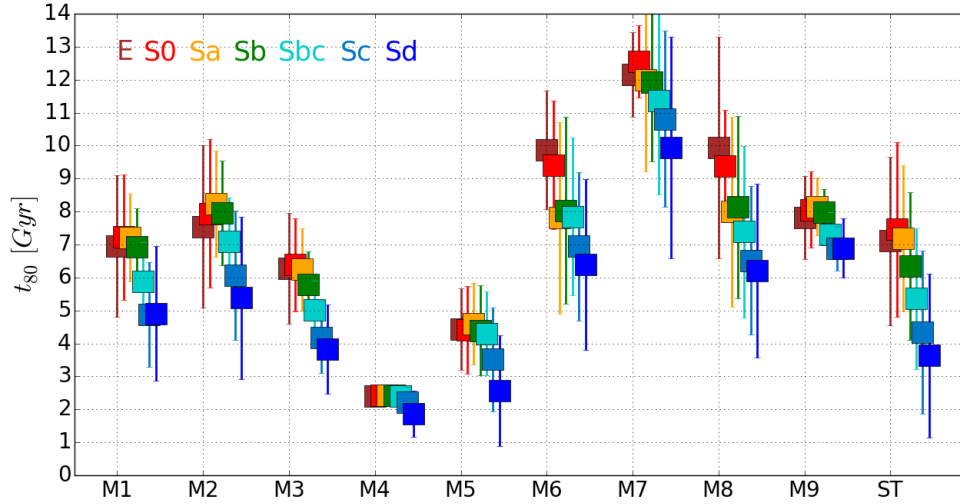
Figure 5.57 Mean t_{80} value for the parametric models and STARLIGHT. The Hubble types are colour-coded.
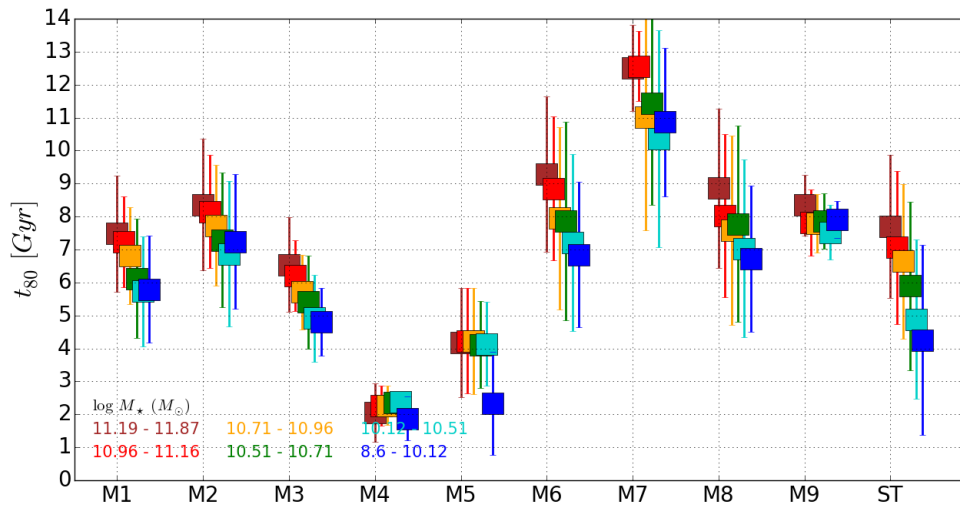
Figure 5.58 Mean t_{80} value for the parametric models and STARLIGHT. Mass bins are colour-coded.

- With STARLIGHT, $t_{80} \sim 7$ Gyr for Sa and earlier types and decreases for later types, obtaining $t_{80} \sim 3.5$ Gyr for Sd galaxies.

- Results with **M1** are very similar to those obtained with STARLIGHT for Sa and earlier types, with $t_{80} \sim 7$ Gyr. On the other hand, larger values are obtained for later morphological types, obtaining $t_{80} \sim 5$ Gyr for Sd galaxies.

- Some differences are obtained with **M2**. In this case, $t_{80} \sim 8$ Gyr for S0 and Sb galaxies, and larger for Sa. For E galaxies, $t_{80} \sim 7.5$ Gyr and lower values are obtained for later spirals, with $t_{80} \sim 5.5$ Gyr for Sd.

- With **M3**, we obtain lower values than those obtained with **M1**. For Sa and earlier types $t_{80} \sim$ 6-7 Gyr, $t_{80} \sim 6$ Gyr for Sb galaxies, and $t_{80} \sim$ for Sc and Sd.

- Results with **M6** and **M8** are very similar. In both cases, t_{80} decreases from 10 Gyr in E galaxies to $t_{80} \sim$ 6-7 Gyr for Sc and Sd galaxies.

- With **M7**, t_{80} is larger for all the Hubble types. For Sd galaxies $t_{80} \sim 10$ Gyr, which is the value obtained for E galaxies with **M6** and **M8**. For E and S0 galaxies, we obtain $t_{80} \sim$ 12-13 Gyr.

- The range of variation of t_{80} with **M9** is lower than with the other models. For Sb and earlier types, $t_{80} \sim 8$ Gyr, obtaining for Sc and Sd $t_{80} \sim 7$ Gyr.

- Comparing t_{80} according to the galaxy mass, we observe also the "downsizing", with t_{80} decreasing with the mass. This indicates that more massive galaxies reached 80% of the total mass earlier in the past. For all models, the range of variation of t_{80} is lower than the obtained according to the Hubble type.

We also compute the mass accreted at the epoch of $z = 1$. Figures 5.59 and 5.60 show the fraction of the total mass reached at $z = 1$ according to Hubble type and galaxy mass:

- For STARLIGHT and the two component models (**M6**, **M7**, **M8** and **M9**) we find a correlation with the Hubble type, indicating that at the epoch of $z = 1$ early type galaxies were more evolved than later types. Larger range of variation is obtained with **M6** and **M8**, with $f_{Mass} \sim$ 0.9 for E galaxies and $f_{Mass} \sim 0.4$ for Sd. On the other hand, with **M7**, $f_{Mass} \geq 0.9$ for all the Hubble types.

- Differences are obtained with **M1** and **M2**, with larger values for Sa and Sb galaxies. With **M1**, $f_{Mass} \sim 0.68$ for Sa and Sb, $f_{Mass} \sim 0.62$ for S0 and Sbc, and lower values are obtained for E galaxies, $f_{Mass} \sim 0.57$, and later type spirals, $f_{Mass} \sim 0.5$. With **M2**, $f_{Mass} \sim 0.75$ for Sa, Sb and Sbc galaxies, and $f_{Mass} \sim 0.65$ for S0 and Sc. For E and Sd galaxies f_{Mass} is similar to the values obtained with **M1**.

- With **M3**, f_{Mass} is larger for S0, Sa and Sb than for E galaxies, and the lower values are also obtained for Sd galaxies. Comparing with **M1** and **M2**, we obtain with **M3** lower values for all the Hubble types.

- Comparing f_{Mass} according to the galaxy mass, we obtain that f_{Mass} decreases from massive to low mass galaxies, indicating that at the epoch of $z = 1$ massive galaxies were more evolved than low massive ones. However, some differences are observed for galaxies in the low mass bin with **M1**, **M2** and **M3**. With **M1**, $f_{Mass} \sim 0.6$ for low mass galaxies, which is larger than for galaxies with $\log M_\star \sim$ 10.12-10.51. With **M2**, $f_{Mass} \sim 0.7$, similar to galaxies with $\log M_\star \sim$ 10.96-11.16. With **M3**, $f_{Mass} \sim 0.5$, similar to galaxies with $\log M_\star \sim$ 10.51-10.71

In the next chapter a further discussion is done by analyzing the galaxy structural components to study the cosmic evolution of inner and outer regions for the different types of galaxies.

Figure 5.59 Mean f_{Mass} at $z = 1$, defined as the mass fraction reached at $z = 1$. The columns show the results for the parametric models and STARLIGHT. The Hubble types are colour-coded.

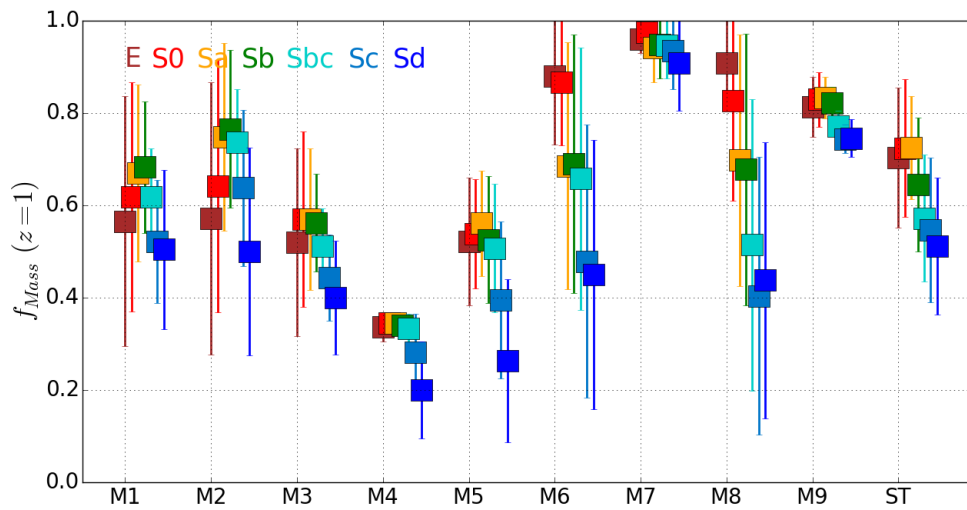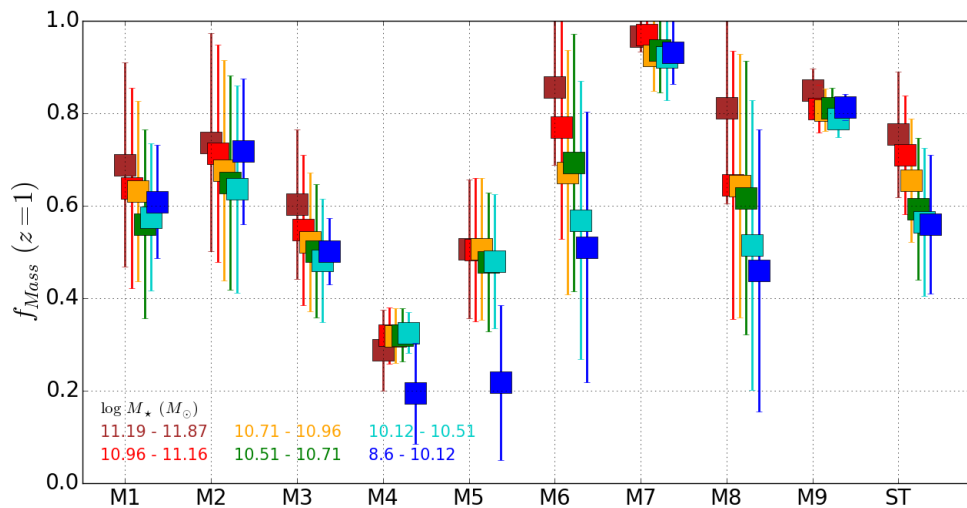Figure 5.60 Mean f_{Mass} at $z = 1$, defined as the mass fraction reached at $z = 1$. The columns show the results for the parametric models and STARLIGHT. Mass bins are colour-coded.

6

Parametric SFHs: spatial resolved results

Contents

6.1   Introduction

In this chapter we analyse the inner and outer regions of galaxies and obtain the stellar population properties of galaxies for both structural components with STARLIGHT and two parametric models, **M1** and **M6**. As we did in Chapter 4, we study four regions: $r < 0.5$, $r < 1$, $1 < r < 2$ and $r > 1$, where r denotes the radial distance to the nucleus in units of the optical HLR. We compare the star formation histories, the stellar population properties and local relations obtained through both methods. This chapter follows the same structure that was used to compare the integrated properties obtained with STARLIGHT and the parametric models.

6.2   Resolved properties: Star Formation History

Figures 6.1, 6.2 and 6.3 show the cumulative mass fraction profiles obtained using STARLIGHT and the parametric models **M1** and **M6**. Red curves represents the growth of stellar mass for the inner region and the blue curves for the outer one. Each panel shows the averaged profile for the different Hubble types. We find that inner regions have grown faster and they reach 80% of the total mass earlier in the past. On the other hand, outer regions show a more extended period of star formation. This is clearly observed for Sbc and earlier types. On the other hand, bulges and disks for Sc and Sd galaxies seem to have grown at the same time. The results indicate that galaxies grow inside-out. It is shown for STARLIGHT, **M1** and **M6**. However, this conclusion is not significant for results for Sd galaxies with STARLIGHT and **M6**, and Sc for model **M6**.
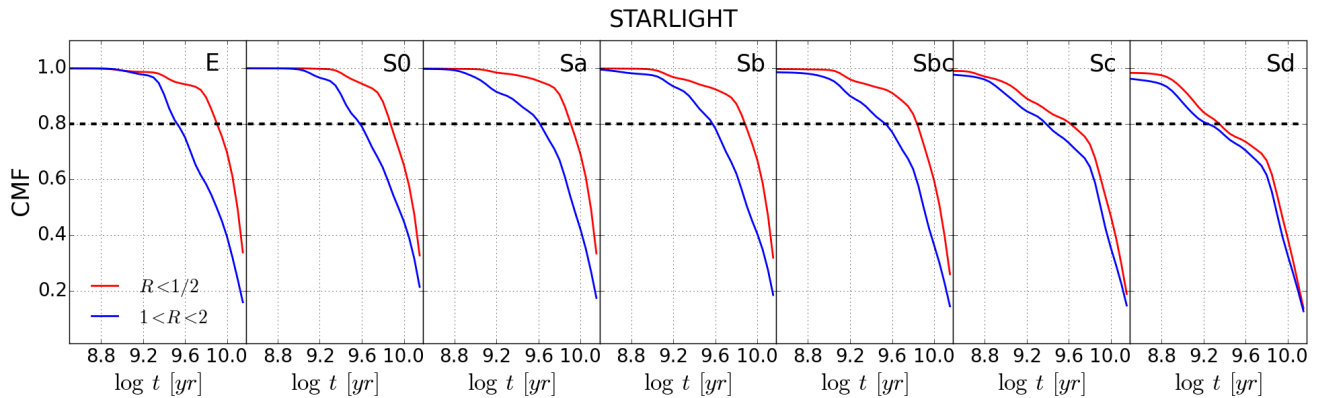
Figure 6.1 The cumulative mass fraction profiles for the inner ($r < 0.5$) and outer ($1 < r < 2$) regions as a function of the Hubble type obtained with STARLIGHT.

Next, we show in more detail the similarities and differences by comparing STARLIGHT, **M1** and **M2** results of the SFH represented by the mass fraction (figures 6.4 and 6.6) and CMF (figures 6.5 and 6.7). Figure 6.4 shows the mass fraction profiles for the inner region (left column) and the outer region (right column). Solid lines represent the results using model **M1** and dashed lines using STARLIGHT. Colours refer to the different morphological types. We obtain similar features in the profiles both in the inner and outer regions. The profiles for the nucleus of galaxies vary from E to Sd galaxies, decreasing the contribution of the old populations and increasing the fraction of young stellar populations. Thus the mass profiles decrease rapidly for early type galaxies, while for later
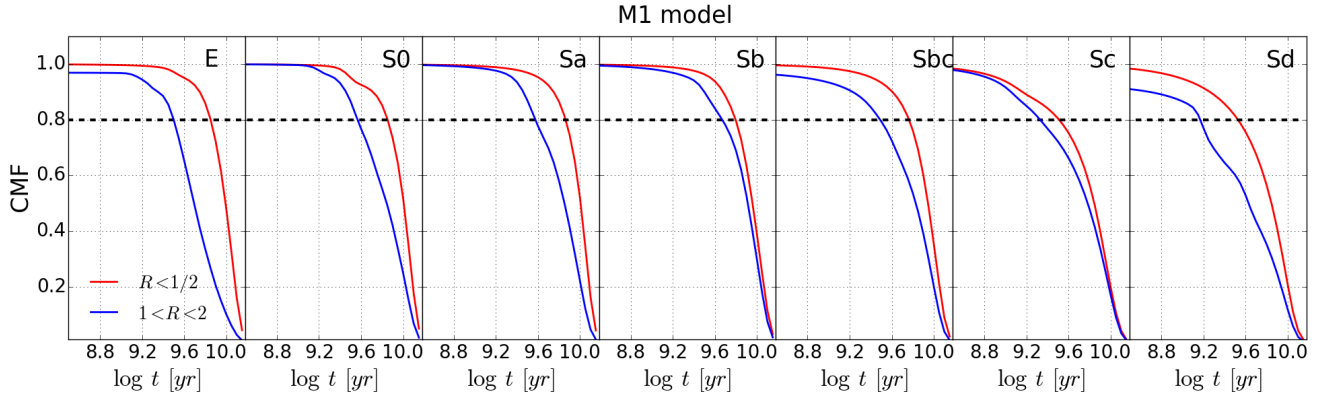
Figure 6.2 Same as figure 6.1 using **M1** model.
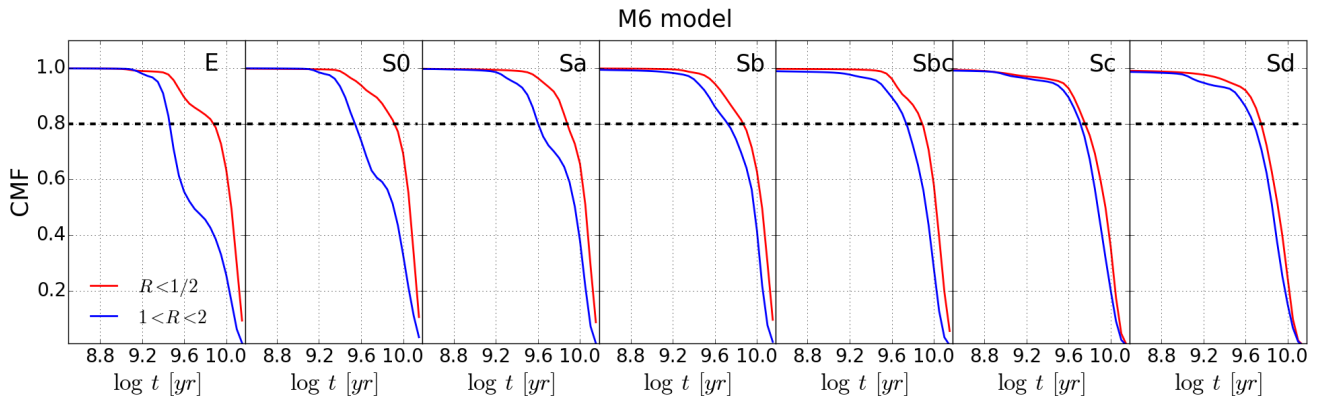
Figure 6.3 Same as figure 6.1 using **M6** model

types the period of star formation is more extended. For the different morphological types we can compare the inner and the outer regions. Sbc galaxies and earlier types show differences between the more extended mass profiles for the outer than inner regions. This indicates that the outer regions have been forming stars more recently than inner ones and grew more slowly. For Sc and Sd galaxies it is not so clear, showing similar profiles for the bulge and disk. The main difference is the location of the peak of star formation. Results with **M1** indicate a more recent peak of star formation, as we obtained when analysing the integrated properties. Using STARLIGHT we find the peak of star formation at the earliest time of Universe. This indicates that the STARLIGHT curves can be better fitted using a purely exponential profile, rather than using a delayed-τ model.

The cumulative mass fractions for **M1** and STARLIGHT are shown in figure 6.5. The left column shows the results for the inner regions and right column for the outer ones. In both cases, the values for t_{80}, the time when the galaxy has formed 80% of the total mass, are similar for the histories derived through both methods, although they are more in agreement for outer regions. For the inner regions we obtain slight differences for Sb and later types. For Sb and Sbc we obtain larger t_{80} when using STARLIGHT and for Sd galaxies t_{80} is larger for model **M1**.
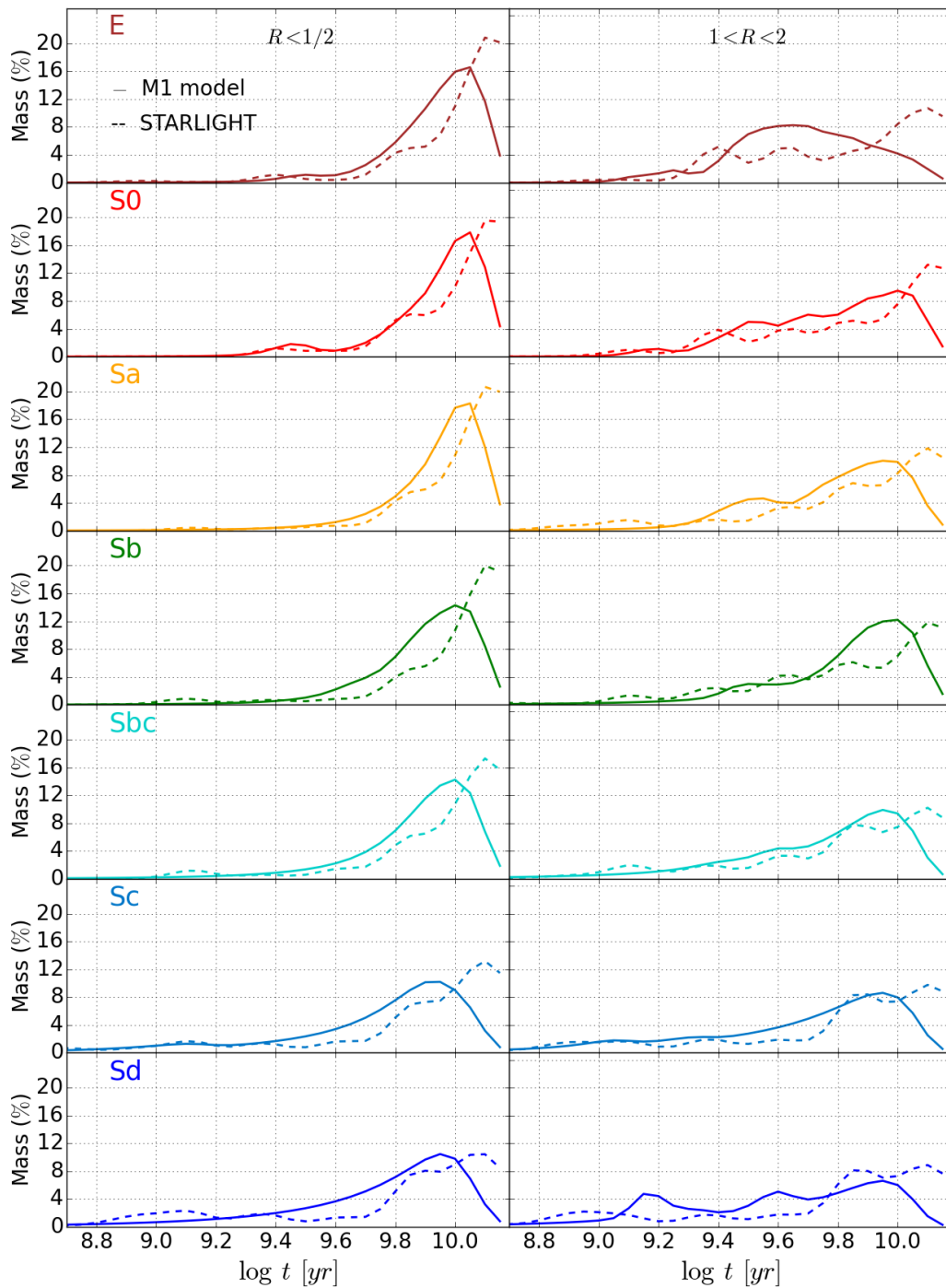
Figure 6.4 Mass fraction profiles for the inner ($r \leq 1/2$, left column) and outer ($1 \leq r \leq 2$, right column) regions. The solid lines show the results using the parametric method and model **M1**. Dashed lines represent the results with STARLIGHT. The different morphological types are colour-coded.

Figure 6.5 Cumulative mass fraction profiles for the inner ($r \leq 1/2$, left column) and outer ($1 \leq r \leq 2$, right column) regions. The solid lines show the results using the parametric method and model **M1**. Dashed lines represent the results with STARLIGHT. The different morphological types are colour-coded.
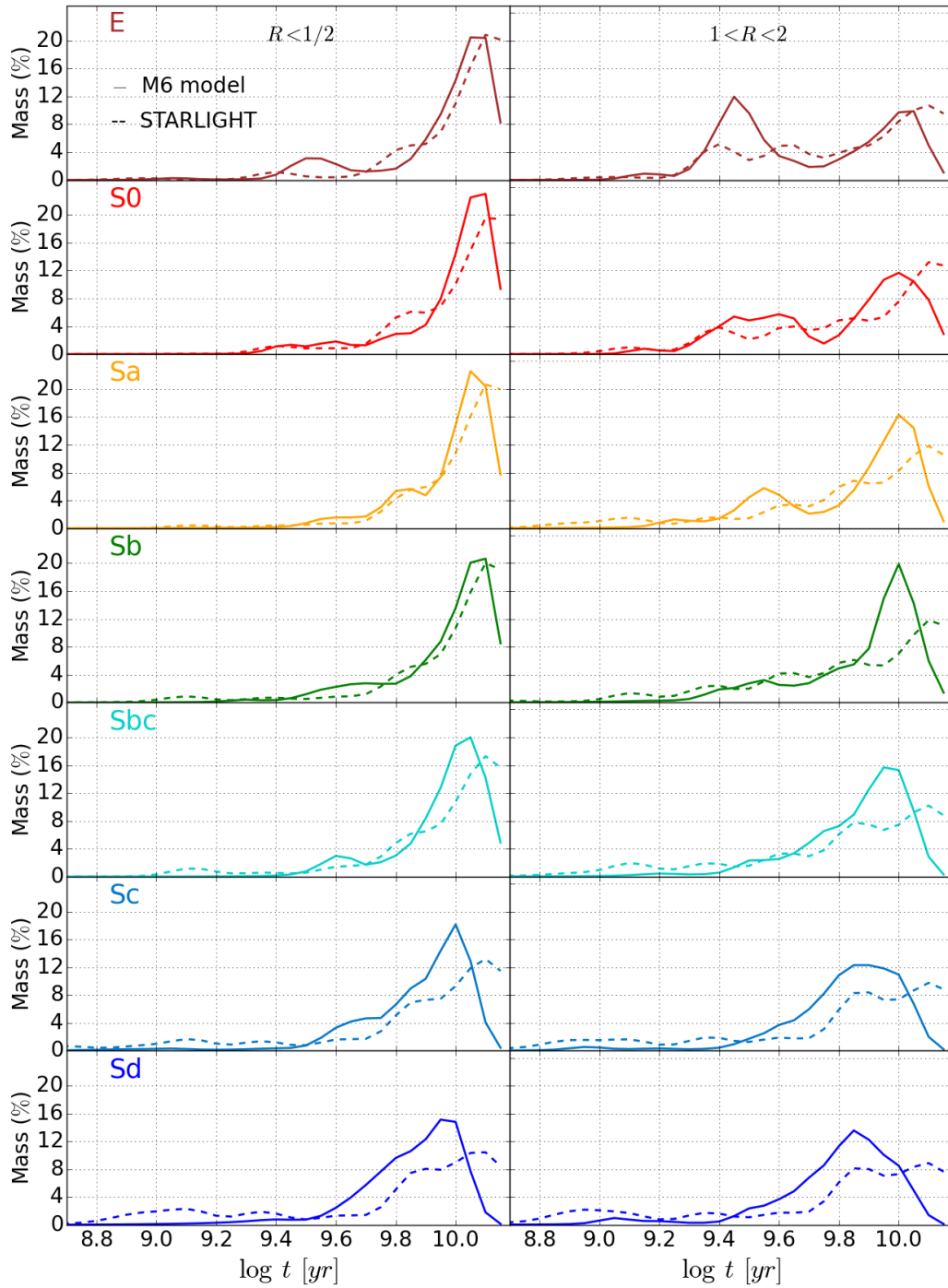
Figure 6.6 Same as figure 6.4 using model **M6**.
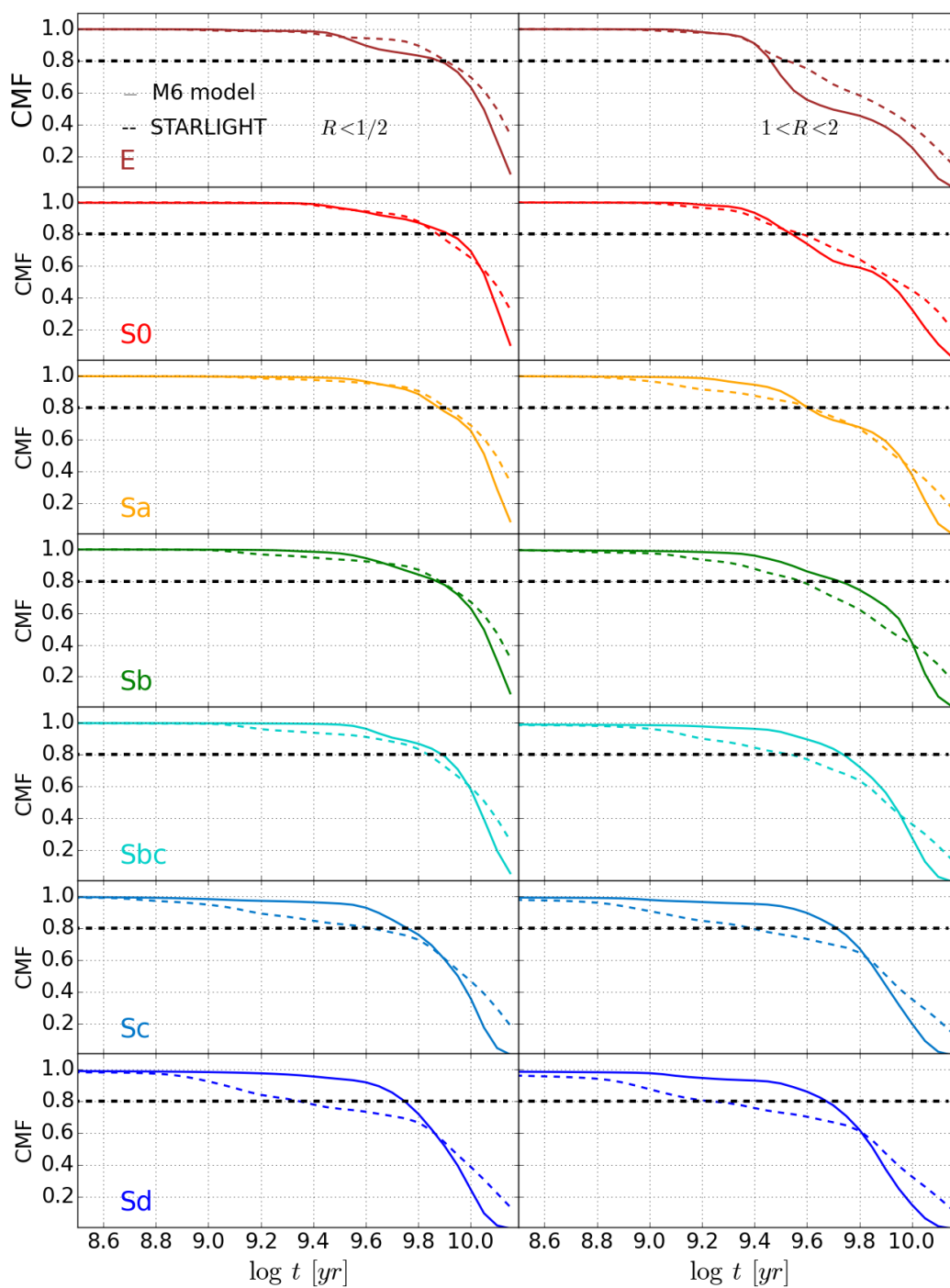
Figure 6.7 Same as figure 6.5 using model **M6**.

Figure 6.6 shows the mass fraction profiles for the inner region (left column) and the outer region (right column) using model **M6**. Solid lines represent the results using model **M6** and dashed lines using Starlight. As previously described, colours represent to the different morphological types. The mass profiles for the inner region vary from E to Sd galaxies, with an important peak of mass fraction at early time, which decreases in intensity from E to Sd galaxies. Also the earlier types present rapid declining profiles compared with more extended ones for later types. Using **M6** we obtain a similar location of the peak of star formation in the inner regions for Sb and earlier types. For later types we find similar results to **M1**, with a more recent peak of star formation. Comparing the mass curves, we find that bulges and disks for Sc and Sd show similar profiles indicating a similar formation, but on the other hand, for Sb and earlier type galaxies we observe that histories for outer regions are more extended than for the inner ones indicating a slower formation.
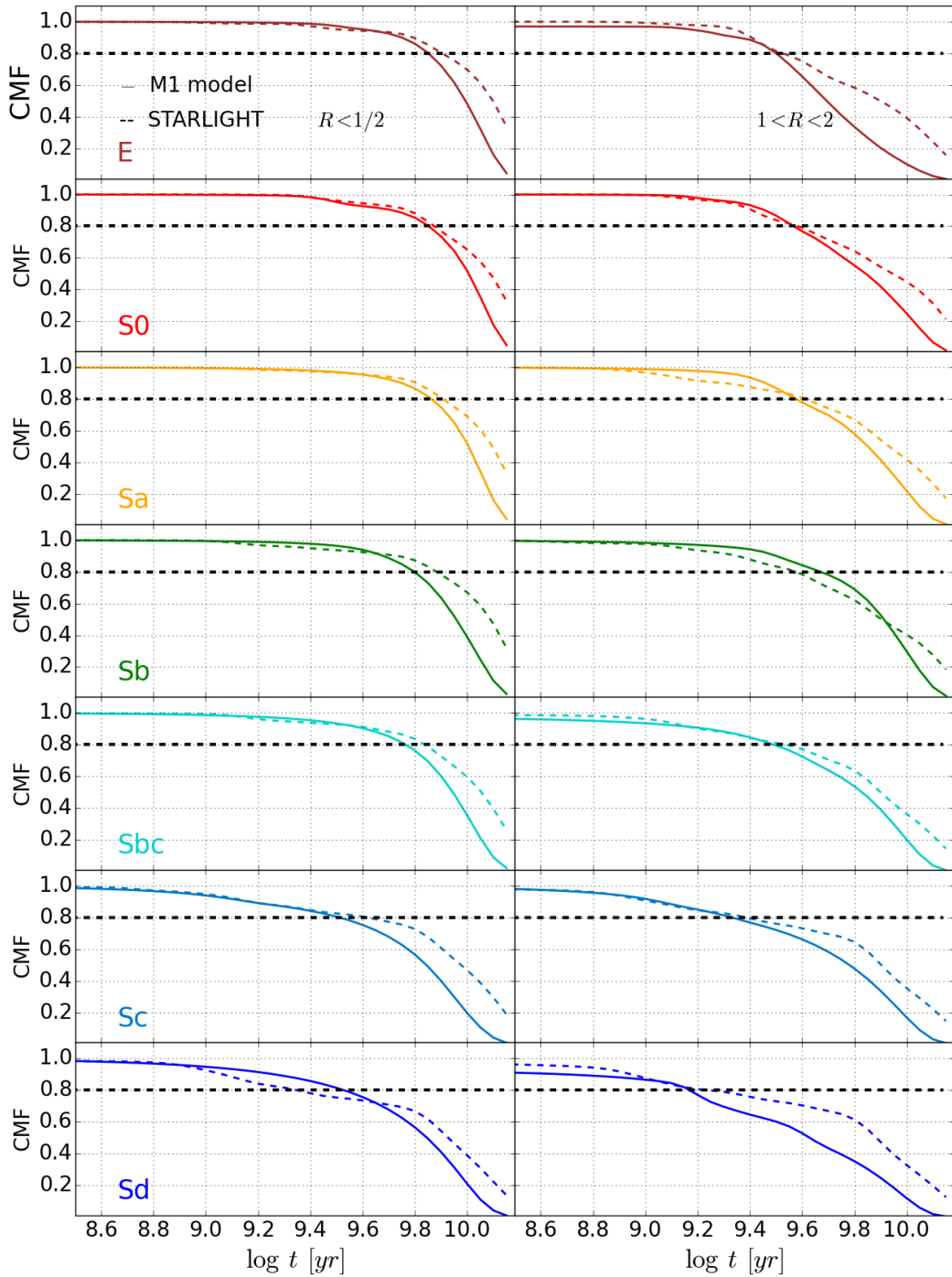
The cumulative mass fraction profiles for STARLIGHT and **M6** are shown in figure 6.7. In the inner regions, the values for t_{80} are similar for both methods, although larger for Sc and Sd galaxies using model **M6**. On the other hand, outer regions present more differences, obtaining larger values of t_{80} when using **M6** for Sb and later types. Thus, both methods point to an inside-out growth of galaxies for Sbc and earlier types, although results with **M6** indicate a more rapid formation of disks for Sd galaxies compared with STARLIGHT. On the other hand, for Sc and Sd galaxies bulges and disks have grown at the same time but results with **M6** indicate a faster growth of both structural components.

6.3   Resolved properties: Stellar population properties

"Delayed-τ" model

Now we compare the stellar population properties for the inner and outer regions obtained with STARLIGHT and model **M1**. In particular we analyse the mass surface density, attenuation, mean stellar age and mean stellar metallicity. For each property we compute the gradient as $\Delta P = P_{1 \leq r \leq 2} - P_{r \leq 1/2}$, which is shown in figure 6.8. For each gradient and different morphological type we show $\overline{\Delta} \pm \sigma_{\Delta}$ in table 6.1.

As we observe in table 6.1, the gradients for all the properties show negative mean values:

- The largest absolute gradients are obtained for mass surface density, in particular for E and S0 galaxies ($\overline{\Delta} = -1.27; -1.28$ using STARLIGHT and $\overline{\Delta} = -1.28; -1.31$ using **M1**), and decrease with the Hubble type. This is expected due to the mass surface density is higher in the inner regions than in outer ones.

- Regarding the attenuation values, small gradients are obtained for E galaxies ($\overline{\Delta} \pm \sigma_{\Delta} = -0.03 \pm 0.06; -0.08 \pm 0.11$ for STARLIGHT and **M1**, respectively), which indicates a similar extinction for the inner region and the envelope. For later spirals, larger absolute values are obtained with larger dispersion, pointing to different dust content in the bulge and disk.

- For stellar metallicity, smaller gradients are obtained for E galaxies, indicating a similar chemical content in the inner region and the envelope. For later types, as was observed for the attenuation, larger gradients are obtained, but also the dispersion increases, which indicate differences between bulges and disks, with inner regions being more metal rich than outer ones.

Gradients of stellar population properties: $\overline{\Delta} \pm \sigma_\Delta$

Property (STARLIGHT)	E	S0	Sa	Sb	Sbc	Sc	Sd
$\log \mu_\star$	-1.27 ± 0.19	-1.28 ± 0.10	-1.22 ± 0.16	-1.14 ± 0.33	-1.05 ± 0.23	-0.83 ± 0.34	-0.75 ± 0.39
τ_V	-0.03 ± 0.06	-0.13 ± 0.16	-0.24 ± 0.21	-0.22 ± 0.25	-0.19 ± 0.19	-0.20 ± 0.31	-0.18 ± 0.45
$\langle \log t \rangle_L$	-0.24 ± 0.15	-0.22 ± 0.17	-0.26 ± 0.25	-0.32 ± 0.22	-0.32 ± 0.24	-0.11 ± 0.27	-0.08 ± 0.34
$\langle \log t \rangle_M$	-0.19 ± 0.17	-0.15 ± 0.17	-0.18 ± 0.23	-0.17 ± 0.16	-0.17 ± 0.15	-0.09 ± 0.26	-0.07 ± 0.23
$\langle \log Z \rangle_M$	-0.08 ± 0.16	-0.08 ± 0.14	-0.14 ± 0.24	-0.25 ± 0.32	-0.45 ± 0.34	-0.40 ± 0.39	-0.24 ± 0.50
Property (M1)	E	S0	Sa	Sb	Sbc	Sc	Sd
$\log \mu_\star$	-1.26 ± 0.14	-1.31 ± 0.11	-1.19 ± 0.19	-1.18 ± 0.29	-1.09 ± 0.22	-0.92 ± 0.25	-0.88 ± 0.30
τ_V	-0.07 ± 0.09	-0.15 ± 0.18	-0.26 ± 0.25	-0.25 ± 0.26	-0.22 ± 0.26	-0.21 ± 0.35	-0.20 ± 0.49
$\langle \log t \rangle_L$	-0.23 ± 0.11	-0.22 ± 0.14	-0.23 ± 0.28	-0.31 ± 0.24	-0.30 ± 0.24	-0.17 ± 0.28	-0.13 ± 0.36
$\langle \log t \rangle_M$	-0.22 ± 0.11	-0.19 ± 0.14	-0.18 ± 0.27	-0.24 ± 0.21	-0.25 ± 0.21	-0.17 ± 0.25	-0.22 ± 0.37
$\langle \log Z \rangle_M$	-0.17 ± 0.12	-0.14 ± 0.17	-0.17 ± 0.19	-0.19 ± 0.29	-0.29 ± 0.31	-0.16 ± 0.37	-0.02 ± 0.39
Property (M6)	E	S0	Sa	Sb	Sbc	Sc	Sd
$\log \mu_\star$	-1.28 ± 0.16	-1.31 ± 0.10	-1.22 ± 0.17	-1.15 ± 0.31	-1.01 ± 0.22	-0.82 ± 0.29	-0.78 ± 0.34
τ_V	-0.08 ± 0.11	-0.17 ± 0.17	-0.24 ± 0.20	-0.22 ± 0.24	-0.16 ± 0.20	-0.18 ± 0.29	-0.14 ± 0.44
$\langle \log t \rangle_L$	-0.25 ± 0.12	-0.23 ± 0.14	-0.23 ± 0.23	-0.28 ± 0.21	-0.26 ± 0.21	-0.09 ± 0.29	-0.10 ± 0.45
$\langle \log t \rangle_M$	-0.24 ± 0.12	-0.21 ± 0.15	-0.18 ± 0.22	-0.18 ± 0.18	-0.11 ± 0.17	-0.03 ± 0.19	-0.06 ± 0.26
$\langle \log Z \rangle_M$	-0.03 ± 0.14	-0.08 ± 0.11	-0.17 ± 0.21	-0.25 ± 0.26	-0.39 ± 0.27	-0.31 ± 0.32	-0.14 ± 0.36

Table 6.1 The stellar population gradients derived with STARLIGHT (top),**M1** (middle) and **M6** (bottom). For each property and morphological type the table lists the mean outer ($1 \leq r \leq 2$) minus inner ($r \leq 1/2$) difference ($\overline{\Delta}$) and its standard deviation (σ_Δ).

- The absolute $\langle \log t \rangle_L$ gradients also decrease with the Hubble type. For Sbc and earlier types, $|\overline{\Delta}| > \sigma_\Delta$, which indicates that inner regions are older than outer ones. For Sc and Sd galaxies, negative mean values are obtained but the dispersion is larger. In particular, for Sd galaxies we obtain $\overline{\Delta} \pm \sigma_\Delta = -0.08 \pm 0.34$; -0.10 ± 0.45, for STARLIGHT and **M1**, respectively. Negative age gradients indicate inside-out formation, which is more clearly observed for Sbc and earlier types. The gradients obtained with STARLIGHT and **M1** for $\langle \log t \rangle_M$ are smaller than for $\langle \log t \rangle_L$ for all the Hubble types, except for Sd galaxies using **M1** ($\overline{\Delta} \pm \sigma_\Delta = -0.22 \pm 0.37$). Again the results suggest an inside-out formation scenario for all the Hubble types, although it is not so clear for Sc and Sd galaxies, with larger dispersion in the gradients.

The gradients for the different properties derived with STARLIGHT are very similar to gradients derived with **M1**. However some differences are obtained. The larger differences are obtained for the metallicity gradients because, as was shown for the integrated data, metallicity is recovered with larger uncertainty than stellar age and attenuation. On the contrary, the most similarities are observed for the mass surface density gradients, due to the mass is the most robust parameter. For the attenuation gradients, larger differences are obtained for E and S0 galaxies. In particular, for E galaxies we obtain $\overline{\Delta} \pm \sigma_\Delta = -0.03 \pm 0.06$; -0.08 ± 0.15 using STARLIGHT and **M1**, respectively. As was analysed with the integrated properties, for these galaxies, the attenuation values derived with STARLIGHT are lower than those obtained with **M1**. This is due to the stellar populations included in the SFH of STARLIGHT being older than those obtained with **M1**. Thus, larger extinction values are obtained. This also happens for the inner regions of E and S0, so larger absolute attenuation gradients are obtained using **M1**. The integrated stellar age obtained with **M1** was in agreement with the STARLIGHT results, although larger dispersion was found for Sd galaxies, compared with earlier Hubble types. Thus, the age gradients are also very similar for all the Hubble types, although larger dispersion is obtained for Sd galaxies ($\overline{\Delta} \pm \sigma_\Delta = -0.08 \pm 0.34$; -0.10 ± 0.45 for STARLIGHT and **M1** respectively).
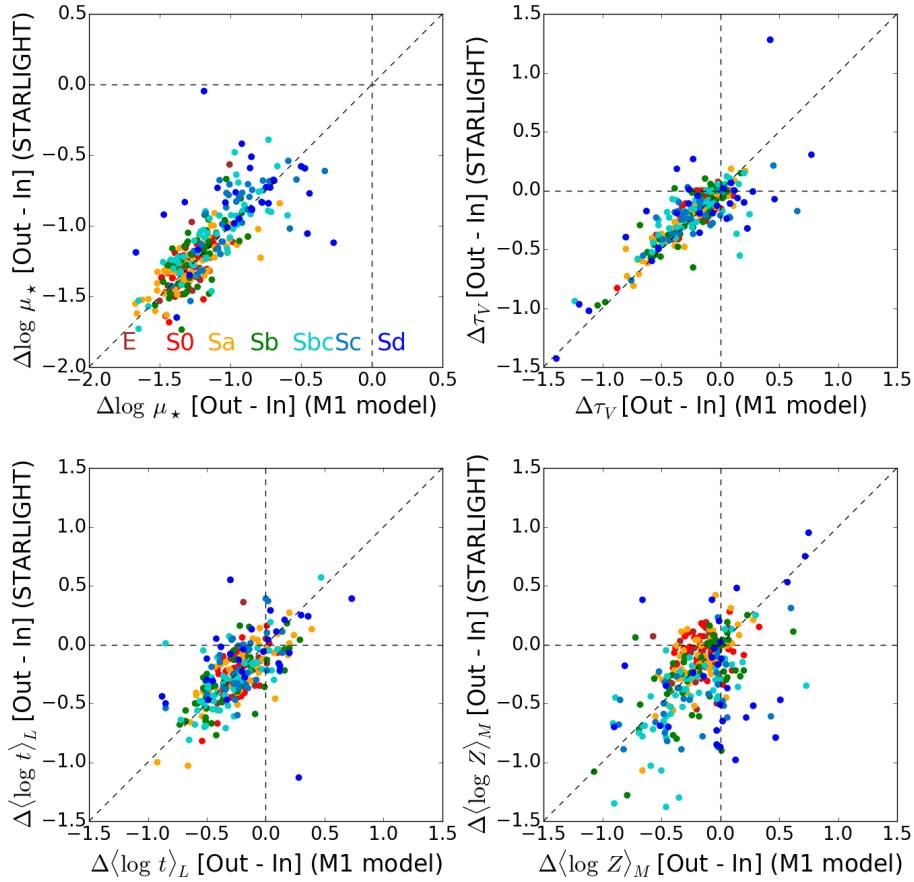
Figure 6.8 Each panel shows $\Delta P = P_{1 \leq r \leq 2} - P_{r \leq 1/2}$, where P indicates a property. The x-axis is the Parametric method using **M1** model and the y-axis STARLIGHT. The analysed properties are the mass surface density (top left), the attenuation (top right), the mean stellar age (bottom left) and the mean stellar metallicity (bottom right).

Two exponential components

In figure 6.9 we compare the stellar population properties for the inner and outer regions obtained with STARLIGHT and model **M6**. As we did with the **M1** model, we analyse the mass surface density, attenuation, mean stellar age and mean stellar metallicity. For each property we again compute the gradient as $\Delta P = P_{1 \leq r \leq 2} - P_{r \leq 1/2}$. The mean and standard deviation values for each gradient and the different morphological type are shown in table 6.1.

A visual inspection of the four panels in figure 6.9 indicates better agreement between STARLIGHT and **M6** than when comparing STARLIGHT and **M1**. Also the gradients obtained with **M6** for all the properties show negative mean values:

- The largest absolute gradients are obtained for mass surface density, decreasing from E to Sd galaxies.

- Regarding the attenuation values, in agreement with **M1**, small gradients are obtained for E

galaxies ($\overline{\Delta} \pm \sigma_\Delta = -0.07 \pm 0.09$) which indicated a similar extinction for the inner region and the envelope. Larger gradients are obtained for later Hubble types, with the largest dispersion for Sd galaxies ($\overline{\Delta} \pm \sigma_\Delta = -0.20 \pm 0.49$).

- For stellar metallicity, the dispersion in the mean gradients increases from E to Sd galaxies, indicating larger variation for later morphological types. It means that more similar chemical content is found in the outer and inner regions in E and S0 galaxies than in later Hubble types, obtaining the largest variation for Sd galaxies ($\overline{\Delta} \pm \sigma_\Delta = -0.02 \pm 0.39$).

- The absolute $\langle \log t \rangle_L$ and $\langle \log t \rangle_M$ gradients obtained with **M6** also decrease with the Hubble type, as obtained with **M1**. For $\langle \log t \rangle_L$, $|\overline{\Delta}| > \sigma_\Delta$ for Sbc and earlier types, which indicates that inner regions are older than outer ones. For Sc and Sd galaxies, negative mean values are obtained but in these cases $|\overline{\Delta}| < \sigma_\Delta$. In particular, we obtain $\overline{\Delta} \pm \sigma_\Delta = -0.17 \pm 0.28; -0.13 \pm 0.36$, for Sc and Sd galaxies, respectively. The results are in agreement with those obtained with **M1** and STARLIGHT. A similar trend is observed with $\langle \log t \rangle_M$, although smaller gradients are observed for all the morphological types. The negative $\langle \log t \rangle_L$ and $\langle \log t \rangle_M$ gradients indicate
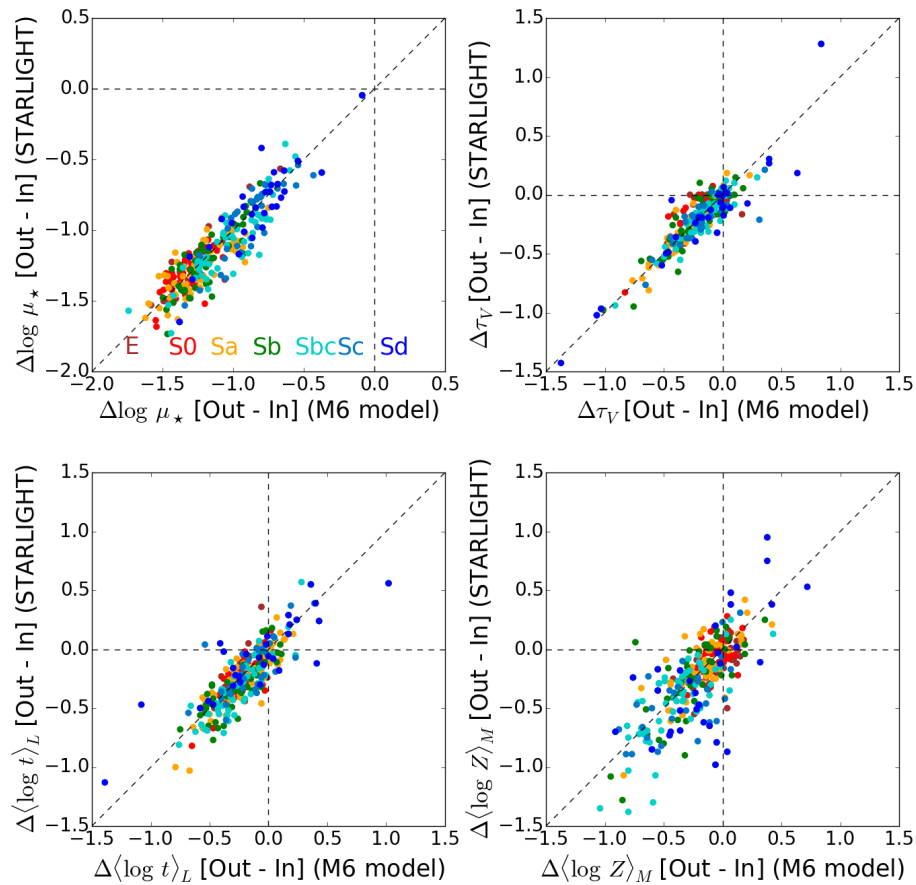
Figure 6.9 Same as figure 6.8 using **M6**.

an inside-out formation for all the Hubble types, although it is more clearly observed for Sbc and later types than in Sc and Sd galaxies.

The gradients obtained with **M6** are also similar to those obtained with STARLIGHT. For the mass surface density gradients some differences are obtained for Sc and Sd galaxies. Larger gradients are observed for **M6** but the dispersion is lower than obtained with STARLIGHT. In particular, for Sc galaxies we obtain $\overline{\Delta} \pm \sigma_\Delta = -0.83 \pm 0.34; -0.92 \pm 0.25$ for STARLIGHT and **M6** respectively. For Sd galaxies $\overline{\Delta} \pm \sigma_\Delta = -0.75 \pm 0.39; -0.88 \pm 0.30$, respectively. It is due to the fact that in Sc and Sd galaxies, the old component of **M6** includes a larger mass fraction for the older stellar populations than STARLIGHT. Again the largest differences are obtained for the metallicity gradients due to the larger uncertainty when recovering this property. The attenuation gradients are very similar for all the Hubble types. Only some differences are obtained for E galaxies, although it is less than 0.04 dex in the mean values ($\overline{\Delta} \pm \sigma_\Delta = -0.03 \pm 0.06$ for STARLIGHT and $\overline{\Delta} \pm \sigma_\Delta = -0.07 \pm 0.09$ for **M6**). The age gradients are also very similar for all the Hubble types, although slight differences in the mean values are found for Sd galaxies ($\overline{\Delta} \pm \sigma_\Delta = -0.08 \pm 0.34; -0.13 \pm 0.36$ for STARLIGHT and **M6** respectively).

6.4   Resolved properties: Local relations

In figure 6.10 we show the local relations obtained with STARLIGHT. The left panel shows the local $\mu_\star - Z$ relation, middle panel shows $\mu_\star - age$ relation and right panel shows $\mu_\star - M_\star$ relation. The different regions are colour-coded.

Regarding the $\mu_\star - Z$ relation we observe that local stellar mass surface density and metallicity are strongly correlated, as was previously shown by González Delgado et al. (2014a). We observe that this relation is stronger within galactic discs, while in spheroids μ does not seem to play a major role in controlling chemical evolution, where some other property must take over the dominant role.
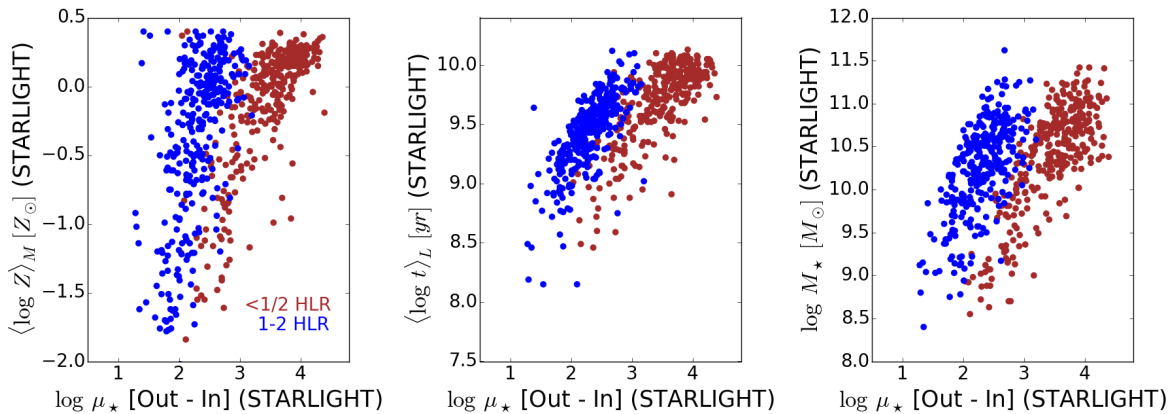
Figure 6.10 This figure shows different local relations derived with STARLIGHT. Left panel: local $\mu_\star - Z$ relation; middle panel: $\mu_\star - age$ relation; right panel: $\mu_\star - M_\star$ relation. The different regions are colour-coded.

The middle panel explores the age-density relation for CALIFA galaxies. On the x-axis we show the

log μ and on the y-axis $\langle \log age \rangle_L$. We observe a correlation in this relation for $\mu_\star \leq 7 \times 10^2 \, M_\odot/\mathrm{pc}^2$. In this region there are mainly young disk galaxies. Above this mass, the relation is flatter, and galaxies are increasingly dominated by a spheroidal component. Below this critical density, $\mu_\star$ increases with age which indicates that regions of low density formed later (are younger) than the regions of higher surface density, while above this critical density the dependence is weaker. This result was also found by González Delgado et al. (2014a) using CALIFA galaxies. A similar result is found by Kauffmann et al. (2003, 2006) for SDSS galaxies.

In the right panel the $\mu_\star - M_\star$ relation reveals the differences between the structural components of galaxies. For massive galaxies, we observe that the inner regions have larger $\mu_\star$ than the outer regions. This indicates that inner regions in massive galaxies are denser than outer regions. On the other hand, this difference decreases toward low mass galaxies. The surface density for lower mass galaxies is more similar for inner and outer regions.
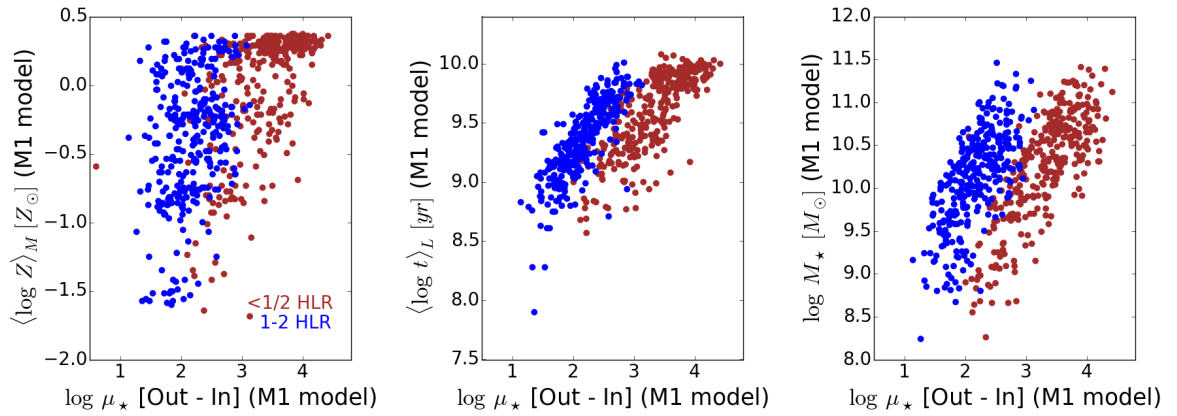
Figure 6.11 Same as figure 6.10 using **M1**.
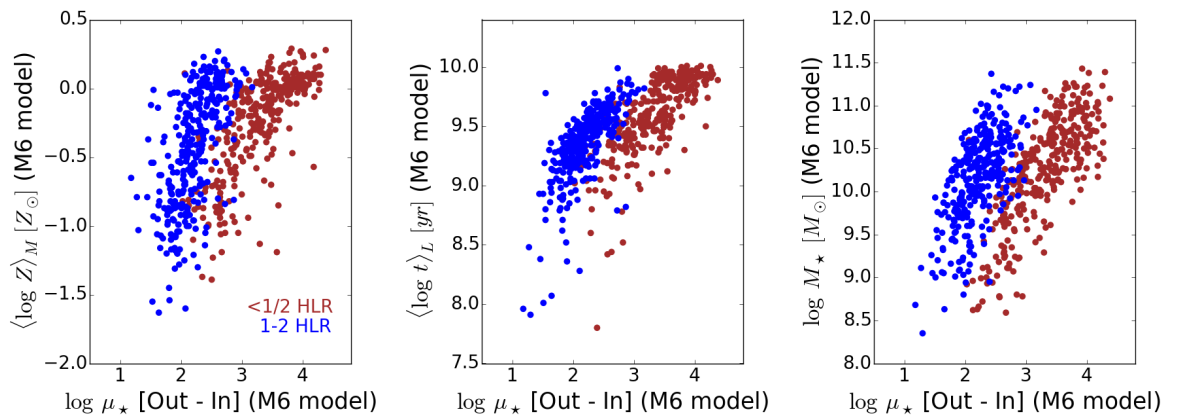
Figure 6.12 Same as figure 6.10 using **M6**.

Figures 6.11 and 6.12 show the local relations derived with **M1** and **M6**, respectively. The $\mu_\star - age$ and $\mu_\star - M_\star$ relations are similar to those found using STARLIGHT due to the correlation in the derived ages and masses for both methods. Regarding the $\mu_\star - Z$ relation we find that mass surface density and metallicity are correlated, but the relation is more concentrated in the metallicity values with parametric models in comparison with STARLIGHT, where a wider range for metallicity values is obtained.

6.5 Conclusions

In this chapter we have analysed the stellar population properties of the inner and outer regions of galaxies. Comparing the star formation histories obtained with STARLIGHT and the parametric models **M1** and **M6**, we obtain differences that come from the intrinsic definition of the models although similar trends are observed, indicating a consistent scenario of galaxy evolution.

On the other hand, the stellar population gradients are also in agreement for both methods, which reinforces the results concerning the stellar properties of inner and outer regions, previously studied by González Delgado et al. (2015). The local relations with STARLIGHT in CALIFA galaxies have been widely studied and the agreement in the stellar population properties lead to local relations obtained with the parametric models, which are consistent and in agreement with previous studies (González Delgado et al. 2014b,a).

6.5.1 Stellar population components

For the different structural components, we have analysed the star formation history of galaxies for the different morphological types by grouping the stellar populations into four age rages: $t \leq 9$ Gyr (red), $4 < t < 9$ Gry (orange), $1 < t < 4$ Gyr (green), and $t \leq 1$ Gry (blue). Tables 6.2 6.3 and 6.4, with Figures 6.13 and 6.14 show the averaged light and mass fractions, respectively, for the different morphological types and structural components obtained with **M1**, **M6** and STARLIGHT. Each panel shows the results for the inner region $R < 0.5$ (left bar), the whole galaxy (middle bar) and the outer region $1 < R < 2$ (right bar). The middle bars are the same as were shown in the previous chapter, which we show again for a complete spatial view of the galaxies. Tables 6.2, 6.3 and 6.4 show the averaged values and the dispersion.

Light fraction, x: Fig. 6.13 shows a progression of the young populations ($t < 1$ Gyr) along the Hubble sequence, being more important for Sd galaxies than for E and S0.

1. Outer regions $1 < R < 2$:

   - $x_{t \leq 1\,Gyr}$: the evolution of the young component in the outer region obtained with STARLIGHT is similar to those obtained with models **M1** and **M6**, increasing from E to Sd galaxies. For E galaxies we obtain $x_{t \leq 1\,Gyr} \sim 5$ % , 4 % and 4 % for STARLIGHT, **M1** and **M6**. For Sd galaxies $x_{t \leq 1\,Gyr} \sim 42$ % , 40 % and 41 %, respectively.

   - $x_{1\,Gyr < t \leq 4\,Gyr}$: for E galaxies, $x_{1 < t < 4\,Gyr} \sim 43$ % and 56 %, for STARLIGHT and **M6**, respectively. This component decreases with morphology in the case of STARLIGHT and

M6, obtaining for Sd galaxies $x_{1<t<4\,Gyr} \sim 20$ % and 13 %, respectively. Using **M1** the lower values of $x_{1<t<4\,Gyr}$ are obtained for Sb galaxies. This component decreases from $x_{1<t<4\,Gyr} \sim 43$ % for E galaxies to 25 % for Sb galaxies, obtaining similar values for Sbc and Sc. For Sd galaxies the fraction increases, obtaining $x_{1<t<4\,Gyr} \sim 37$ %.

- $x_{4\,Gyr<t\leq9\,Gyr}$: the evolution of this component varies for the different models. With STARLIGHT we obtain similar values for all the Hubble types, 21 % $< x_{4<t\leq9\,Gyr} <$ 29 %. Using **M1**, this component is similar for Sb and earlier types galaxies, with 39 % $< x_{4<t\leq9\,Gyr} <$ 46 %, and decreases for later spirals, obtaining $x_{4<t\leq9\,Gyr} \sim 18$ % for Sd galaxies. Using **M6** the $x_{4<t\leq9\,Gyr} \sim 22$ % for E galaxies and increases for later types, with 30 % $< x_{4<t\leq9\,Gyr} <$ 40 %, but with no correlation with morphology.

- $x_{t>9\,Gyr}$: for this component we again obtain similarities between STARLIGHT and **M6**. $x_{t>9\,Gyr}$ decreases from E to Sd galaxies although the fractions obtained are slightly different. For STARLIGHT, 28 % $< x_{t>9\,Gyr} <$ 31 % for E, S0 and Sa galaxies and decreases for later types, obtaining the lower values for Sd galaxies, $x_{t>9\,Gyr} \sim 16$ %. Using **M6**, we find similar values for S0 Sa and Sb galaxies, with 24 % $< x_{t>9\,Gyr} <$ 30 %. For E and Sbc galaxies $x_{t>9\,Gyr} \sim 18$ % and 17 %, respectively, and the fraction decreases for Sc and Sd, obtaining $x_{t>9\,Gyr} \sim 12$ % and 9%.

2. Inner regions $R < 0.5$:

- $x_{t\leq1\,Gyr}$: for the inner regions, we also obtain an evolution of the young component, increasing from E to Sd galaxies. For E galaxies we obtain $x_{t\leq1\,Gyr} \sim 3$ % , 6 % and 8 % for STARLIGHT, **M1** and **M6**. For Sd galaxies $x_{t\leq1\,Gyr} \sim 34$ % , 39 % and 39 %, respectively.

- $x_{1\,Gyr<t\leq4\,Gyr}$: on average, this component is less important in the inner regions than in the outer ones for all the Hubble types. Using STARLIGHT and **M1** the fraction increase from E to Sd galaxies. For E galaxies we obtain $x_{1<t\leq4\,Gyr} \sim 13$ % and 10 %, for STARLIGHT and **M1**. For Sd galaxies $x_{1<t\leq4\,Gyr} \sim 26$ % and 25 %, respectively. The opposite trend is obtained with **M6**, decreasing $x_{1<t\leq4\,Gyr}$ from 23 % in E galaxies to 6 % in Sd galaxies.

- $x_{4\,Gyr<t\leq9\,Gyr}$: using STARLIGHT we also obtain similar values of $x_{4\,Gyr<t\leq9\,Gyr}$ for all the Hubble types, and with fractions similar to the outer regions. For the inner region, 23 % $< x_{4<t\leq9\,Gyr} <$ 32 %. For **M1**, the values of this component are larger than those obtained with STARLIGHT. For Sbc and earlier types, 39 % $< x_{4<t\leq9\,Gyr} <$ 48 %, and lower values are obtained for Sc, $x_{4<t\leq9\,Gyr} \sim 30$ % and Sd galaxies, $x_{4<t\leq9\,Gyr} \sim 27$ %. With **M6** this component increases from E to Sd galaxies, being lower for the outer region than for the inner one for Sc and earlier types and larger in the outer region for Sd galaxies. In particular, for E galaxies $x_{4\,Gyr<t\leq9\,Gyr} \sim 17$ % and for Sd, $x_{4\,Gyr<t\leq9\,Gyr} \sim 40$ %.

- $x_{t>9\,Gyr}$: for Sbc and earlier types we clearly find that the old component is larger in the inner regions than in the outer ones, for all the models. However, for Sc and Sd galaxies the light fraction obtained for the inner and outer regions are more similar, which is clear evidence of the inside-out growth of galaxies (Pérez et al., 2013; González Delgado et al.,

2015), at least for Sbc and earlier types. Another point of agreement between the models is that this component decrease from E to Sd galaxies. For E galaxies, $x_{t>9\,Gyr} \sim 59$ %, 38 % and 52 % for STARLIGHT, **M1** and **M6**, respectively. On the other hand, for Sd galaxies $x_{t>9\,Gyr} \sim 19$ %, 9 % and 15 %, respectively.

Mass fraction, μ: figure 6.14 shows that most of the stellar mass in galaxies formed very earlier, with very little mass in stars younger than 1 Gyr.

1. Outer regions $1 < R < 2$:

   - $\mu_{t\leq 1\,Gyr}$: in the outer region, the young component is $\leq 4\%$ for all the Hubble types using **M6**, being 0 % for E and S0 galaxies. Using STARLIGHT $\mu_{t\leq 1\,Gyr} \leq 4$ % for Sbc and earlier types and larger values are obtained for Sc, $\mu_{t\leq 1\,Gyr} \sim 11$ %, and Sd galaxies, $\mu_{t\leq 1\,Gyr} \sim 14$ %. On the other hand, using **M1**, $\mu_{t\leq 1\,Gyr} \leq 3$ % for Sb and earlier types and the fraction increases for Sbc, Sc and Sd galaxies, obtaining $\mu_{t\leq 1\,Gyr} \sim 7$ %, 10 % and 15 %.

   - $\mu_{1\,Gyr<t\leq 4\,Gyr}$: using STARLIGHT and **M6**, this component decreases from E to Sd galaxies. For E galaxies, $\mu_{1\,Gyr<t\leq 4\,Gyr} \sim 28$ % and 50 %, for STARLIGHT and **M6**, and for Sd galaxies $\mu_{1\,Gyr<t\leq 4\,Gyr} \sim 17$ % and 15 %, respectively. On the other hand, using **M1**, the mass fraction of this component decreases from 40 % in E galaxies to 17 % in Sd galaxies and increases again for later types, obtaining $\mu_{1\,Gyr<t\leq 4\,Gyr} \sim 25$ %, 28 % and 38 % for Sbc, Sc and Sd galaxies.

   - $\mu_{4\,Gyr<t\leq 9\,Gyr}$: using STARLIGHT and **M1** we find similar mass fraction of this component for all the Hubble types. For STARLIGHT, 28 % $\leq \mu_{1\,Gyr<t\leq 4\,Gyr} \leq 36$ %. Using **M1**, we obtain for Sc and earlier types, 46 % $\leq \mu_{1\,Gyr<t\leq 4\,Gyr} \leq 51$ %, while for Sd galaxies $\mu_{4<t\leq 9\,Gyr} \sim 35$ %. On the other hand, using **M6** the mass fraction increases from 27 % in E galaxies to 68 % in Sd.

   - $\mu_{t>9\,Gyr}$: for STARLIGHT, 43 % $\leq \mu_{t>9\,Gyr} \leq 48$ % for Sb and earlier Hubble types, and the mass fraction decreases for later types, obtaining $\mu_{t>9\,Gyr} \sim 38$ %, 37 % and 35 % for Sbc, Sc and Sd galaxies, respectively. Using **M1** and **M6** this component increases from E to Sb galaxies and decreases for later types. In particular, for **M1**, $\mu_{t>9\,Gyr} \sim 10$ % for E galaxies, 30 % for Sb and 12 % for Sd galaxies. Using **M6**, $\mu_{t>9\,Gyr} \sim 23$ % for E galaxies, 42 % for Sb and 14 % for Sd galaxies.

2. Inner regions $R < 0.5$:

   - $\mu_{t\leq 1\,Gyr}$: the mass fraction of the young component increases from E to Sd, although the fraction is lower in the inner regions than in the outer ones. Using STARLIGHT, $\mu_{t\leq 1\,Gyr} \leq 1$ % in Sbc and early types, and larger for Sc and Sd galaxies, obtaining $\mu_{t\leq 1\,Gyr} \sim 6$ % and 9 %, respectively. Using **M1**, $\mu_{t\leq 1\,Gyr} \leq 2$ % in Sbc and early types and again larger fractions are obtained for Sc and Sd galaxies, $\mu_{t\leq 1\,Gyr} \sim 7$ % and 6 %, respectively. For **M6**, larger fractions are again obtained for Sc and Sd galaxies, $\mu_{t\leq 1\,Gyr} \sim 2$ %, but the values are lower than those obtained with STARLIGHT and **M1**.

- $\mu_{1\,Gyr<t\leq4\,Gyr}$: on average, we obtain lower mass fractions of this component in the inner regions than in the outer one for all the Hubble types and all the models. Using STARLIGHT and **M1**, the mass fraction of this component increases from early to late type galaxies. For E galaxies, $\mu_{1\,Gyr<t\leq4\,Gyr} \sim 5$ % and 6 %, for STARLIGHT and **M1**, respectively. On the other hand, for Sd galaxies, $\mu_{1\,Gyr<t\leq4\,Gyr} \sim 19$ % and 22 %, respectively. Using **M6**, larger mass fractions are obtained for E, $\mu_{1\,Gyr<t\leq4\,Gyr} \sim 15$ %, and S0 galaxies, $\mu_{1\,Gyr<t\leq4\,Gyr} \sim 11$ % and remains almost constant, $\mu_{1\,Gyr<t\leq4\,Gyr} \sim 8$ % for later Hubble types.

- $\mu_{4\,Gyr<t\leq9\,Gyr}$: using STARLIGHT and **M1**, we obtain similar mass fractions of this component for all the Hubble types, as was found for the outer regions. For STARLIGHT, 20 % $\leq \mu_{4<t\leq9\,Gyr} \leq 30$ %. For **M1**, we obtain 38 % $\leq \mu_{4<t\leq9\,Gyr} \leq 46$ % for E, S0 and Sa galaxies; $\mu_{4<t\leq9\,Gyr} \sim 53$ % for Sb, Sbc and Sc; and $\mu_{4<t\leq9\,Gyr} \sim 52$ % for Sd galaxies. Using **M6** the mass fraction of this component increases from 19 % in E galaxies to 65 % in Sd galaxies.

- $\mu_{t>9\,Gyr}$: the old component decreases from E to Sd galaxies for all the models and is larger in the inner region than in the outer one. For E galaxies, $\mu_{t>9\,Gyr} \sim 74$ %, 48 % and 65 %, for STARLIGHT, **M1** and **M6**, respectively. On the other hand, for Sd galaxies, $\mu_{t>9\,Gyr} \sim 42$ %, 21 % and 25 %, respectively.

6.5.2   Parameters of the models

We have analysed the mean star formation histories by averaging the individual ones. As was done for the integrated results we compute the mean parameters for the different Hubble types, to obtain another approach to the results. Figures 6.15 and 6.16 show the mean parameters for **M1** and **M6**. Regarding results with **M1** (figure 6.15), we obtain clear correlation of τ with the Hubble type, for inner and outer region. In both cases, lower values are obtained for E and S0 galaxies and larger for Sc and Sd galaxies. In particular, for the inner region of E and S0 $\tau \sim 1.5$ Gyr and it increases to ~ 4.3 Gyr for Sd galaxies. For the outer region we obtain $\tau \sim 1.4$ Gyr for E and S0 and the largest mean value is obtained for Sc galaxies, with $\tau \sim 5.5$ Gyr. It indicates that the evolution of early type galaxies occurs faster than for later morphological types, in both structural components. Comparing the mean t_0 for the inner regions, we obtain similar values for Sbc and earlier types, and lower for Sc and Sd galaxies. On the other hand, the dispersion of t_0 for the outer region is larger, obtaining similar values for E, S0, Sc and Sd, with $t_0 \sim 9.5$ Gyr. For Sa, Sb and Sbc larger values are obtained. However, that doesn't mean that the envelope of E and disk of S0 grew at the same time as for Sc and Sd. It possible that they started to form the first stars at the same time, but the τ values indicate that the accretion of mass was faster in the envelope of E and disk of S0. The results are in agreement with those obtained for the integrated properties, showing a faster growth for E and S0 galaxies and a more extended period of star formation for later types, for both structural components.

STARLIGHT		$x_{t<1\,Gyr}$	$x_{1<t<4\,Gyr}$	$x_{4<t<9\,Gyr}$	$x_{t>9\,Gyr}$
	$R<0.5$	3 ± 11	13 ± 12	26 ± 20	59 ± 23
E	Galaxy	7 ± 11	23 ± 17	30 ± 19	40 ± 22
	$1<R<2$	5 ± 11	43 ± 21	24 ± 17	28 ± 23
	$R<0.5$	1 ± 1	14 ± 16	32 ± 21	54 ± 25
S0	Galaxy	4 ± 6	21 ± 20	31 ± 17	44 ± 22
	$1<R<2$	3 ± 4	38 ± 24	28 ± 15	31 ± 23
	$R<0.5$	4 ± 6	13 ± 14	27 ± 16	55 ± 20
Sa	Galaxy	8 ± 8	20 ± 13	30 ± 14	42 ± 19
	$1<R<2$	11 ± 16	32 ± 19	29 ± 15	28 ± 22
	$R<0.5$	5 ± 5	17 ± 19	23 ± 16	54 ± 25
Sb	Galaxy	11 ± 7	26 ± 15	31 ± 15	33 ± 18
	$1<R<2$	14 ± 14	37 ± 21	26 ± 13	23 ± 19
	$R<0.5$	10 ± 6	23 ± 14	27 ± 11	40 ± 18
Sbc	Galaxy	18 ± 9	29 ± 15	29 ± 12	23 ± 14
	$1<R<2$	25 ± 14	31 ± 17	26 ± 12	18 ± 12
	$R<0.5$	24 ± 18	26 ± 16	25 ± 16	25 ± 14
Sc	Galaxy	30 ± 15	26 ± 15	25 ± 13	19 ± 12
	$1<R<2$	34 ± 20	22 ± 18	26 ± 19	18 ± 15
	$R<0.5$	34 ± 17	26 ± 14	21 ± 14	19 ± 13
Sd	Galaxy	41 ± 21	20 ± 14	22 ± 11	17 ± 12
	$1<R<2$	42 ± 22	20 ± 18	21 ± 16	16 ± 16
		$\mu_{t<1\,Gyr}$	$\mu_{1<t<4\,Gyr}$	$\mu_{4<t<9\,Gyr}$	$\mu_{t>9\,Gyr}$
	$R<0.5$	1 ± 6	5 ± 6	20 ± 16	74 ± 21
E	Galaxy	1 ± 3	11 ± 11	30 ± 21	58 ± 25
	$1<R<2$	1 ± 3	28 ± 20	28 ± 20	44 ± 30
	$R<0.5$	1 ± 1	6 ± 11	25 ± 19	69 ± 22
S0	Galaxy	1 ± 1	10 ± 14	28 ± 18	61 ± 23
	$1<R<2$	1 ± 2	23 ± 22	28 ± 17	48 ± 27
	$R<0.5$	1 ± 1	5 ± 7	22 ± 14	73 ± 17
Sa	Galaxy	1 ± 1	9 ± 8	29 ± 16	61 ± 20
	$1<R<2$	4 ± 15	18 ± 16	33 ± 18	45 ± 27
	$R<0.5$	1 ± 1	8 ± 15	21 ± 16	71 ± 23
Sb	Galaxy	1 ± 1	12 ± 10	32 ± 17	54 ± 22
	$1<R<2$	3 ± 9	23 ± 17	32 ± 14	43 ± 25
	$R<0.5$	1 ± 1	9 ± 9	26 ± 13	64 ± 18
Sbc	Galaxy	2 ± 2	18 ± 14	35 ± 12	45 ± 19
	$1<R<2$	4 ± 5	22 ± 14	36 ± 13	38 ± 18
	$R<0.5$	6 ± 15	15 ± 11	29 ± 16	50 ± 19
Sc	Galaxy	7 ± 14	19 ± 16	33 ± 15	40 ± 20
	$1<R<2$	11 ± 20	18 ± 19	34 ± 20	37 ± 25
	$R<0.5$	9 ± 9	19 ± 15	30 ± 16	42 ± 19
Sd	Galaxy	13 ± 18	16 ± 14	34 ± 15	36 ± 19
	$1<R<2$	14 ± 19	17 ± 18	34 ± 20	35 ± 27

Table 6.2 Average light and mass fraction due to stars in different age ranges,, according to the Hubble type obtained with STARLIGHT.

M1 model		$x_{t<1\,Gyr}$	$x_{1<t<4\,Gyr}$	$x_{4<t<9\,Gyr}$	$x_{t>9\,Gyr}$
	$R < 0.5$	6 ± 6	10 ± 14	47 ± 24	38 ± 24
E	Galaxy	6 ± 9	21 ± 29	49 ± 28	24 ± 22
	$1 < R < 2$	4 ± 15	43 ± 20	46 ± 37	7 ± 16
	$R < 0.5$	5 ± 3	13 ± 21	40 ± 20	42 ± 21
S0	Galaxy	7 ± 5	19 ± 26	49 ± 26	25 ± 20
	$1 < R < 2$	5 ± 5	31 ± 36	46 ± 31	18 ± 21
	$R < 0.5$	10 ± 7	11 ± 6	39 ± 9	39 ± 16
Sa	Galaxy	15 ± 9	18 ± 13	45 ± 18	22 ± 15
	$1 < R < 2$	14 ± 11	31 ± 30	41 ± 25	13 ± 14
	$R < 0.5$	10 ± 7	14 ± 8	48 ± 17	286 ± 20
Sb	Galaxy	22 ± 9	20 ± 9	39 ± 14	19 ± 11
	$1 < R < 2$	20 ± 11	25 ± 19	39 ± 18	16 ± 11
	$R < 0.5$	19 ± 7	18 ± 6	41 ± 7	22 ± 14
Sbc	Galaxy	34 ± 10	26 ± 11	29 ± 8	11 ± 7
	$1 < R < 2$	36 ± 17	30 ± 18	27 ± 12	8 ± 6
	$R < 0.5$	36 ± 15	25 ± 4	30 ± 13	9 ± 9
Sc	Galaxy	40 ± 13	28 ± 12	23 ± 9	8 ± 8
	$1 < R < 2$	44 ± 13	28 ± 17	22 ± 12	6 ± 6
	$R < 0.5$	39 ± 14	25 ± 4	27 ± 10	9 ± 9
Sd	Galaxy	37 ± 15	29 ± 14	25 ± 14	10 ± 11
	$1 < R < 2$	40 ± 26	37 ± 17	18 ± 14	5 ± 6
		$\mu_{t<1\,Gyr}$	$\mu_{1<t<4\,Gyr}$	$\mu_{4<t<9\,Gyr}$	$\mu_{t>9\,Gyr}$
	$R < 0.5$	1 ± 1	6 ± 15	46 ± 27	48 ± 29
E	Galaxy	1 ± 1	17 ± 31	51 ± 30	32 ± 28
	$1 < R < 2$	3 ± 15	40 ± 42	48 ± 39	10 ± 21
	$R < 0.5$	1 ± 1	8 ± 22	38 ± 22	53 ± 25
S0	Galaxy	1 ± 1	14 ± 27	51 ± 28	35 ± 27
	$1 < R < 2$	1 ± 1	27 ± 38	48 ± 33	25 ± 28
	$R < 0.5$	1 ± 1	5 ± 4	41 ± 14	54 ± 18
Sa	Galaxy	1 ± 1	10 ± 13	53 ± 20	36 ± 21
	$1 < R < 2$	1 ± 1	25 ± 33	51 ± 27	22 ± 21
	$R < 0.5$	1 ± 1	7 ± 7	53 ± 22	39 ± 27
Sb	Galaxy	2 ± 2	12 ± 11	51 ± 16	34 ± 16
	$1 < R < 2$	2 ± 2	17 ± 22	51 ± 20	30 ± 17
	$R < 0.5$	2 ± 1	10 ± 5	53 ± 15	36 ± 20
Sbc	Galaxy	4 ± 2	20 ± 14	49 ± 10	27 ± 11
	$1 < R < 2$	7 ± 15	25 ± 21	48 ± 17	20 ± 12
	$R < 0.5$	7 ± 11	21 ± 9	53 ± 16	19 ± 15
Sc	Galaxy	6 ± 3	26 ± 17	46 ± 10	21 ± 12
	$1 < R < 2$	10 ± 11	28 ± 14	46 ± 15	17 ± 11
	$R < 0.5$	6 ± 3	22 ± 9	52 ± 7	21 ± 13
Sd	Galaxy	7 ± 4	28 ± 21	45 ± 15	21 ± 17
	$1 < R < 2$	15 ± 25	38 ± 21	35 ± 23	12 ± 12

Table 6.3 Average light and mass fraction due to stars in different age ranges, according to the Hubble type, obtained with **M1** model.

M6 model		$x_{t<1\,Gyr}$	$x_{1<t<4\,Gyr}$	$x_{4<t<9\,Gyr}$	$x_{t>9\,Gyr}$
	$R < 0.5$	8 ± 12	23 ± 21	17 ± 16	52 ± 21
E	Galaxy	9 ± 12	17 ± 16	17 ± 16	57 ± 28
	$1 < R < 2$	4 ± 9	56 ± 22	22 ± 18	18 ± 19
	$R < 0.5$	10 ± 17	16 ± 21	19 ± 20	56 ± 22
S0	Galaxy	8 ± 9	15 ± 16	31 ± 29	45 ± 23
	$1 < R < 2$	4 ± 4	39 ± 21	32 ± 30	24 ± 22
	$R < 0.5$	12 ± 13	11 ± 14	24 ± 25	53 ± 23
Sa	Galaxy	15 ± 16	16 ± 23	43 ± 25	27 ± 23
	$1 < R < 2$	15 ± 15	26 ± 19	30 ± 24	29 ± 21
	$R < 0.5$	10 ± 13	12 ± 16	27 ± 22	51 ± 26
Sb	Galaxy	21 ± 18	13 ± 23	37 ± 24	29 ± 21
	$1 < R < 2$	25 ± 18	16 ± 26	30 ± 21	30 ± 33
	$R < 0.5$	21 ± 15	7 ± 17	26 ± 28	46 ± 25
Sbc	Galaxy	29 ± 13	8 ± 20	43 ± 30	19 ± 28
	$1 < R < 2$	33 ± 15	11 ± 22	38 ± 27	17 ± 29
	$R < 0.5$	29 ± 15	7 ± 17	37 ± 20	26 ± 23
Sc	Galaxy	35 ± 12	7 ± 14	46 ± 24	13 ± 24
	$1 < R < 2$	38 ± 13	9 ± 20	40 ± 25	12 ± 22
	$R < 0.5$	39 ± 13	6 ± 13	40 ± 25	15 ± 24
Sd	Galaxy	38 ± 13	12 ± 18	40 ± 23	11 ± 22
	$1 < R < 2$	41 ± 14	13 ± 23	37 ± 22	9 ± 19
		$\mu_{t<1\,Gyr}$	$\mu_{1<t<4\,Gyr}$	$\mu_{4<t<9\,Gyr}$	$\mu_{t>9\,Gyr}$
	$R < 0.5$	1 ± 3	15 ± 20	19 ± 22	65 ± 24
E	Galaxy	1 ± 1	11 ± 17	20 ± 21	69 ± 28
	$1 < R < 2$	1 ± 1	50 ± 21	27 ± 2	23 ± 23
	$R < 0.5$	1 ± 4	11 ± 20	22 ± 28	66 ± 25
S0	Galaxy	1 ± 1	9 ± 12	35 ± 26	55 ± 28
	$1 < R < 2$	1 ± 1	33 ± 29	40 ± 32	30 ± 26
	$R < 0.5$	1 ± 1	7 ± 15	28 ± 23	64 ± 27
Sa	Galaxy	1 ± 4	14 ± 22	49 ± 20	36 ± 21
	$1 < R < 2$	1 ± 2	23 ± 28	37 ± 21	39 ± 29
	$R < 0.5$	1 ± 1	8 ± 14	30 ± 27	61 ± 20
Sb	Galaxy	2 ± 5	11 ± 21	47 ± 20	40 ± 21
	$1 < R < 2$	1 ± 2	15 ± 26	42 ± 20	42 ± 24
	$R < 0.5$	1 ± 1	7 ± 19	34 ± 29	58 ± 22
Sbc	Galaxy	2 ± 3	8 ± 21	62 ± 21	28 ± 20
	$1 < R < 2$	2 ± 2	12 ± 26	61 ± 21	25 ± 23
	$R < 0.5$	2 ± 8	9 ± 21	54 ± 21	35 ± 22
Sc	Galaxy	2 ± 3	8 ± 17	71 ± 25	19 ± 24
	$1 < R < 2$	3 ± 10	11 ± 24	66 ± 28	20 ± 25
	$R < 0.5$	2 ± 3	8 ± 19	65 ± 27	25 ± 27
Sd	Galaxy	3 ± 7	14 ± 23	67 ± 26	16 ± 22
	$1 < R < 2$	3 ± 4	15 ± 26	68 ± 25	14 ± 29

Table 6.4 Average light and mass fraction due to stars in different age ranges, according to the Hubble type, obtained with **M6** model.
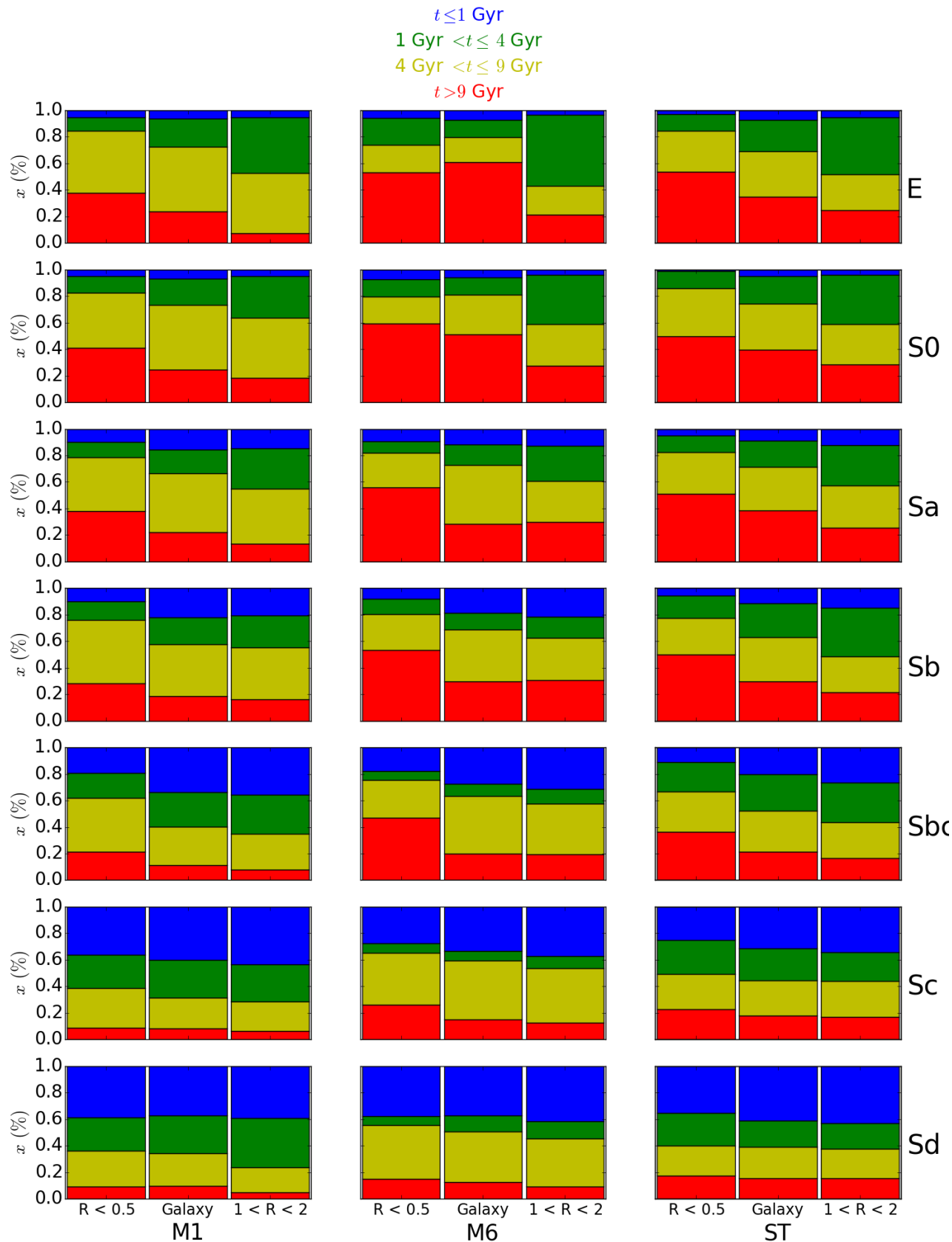
Figure 6.13 Average light fractions due to stars in different age ranges, according the Hubble type. Age (lookback time) ranges are colour-coded: old, intermediate and young populations are defined as those with $age \geq 9$ Gyr (red), 4 Gyr $< age < 9$ Gyr (yellow), 1 Gyr $< age < 4$ Gyr (green), and $age \leq 1$ Gyr (blue), respectively. The averaged values are presented for different galaxy regions: the inner region $R < 0.5$ HLR (left bar); the whole galaxy $R < 2$ HLR (middle bar); and the outer region $1 < R < 2$ HLR (right bar). The columns show the results for **M1**, **M6** and STARLIGHT.

Figure 6.14 Same as figure 6.13 for the mass fraction.

In summary:

1. Sbc and earlier type galaxies start to form at the same epoch ~ 12 Gyr ago.

2. Envelope of E and S0 start to form at later epoch than outer regions in Sa, Sb and Sbc.

3. Sc and Sd galaxies start to form later than earlier types, but at $t_0 > 10Gyr$. Their envelopes form later on.
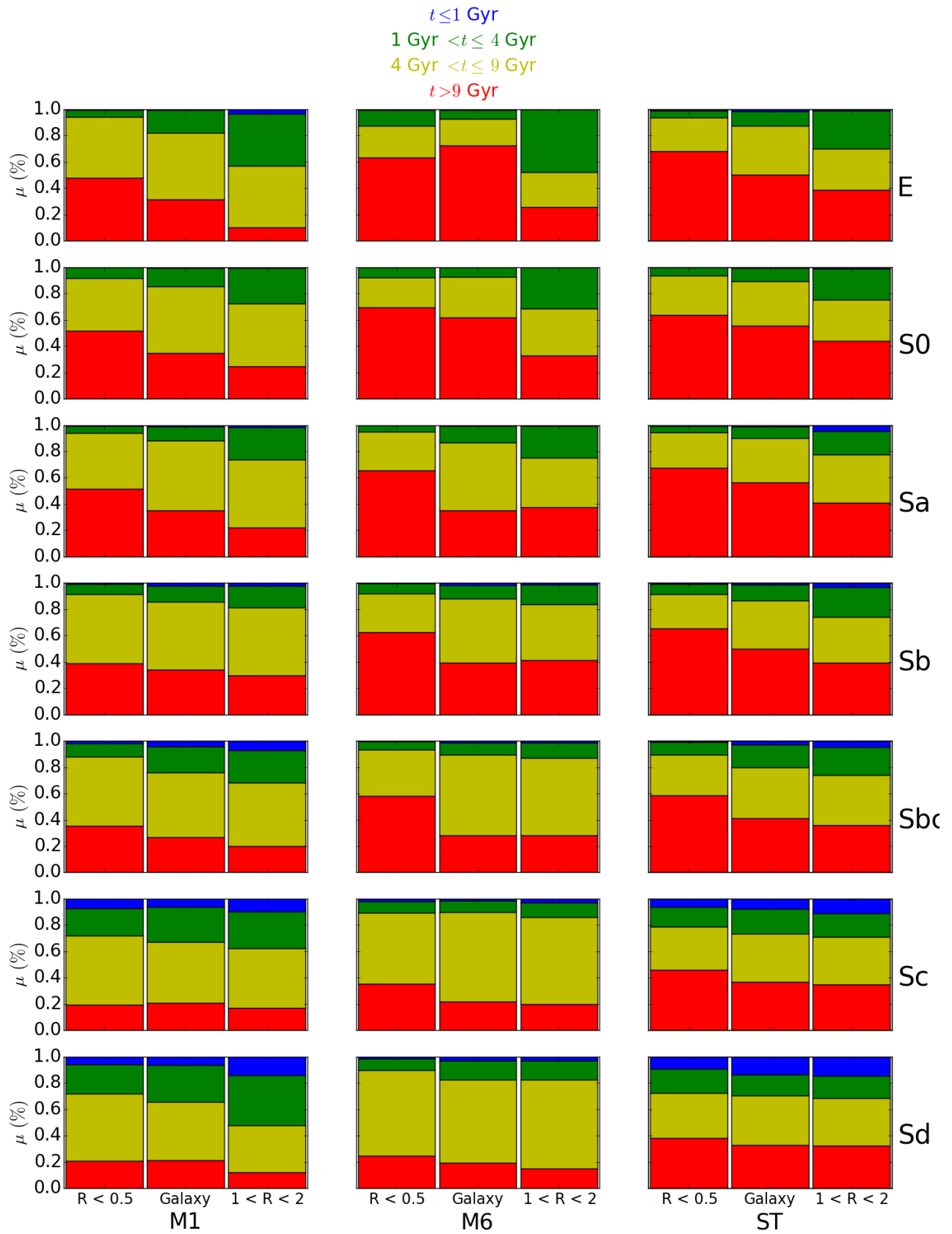
4. Because $t_0(R < 0.5) > t_0(1 < R < 2)$, galaxies form inside-out.

5. τ increases in the inner and outer region with the Hubble type, with more extended period of star formation in late type spirals.

6. In spirals, $\tau(R < 0.5) < \tau(1 < R < 2)$, indicating that the period of star formation is more extended in the outer parts.

7. τ is similar in the inner and outer regions.
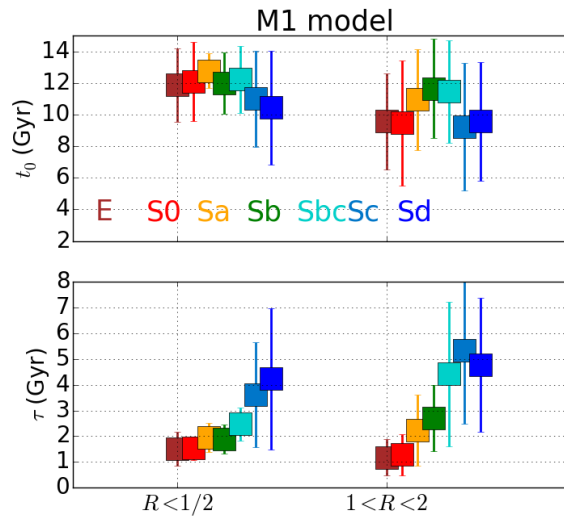
Figure 6.15 Mean parameters for model **M1**: t_0 and τ. The left column shows the result for the inner region $(R < 0.5)$ and the right column for the outer one $(1 < R < 2)$. The different Hubble types are colour-coded.

Figure 6.16 shows the mean parameters for **M6**, for both the inner and outer regions. The first and second panels show the parameters of the old component, while the third and fourth the parameters of the young component, t_0 and τ, respectively. The last panel indicates the mass fraction of the old component with respect to the younger one. On the left we show the results for the inner region and on the right for the outer one.

Regarding the last panel, we find that the old component accounts for almost the total mass of galaxies for all the Hubble types. Lower mean values are obtained for Sb galaxies, but larger than 90
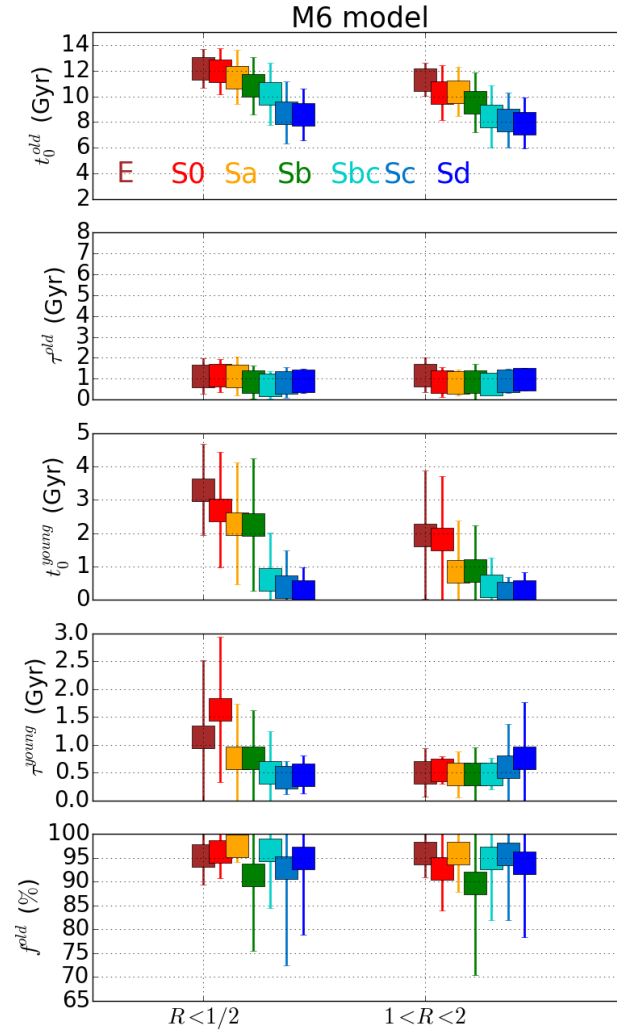
Figure 6.16 Mean parameters for **M6** model: t_0^{old}, τ^{old}, t_0^{young}, τ^{young} and f^{old}. The left column shows the result for the inner region ($R < 0.5$) and the right column for the outer one ($1 < R < 2$). The different Hubble types are colour-coded.

%. A clear correlation is obtained between t_0^{old} and the Hubble type, with larger values for the inner region

of E and S0, $t_0^{old} \sim 12$ Gyr. For the bulge of Sc and Sd galaxies we obtain $t_0^{old} \sim 8.8$ Gyr. The same correlation is obtained for the outer regions although with slightly lower values. On the other hand, this trend is not observed for τ^{old}, obtaining similar values for all the Hubble types. For the young component, the same correlation between t_0 and the morphology is obtained, although in this case the error bars indicate a larger uncertainties. The rejuvenation period represented for this component occurred 3 Gyr ago for the inner region in E galaxies and in the last 0.5 Gyr for Sd. On the other hand, for the outer region this period began 2 Gyr ago for E and S0 galaxies and in the last 0.5 for Sc

and Sd. Because the mass fraction of the young component accounts for less than 10 % on average, the results obtained with **M6** suggest again that both the inner and outer regions for early type galaxies formed the total mass earlier in the past than later types. In summary:

1. Sbc and earlier type galaxies start to form at $t_0^{old} > 10$ Gyr, with Sa, Sb and Sbc later than E and S0.

2. Sc and Sd galaxies start to form later than earlier types, at $t_0^{old} \sim 9 Gyr$. Their envelopes form later, at $t_0^{old} \sim 8 Gyr$

3. Envelope of E start to form at an earlier epoch than S0, Sa and Sb. Envelope in later spirals form later.

4. Because $t_0^{old}(R < 0.5) > t_0^{old}(1 < R < 2)$, galaxies form inside-out.

5. τ^{old} is similar for all the morphological types, less than 2 Gyr.

6. t_0^{young} changes with morphology, with the epoch of star formation being earlier in early type galaxies than in late type spirals. For Sb and earlier types, t_0^{young} is larger in the inner region than in the outer one. For Sbc, Sc and Sd t_0^{young} is similar in the inner and outer region.

7. τ^{young} decreases with morphology in the inner region and remains almost constant in the outer one.

8. While the larger fraction of the mass formed between 12 and 8 Gyr ago, the young component accounts for less than 10% of the mass and occurs from 3 Gyr (E) to now (Sd).

6.5.3 The mass assembly in galaxies

Models of galaxy formation predict a common inside-out view of the mass assembly (Kauffmann et al., 1993; Aumer & White, 2013). First, the bulge formed at high redshift; then, the disk was built around the bulge in the case of spirals. In the case of ellipticals, the central core formed at z≥2, and the envelope grew later through minor mergers (Oser et al., 2010; Hilz et al., 2013). Previous works with CALIFA data (Pérez et al., 2013; González Delgado et al., 2014b,a, 2015), deriving spatially resolved information on the mass growth of galaxies and stellar population properties, also point to an inside-out scenario for the formation of galaxies. For Sc and Sd galaxies this view of the mass assembly is not so clear. For late spirals, our results indicate that inner and outer regions have grow at the same time, in a similar period of time, which is also more recently found by van Dokkum et al. (2014). They find evidence against the inside-out formation scenario for spirals, analysing a sample of MW-like spirals at redshift z = 2.5. They conclude that the mass growth took place in a fairly uniform way, with the galaxies increasing their mass at all radii. These results also seem to be supported by numerical simulation by Elmegreen et al. (2008), which finds that bulges can be formed by migration of unstable disks. Other observational evidence comes from the detection of clumpy star-forming disks in galaxies at z ∼ 2 (Genzel et al., 2008; Förster Schreiber et al., 2011), which may indicate an early build-up of bulges by secular evolution.

As was done for the integrated results, we compute t_{80} as the age at which 80% of the total mass is reached (figure 6.17), and also the fraction of the total mass reached at $z = 1$ (figure 6.18). These quantities are shown for the inner and outer regions and for the different morphological types. The top panels in both figures show the results for the inner region and bottom panel for the outer one. On the left the results for **M1** are represented, in the middle for **M6** and on the right for STARLIGHT.

1. Inner regions:

   - With **M1**, t_{80} decreases with Hubble type, with E, S0, and Sa having similar values, $t_{80} \sim$ 9-8 Gyr, and obtaining for Sc and Sd $t_{80} \sim 5$ Gyr.

   - The results with STARLIGHT are very similar to with **M1**, decreasing t_{80} from early type galaxies to late types. For Sb and earlier types, $t_{80} \sim$ 8-9 Gyr. For Sc, $t_{80} \sim 5$ Gyr, and for Sd $t_{80} \sim 4$ Gyr, slighly lower than for **M1**. So, the range of variation of t_{80} is higher than with **M1**.

   - **M6** presents larger values of t_{80} for all the Hubble types and a clearer correlation is observed, decreasing the values from E galaxies, $t_{80} \sim 11$ Gyr, to Sd galaxies, $t_{80} \sim 7$ Gyr. These results point to a faster formation of galaxies with model **M6**.

2. Outer regions:

   - Using **M1** we again find that t_{80} decreases with the morphology. The values for the outer regions are lower than for the inner ones for Sc and earlier types. For Sb and earlier types $t_{80} \sim$ 6-7 Gyr, and for Sd galaxies $t_{80} \sim 5$ Gyr, which is similar to the value for the inner region.

   - With STARLIGHT t_{80} again, decreases with the Hubble type, from $t_{80} \sim$ 5-6 Gry for Sa and later types to $t_{80} \sim 4$ Gry for Sd galaxies. Thus the range of variation is lower than that obtained with **M1**.

   - With **M6** the same correlation for the inner regions is obtained as for the outer ones, although the values are lower. With this model, t_{80} decreases from $t_{80} \sim$ 9-10 Gry for Sa and earlier types to $t_{80} \sim 6$ Gry for Sd galaxies.

Thus, the outer regions span their star formation for a longer period of time than inner ones, reaching 80% of the total mass more recently. However, for Sc and Sd galaxies, the results with STARLIGHT and **M1** indicate a similar period for both structural components, with similar values of t_{80}. Figure 6.18 shows the mass fraction at $z = 1$. From this figure we obtain:

1. Inner regions:

   - With **M1** $f_{z=1} \sim 0.8$ for E, S0 and Sa galaxies, and decreasing for later types, obtaining $f_{z=1} \sim 0.5$ for Sd galaxies.

   - Using STARLIGHT $f_{z=1}$ also decreases with the Hubble type, but the range of variation is lower than with **M1**. For Sb and earlier types $f_{z=1} \sim 0.8$ and for Sd galaxies $f_{z=1} \sim 0.6$

- For **M6**, values of $f_{z=1}$ for Sbc and earlier types are higher than those obtained with STARLIGHT and **M1**. For E galaxies $f_{z=1} \sim 0.9$ and for Sbc $f_{z=1} \sim 0.8$. The values of $f_{z=1}$ for Sc an Sd galaxies are similar with the three models.

Figure 6.17 Mean t_{80} value for **M1**, **M6** and STARLIGHT. Top panel shows the results for the inner regions ($R < 0.5$) and bottom panel for the outer one ($1 < R < 2$). The Hubble types are colour-coded.

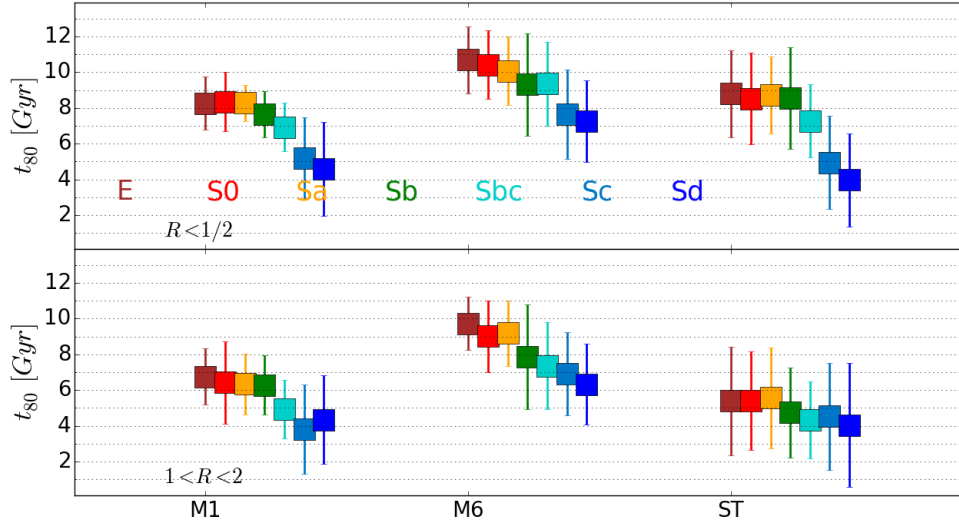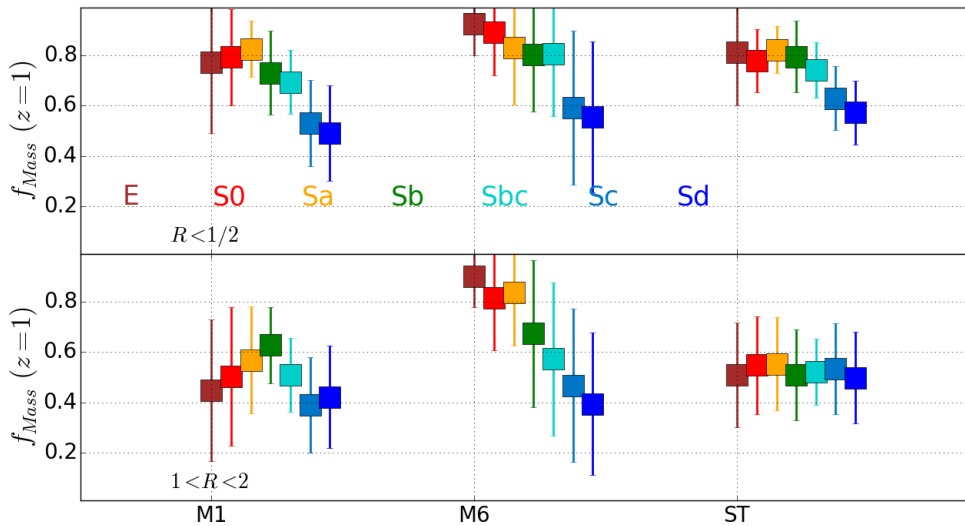Figure 6.18 Mean f_{Mass} at $z = 1$, defined as the mass fraction reached at $z = 1$. The columns show the results for **M1**, **M6** and STARLIGHT. The top panel shows the results for the inner regions ($R < 0.5$) and bottom panel for the outer one ($1 < R < 2$). The Hubble types are colour-coded.

2. Outer regions:

- Using **M1** we obtain different behaviour for the outer regions from that the observed for the inner regions. $f_{z=1}$ increases from $f_{z=1} \sim 0.4$ for E galaxies to $f_{z=1} \sim 0.6$ for Sb galaxies and then $f_{z=1}$ decreases for late type spirals, obtaining for Sc and Sd galaxies $f_{z=1} \sim 0.4$. The values for the outer regions are lower than those obtained for the inner regions, indicating that at $z = 1$ the inner regions were more evolved than the outer ones.

- With STARLIGHT we obtain an almost constant $f_{z=1}$. For all the Hubble types, $f_{z=1} \sim 0.5$, which is lower than the mass fraction obtained for the inner regions for all the Hubble types.

- A clear correlation with the Hubble type is again obtained for the outer regions with **M6**. For E galaxies $f_{z=1} \sim 0.9$, while $f_{z=1} \sim 0.4$ for Sd galaxies. For E and Sa galaxies, $f_{z=1}$ in the inner and outer regions are similar, but for the other Hubble types, lower values of $f_{z=1}$ are obtained in the outer regions.

The results indicate that for all the Hubble types, the inner regions were more evolved at $z = 1$ than outer regions, although the mass fraction reached at $z = 1$ in the bulge and disk in Sc and Sd galaxies is more similar than in earlier type galaxies for all the models.

7

The evolution of the Star Formation Rate

Contents

7.1 Introduction

In the previous chapter we presented a parametric method to derive the stellar population properties of galaxies. We have analysed both the quality of fits, in terms of $\chi 2$, as well as the agreement between the results provided by the different parametric models and those derived with STARLIGHT. In this chapter we focus on the evolution process of galaxies.

On the one hand, galaxies are stacked according to morphological type and mass. This method lets us compare the results involving the SFR, the growth of mass and the sSFR derived with the different models for the different galaxies.

On the other hand, from the SFH, we derive the properties of galaxies as a whole. In particular we compute the star formation rate density (ρ_{SFR}), the mass density (ρ_{Mass}) and also the evolution of $sSFR$ with redshift. Theses quantities have been widely studied and we compare our results with other values from the literature, coming from different surveys and methods. A suitable and realistic parametric SFH model has to provide consistent ρ_{SFR}, ρ_{Mass} and $sSFR$ values. On the other hand, if the obtained values vary significantly from the expected ones, it is an insight that the parametric model is not appropriate. In section 7.7 we present the collection of figures showing the results for the different models.

7.2 Volume corrections for the CALIFA sample.

In this chapter we use the CALIFA data to generalize some results such as the star formation rate density or the mass density. For this purpose, it is necessary to compute an accessible volume per CALIFA galaxy. In this section we explain how this is done.

The CALIFA sample is not a purely volume-limited sample, but can be "volume-corrected" to reconstruct sample averages and distribution functions that are statistically equivalent to those of a volume-limited sample. The CALIFA sample has three principal selection criteria:

1. Limits in right ascension α and declination δ, from the SDSS DR7, plus the additional condition

$$\delta > 7 \text{ only for } 9^{\text{h}} < \alpha < 18^{h}$$

2. A redshift range:

$$0.005 < z < 0.03$$

3. A minimum and a maximum apparent isophotal diameter, using the **isoA_r** value provided by the SDSS photometric catalogue:

$$45'' < \textbf{isoA\_r} < 80''$$

To compute a volume correction it is necessary to know the solid angle Ω_C for the CALIFA sample. From the first selection criteria, a rough estimate is that this number should be around $\Omega_C \approx 2$ steradians. The fraction f of galaxies with IFU data is not the whole mother sample, so we can adopt an "effective" solid angle as $\Omega_{eff} = f \times \Omega_C$. For the sample of this thesis, where 366 galaxies are used, we obtain $f = 366/937 \approx 0.391$, thus $\Omega_{eff} \approx 0.782$.

Using Hubble's law to convert redshift to distance ($d = zc/H_0$) we can convert a redshift range into a volume as follows:

$$V = \frac{\Omega_{eff}}{3} \times \left[\frac{c}{H_0} \right]^3 \left(z_2^3 - z_1^3 \right), \tag{7.1}$$

where z_1 and z_2 are the survey redshift limits. In our case $z_1 = 0.005$ and $z_2 = 0.03$, thus $V \sim 596749$ Mpc^3.

We focus now on the real volume correction that differs from galaxy to galaxy, which doesn't occur in a volume-limited sample. For a galaxy of intrinsic diameter D at a distance $d = cz/H_0$, the apparent angular diameter is $\theta = D/d$. The third selection criteria set a minimum θ_{min} so that, if a galaxy verifies $\theta > \theta_{min}$ and is moved to a larger distance, it would stay in the sample until $\theta = \theta_{min}$. On the other hand, if a galaxy verifies $\theta < \theta_{max}$ and is moved to a closer distance, it would stay in the sample until $\theta = \theta_{max}$. We can then compute the redshift range for an object of the same intrinsic diameter to be part of the sample:

$$z_{max} = min(z \times \theta/\theta_{min} \, , \, 0.03))$$

$$z_{min} = max(z \times \theta/\theta_{max} \, , \, 0.005))$$

Thus, to obtain the "accessible volume" V_a for each galaxy we replace z_{min} and z_{max} in equation 7.1.

We use this method to extend our results for galaxies as a whole. In particular, we transform our SFR and mass estimate into the volume density of SFR, ρ_{SFR}, and mass density, ρ_{Mass} by adding SFR/Va and $M_\star/V_a$.

7.3   Model M1

In this section we present the results related to the SFH of galaxies obtained with model M1, both the integrated properties and also spatially resolved ($R < 0.5$ HLR and $1 < R < 2$ HLR). The analysed properties are: SFR ($M_\odot yr^{-1}$), CMF, $sSFR$ (Gyr^{-1}), ρ_{SFR} ($M_\odot yr^{-1} Mpc^{-3}$) and ρ_{Mass} ($M_\odot Mpc^{-3}$). Hereafter, we omit the units when describing each one of the properties for a clearer reading.

7.3.1   Integrated properties: Star formation rate and cumulative mass fraction

The top left panel and middle left panel in Figure 7.1 show the evolution of SFR and cumulative in lookbacktime, respectively, obtained with model **M1**. This SFR measures the rate at which the gas is transforming into stars or galaxies are growing their mass. We show the results stacking galaxies according to morphological type but also according to mass (Figure 7.2).
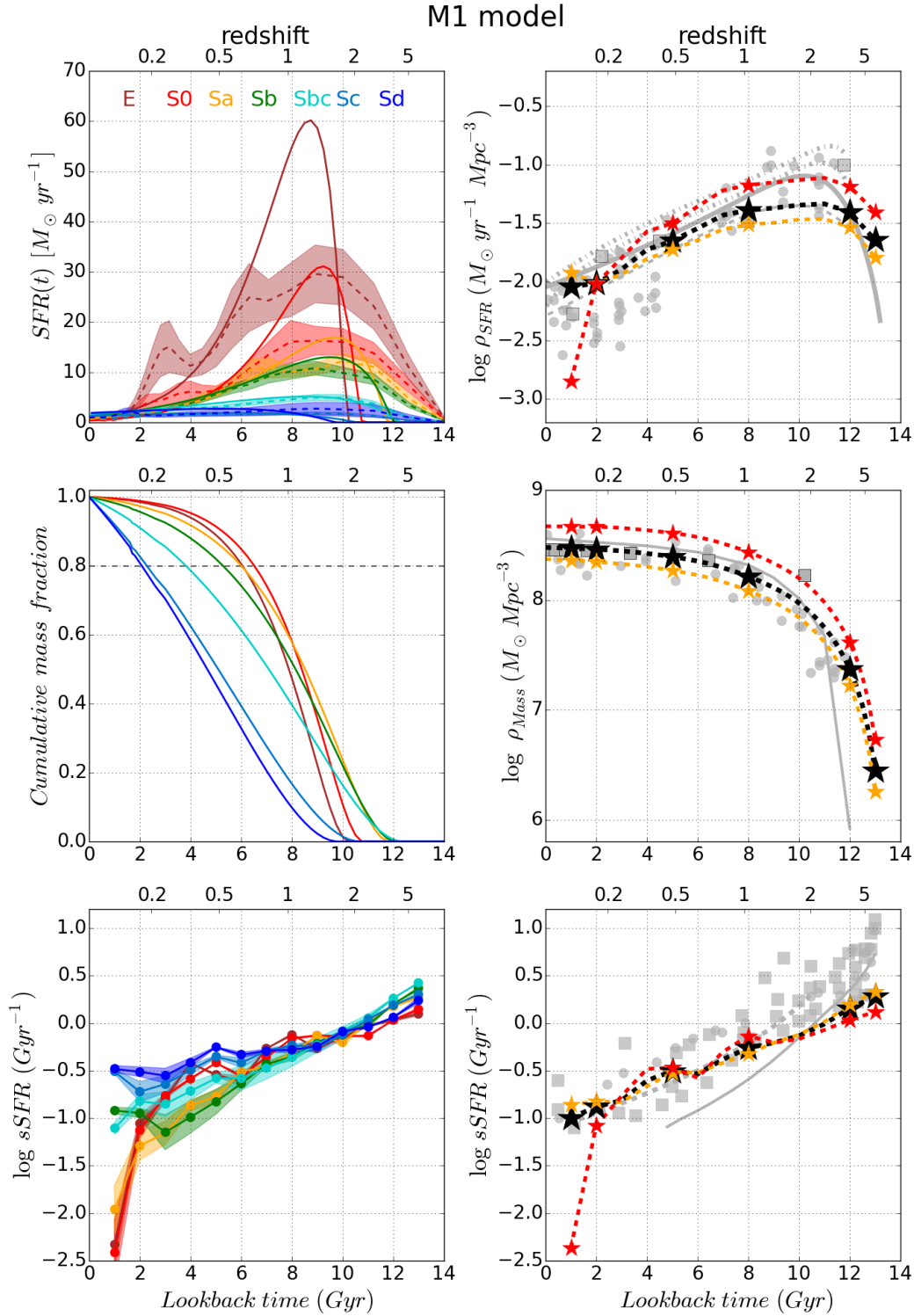
Figure 7.1 Top left: The star formation rate, by averaging the mean parameters (solid lines) and by averaging the SFR for the individual galaxies (dashed line), for the different morphological types obtained with model **M1**. Shaded regions indicate the dispersion. Top right: The evolution of star formation rate density with redshift. Middle left: The cumulative mass fraction curves for the different morphological types. Middle right: The evolution of mass density with redshift. Bottom left: The specific star formation rate for the different morphological types and the dispersion. Bottom right: The specific star formation rate for the whole sample. In the three right panels the grey values represent measurements from the literature. Black lines show the result for the whole sample in this thesis. Red lines show the results considering only ellipticals and S0 galaxies while orange lines show the result considering late-type spirals.

The SFR is computed by averaging the parameters of the SFH and the stellar mass for the different morphological types or mass bin (solid lines). In the figures we also show the results by averaging the individual SFR for the different galaxies (dashed lines) and the dispersion (shaded regions). This comparison is done to show that the results are quite different, and depending on the goal of the study one or another approximation would be more convenient. In this chapter we analyze the SFR using the averaged parameters.

Sa, Sb and Sbc galaxies show t_0 values (11.7, 11.9 and 12.05 Gyr respectively) larger than E and S0 galaxies ($t_0 = 10.2$ and 10.6 Gyr, respectively), but larger τ values indicating a more extended growth. For Sa, Sb and Sbc we obtain $\tau = 2.0$, 2.5 and 3.7 Gyr, respectively, while $\tau = 1.4$ and 1.5 Gyr for E and S0, respectively. On the other hand for Sc and Sd galaxies we obtain more extended star formation histories with larger values for the τ parameter. Also we observe that the absolute SFR correlates with the Hubble type, obtaining the highest values for E galaxies. The cumulative mass fraction curves (middle right panel in Figure 7.1) show that E and S0, although with lower t_0 than Sa, Sb and Sbc galaxies, has growth more rapidly.

Stacking galaxies in different mass bins, and comparing the SFR and cumulative mass fraction curves for the different masses (figure 7.2), we find that massive galaxies show a SFR that declines rapidly and also have the highest absolute values. Downsizing is clearly observed in CMF curves, with more massive galaxies forming their mass earlier. This suggests that mass is one driver of galaxy evolution, obtaining different properties for galaxies with different masses, but also the morphology, obtaining larger differences in the stellar properties among the different Hubble type than for the different mass bins.
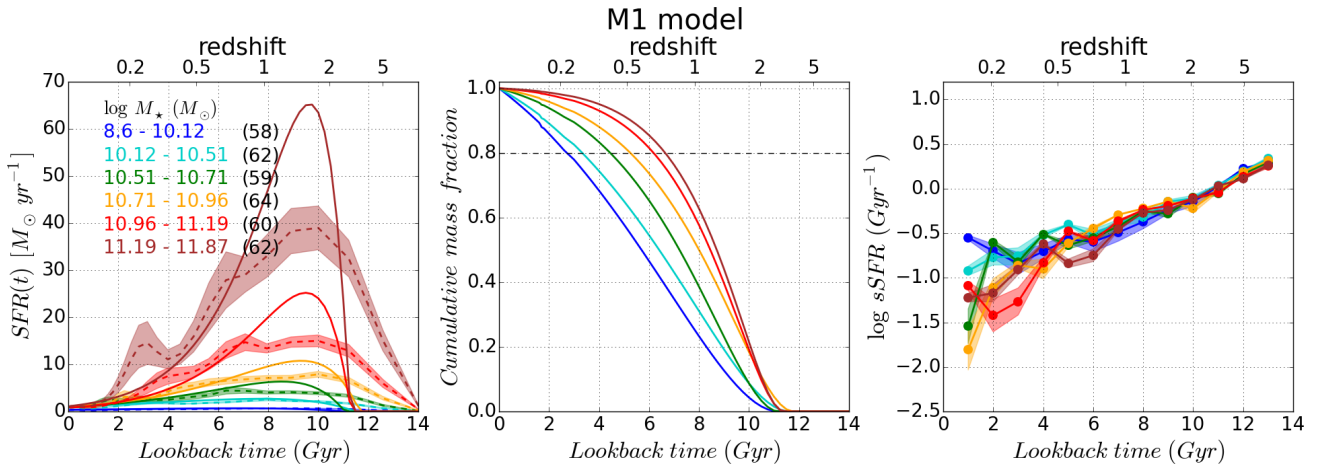
Figure 7.2 The panels are the same as the left panels in Figure 7.1, stacking galaxies in mass bins.

7.3.2 Integrated properties: Star formation rate density

The ρ_{SFR} is a powerful tool for investigating the cosmic star formation history. The ρ_{SFR} is usually derived from a mean luminosity density, defined as LD $= \int_0^\infty \phi(L)L \, dL$, with $\phi(L)$ being the Luminosity Function (LF) and L a luminosity related to the SFR. Because of the number of uncertainties that remain along the chain of transformations to be applied to galaxy counts and luminosities to be

converted into star formation rates, the exact shape of the ρ_{SFR} evolution is still uncertain in several aspects. The selection function of each galaxy sample, including the imaging surveys depth and image quality or the redshift completeness, requires a number of corrections to compute volume densities, and the complete shape of the luminosity function remains speculative, particularly at the faint end. Moreover, the transformation of luminosities to SFR depends on assumptions on the conversion factors and on the amount of dust attenuation. However, the various data from different samples have persistently shown a broad picture consistent within a rise from z=0 to z $\simeq$ 1 and a decline from z $\simeq$ 3 to z= inf, with an unclear evolution within $1 \lesssim$ z $\lesssim$ 2. From the present day to z $\simeq$ 1 a steady rise of the SFRD by one order of magnitude is firmly corroborated using various calibrators of SFR - like far ultraviolet (FUV), far infrared (FIR), Hα and radio - but the scatter among different measurements remains large.

The top right panel in Figure 7.1 shows the evolution of ρ_{SFR} with redshift. The black curve shows the results for the whole sample studied in this thesis. The red curve is computed taking into account only elliptical and S0 galaxies while the orange curve is computed taking into account Sa and later spiral galaxies. To compute the red and orange curves we need to correct the effective solid angle $\Omega_{eff} = \overline{f} \times \Omega_C$. For late type f=264/937, while for early type f=102/937. The time resolution in the curves is one Gyr, but we highlight the values at 1, 2, 5, 8, 12 and 13 Gyr with stars. The grey values show different measurement from the literature: Madau & Dickinson (2014) (solid line); Fardal et al. (2007) (dashed line); Hopkins & Beacom (2006) (dash-dot lines, $\pm 1\sigma$); Gunawardhana et al. (2013) Figure 14 (circles); Panter et al. (2003) (squares). The values of Madau & Dickinson (2014) have been scaled to a Chabrier IMF.

Using model **M1** the curve matches very well with the curve of Fardal et al. (2007). We obtain a peak of ρ_{SFR} at $z \sim 2$, as the other values from literature show. Compared to the curve of Madau & Dickinson (2014), our curve is similar from $z = 0$ to $z = 1$. The peak of the ρ_{SFR} occurs at the same epoch, but our curve remains 0.3 dex below. Besides the Fardal et al. (2007) curve, our curve is also in agreement with some values from Gunawardhana et al. (2013). On the other hand, the red curve reaches the peak of the Madau & Dickinson (2014) curve, which could indicate that progenitors of these early type galaxies were those that dominated the ρ_{SFR} at $z = 2$. In contrast, in the local Universe we obtain that spirals dominate the ρ_{SFR} budget. This is in agreement with González Delgado et al. (2016). They obtain that the majority of the star formation at z = 0 takes place in Sbc, Sc, and Sd galaxies with masses below $10^{11} M_\odot$. The differences observed at high redshift are mainly due to differences in timescales between redshift studies and our measurements. A time scale lower than a few Gyr is not possible for lookback time > 4 Gyr due to limitations of the stellar evolution. On the other hand, redshift studies achieve the measurement of the star formation in time scales $\leq 10^8$ yr, using H$_\alpha$, UV or FIR emission. So, our measurements of the SFR are time averaged for a significantly longer period than in redshift studies.

7.3.3 Integrated properties: The global main sequence of star-forming galaxies

The main sequence of star-forming galaxies (MSSF) is the name given to the correlation between SFR and $M_\star$ (Noeske et al. 2007), which has been found in star-forming galaxies of the local Universe

(Brinchmann et al. 2004) and seen to persist at least to redshift ~ 4 (Peng et al., 2010; Wuyts et al., 2011). The logarithmic slope of the relation varies in the range from 0.4 to 1, depending on the galaxy selection criteria and on the indicator used to estimate the SFR (Speagle et al. 2014).

Figure 7.3 shows the log SFR vs. log $M_\star$ relation obtained with **M1** for different redshift. In our case, for large redshift, we obtain an almost linear relation due to our methodology. The dashed grey-blue lines in all panels show log $SFR = a \log M_\star + b$ fits obtained for Sc galaxies. For the local Universe, at z=0, we obtain $a = 0.66$ and $b = -6.58$. These values are similar to those obtained by Renzini & Peng (2015) for the whole SDSS sample and González Delgado et al. (2016). This coincidence is not surprising because Sc and Sbc are the galaxies that contribute the most to the local star formation rate density, which are the ones that produce the ridge line in the MSSF relation.
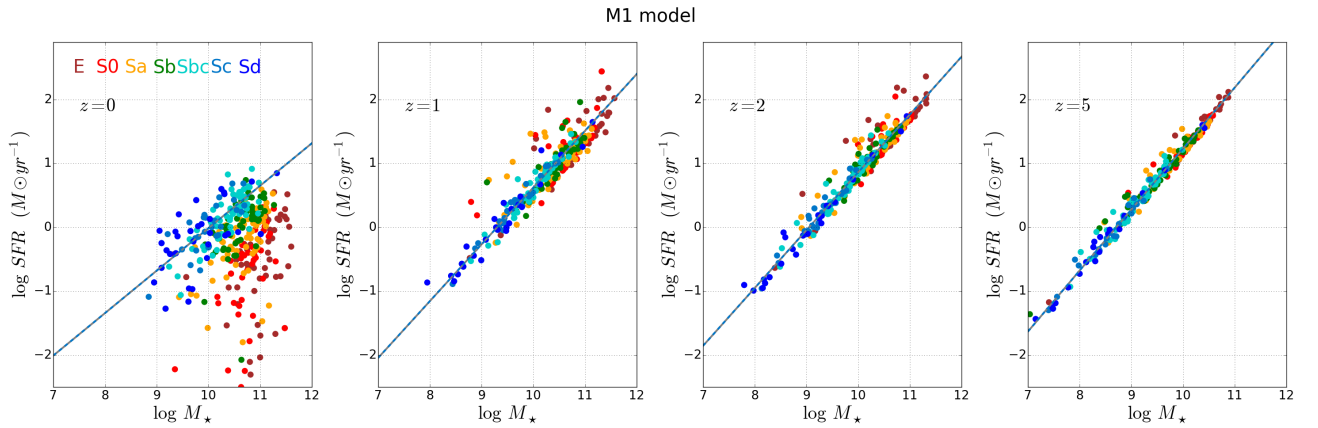
Figure 7.3 Relation between SFR and stellar mass, colour coded by Hubble type. A linear fit to the points of Sc galaxies is shown as a gray-blue dashed line. Different panels show the relation at different redshift.

The spread in SFR at fixed $M_\star$ is related to galaxy morphology and the bending in the main sequence is produced by the inclusion of large bulges, such as those in Sa and S0, and also E, where the star formation is already quenched or in the process of being quenched. These galaxies (Sa, S0, and E) are on average the most massive ones in our sample, but they contribute little to the cosmic star formation, because they are clearly below the MSSF.

7.3.4 Integrated properties: Mass density

The ρ_{Mass} is another key observable for testing galaxy evolution. This observable allows for a more direct and robust test of theoretical models than the ρ_{SFR}, since luminosities are more difficult to predict than $M_\star$ because of effects such as the age and metallicity of the stellar population, the dust content of the interstellar medium, etc. Most determinations of the ρ_{SFR} appears to have a flat slope from the present day to z $\simeq 1$, while for z $\gtrsim 1$ the stellar mass density steepens with z.

The middle right panel in Figure 7.1 shows the evolution ρ_{Mass} with redshift. The black curve represents the results for the whole sample. The red curve is computed taking into account only elliptical and S0 galaxies while the orange curve is computed taking into account Sa and later spiral galaxies. As we did to compute the ρ_{SFR}, we need to correct the effective solid angle $\Omega_{eff} = \overline{f} \times \Omega_C$.

For late type f=264/937, while for early type f=102/937. The time resolution of curves is again one Gyr, but we highlight the values at 1, 2, 5, 8, 12 and 13 Gyr with stars. The grey values show different measurements from the literature: Madau & Dickinson (2014) (solid line); Gunawardhana et al. (2013) Figure 21 (circles); Panter et al. (2003) (squares). As the red curve is computed assuming that we only have elliptical and S0 galaxies, with high mass, it is expected that this curve remains above the black one. On the other hand, the orange curve is computed taking into account Sa and later spiral galaxies, with lower masses than earlier types. Thus, this curve remains below the black one, which takes all galaxies into account.

7.3.5 Integrated properties: Specific star formation rate

After analyseing ρ_{SFR} and ρ_{Mass}, we focus on the evolution of the specific star formation rate ($sSFR$), which is the SFR per unit stellar mass. Different results from literature obtain that $sSFR$ increases out to $z \sim 2$ (Elbaz et al., 2007, 2011; Daddi et al., 2007, 2009; Noeske et al., 2007; Dunne et al., 2009; Stark et al., 2009; Oliver et al., 2010; Rodighiero et al., 2010) and is constant, or perhaps slowly increasing, from $z = 2$ out to $z = 6$, (Feulner et al., 2005; Dunne et al., 2009; Magdis et al., 2010; Stark et al., 2013).

The bottom panels in Figure 7.1 shows the evolution of $sSFR$ with redshift. In the bottom left panel we observe the $sSFR$ according to morphological types. The bottom right panel shows the evolution of $sSFR$ with redshift, considering the whole sample (black curve); E and S0 galaxies (red curve); Sa and later types (orange curve). The resolution in time is again one Gyr, but we highlight the values at 1, 2, 5, 8, 12 and 13 Gyr with stars. The grey values show different measurements from the literature: Madau & Dickinson (2014) (solid line); Elbaz et al. (2011) (dashed line); Daddi et al. (2007), Noeske et al. (2007), Damen et al. (2009) and Stark et al. (2013) (circles); Feulner et al. (2005), Daddi et al. (2007), Daddi et al. (2009), Elbaz et al. (2007), Elbaz et al. (2011), Dunne et al. (2009), Stark et al. (2009), Stark et al. (2013), Oliver et al. (2010), Rodighiero et al. (2010) and Magdis et al. (2010) (squares). Also we present the results stacking galaxies by mass (bottom right panel in Figure 7.2)

Using model **M1** we obtain that $sSFR$ increases from $z = 0$ to $z = 5$, varying from log $sSFR = -1$, at $z = 0$, to log $sSFR \sim 0.16$ at $z = 5$. Comparing the red and orange curves, we observe that both are similar for $z > 0.2$ and only for $z < 0.2$ the $sSFR$ decreases rapidly for E and S0 galaxies, obtaining log $sSFR \sim -2.4$ for these galaxies. For the local Universe our results are in agreement with those obtained from literature, but the slope obtained with our models is less step than that obtained in the other studies. In particular, compared to the curve from Elbaz et al. (2011) curve, the results for $z < 1$ are in agreement, but our curve increases slowly when increasing the redshift. We find that $sSFR$ decreases as the universe evolves, suggesting that galaxies become progressively less efficient at forming stars over the course of their lifetime. Again we observe larger differences at high redshift, which come from the different timescales. Our $sSFR$ is time averaged for a longer period of time than in redshift studies.

Stacking galaxies according to morphological types, we obtain similar curves for the different types for $z > 1$. For $z < 1$ the curves decrease with a different slope, according to morphological type. For

E and S0 galaxies the $sSFR$ decreases reaching $\log sSFR \sim -2.3$ at $z = 0$, while for Sd galaxies we obtain $\log sSFR \sim -0.5$. The values at $z = 0$ decrease from Sd to E galaxies with the morphological type.

The results by stacking galaxies in different mass bins (right panel in figure 7.2)are: for $z > 1$, the $sSFR$ for galaxies in the different mass bins are very similar. For $0.2 < z < 1$, the $sSFR$ scale with the mass of galaxies, obtaining higher values for less massive galaxies. In the local Universe, we find that more massive galaxies have larger $sSFR$ than galaxies with intermediate mass. However, we observe that $sSFR$ curves are more similar for the different masses than comparing for the different morphological types. This reinforce the conclusion that morphology is one driver of galaxy evolution, as previously shown by González Delgado et al. (2015, 2016).

7.3.6 Resolved properties: SFR, CMF and $sSFR$

The top panels in figure 7.4 show the SFR for $R < 0.5$ HLR (left) and $1 < R < 2$ HLR (right) regions using model **M1**. Without regarding the initial rising of models, we obtain that SFR declines with time, both for inner and outer regions, except for Sc and Sd galaxies, which show an almost constant SFR. The SFR declines more rapidly in the inner regions and the peak occurs earlier in the inner regions than in the outer ones. On the other hand the peak in SFR is higher in the inner region. The more rapid decline is clearer in Sa, Sb and Sbc. For S0 galaxies we obtain $\tau = 1.5$ Gyr for the inner region and $\tau = 2.6$ Gyr for outer regions. For E galaxies we obtain $\tau = 1.1$ Gyr and $\tau = 1.5$ Gyr for inner and outer regions, respectively.

The middle panels in figure 7.4 show the CMF. For Sbc and earlier types, we obtain that inner regions accrete the 80% of their total mass earlier in the past and in a shorter period of time than outer regions. However, for Sc and Sd galaxies we obtain a more parallel formation process, although t_{80} is larger in the inner region than in the outer one, suggesting that late type galaxies also formed inside-out.

The bottom panels in 7.4 show the $sSFR$ for inner and outer regions stacking galaxies according to Hubble type and obtained with model **M1**. For the inner regions the curves are similar for $z > 1$ and for $z < 1$ the curves decrease with different slopes, with $sSFR$ of early type galaxies declining more rapidly. Also, we found that $sSFR$ declines for the outer regions, although with a less step. Note however the behaviour of the outer regions in E and S0 galaxies for $z > 0.4$: the $sSFR$ declines slower and in epoch of $0.4 < z < 1$ is larger than for spirals. This probably reflects the growth of the envelope of E and S0 through mergers.

7.3.7 Resolved properties: $SFRSD$, SMD and $sSFR$

The top panel in figure 7.5 shows the ρ_{SFR} for the inner and outer regions. Also the curve for the whole galaxies is shown (black) and references from literature (grey). For $z > 1$ the ρ_{SFR} is larger in the inner regions while for $z < 1$, ρ_{SFR} is dominated by the outer regions. Most of the ongoing star formation thus occurs outside the centres, in disk dominated regions, mainly in the disks of spirals, which is in agreement with González Delgado et al. (2016). On the other hand, at high redshift the ρ_{SFR} is dominated by the central components of present day early type galaxies.
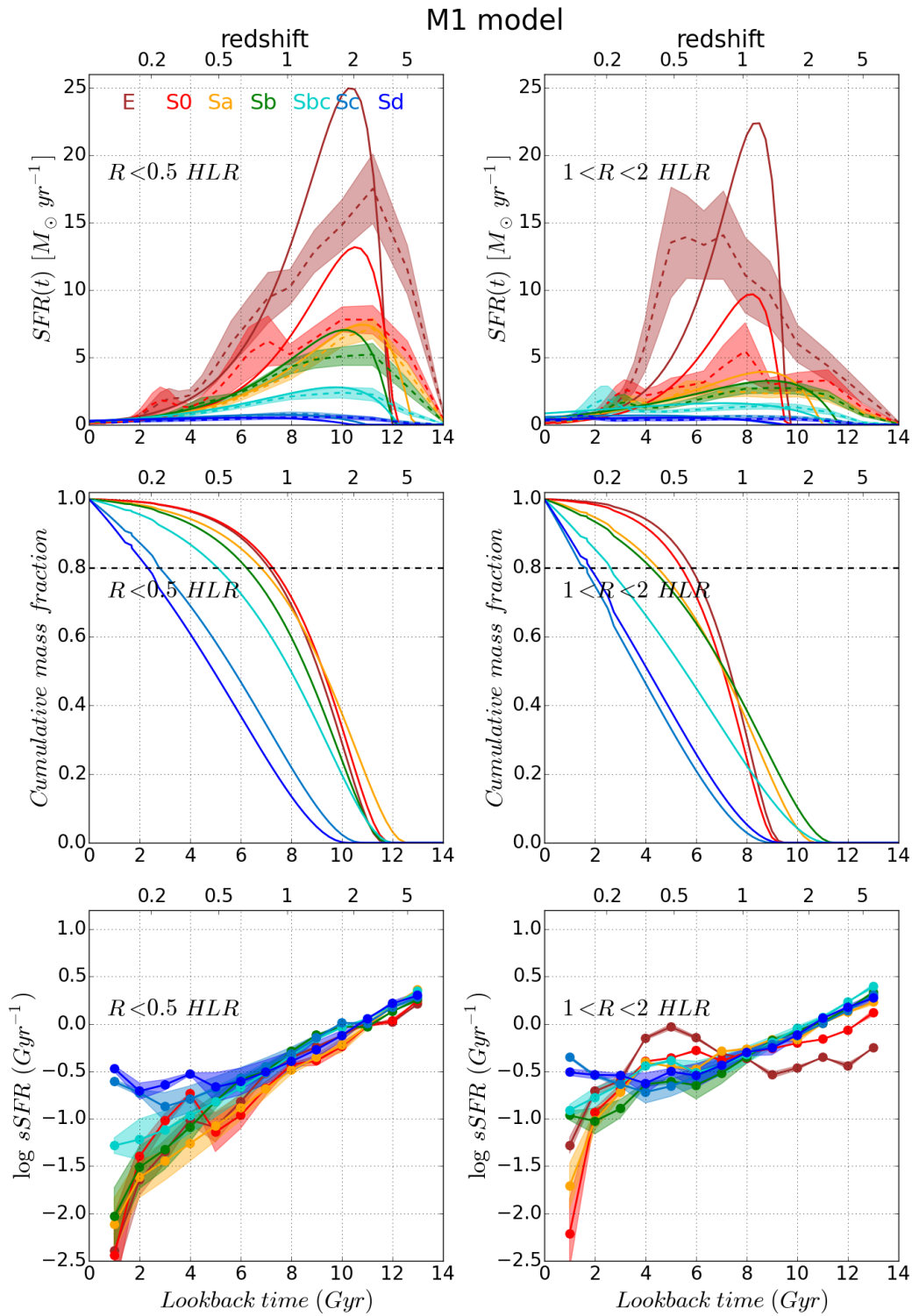
Figure 7.4 Top: The star formation rate for inner (left) and outer (right) regions obtained with model **M1**. Middle: The cumulative mass fraction for inner (left) and outer (right) regions. Bottom: The specific star formation rate for inner (left) and outer (right) regions. The different Hubble types are colour-coded.
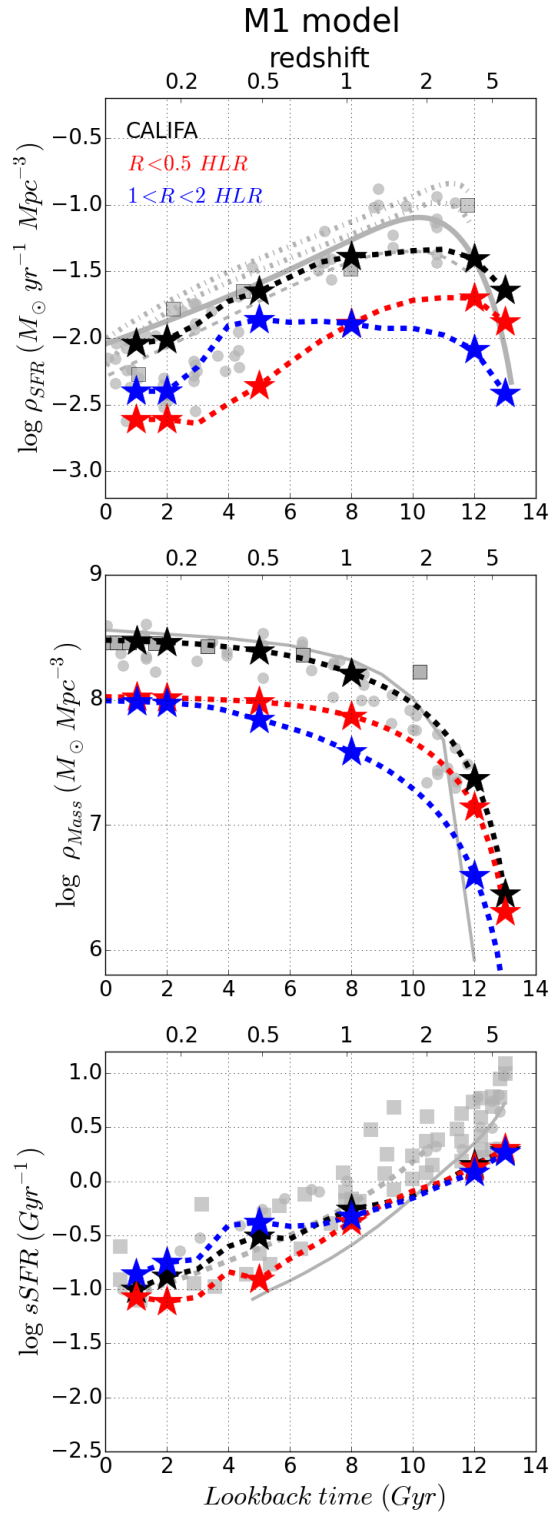
Figure 7.5 Left: The evolution of star formation rate density with redshift obtained with **M1**. Middle: The evolution of mass density with redshift. Right: The specific star formation rate for the whole sample. The panels show the results for the whole galaxies (black), $R < 0.5$ (red) and $1 < R < 2$ (blue).

$\log \rho_{SFR} \ [M_\odot yr^{-1} Mpc^{-3}]$		$z = 0$	$z = 1$	$z = 2$	$z = 5$
	$R < 0.5$	-2.61	-1.89	-1.72	-1.70
M1	Galaxy	-2.04	-1.39	-1.34	-1.41
	$1 < R < 2$	-2.40	-1.89	-1.93	-2.09
	$R < 0.5$	-2.61	-2.09	-1.76	-1.59
M6	Galaxy	-2.01	-1.39	-1.34	-1.27
	$1 < R < 2$	-2.39	-2.08	-1.75	-1.91
Madau & Dickinson 14	Galaxy	-2.05	-1.27	-1.10	-1.41
Fardal+07	Galaxy	-2.28	-1.42	-1.35	-1.51

| $\log \rho_{Mass} \ [M_\odot Mpc^{-3}]$		$z = 0$	$z = 1$	$z = 2$	$z = 5$
	$R < 0.5$	8.02	7.87	7.66	7.14
M1	Galaxy	8.47	8.21	7.97	7.35
	$1 < R < 2$	7.99	7.58	7.29	6.60
	$R < 0.5$	8.09	8.01	7.91	7.61
M6	Galaxy	8.49	8.29	8.08	7.59
	$1 < R < 2$	7.95	7.71	7.45	6.62
Madau & Dickinson 14	Galaxy	8.56	8.32	8.01	5.92

$\log sSFR \ [Gyr^{-1}]$		$z = 0$	$z = 1$	$z = 2$	$z = 5$
	$R < 0.5$	-1.07	-0.37	-0.09	0.13
M1	Galaxy	-1	-0.26	-0.13	0.16
	$1 < R < 2$	-0.85	-0.32	-0.16	0.08
	$R < 0.5$	-1.43	-0.49	-0.26	-0.05
M6	Galaxy	-1.12	-0.27	-0.06	-0.19
	$1 < R < 2$	-1.14	-0.21	-0.07	-0.16
Elbaz+11	Galaxy	-1.12	-0.21	0.18	

Table 7.1 $\log \rho_{SFR}$, $\log \rho_{Mass}$ and $\log sSFR$ at different redshift obtained with **M1** and **M6**.

The middle panel in figure 7.5 shows the evolution of ρ_{Mass} with redshift. Red and blue curves show ρ_{Mass} for inner and outer regions, respectively, with black curves for the whole galaxies. For high redshift we obtain that the mass density of galaxies comes from the inner regions as suggested by the similarity of the black and red curves. Also we observe that inner regions have grown more rapidly, accreting their total mass in a shorter period of time. At $z \sim 1$ the inner regions have almost their total mass that we observe today, while outer regions grow more slowly.

The bottom panel in figure 7.5 shows the $sSFR$ for all galaxies in our sample. Black curves are for the whole galaxies, which was shown previously as well as the grey values from literature. Red and blue curves represents the $sSFR$ for inner and outer regions, respectively. For $z > 1$ the curves are very similar while for $z < 1$ the $sSFR$ in the outer regions is larger than in the outer regions.

Table 7.1 shows the values of ρ_{SFR}, ρ_{Mass} and $sSFR$ at different redshift for the whole galaxies and also for the inner and outer regions. The table lists the results with **M1**, **M6** and other values from literature (Madau & Dickinson (2014) and Panter et al. (2003) for ρ_{SFR}; Elbaz et al. (2011) for $sSFR$).

7.4   Model M6

This section follows a similar structure to the previous one, but in this case we analyse our SFH related results obtained with **M6**.

7.4.1   Integrated properties: Star formation rate and cumulative mass fraction

Now we add more complexity to the models, including a second component and increasing the dimension of the parameter space. Figure 7.6 shows the mean SFH and cumulative mass fraction according to morphological type using model **M6**. We compute the mean parameters for the different morphological types and then obtain the SFH, as we did for one component SFHs. E and S0 galaxies show higher t_0 values for the old component indicating that they formed earlier in the past. For E and S0 we obtain $t_0 = 11.8$ and 11.6 Gyr for the old component, respectively, while for later morphological types $t_0 \leq 10$ Gyr. From the cumulative mass fraction curves we observe that the old component provides almost the total mass of the galaxies. The young component shows that galaxies have suffered a recent star formation event and it occurred in the last ~ 1.5 Gyr for Sa, Sb and later morphological types, involving $1 - 15$ % of their total stellar mass, as found by Schawinski et al. (2007).

Figure 7.7 shows the SFR and cumulative mass fraction, stacking galaxies in different mass bins (left and middle panels). More massive galaxies present larger values of SFR and also higher t_0 values both for the old and young component, which means that more massive galaxies formed earlier than less massive ones.

7.4.2   Integrated properties: Star formation rate density

Figure 7.6 shows ρ_{SFR} using model **M6**, combining two exponential components. For the local Universe we obtain $\log \rho_{SFR} = -2.01$. The curve remains between Madau & Dickinson (2014) and Fardal et al. (2007) curves from $z = 0$ to $z = 3$. The curve declines from $z \sim 3$, but the peak of ρ_{SFR} occurs at higher redshift than values from literature show. When observing the red and orange curve we see the differences in the SFHs. For $z > 1$, ρ_{SFR} is higher for ellipticals and S0 galaxies. At $z = 1$, the curves cross due to the differences in τ parameter computed for both types of galaxies. In the local Universe we obtain that ρ_{SFR} is lower for E and S0 than for later types, but from $z \sim 0.19$ to $z = 0.5$ the ρ_{SFR} remains larger for E and S0 galaxies due to the effect of the young component that appear at $z \sim 0.2$ for E and S0 galaxies. For later types, the young component appear for $z < 0.15$.

7.4.3   Integrated properties: Mass density

Using model **M6**, we again obtain a ρ_{Mass} curve in agreement with values from literature. Figure 7.6 shows that from $z = 0$ to $z = 1$ the values are similar, but for $z > 1$ we obtain values slightly larger than Gunawardhana et al. (2013) and Madau & Dickinson (2014), as happens when using model **M1**.

7.4.4   Integrated properties: Specific star formation rate

In Figure 7.6 (bottom right panel) we show the $sSFR$ for the whole sample. The black curve matches very well with Elbaz et al. (2011) from $z = 0$ to $z \sim 1$. At $z \sim 2$ we obtain a peak, reaching

log $sSFR = -0.06$ and for $z > 1$ our curve declines, obtaining $sSFR \sim -0.19$ at $z = 5$. Comparing red and oranges curve we observe that at $z = 5$, the $sSFR$ for E and S0 galaxies is higher than for Sa and later types. From $z \sim 0.5$ to $z \sim 2$ the orange curve remains above the red one, but from
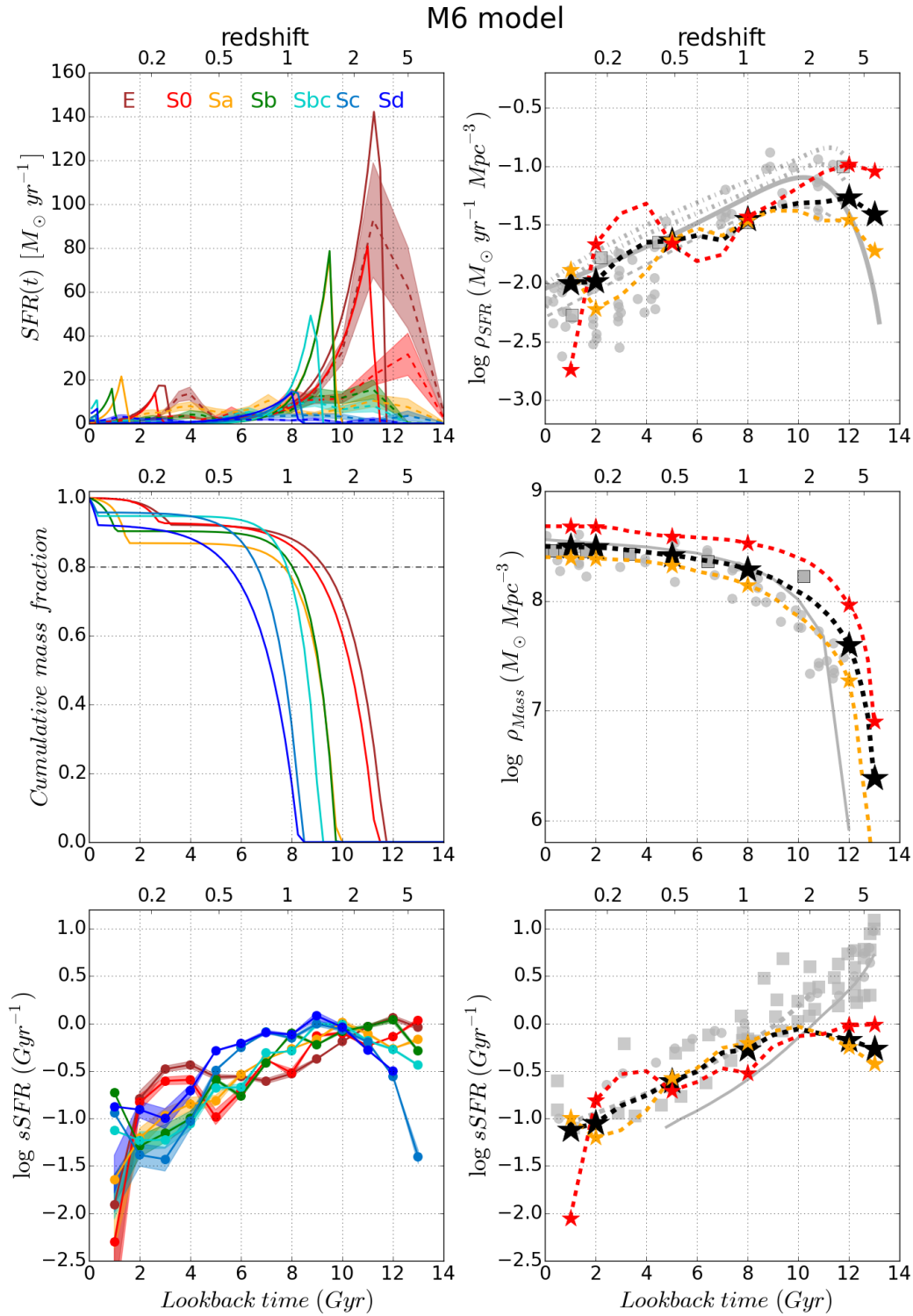

Figure 7.6 Same as Figure 7.1 using model **M6**.

$z \sim 0.18$ to $z \sim 0.5$ the $sSFR$ grows for E and S0 galaxies due yo the young component. For the local Universe, the $sSFR$ is dominated by spiral galaxies with log $sSFR = -1$, while for E and S0 the $sSFR$ decreases obtaining log $sSFR \sim -2$.

Stacking galaxies according to morphology (bottom left panel) we observe that for $z = 5$ the $sSFR$ decreases with the Hubble type from E to Sd galaxies. From $z \sim 0.5$ to $z \sim 2$ the $sSFR$ is higher for later types and the curves scale with morphology, but the contribution of the young component in the model produces the growth of the $sSFR$ for E and S0 from $z \sim 0.18$ to $z \sim 0.5$. The more recent location of the young component for later types produces the growth of $sSFR$ for $z < 0.25$. In the local Universe the $sSFR$ declines from Sd to E and S0 galaxies, although we obtain slightly larger values for Sb galaxies than for Sd.

The left panel in figure 7.7 shows the $sSFR$ stacking galaxies in different mass bins. We obtain that the $sSFR$ scale with the mass of galaxies for $z < 2.5$, obtaining lower $sSFR$ for massive galaxies. For $z > 2.5$, lower $sSFR$ is obtained for low mass galaxies because, on average, they started to form more recently. In the local Universe we also find that $sSFR$ correlates with the galaxy mass, except for galaxies with log $M_\star > 11.19$.
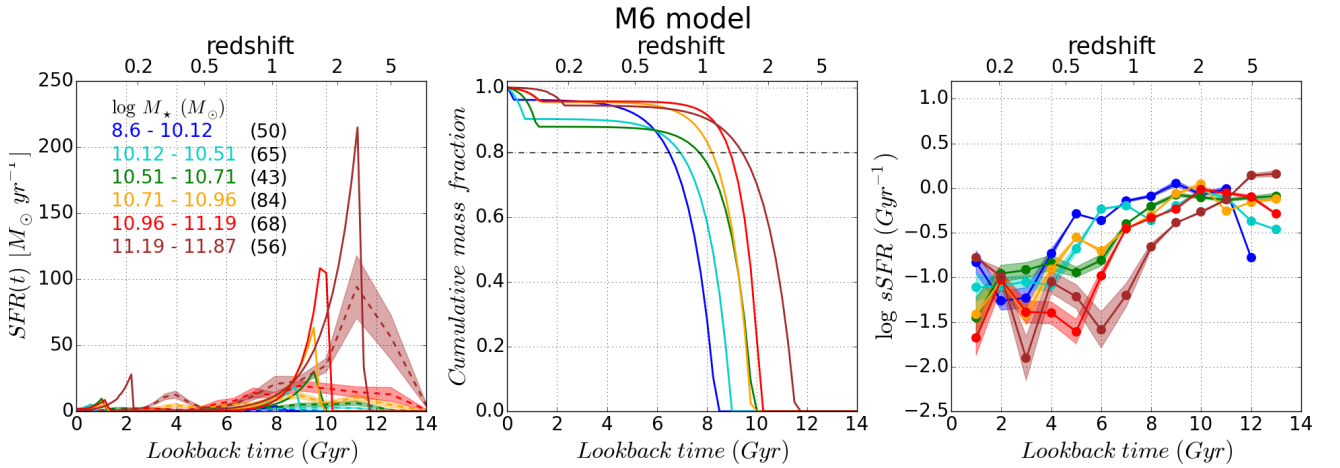

Figure 7.7 Same as Figure 7.2 using model **M6**.

7.4.5 Resolved properties: SFR, CMF and $sSFR$

The top panels in figure 7.8 show the SFR for inner and outer regions using model **M6**. For Sc and Sd galaxies we find similar values for the SFR in the inner and outer regions. For the inner regions we obtain $t_0 \sim 9$ Gyr for the old component and $t_0 \sim 8$ Gyr for the outer one. For both inner and outer regions the young component occurs in the last 0.5 Gyr. On the other hand, for earlier types the SFR is higher in the inner regions than in the outer ones, and $t_0^{old}(R < 0.5) > t_0^{old}(1 < R < 2)$. For the young component, we also obtain $t_0^{young}(R < 0.5) > t_0^{young}(1 < R < 2)$, except for Sbc galaxies with $t_0 \sim 0.5$ Gyr in both regions. Using this model we obtain larger τ values for the outer regions, indicating that inner regions have grown earlier in the past and in a shorter period of time than regions at $R > 1$ HLR. However the differences in τ values for inner and outer regions are more clearly observed using **M1**.

The middle panels in figure 7.4 show the CMF. For Sc and Sd galaxies, both regions reached the 80% of the total mass 6 Gyr ago, which suggests a similar formation process. On the other hand, for Sbc and earlier types we find that central regions formed earlier in the past, pointing to an inside-out
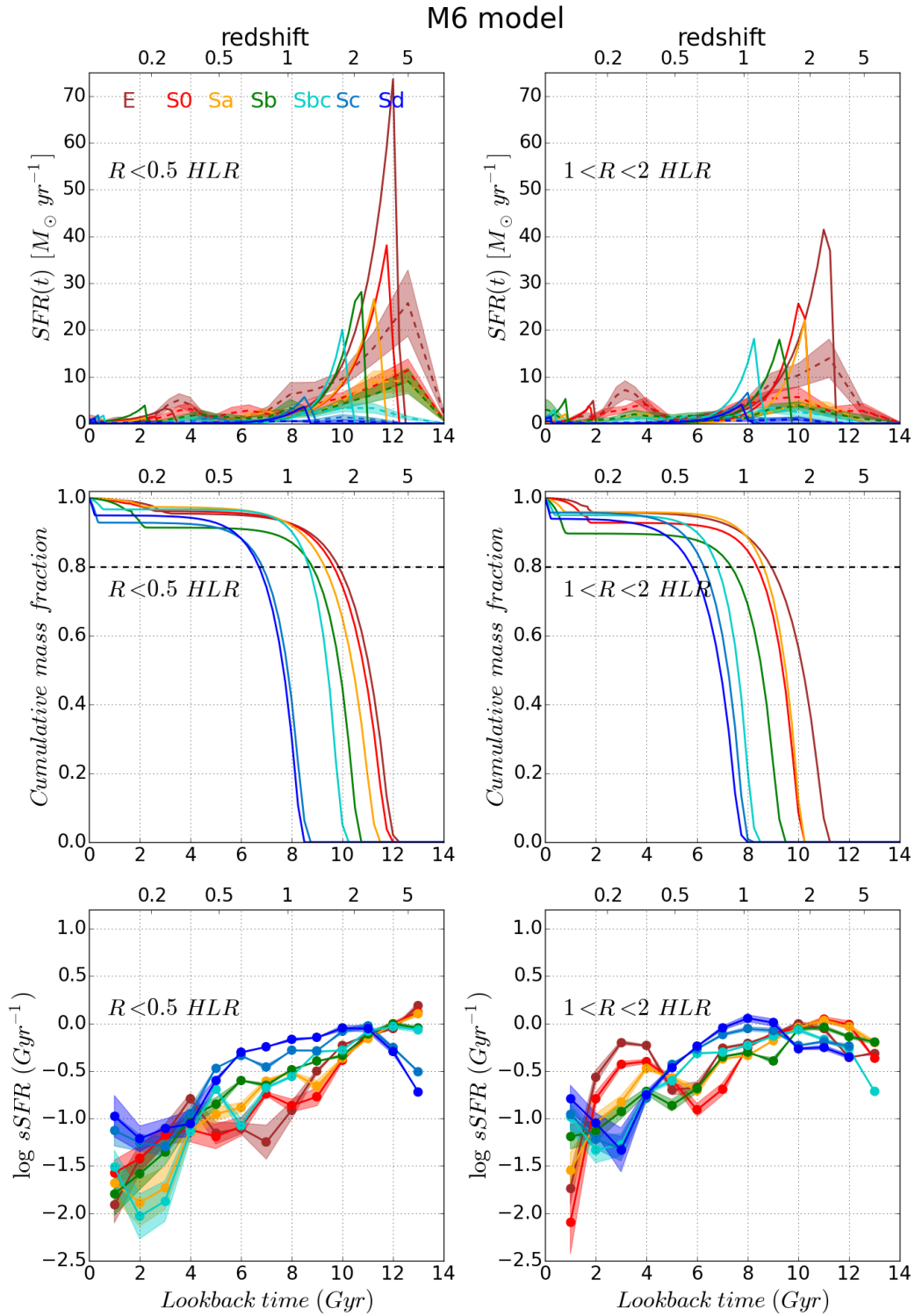

Figure 7.8 Same as Figure 7.4 using model **M6**.

growth of galaxies. In particular, for Sbc and earlier types, 80% of the total mass in regions at $R < 0.5$ HLR is accreted in the epoch $1 < z < 2$, while for the outer ones 80% of the total mass is reached for $z < 1$.
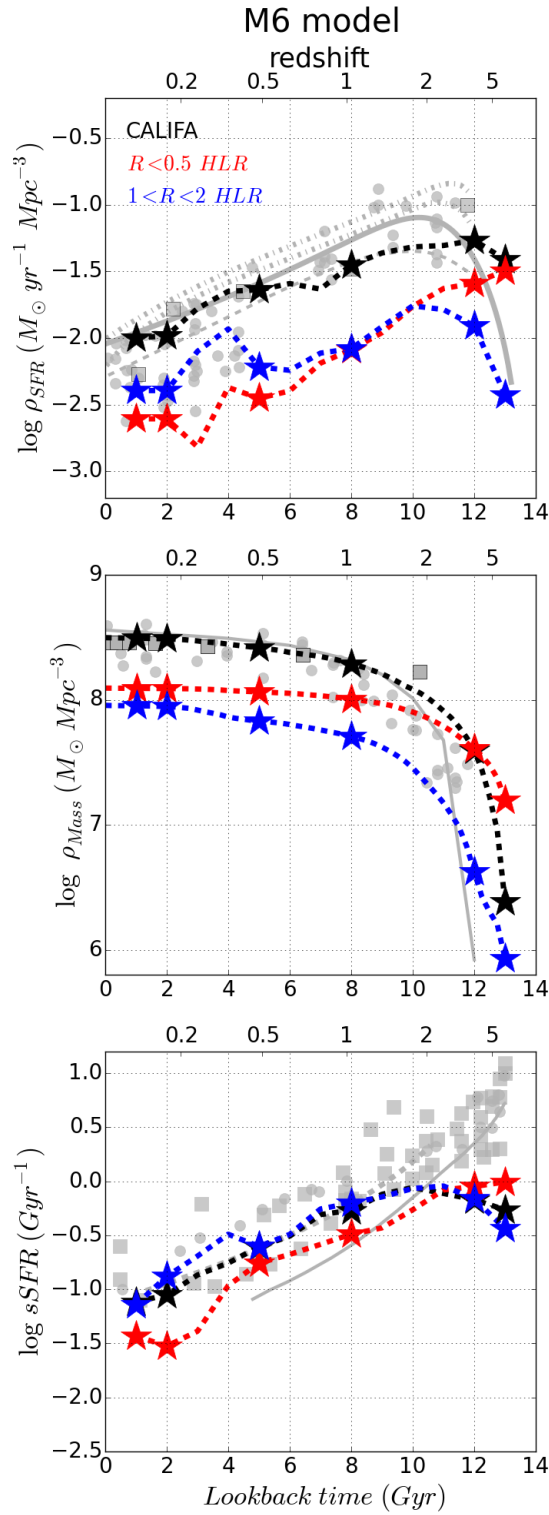

Figure 7.9 Same as Figure 7.5 using model **M6**.

The bottom panels in 7.8 show the $sSFR$ for inner and outer regions using model **M6** and stacking galaxies according to Hubble type. For the inner regions we obtain that $sSFR$ declines with redshift for Sbc and earlier types. For Sc and Sd galaxies the $sSFR$ declines for $z < 2$ but we obtain an initial increase for $z > 2$. For the outer regions we observe that $sSFR$ is almost constant for $z \sim 2$. For $z < 2$ the $sSFR$ declines, although we observe again the same behaviour for E and S0 obtained with model **M1**. In this case we find that $sSFR$ for E and S0 is larger than for later types in epoch of $0.2 < z < 0.5$. With the previous model we obtained that the largest $sSFR$ for E and S0 happen for $0.4 < z < 1$, which means that the growth of the envelope would occur more recently using model **M6**.

7.4.6   Resolved properties: $SFRSD$, SMD and $sSFR$

The top panel in figure 7.9 shows the ρ_{SFR} for the inner and outer regions. ρ_{SFR} declines with redshift for inner regions, while ρ_{SFR} increases for $z > 2$ and declines for $z < 2$. For $1 < z < 1.5$ we obtain similar values of ρ_{SFR}, indicating that at this redshift inner and outer regions are competing in building the ρ_{SFR}. For $z > 2$ we clearly observe that ρ_{SFR} is dominated by the inner regions. On the other hand, in the local Universe, the current ρ_{SFR} is dominated by the outer regions of galaxies.

In the middle panel in figure 7.9 we present ρ_{Mass}. As with the previous model, red and blue curves show ρ_{Mass} for inner and outer regions, respectively. Also we show the evolution of ρ_{Mass} for the whole galaxies (black) and other values from literature (grey). As found with the previous model, at high redshift all the mass comes from the inner regions of galaxies. The evolution of the ρ_{Mass} indicates that inner regions have been formed more rapidly than outer ones, and at $z \sim 1$ they have almost reached their total present mass.On the other hand we observe that the growth of outer regions occurs along a longer period of time and they accrete mass more slowly.

The bottom panel in figure 7.9 shows the $sSFR$ for all galaxies using model **M6** model. With this model, the $sSFR$ for $z > 2$ is larger for the inner regions, being similar at $z \sim 2$. For $z < 2$ the $sSFR$ decreases both in the inner and outer regions, but it is dominated by the outer regions, indicating more efficiency in forming new stars.

7.5   Integrated SFH: Results with other models

In this section we present the results found with the other models used in this thesis. We follow the same structure as in previous section to present the integrated results. The figures that summarises the results are included in Section 7.7. Table 7.2 shows the values of ρ_{SFR}, ρ_{Mass} and $sSFR$ at different redshift and for the different models.

7.5.1   Model M2

Star formation rate and cumulative mass fraction

Observing the SFR derived with model **M2** (top left panel in Figure 7.10) we find similar results to those found with model **M1**. The peak of star formation occurs later in E and S0 than for early spirals, but on the other hand they show larger τ values indicating a slower star formation. For Sa,

$\log \rho_{SFR} \, [M_\odot yr^{-1} Mpc^{-3}]$	$z = 0$	$z = 1$	$z = 2$	$z = 5$
M2	-1.99	-1.49	-1.43	-1.31
M3	-1.91	-1.36	-1.46	-1.76
M4	-1.23	-1.71	-1.89	-2.19
M5	-1.28	-1.54	-1.59	-1.66
M7	-1.99	-2.42	-2.01	-1.46
M8	-1.99	-1.33	-1.35	-1.32
M9	-2.31	-1.49	-1.36	-1.35

$\log \rho_{Mass} \, [M_\odot Mpc^{-3}]$				
M2	8.46	8.27	8.11	7.76
M3	8.41	8.03	7.66	6.94
M4	8.31	7.61	7.23	6.54
M5	8.44	8.01	7.77	7.35
M7	8.58	8.52	8.51	8.45
M8	8.49	8.26	8.04	7.45
M9	8.51	8.33	8.17	7.88

$\log sSFR \, [Gyr^{-1}]$				
M2	-0.85	-0.45	-0.34	0.1
M3	-0.95	-0.21	0.01	0.19
M4	-0.31	-0.21	-0.09	0.12
M5	-0.45	-0.31	-0.18	0.04
M7	-1.22	-1.49	-1.12	-0.62
M8	-1.19	-0.17	-0.11	-0.17
M9	-1.36	-0.56	-0.35	-0.08

Table 7.2 $\log \rho_{SFR}$, $\log \rho_{Mass}$ and $\log sSFR$ at different redshift for different models.

Sb and Sbc we obtain $t_0 = 11.8$, 12.1, 12.2 Gyr, and $\tau = 3.4$, 4.5, 8.1 Gyr, respectively. For E and S0, $t_0 = 10.02$, 10.4 Gyr and $\tau = 1.8$, 2.1 Gyr, respectively. From the cumulative mass fraction curves (middle left panel), we observe steeper curves for E and S0 which indicate more rapid growth, reaching 80% of the total mass earlier in the past.

Star formation rate density

The top right panel in Figure 7.10 shows the ρ_{SFR} curve using model **M2**. In the local Universe, at $z = 0$, we obtain good agreement with values in literature, with $\log \rho_{SFR} = -1.99$. For $z \leq 1$ our curve is very similar to the curve derived by Fardal et al. (2007), but for higher redshift our curve continues to rise. The difference in the curve compared with model **M1** at high redshift is due to the initial rise of the last one. Comparing the red and orange curves we observe that the curves cross for $z \sim 0.2$, which indicates lower SFR for elliptical and S0 galaxies in the local Universe.

Mass density

The middle right panel shows our estimation of ρ_{Mass}. The global stellar mass density (black curve) matches very well with those values obtained by other authors from z=0 to z=1. However, at higher redshift we find larger values than those found by Gunawardhana et al. (2013) and Madau & Dickinson (2014).

Specific star formation rate

The bottom right panel shows the $sSFR$ obtained with model **M2**. We obtain an increasing curve from $\log sSFR \sim -0.85$, at $z = 0$, to $\log sSFR \sim 0.1$ at $z = 5$. Red and orange curves are very similar for $z > 0.2$, but the red curve for $z < 0.2$ decreases rapidly, reaching $\log sSFR \sim -2.25$. Again, the slope obtained with our models is lower than that found in other studies.

Stacking galaxies according to morphological types (bottom left panel) we observe similarities with the results obtained with model **M1**. For $z < 1$ the curves decrease with different slopes, varying according to morphological type. For E and S0 galaxies the $sSFR$ decreases reaching $\log sSFR \sim -2.5$ at $z = 0$, while for Sd galaxies we obtain $\log sSFR \sim -0.2$. The main difference is observed for Sd galaxies, which show an almost flat curve.

7.5.2   Model M3

Star formation rate and cumulative mass fraction

Model **M3** is also a delayed model but differs from **M1** in the location of the peak of the SFR (top left panel in Figure 7.11). With this model, the peak is more delayed with respect to the beginning of the SFH. Sa, Sb and Sbc galaxies again show t_0 values ~ 12 Gyr, higher than in E and S0 (10.7 and 11.3 Gyr), and also larger τ values. $\tau = 4.0$, 4.5 and 5.7 Gyr for Sa, Sb and Sbc, while for E and S0 we obtain $\tau = 2.9$ and 3.3 Gyr. The steeper curves of the cumulative mass fraction for E and S0, indicate a faster growth than Sa galaxies and later morphological types.

Star formation rate density

Compared to model **M1**, the peak of SFR occurs more recently and the initial rise in the SFR occurs slowly. This behaviour is reflected in the ρ_{SFR} (top right panel). Our curve is in agreement with the other values from literature from $z = 0$ to $z = 1$, but for higher redshift our curve declines, showing 0.5 dex lower value for the ρ_{SFR} at $z = 2$.

Mass density

The middle right panel shows that the ρ_{Mass} curve has a similar shape to that found with **M1** but remains below the values from literature for all redshifts. The lower values with respect to model **M1** come from the more recent peak of SFR and the longer period of time to shut off the star formation, which means a longer time to accrete the total mass.

Specific star formation rate

The averaged curve (bottom right) using model **M3** increases from $\log sSFR \sim -0.95$, at $z = 0$, to $\log sSFR \sim 0.19$ at $z = 5$. The bottom left panel shows similar curves for $z > 1$. For $z < 1$ the curves decrease with different slopes that correlate with morphology. In particular, for E and S0 galaxies $\log sSFR \sim -2.25$ at $z = 0$ while for Sc and Sd galaxies we obtain $\log sSFR \sim -0.5$

Stacking galaxies according to morphological types (bottom left panel) we observe similarities with the results obtained with model **M1**. For $z < 1$ the curves decrease with different slopes, varying according to morphological type. For E and S0 galaxies the $sSFR$ decreases reaching $\log sSFR \sim -2.5$ at $z = 0$, while for Sd galaxies we obtain $\log sSFR \sim -0.5$.

7.5.3   Models M4 and M5

Star formation rate and cumulative mass fraction

Figures 7.12 and 7.13 show the mean SFR and cumulative mass fraction according to morphological type for rising models. The functional forms are very different from previous models. Previous models show decaying SFR at recent epoch, unlike rising models. Model **M4** shows the linear behaviour of the SFR with different slopes for each one of the morphological types. On the other hand, we observe a similar mass accretion process from the cumulative mass fraction curves. Model **M5** represents the SFR using the power-law-rising models. For Sc and Sd galaxies we obtain an almost linear rising behaviour, with $\alpha \sim 1$ while for E galaxies we obtain a very fast initial growth followed by an almost constant SFR, which points again to a faster growth of early type galaxies than late type, as can be seen in the right panel, with a steeper curve for E than for Sd. For intermediate morphological types the curves show similar behaviour.

Star formation rate density

As we discussed previously, the rising models are not suitable for describing the SFR of local galaxies. Comparing the ρ_{SFR} derived with models **M4** and **M5** with the values from the literature we corroborate this conclusion. We obtain a decreasing curve from $z = 0$ to $z = 5$ using model **M4** and almost constant curve using model **M5**. In both cases, we conclude that the picture is not consistent with the known cosmic star formation rate scenario.

Mass density

Figures 7.12 and 7.13 show the ρ_{Mass} curve for rising models, **M4** and **M5**. Although the results do not match the trend from the values in literature, we find good agreement for mass density at $z = 0$. This happens due to the mass is the most robust parameter derived from the model.

Specific star formation rate

The rising models show a flatter $sSFR$ curves than that obtained with previous models. The curves also increase with redshift, reaching $\log sSFR \sim 0.2$ for $z = 5$, but using these models the $sSFR$ is

larger for $z = 0$ obtaining log $sSFR \sim -0.5$. Thus, more differences with values from literature are also observed. Comparing red and orange curves we obtain almost the same curve.

For the different morphological types (bottom left panels) we also observe flatter curves than those obtained with models **M1**, **M2** and **M3**. For the local Universe and **M4** we obtain log $sSFR \sim -0.31$ and log $sSFR \sim 0.12$ at $z \sim 5$. For **M5**, log $sSFR \sim -0.45$ at $z \sim 0$ and log $sSFR \sim 0.4$ at $z \sim 5$. The curves are similar, although for Sc ad Sd galaxies the curves remain above the others.

7.5.4 Model M7

Star formation rate and cumulative mass fraction

The model **M7** is built as a restriction of the previous one. Figure 7.14 shows the mean SFH and cummulative mass fraction according to morphological type using model **M7**. The old component begins at the same time for all Hubble types but we observe differences in the τ parameter. Sbc galaxies and earlier morphological types show lower τ values than Sc and Sd galaxies, indicating that they formed the mass faster. For Sc and Sd we obtain $\tau \geq 3$ Gyr, while for earlier types $\tau \leq 2$ Gyr. The old component accounts for almost the total stellar mass but a young component again appears, indicating that galaxies have experienced a recent star formation event in the last ~ 2 Gyr for Sa, Sb and later morphological types. The cumulative mass fraction curve indicates slower growth for Sc and Sd galaxies than for earlier types.

Star formation rate density

Figure 7.6 shows ρ_{SFR} using model **M7**. With this model we obtain a picture for the evolution of ρ_{SFR} very different from what other works show. The rapid decline of the SFR for the old component produce the decrements of ρ_{SFR} from $z \sim 5$ to $z \sim 0.6$, followed by an increment for lower redshift. Only consistent values are found for the local Universe.

Mass density

On the other hand, model **M7**, fixing t_0 value to 14 Gyr, provides an inconsistent picture of ρ_{SFR} as we observe in Figure 7.14. Although this model could match the observed features in galaxies, such as Lick indices or magnitudes, it is not representative of the cosmic evolution of galaxies.

Specific star formation rate

In Figure 7.14 we observe the $sSFR$ derived with model **M7**. As we observe in the bottom right panel, this model produces an inconsistent picture of the evolution of $sSFR$, as also happened with ρ_{SFR} and ρ_{Mass}. Only for $z < 0.35$ we obtain values that are in agreement with Elbaz et al. (2011), which come from the evolution of the young component of the model. For $z > 0.355$ the values for the $sSFR$ are very low.

This behaviour is also observed when stacking galaxies according to morphology (bottom left panel). From $z > 0.19$ to $z < 0.35$ we obtain that $sSFR$ declines with morphology, from E to Sd galaxies. For $z < 0.18$, the more recent young component for Sa and later types, produces larger

values for spiral galaxies. In the local Universe, we obtain $sSFR \sim -1$ for Sb and later types. For Sa $sSFR \sim -1.6$ while $sSFR < -2$ for E and S0. The results suggest that assuming an initial exponential decaying SFR at the same time (14 Gyr) for all the galaxies is not a consistent picture for the cosmic evolution.

7.5.5 Model M8

Star formation rate and cumulative mass fraction

The mean SFH and cumulative mass fraction curves for model **M8** can be seen in Figure 7.15. Comparing the mean SFHs for the different morphological types with those obtained using **M6** model we observe that the histories are very similar, both the location of the star formation events, it means, t_0 and τ parameters, and also the mass fraction of each component to the total mass. Again E and S0 galaxies show larger t_0 values for the old component indicating that they formed earlier in the past. For E and S0 we obtain $t_0 = 11$ Gyr. The t_0 values decrease for later types, from $t_0 = 9.7$ Gyr for Sa galaxies to $t_0 = 8$ Gyr for Sd galaxies. The old component provides almost the total mass of the galaxies and the young component indicates a recent star formation event in the last ~ 1.5 Gyr for Sa, Sb and later morphological types.

Star formation rate density

Due to the similarity of the models, the result obtained with **M8** is very similar to that obtained with **M6**, as we observe in Figure 7.15, both the black curve, considering the whole sample, as the results for E, S0 (red curve) and later morphological types (orange curve).

Mass density

The result with **M8** model is also very similar to that found with **M6**. Figure 7.15 shows that from $z = 0$ to $z = 2$ our results match very well with Madau & Dickinson (2014), but for $z > 2$ our curve remains slightly above the Gunawardhana et al. (2013) values.

Specific star formation rate

For **M8** we obtain similar results to those obtained with model **M6**, as we observe in Figure 7.15 (bottom panels). The black curve in the bottom right panel matches very well with Elbaz et al. (2011) from $z = 0$ to $z \sim 1$, although for $z = 0$ we obtain log $sSFR = -1.19$, slightly lower than -1. From $z \sim 1$ to $z \sim 0.2$ the curve flattens and decreases for $z > 2$. Comparing red and orange curves we observe larger values for $sSFR$ at $z = 5$ for E and S0 than for Sa and later types. From $z \sim 0.3$ to $z \sim 1$ the orange curve remains above the red one, but from $z \sim 0.18$ to $z \sim 0.3$ the young component in E and S0 galaxies produce a growth in the $sSFR$. In the local Universe we again obtain $sSFR \sim -1$ for Sa and later types, while for E and S0 galaxies the curve decreases obtaining $sSFR \sim -2$.

Stacking galaxies according to morphology (bottom left panel) we observe the same behaviour as found using **M6**, but in this case the curves for Sc and Sd galaxies show larger values from $z \sim 0.18$

to $z \sim 0.5$ to than those obtained with model **M6**. The reason is a more extended old component in these galaxies, which means a larger τ parameter.

7.5.6   Model M9

Star formation rate and cumulative mass fraction

Figure 7.16 shows the results for model **M9**. As found by Schawinski et al. (2014), τ varies from early to late type galaxies. Sc and Sd galaxies show the largest values (~ 8.5 Gyr), indicating that the shutdown of the star formation occurs slowly and such galaxies are still forming stars. On the other hand, E and S0 galaxies show the lowest values (~ 1.5 Gyr), which indicates that the shut down of the star formation occurs faster. These galaxies show very low values of the current SFR which indicates that today they are passive systems. Regarding t_0 values we find that the time of quenching occurs between 6 and 8 Gyr. We obtain $t_0 = 6.1$, 6.8 and 6.7 Gyr for E, S0 and Sd galaxies, respectively, and $t_0 \sim 8$ Gyr for the intermediate morphological types. The cumulative mass fraction curves indicate the E and S0 galaxies form the total stellar mass earlier than later morphological types.

Star formation rate density

Figure 7.16 shows the result using **M9** model. In this case we obtain $\log \rho_{SFR} \sim -2.36$ in the local Universe, lower than the value obtained with previous models ($\log \rho_{SFR} \sim -2$). We obtain a constant rise from $z = 0$ to $z = 5$, although for $z > 2$ the curve flattens. The black curve is similar to that of Fardal et al. (2007), except for $z > 2$, where the this curve decreases. On the other hand, the observed flattening is expected because with this model we are assuming an initial constant SFR from 14 Gyr to t_0. Analysing the different types of galaxies, we obtain that ρ_{SFR} is larger for E and S0 from $z \sim 0.2$ to $z = 5$. However, in the local Universe the ρ_{SFR} is dominated for Sa and later morphological types.

Mass density

Figure 7.16 shows ρ_{Mass} obtained with model **M9**. As with the previous model, from $z = 0$ to $z = 1$ our result matches very well with Madau & Dickinson (2014), but for $z > 1$ we obtain larger values. This model assumes an initial constant SFR, which means that all galaxies begun to form stars at 14 Gyr, which produces large values of ρ_{Mass} at $z > 2$.

Specific star formation rate

Model **M9** produces an almost linear growth curve of $sSFR$ for the whole sample, as we observe in Figure 7.16 (bottom right panel). In this case our curve remains below Elbaz et al. (2011), growing from $\log sSFR = -1.36$ at $z = 0$ to $\log sSFR = -0.08$ at $z = 5$. The red and orange curves are similar for $z > 0.5$, while for $z < 0.5$ the curve for E and S0 declines, obtaining $\log SFR = -2.2$ in the local Universe.

Comparing the results for the different morphological types, we obtain the same curves for $z > 1.5$, due to the initial constant SFR. For $z < 1.5$ the different values of t_0 and τ parameters produce the

different slopes in the curves. The curves scale with the morphological types, decreasing from Sd to E galaxies, which reflects the correlation between the τ parameter and the morphological type.

7.6 Conclusions

In this chapter we have analysed different properties derived with our models to analyse which one produces a more consistent scenario to explain the evolution of galaxies. Our main results are:

- Delayed models combine an initial rising SFR until the peak of star formation rate is reached followed by declining SFR. They are a mixture of the rising models and purely exponentially declining models. Thus, considering one component models, delayed-τ models are the most complete and representative of the evolution of the SFR, which is supported by the results presented in this chapter.

- Our results are compared with other works from literature, which are in agreement on the evolution of ρ_{SFR}, ρ_{Mass} and $sSFR$, being **M1** more in agreement with results from other works. There are some models that we can discard due to the inconsistency of results. In particular, the rising models **M4** and **M5** could be useful for representing the initial growth of galaxies, but not to completely explain their evolution through the cosmic time.

- Models **M6** and **M8** produce very similar results. As we introduce more parameters into the model, the values in terms of $\chi 2$ are lower than using one component models, and the evolution of ρ_{SFR} matches reasonably well with Fardal et al. (2007). On the other hand, the $sSFR$ decreases for $z > 2$, which is in contrast with what other works show. The results using **M7** indicate that the assumption of an initial common birth at 14 Gyr followed by an exponential decaying model combined with a young exponential component is not consistent with the evolution of ρ_{SFR}, ρ_{Mass} and $sSFR$ with redshift. Model **M9** assumes a constant SFR followed by an exponential decay. This is useful for analysing some particular property of galaxy evolution, such as the quenching of galaxies (Schawinski et al. 2014, but better results are obtained with other models when analysing the evolution of the SFR. We find the maximum ρ_{SFR} at $z = 2$, but for $z > 2$ the ρ_{SFR} remains constant. On the other hand, the $sSFR$ shows lower values than those found in literature.

To analyse the resolved properties of galaxies we have used **M1** and **M6**, as we did in the previous chapter. The models represent single and two component SFH, respectively, and both of them provide consistent pictures of the evolution of ρ_{SFR}, ρ_{Mass} and $sSFR$. Although completely different parametrizations, we find several points in agreement between them:

- Both models indicate an earlier formation of E and S0 galaxies, but differences in the location of the peak of star formation is observed. Using model **M1**, the peak of star formation occurs at $1 < z < 2$ but for E and S0 the peak occurs more recently than for later types. On the other hand, the accretion of mass is faster in E and S0. Using **M6**, we find that the peak of star formation is located at $1 < z < 2$ for Sa and later types and at $z > 2$ for E and S0. Using this model, we obtain time scales for the accretion of the total mass similar for all the Hubble types.

- ρ_{SFR} decreases from $z = 2$ to $z = 0$. For the local Universe we obtain $\log \rho_{SFR} \sim -2$, in agreement with Madau & Dickinson (2014). The peak of ρ_{SFR} is located at $z = 2$ using **M1** and for $z \sim 2.5$ using **M6**. Beyond this peak, ρ_{SFR} decays for larger redshift. We find that the majority of the star formation at $z = 0$ takes place in late type spiral galaxies, which is also obtained from the MSSF. Analysing the different spatial components, we find most of the star formation in the local Universe is occurring outside galaxy centres, mainly in the disks of spirals. For $z > 1$ it is dominated by the inner regions. Both structural components are competing in building the ρ_{SFR} at $z = 1$.

- As it is observed from ρ_{Mass}, central regions of galaxies have accreted most of their mass at $z > 1$. Model **M6** points to a faster growth of central regions, having formed almost the total mass at $z > 2$. **M1** indicates that the most of the mass growth occurs for $z > 1$. On the other hand, regions at $1 < R < 2$ HLR have evolved more slowly than inner regions and over a more extended period of time.

- The $sSFR$ decays with time indicating that, on average, galaxies become progressively less efficient at forming stars. In the inner regions we observe the same behaviour and obtain larger values of $sSFR$ for late type galaxies. However, in the outer regions, the $sSFR$ is larger for E and S0 in the epoch of $z < 2$. This epoch is $0.2 < z < 0.5$ when using **M6** and $0.4 < z < 1$ when using **M1**. These results are in agreement with the two phase formation scenario for early type galaxies, where the central part formed most of its mass at high redshift and an outer envelope during a more extended period, in which galaxies grow in mass and significantly in size through dry mergers.
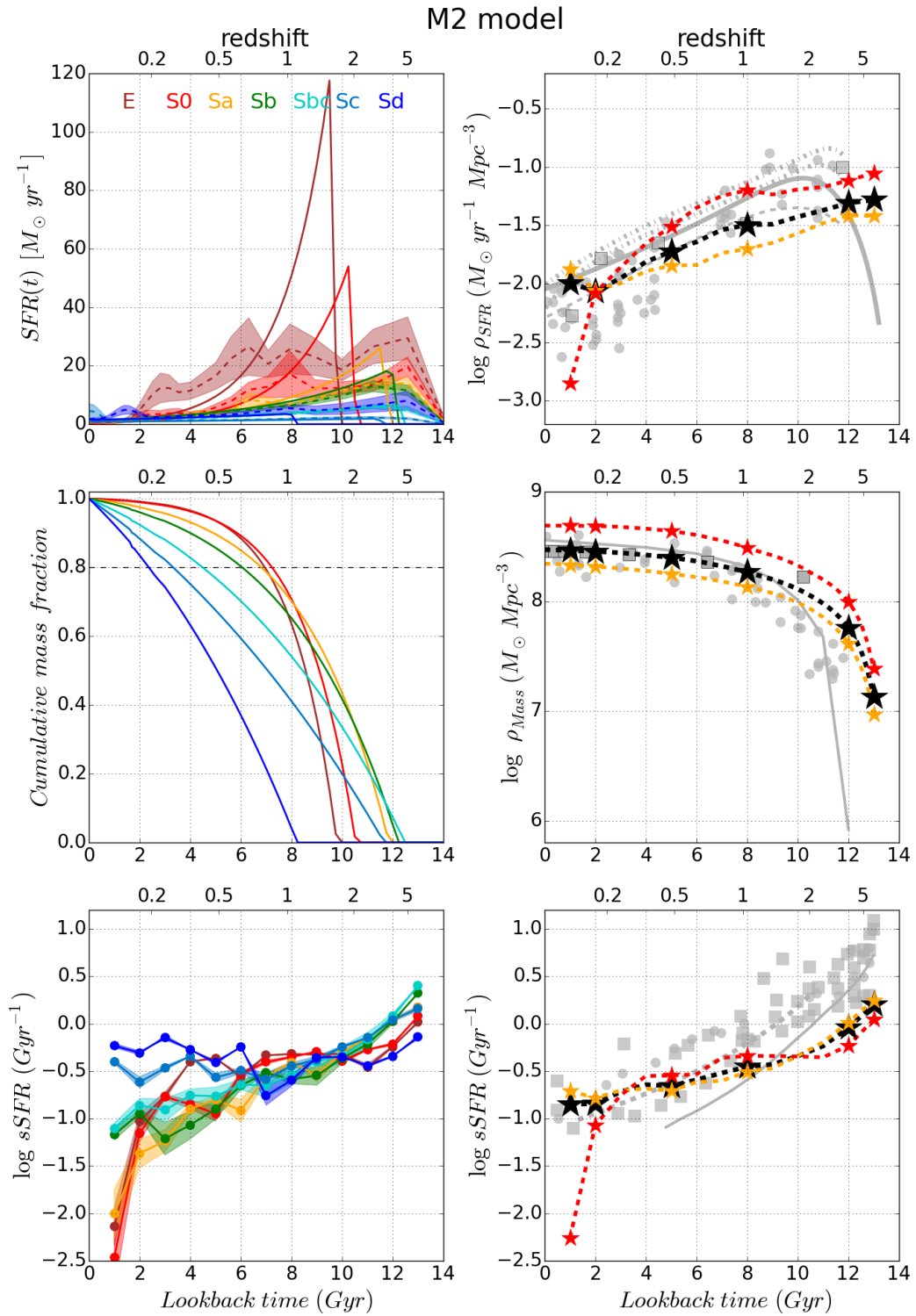
7.7   Dossier of figures

Figure 7.10 Same as Figure 7.1 using model **M2**.
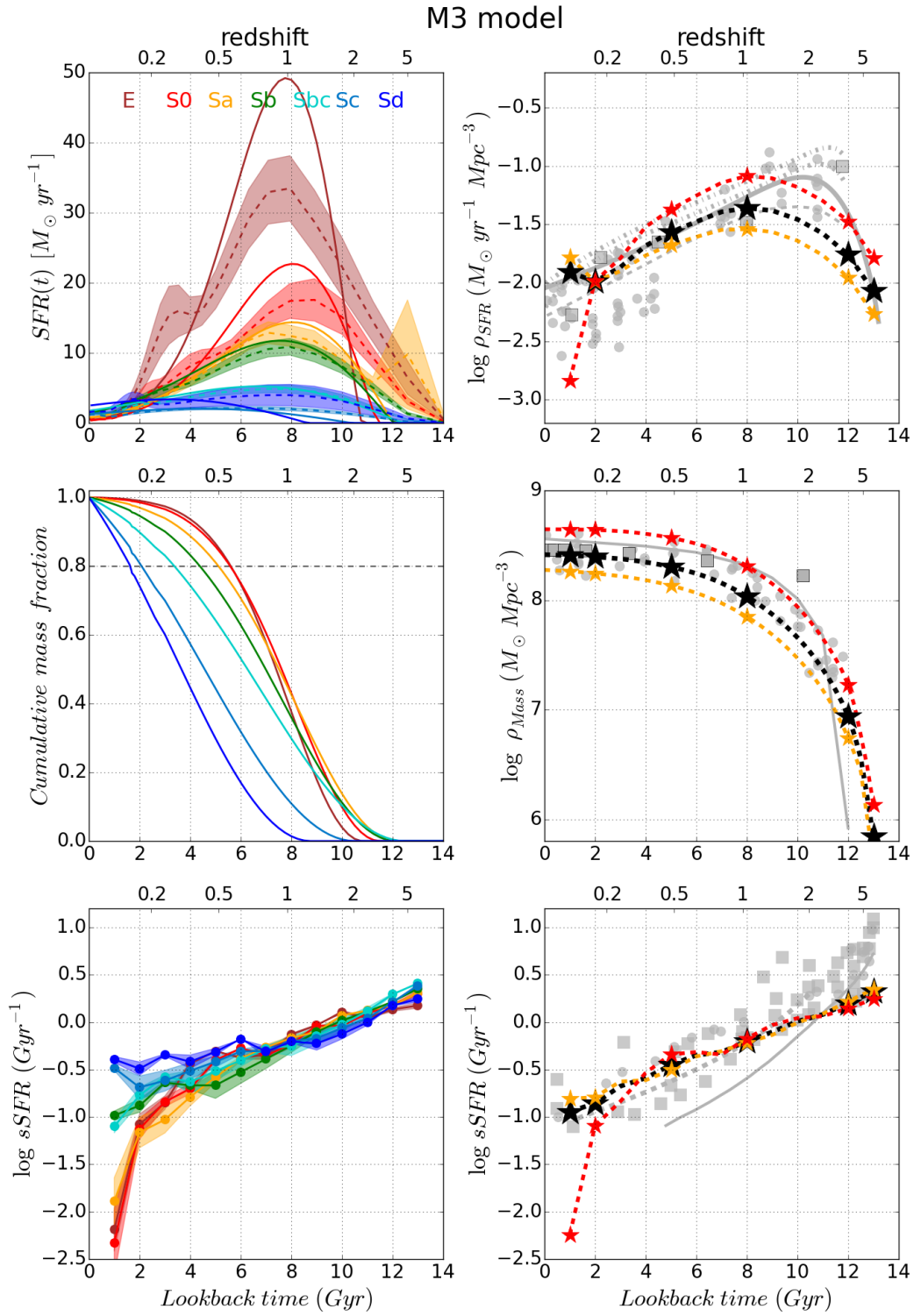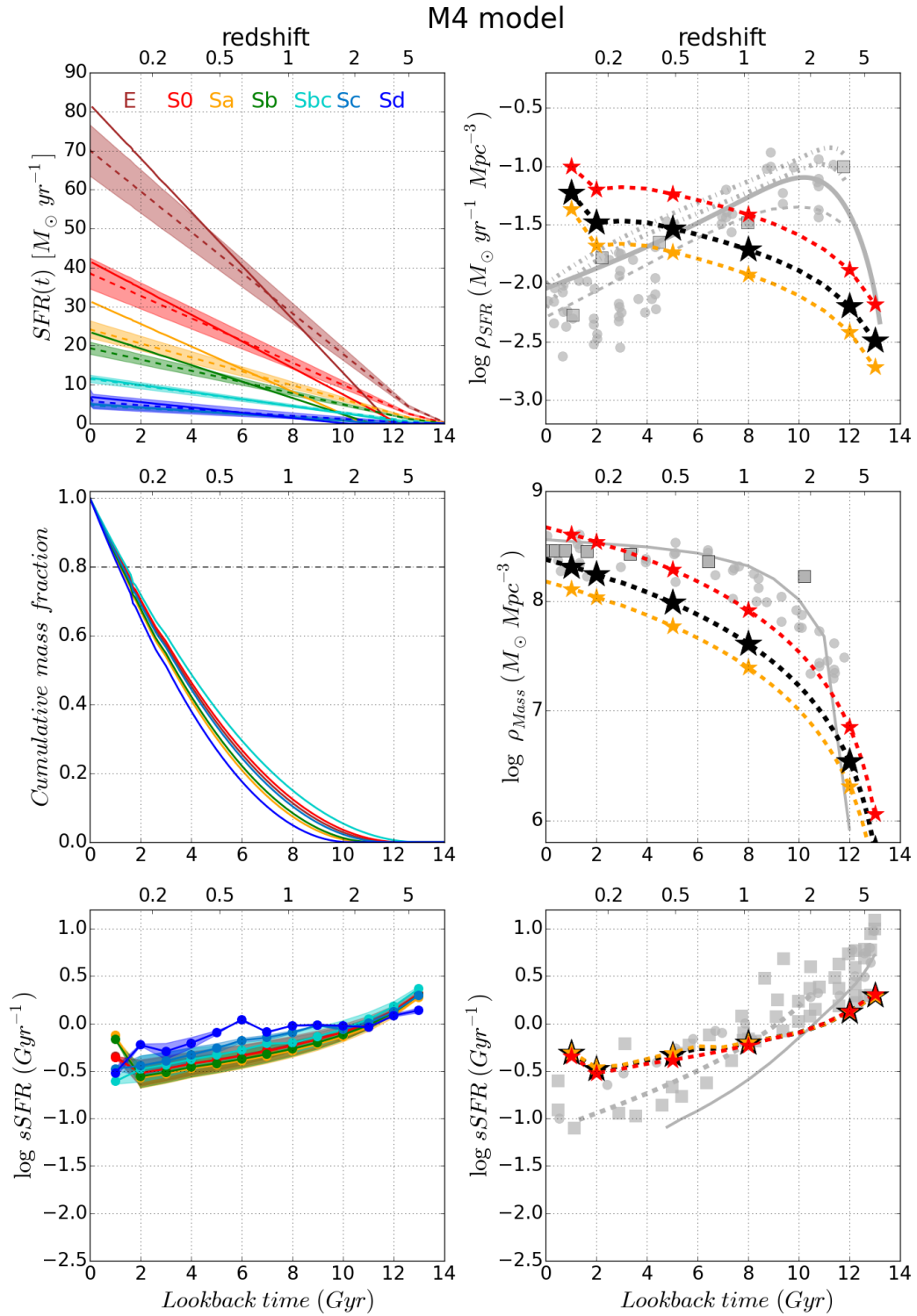
Figure 7.11 Same as Figure 7.1 using model **M3**.
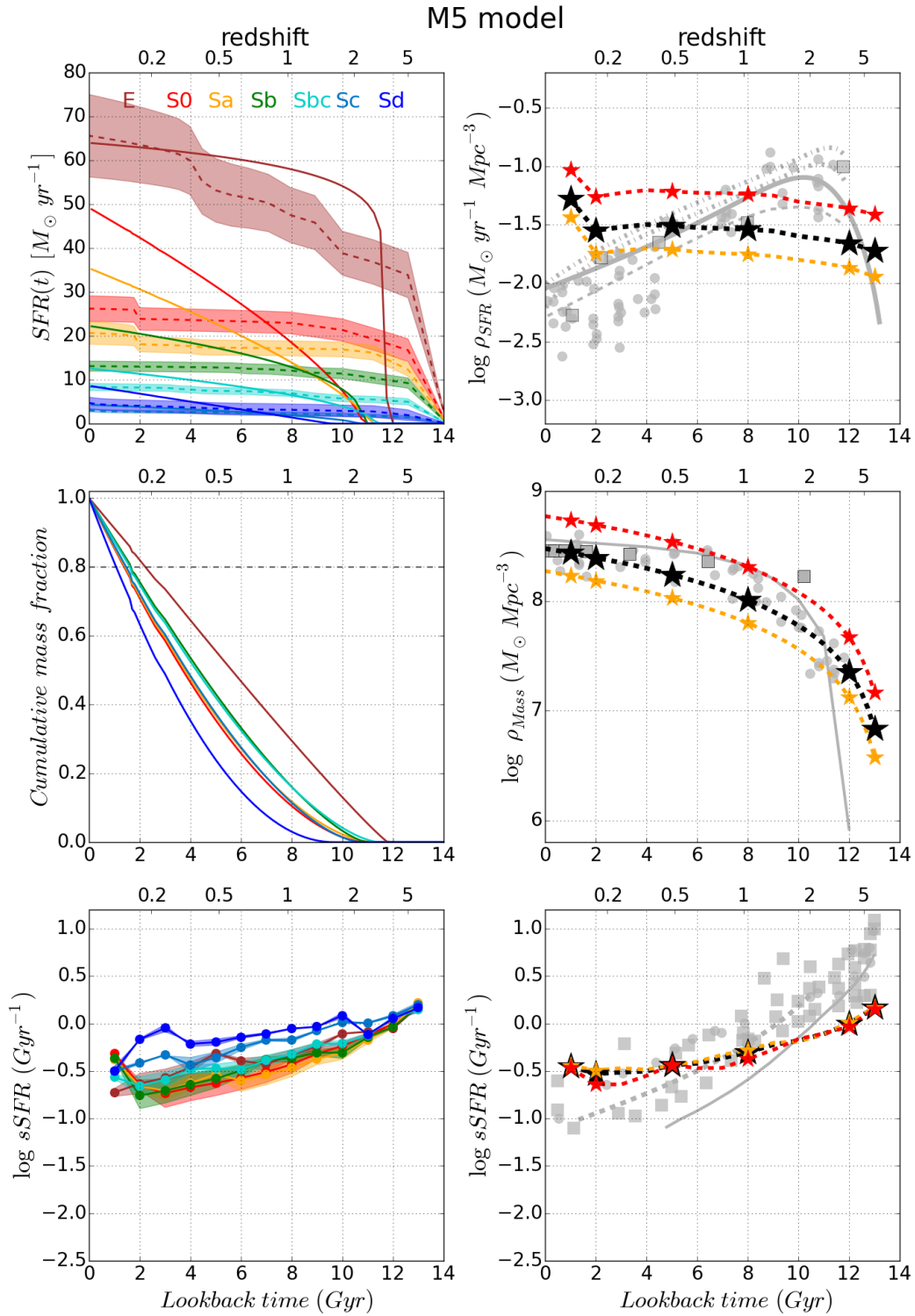
Figure 7.12 Same as Figure 7.1 using model **M4**.

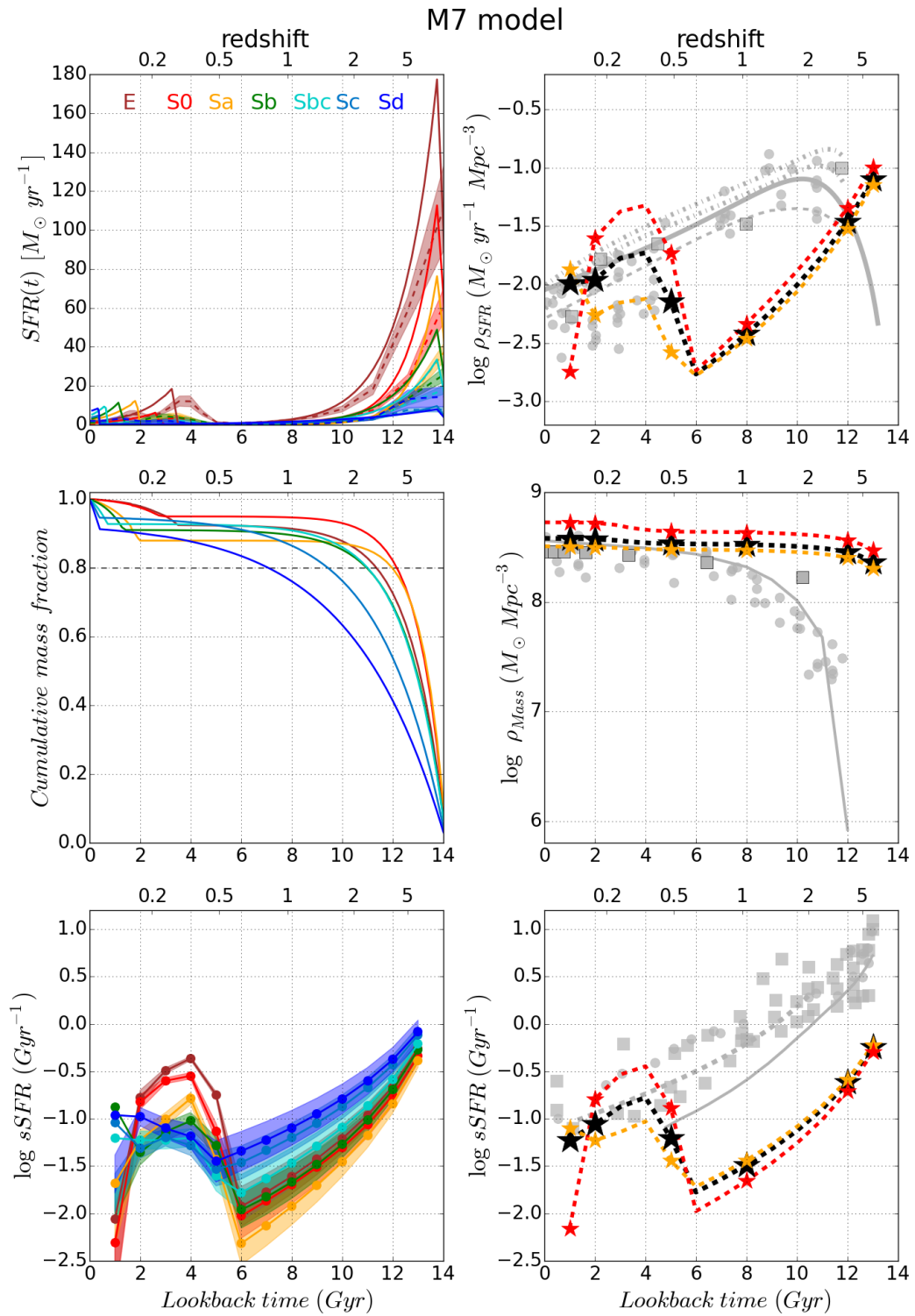Figure 7.13 Same as Figure 7.1 using model **M5**.
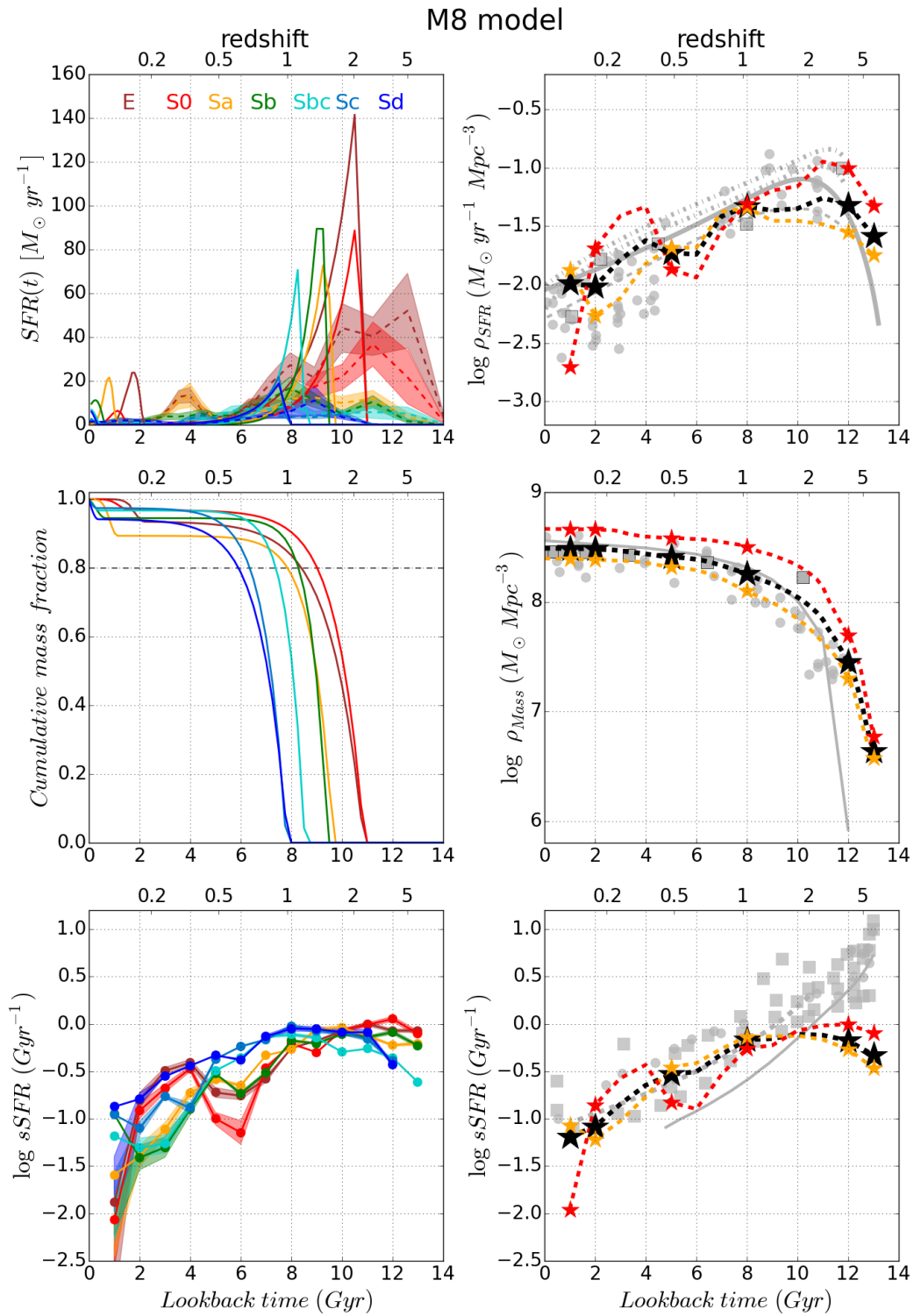
Figure 7.14 Same as Figure 7.1 using model **M7**.

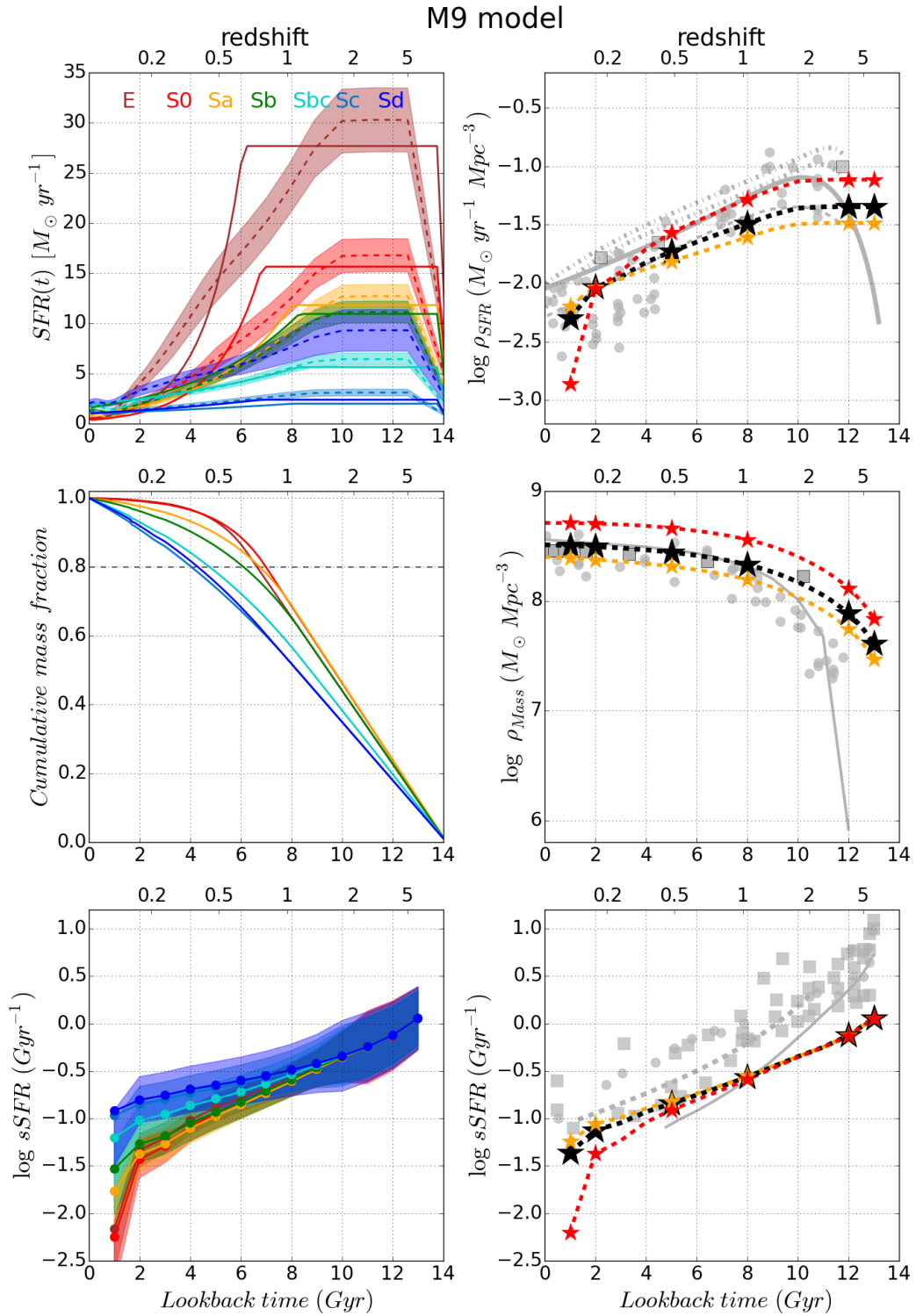Figure 7.15 Same as Figure 7.1 using model **M8**.

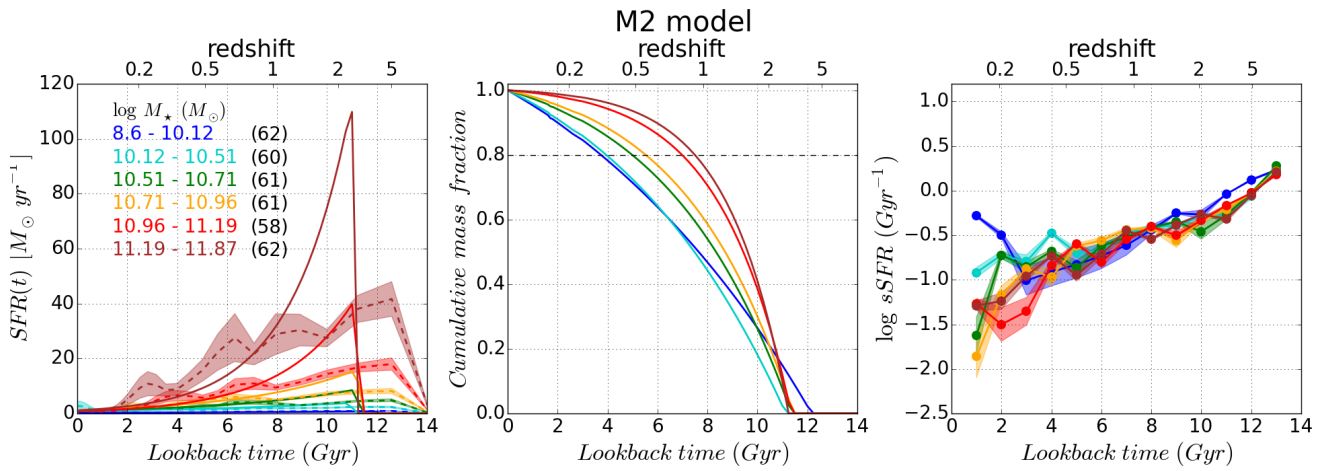Figure 7.16 Same as Figure 7.1 using model **M9**.

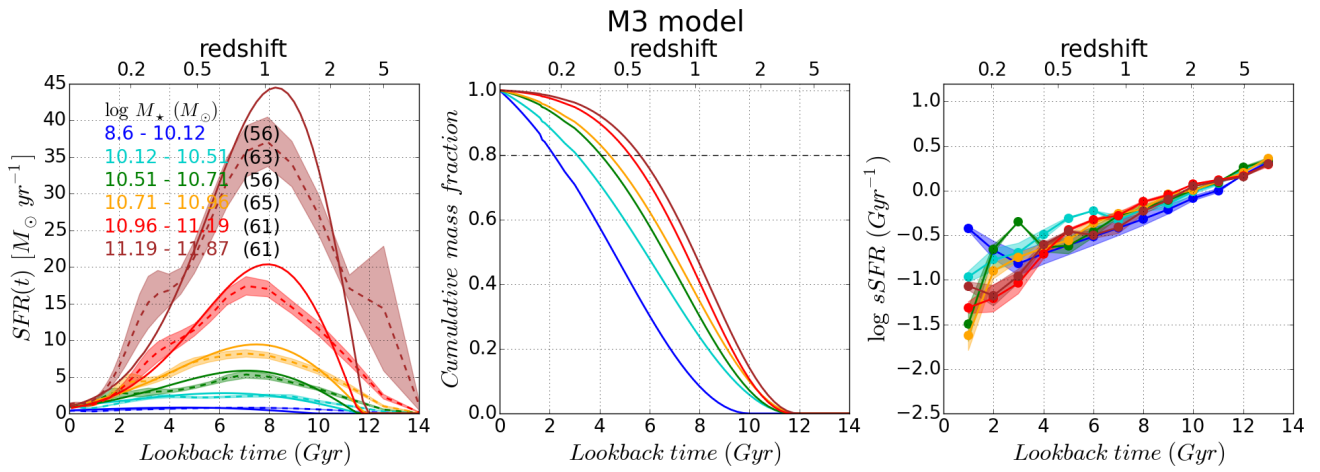Figure 7.17 Same as Figure 7.2 using model **M2**.

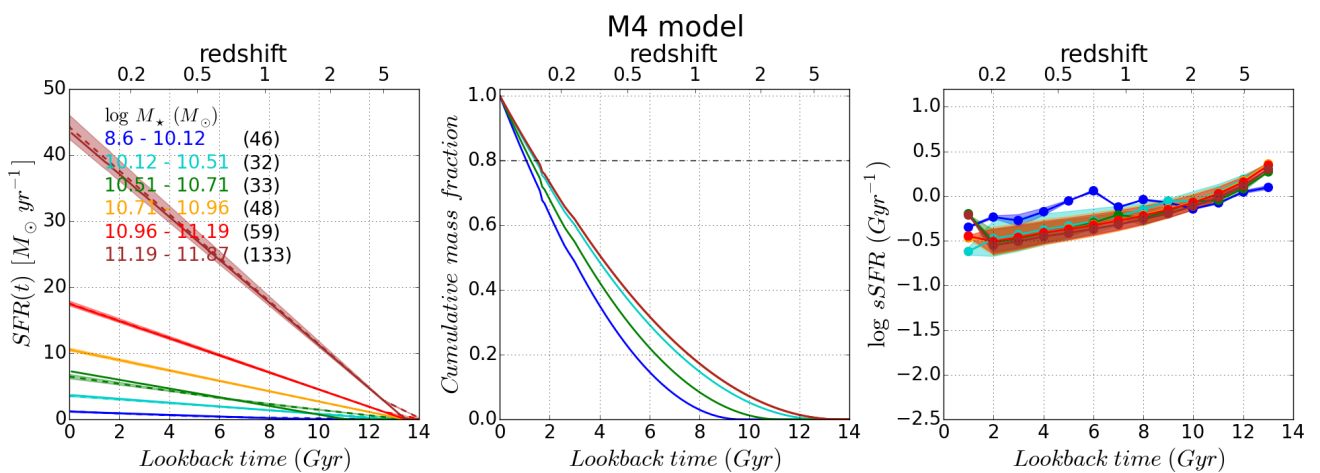Figure 7.18 Same as Figure 7.2 using model **M3**.

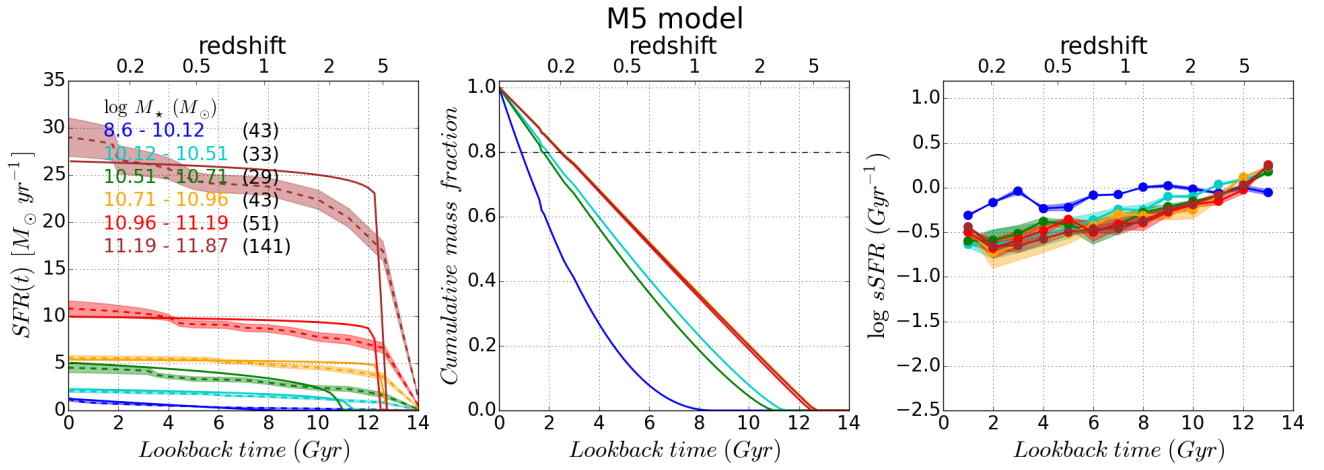Figure 7.19 Same as Figure 7.2 using model **M4**.
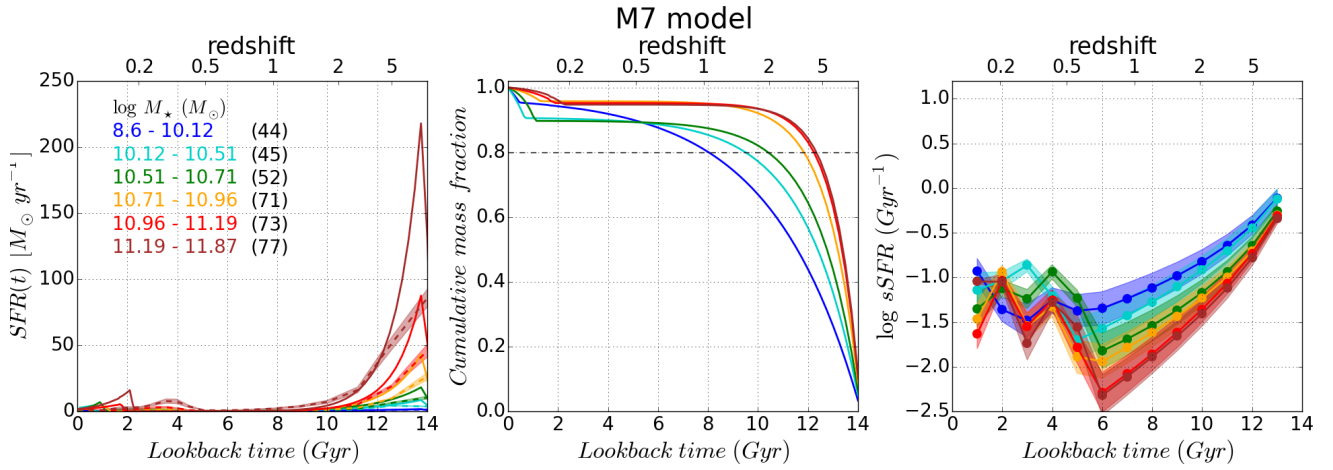
Figure 7.20 Same as Figure 7.2 using model **M5**.

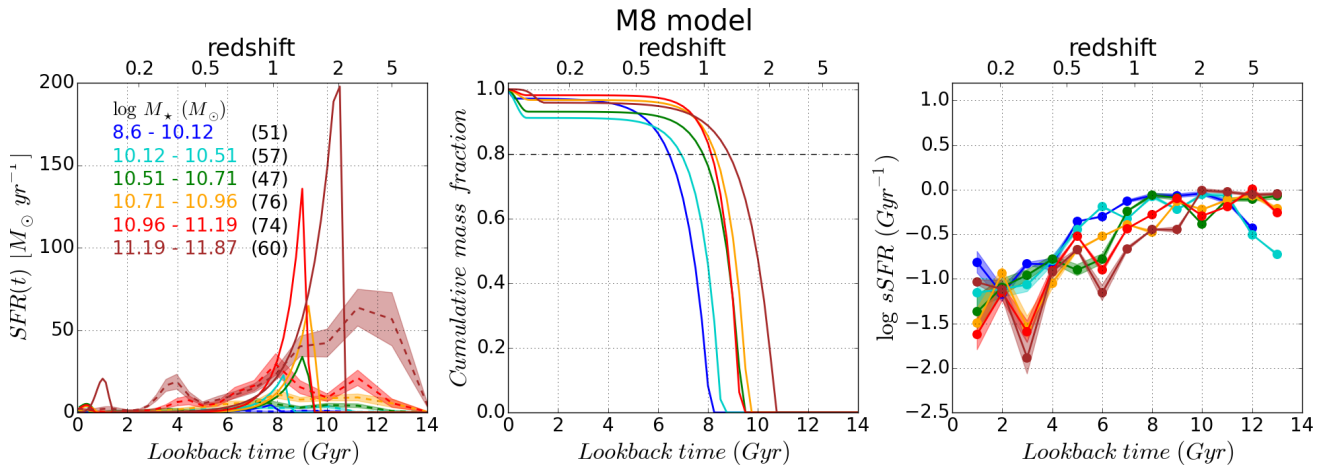
Figure 7.21 Same as Figure 7.2 using model **M7**.
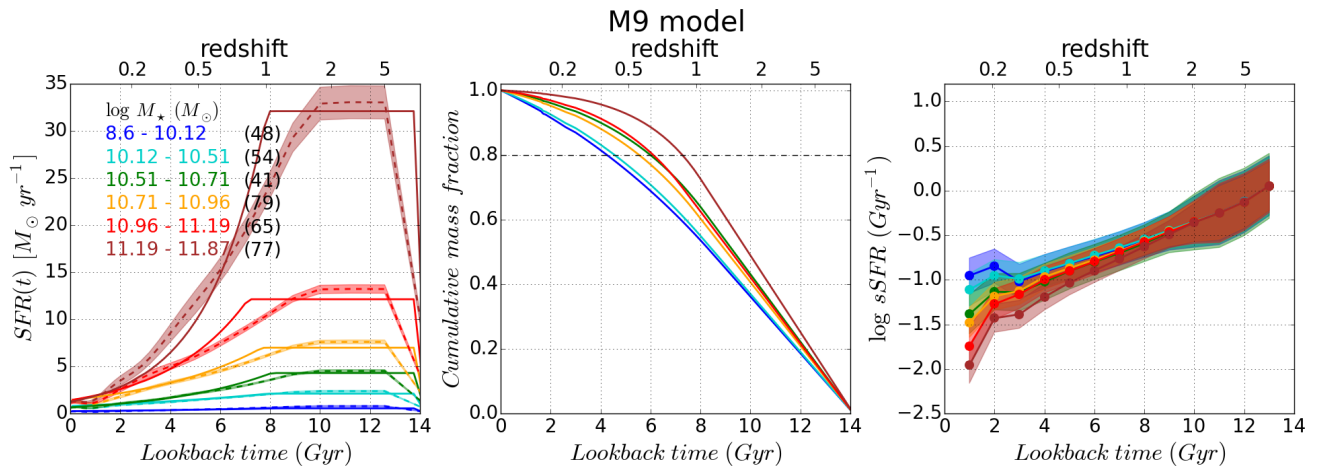

Figure 7.22 Same as Figure 7.2 using model **M8**.

Figure 7.23 Same as Figure 7.2 using model **M9**.

8

Conclusions

The study in this thesis is based on the statistical analysis of the stellar population properties of galaxies, combining different kinds of data. In particular we use Integral Field Spectroscopy (IFS) provided by CALIFA data and images in optical and UV range provided by SDSS and GALEX. The main goal is to obtain the cosmic evolution of the star formation and mass assembly history of galaxies using integrated and spatially resolved information of galaxies in the near Universe.

The objects in this study are those for which CALIFA+GALEX+SDSS data are available. This is a sub-sample of 366 galaxies which is unbiased with respect to the CALIFA mother sample, including from E to late type spirals and with $M_\star$ from 10^9 to 8×10^{11} $M_\odot$. The CALIFA mother sample is not a purely volume-limited sample, but can be "volume-corrected". As the sub-sample is representative of the CALIFA mother sample, our results can be used to estimate the star formation rate density, the specific SFR, and the stellar mass density up to $z > 2$, and the contribution of central (<0.5 HLR) and outermost regions ($1 < R < 2$ HLR) in nearby galaxies to these fundamental observables in astrophysical cosmology. We have developed two different methodologies to analyse the stellar population properties of galaxies, which use different kinds of data.

The first one is a new version of the full spectral fitting code STARLIGHT of Cid Fernandes et al. (2005), which in principle allows any combination of spectroscopy + photometry, although the actual application explored in this thesis focuses on the combined analysis of a 3700 - 7000 Å optical spectrum and NUV ($\sim$ 2274 Å) plus FUV ($\sim$ 1542 Å) photometry from GALEX. Using this code, we fit the observed data with a combination of $N_\star$ SSP. The code returns the fractional contribution x_j ($j = 1, ..., N_\star$) of the SSP with age t_j and metallicity Z_j to the model.

The second one is based on parametric SFHs, which allows any kind of parametrization. In this thesis nine different models are used. The code returns the PDFs for the parameters that define the SFH by fitting a combination of UV+optical photometry and different spectral features: H_β, $[MgFe]'$, and the 4000 Å break index (D4000). H_β and D4000 are more sensitive to the stellar age while $[MgFe]'$ is used as a metallicity tracer. D4000 and $[MgFe]'$ are measured in the CALIFA spectrum and H_β in the STARLIGHT synthetic spectrum.

Previously to the application to real data, the codes have been tested through a set of simulations

to gauge the performance of the codes under different levels of signal-to-noise (S/N).

The main specific conclusions are:

- Purely optical spectral fits are poor predictors of the UV properties, having a tendency to over-predict the UV fluxes. Besides, the new optical+UV fits reduce the uncertainties in the derived stellar properties. Including UV photometry in the fits, we better constrain the contribution of stellar populations younger than $\sim$ 300 Myr. UV+optical fits tend to replace $\leq$ 30 Myr components by populations in the neighbourhood of 100 Myr. Despite their poor performance in predicting the UV fluxes the optical fits yield stellar population properties which agree with those obtained with UV+optical fits to within the expected uncertainties. The differences are exclusively found in low-mass, late-type galaxies, precisely the systems where, because of their significant $\leq$ 300 Myr population, one would expect the addition of UV constraints to play a more relevant role. Also, the inclusion of UV constraints helps to mitigate degeneracies between age and metallicity.

- With STARLIGHT no initial assumption on the SFR(t) is done, while with the parametric method we set a prior for the parameters that define SFR(t). The main advantage with parametric models is that we can clearly explain the evolution of the star formation rate through an analytic function. Also the parameters of the model provide very useful information about star formation in galaxies. For example, in the "delayed-τ model used in this thesis, t_0 gives information about when the star formation begins and τ is the SFR e-folding time, which measures the time interval required to turn gas into stars. On the other hand, a troubled point is that for a statistical analysis of galaxies two different paths are possible, which produce different results: by averaging the mean parameters or by averaging the individual SFR(t), as we do with STARLIGHT. The second and main disadvantage is that if it is precisely the form of this function that we are trying to recover from the data we shall assume absolutely nothing about the SFR(t).

- The comparison with cosmological observational results from literature indicates that a "delayed-τ" model (**M1** in this thesis) provides the best results for describing the cosmic evolution of the star formation and mass assembly history of galaxies. The stellar population properties, $M_\star$, τ_V, $\langle \log t \rangle_L$ and $\langle \log Z \rangle_M$, derived with this model are in agreement with those obtained with STARLIGHT to within the expected uncertainties.

- A purely exponential profile (**M2**) and the "Sandage" profile (**M3**), the last one also being a "delayed-τ" model, provide similar results to those obtained with **M1**. However, they are not able to describe the evolution of the star formation rate density, the mass density and the specific star formation rate as well as **M1** does. On the other hand, the rising models have been used to study high redshift galaxies, but our results indicate that they can be discarded as representative of the star formation history of nearby galaxies. The two component models used in this thesis provide better fits in terms of $\chi 2$ as they introduce more parameters into the model, but they are worse than **M1** for describing the evolution of the fundamental observables analysed in this thesis.

The main specific results obtained with **M1** are:

- For Sa, Sb and Sbc we obtain $t_0 \sim$12 Gyr, which start to form earlier than E and S0, $t_0 \sim$10 Gyr. For Sc galaxies, $t_0 \sim$10 Gyr, similar to E galaxies, while Sd starts to form later on. We obtain that τ increases with the Hubble type, with more extended periods of star formation in late type spirals than early on. For E galaxies $\tau \sim 1.5$ Gyr and for Sbc and later spirals $\tau \sim 4$ Gyr.

- The results agree with a "downsizing" scenario, in which more massive galaxies form at higher redshift. t_{80} decreases from $\sim$7.5 Gyr for massive galaxies to $\sim$5.5 Gyr for lower mass galaxies. The same scenario is obtained with STARLIGHT, although with a larger range of variation, decreasing t_{80} from $\sim$7.5 Gyr for massive galaxies to $\sim$4 Gyr for lower mass galaxies.

- The analysis of the inner and outer regions suggest an inside-out formation scenario of galaxies, with $t_0^{in} > t_0^{out}$ for all the Hubble types. Sbc and earlier type galaxies start to form at the same epoch ~ 12 Gyr ago. Envelope of E and S0 start to form at later epoch than outer regions in Sa, Sb and Sbc. Sc and Sd galaxies start to form later than earlier types, but at $t_0 > 10 Gyr$. Their envelopes form later on. We find that t_{80} decreases with the morphology for the inner and outer regions, the values for the outer regions being lower than those for the inner ones for Sc and earlier types. For Sb and earlier types $t_{80} \sim$ 7-9 Gyr for the inner regions and $\sim$ 6-7 Gyr for the outer ones. For Sbc, Sc and Sd galaxies we obtain $t_{80} \sim$ 7, 5 and 4.5 Gyr for the inner regions, respectively, while for the outer ones $t_{80} \sim$ 7, 5 and 4.5 Gyr.

- The ρ_{SFR} results indicate that the majority of the star formation at $z = 0$ takes place in late type spirals. We find that most of the star formation at $z = 0$ occurs outside galaxy centres, mainly in the disks of spirals, while for $z > 1$ it is dominated by the actual inner regions. Both structural components are competing in building the ρ_{SFR} at $z = 1$. Our values are in agreement with those obtained by Fardal et al. (2007), although other cosmological results show a larger peak of ρ_{SFR} at $z = 2$. For $z = 0$, 2 and 5 we obtain log ρ_{SFR} $(M_\odot yr^{-1} Mpc^{-3}) = -2.04, -1.34$ and -1.41, respectively.

- ρ_{Mass} increases from $z = 5$ to $z = 0$. Our results are in agreement with those obtained from cosmological surveys, and in particular with Madau & Dickinson (2014) from $z = 0$ to $z = 2$. For $z = 0$, 2 and 5 we obtain log ρ_{Mass} $(M_\odot Mpc^{-3}) = 8.47, 7.97$ and 7.35 , respectively. The analysis of ρ_{Mass} indicates that regions at $1 < R < 2$ HLR have assembled their mass more slowly than inner regions and over a more extended period of time. We obtain that the central regions of galaxies have accreted most of their mass at $z > 1$. In terms of morphology, we obtain that E and S0 galaxies have assembled their mass in a shorter period of time than later types, Sc and Sd galaxies being those with a slower growth.

- The $sSFR$ declines as the universe evolves. This indicates that, on average, galaxies become progressively less efficient at forming stars. Our estimation of $sSFR$ agrees well with the cosmological surveys results, which find that $sSFR$ decreases as $(1 + z)^2$ from $z = 2$ to $z = 0$ (Elbaz et al. 2011). However, for $z > 2$ our derived $sSFR$ increases with a lower slope. For the different

Hubble types, we obtain similar curves for $z > 1$. For $z < 1$ the $sSFR$ decreases with a different slope, according to morphological type. For E and S0 the $sSFR$ decreases reaching $\log sSFR$ $(Gyr^{-1}) \sim -2.3$ at $z = 0$, while for Sd galaxies we obtain $\log sSFR (Gyr^{-1}) \sim -0.5$. The values at $z = 0$ correlate with morphology, decreasing from Sd to E galaxies. For the inner regions we obtain similar results to the whole galaxies, but for outer regions in E and S0 galaxies we obtain that $sSFR$ increases at $0.2 < z < 1$. This is in agreement with the two phase formation scenario for early type galaxies, where the central part formed most of its mass at high redshift and an outer envelope during a more extended period, in which galaxies grow in mass and significantly in size through dry mergers.

A

Composite stellar populations

A Composite Stellar Population (CSP) is a collection of stars formed at different time and with different initial chemical compositions. The SSPs are the building blocks for these more complex stellar systems. The CSPs differ from SSPs in three respects:

1. They contain stars with a range of ages given by their SFR.

2. They contain stars with a range in metallicities as given by their time-dependent metallicity distribution function, P(Z, t).

3. They contain dust.

These components are combined in the following way:

$$F_{\mathrm{CSP}}(\lambda) = \int_t \int_Z \mathrm{SFR(t)} * \mathrm{P(Z,\ t)} * \mathrm{SSP}(\lambda; \mathrm{t},\ \mathrm{Z}) * e^{-\tau_V(t)}\, dZ\, dt. \tag{A.1}$$

In this thesis, the base used in STARLIGHT to perform the photometric+spectral fits is composed by a collection of SSP_i (i= $1, ..., N$), with age t_i and metallicity Z_i. However, there are other kind of bases that can be used to fit the desired observables of galaxies. In particular, we have created a base of CSPs using the SSPs. Equation A.1 is the general definition of a CSP but, in our case, each one of the CSPs have the same initial chemical composition and we do not consider dust. Besides, we assume a constant SFR of $1 M_\odot yr^{-1}$. Thus, we begin by defining t_j (i= $1, ..., M$), which are the different ages of our CSPs, and Δ_{t_j}, which is the time interval for CSP_j. The time interval can depend on j or it can be fixed for all or some CSPs. Then, we construct the CSPs as follow:

- Lets define t_i^+ as $(t_i + t_{i+1})/2$ and t_i^- as $(t_{i-1} + t_i)/2$ for $i = 1, ..., N$, where t_i is the age of SSP_i. Then we define the CSP_j of age t_j as

$$\mathrm{CSP}_j(\lambda, Z, t_j) = \int_{t_j - \Delta t_j/2}^{t_j + \Delta t_j/2} \mathrm{SFR(t)} \times \mathrm{SSP}(\lambda, t, Z)\, dt = \sum_{t_j - \Delta t_j/2}^{t_j + \Delta t_j/2} \mathrm{SSP}(\lambda, t_i, Z) \times\ w_i, \tag{A.2}$$

where

$$w_i = \int_{t_i^-}^{t_i^+} SFR(t)\,dt.$$

- To deal with boundaries, we integrate only until the corresponding age. Lets define t_k as the age of the SSP such as $t_j + \Delta t_j/2 \in [t_k^-, t_k^+]$. Then we define w_k as

$$w_k = \int_{t_k^-}^{t_j+\Delta t_j/2} SFR(t)\,dt.$$

In the same way, we define t_h as the age of the SSP such as $t_j - \Delta t_j/2 \in [t_h^-, t_h^+]$. Then we define w_h as

$$w_h = \int_{t_j-\Delta t_j/2}^{t_h^+} SFR(t)\,dt.$$

- Finally, we scale CSP_j to $1M_\odot$ dividing by

$$\int_{t_j-\Delta t_j/2}^{t_j+\Delta t_j/2} SFR(t)\,dt.$$

There are some advantages in using this kind of base. One of them is the interpretation and robustness of the results. Using a base composed by SSPs we need to include a large number of them to obtain the SFH. We obtain an stochastic SFH where is difficult to distinguish between two different SSPs with similar ages. Varying the mass fraction between these SSPs with near ages, a similar spectral energy distribution can be obtained. However, each one of the CSPs contains information of all the SSPs in a time interval. Thus, by one hand, the number of CSPs in the base is lower than for SSPs, and, on the other hand, the differences between them are larger, being each one of the CSPs representative of a different epoch. It means that the mass fraction obtained in the fits for the CSPs are more robust than the obtained for the SSPs. In STARLIGHT the total time to achieve the fit is $\propto N^2$, where N is the number of elements in the base. Thus, as the CSP base contains less element than an SSP base, the computational time is significantly reduced.

This technique has been used in González Delgado et al. (2017), which uses CSPs to build the base used in STARLIGHT to perform the full spectral fit. These CSPs were built using the whole set of SSPs from Vazdekis et al. (2015) for populations older than $t = 63$ Myr, and from the GRANADA models of González Delgado et al. (2005) for younger ages. The base contains 144 CSP spectra distributed in 18 age bins and 8 metallicities. Each of these CSP contains stars with a range of ages, but all of the same metallicity. They are obtained assuming that the star formation has proceeded at a constant rate of $1M_\odot yr^{-1}$ for a period of $\Delta \log t = 0.2$ dex (except for the two younger components, for which $\Delta \log t = 0.4$ dex) in 18 different epochs at t_0 (Gyr) = 0.00245, 0.00575, 0.011, 0.018, 0.028, 0.045, 0.072, 0.114, 0.180, 0.285, 0.455, 0.725, 1.14, 1.18, 2.85, 4.55, 7.25, 11.50. Some results from this work are shown in the next figures as an example.
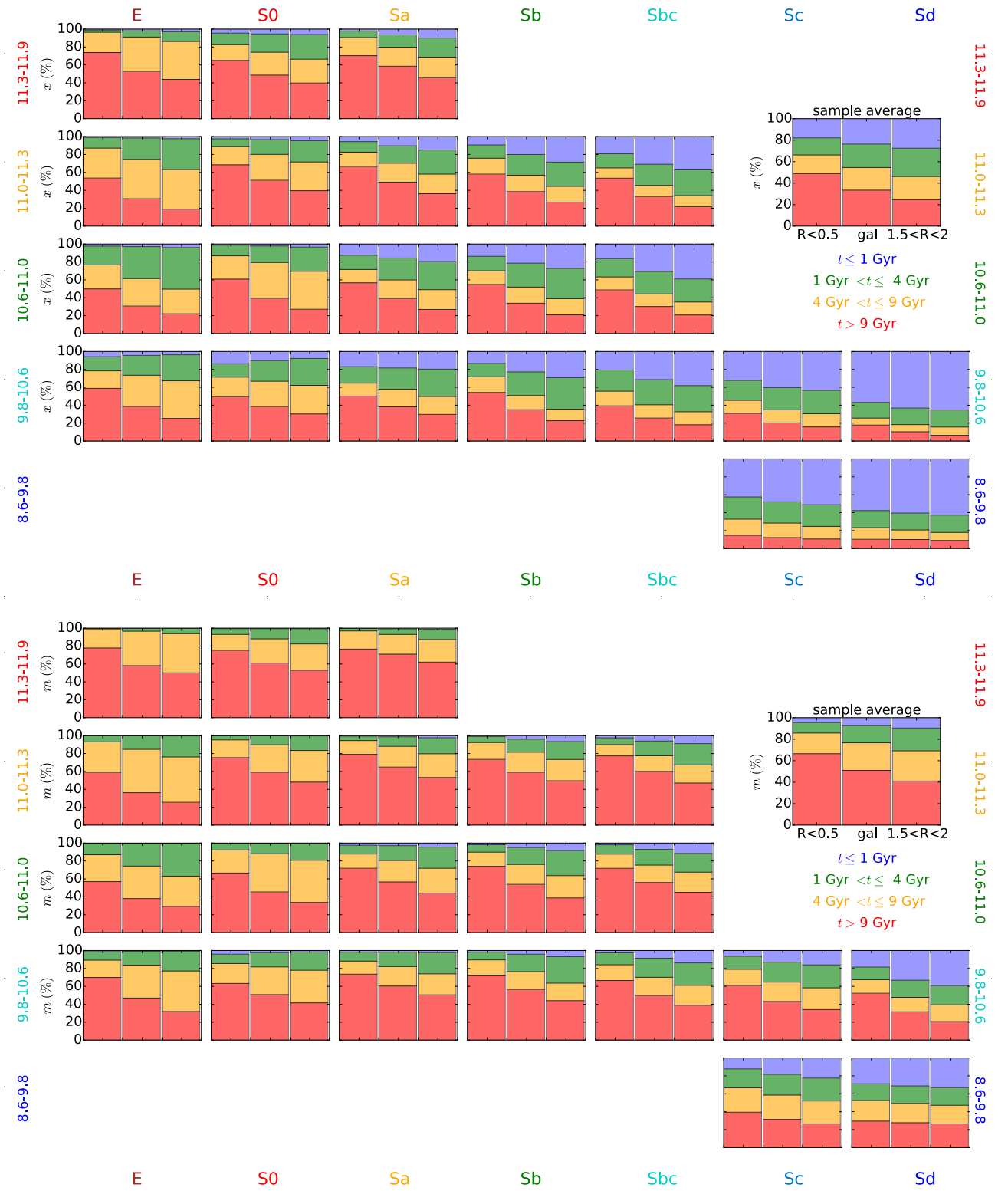
Figure A.1 Average mass (bottom panels) and light (upper panels) fractions due to stars in different age ranges as a function of the Hubble type and $M_\star$. Age (lookback time) ranges are color coded: old, intermediate, and young populations defined as those with $age \leq 9$ Gyr (red), 4 Gyr $< age < 9$ Gyr (orange), 1 Gyr $< age < 4$ Gyr (green), and $age \leq 1$ Gyr (blue), respectively. The averaged values are presented for different galaxy regions: the inner region $R \leq 0.5$ HLR (left bar); the whole galaxy $R \leq 2$ HLR (middle bar), which is equivalent to the central regions; and the outer regions $1.5 < R < 2$ HLR (right bar).

Figure A.1 is obtained by González Delgado et al. (2005) using the base of CSPs. The figure tracks the percent contributions in light (top panels) and mass (bottom) of four stellar populations components. The results are stacked in seven morphology bins and five mass bins. Each sub-panel is divided in three columns that show the averaged light (x) or mass (m) fraction for regions located (i) inside the central 0.5 HLR (left), (ii) nearly the whole galaxy ($R < 2$ HLR, equivalent to the central regions) (right), and (iii) at a distance similar to the solar neighborhood ($1.5 < R < 2$ HLR) (right).
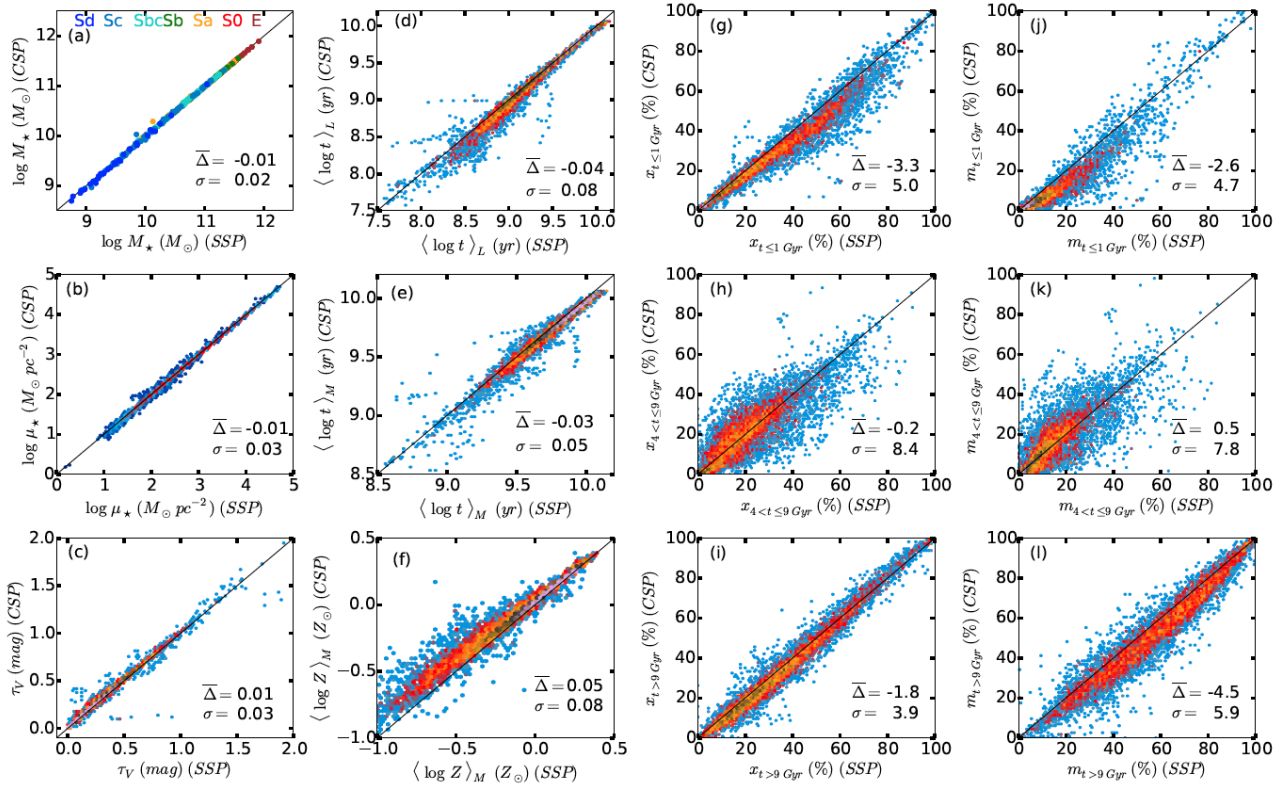

Figure A.2 Comparison of spatial resolved properties of galaxies analysed by González Delgado et al. (2017) with CSPs and SSPs. Each panel lists the averaged difference (CSP $-$ SSP) $\overline{\Delta}$ and σ. Colour in top left panel indicates the Hubble type. In the other panels the colour indicates the density of points.

Figure A.2 compares the spatial resolved properties of CALIFA galaxies analysed by González Delgado et al. (2017) obtained with CSPs and SSPs. Top left panel compares the total stellar mass and the colour codes the Hubble type. In the rest of panel the spatial resolved properties are shown and the colour indicates the density of points. The figure shows that the differences between both set of bases are small, obtaining similar stellar population properties. The lower differences are obtained for the total stellar mass, with $\overline{\Delta} \pm \sigma = -0.01 \pm 0.02$, which are similar to those found for the mass surface density ($\mu_\star$) and the attenuation (τ_V). For $\langle \log t \rangle_L$ we obtain $\overline{\Delta} \pm \sigma = -0.04 \pm 0.08$, obtaining the same dispersion for $\langle \log Z \rangle_M$ and $\overline{\Delta} = 0.05$. For $\langle \log t \rangle_M$ we obtain less differences, with $\overline{\Delta} \pm \sigma = -0.03 \pm 0.05$. On average we obtain younger ages with the CSPs base, but larger metallicities.

Comparing the light and mass fractions for different stellar components, the largest dispersion is obtained for the intermediate component in both cases, $4 < t < 9$ Gyr, but also the lowest offset. For $x_{4<t<9\,\text{Gyr}}$, $\overline{\Delta} \pm \sigma = -0.02 \pm 8.4\,\%$ and for $m_{4<t<9\,\text{Gyr}}$, $\overline{\Delta} \pm \sigma = 0.5 \pm 7.8\,\%$. The figure shows that the differences between the light and mass fraction are also small, with the largest being $\sim 10\,\%$ for $m_{>9\,\text{Gyr}}$.

B

SFR calibration

We can calibrate FUV luminosity (L_{FUV}) as an SFR (ψ) indicator. Let see how to do it.

- $dM(t) = \psi(t)dt$ is the mass turned into stars between t and $t + dt$

- $l(t)$ is a function which describes the evolution of some generic radiative output per unit formed mass of an SSP. In our case we will take FUV luminosity ($l_{FUV}(t)$) as $l(t)$ function. So, $l_{FUV}(t)$ describes the evolution of FUV luminosity with time.

The amount of l-light we receive from stars formed t years ago is just

$$d\Lambda(t) = l(t)dM(t). \tag{B.1}$$

We assume that the SFR has been constant from a period of T years ago until today ($t = 0$) and zero before that. Adding all the stars formed since $t = T$ we would see, today, a total of

$$\Lambda = \Lambda(T, \psi) = \int_0^T l(t)dM(t). \tag{B.2}$$

Under the previous hypothesis

$$\int_0^T l(t)dM(t) = \psi \int_0^T l(t)dt. \tag{B.3}$$

Taking $l_{FUV}(t)$ (units of $L_\odot/M_\odot$), we have

$$L(FUV) = \psi_{FUV} \int_0^T l_{FUV}(t)dt. \tag{B.4}$$

We define

$$l_{FUV}^S(T) = \int_0^T l_{FUV}(t)dt. \tag{B.5}$$

In Fig.B.1 we see the evolution of l_{FUV}^S in function of time. For models with solar metallicity, $l_{FUV}^S(t)$ reaches the 90% of the total l_{FUV}^S at $T = 90.48$ Myr. Using this value we obtain

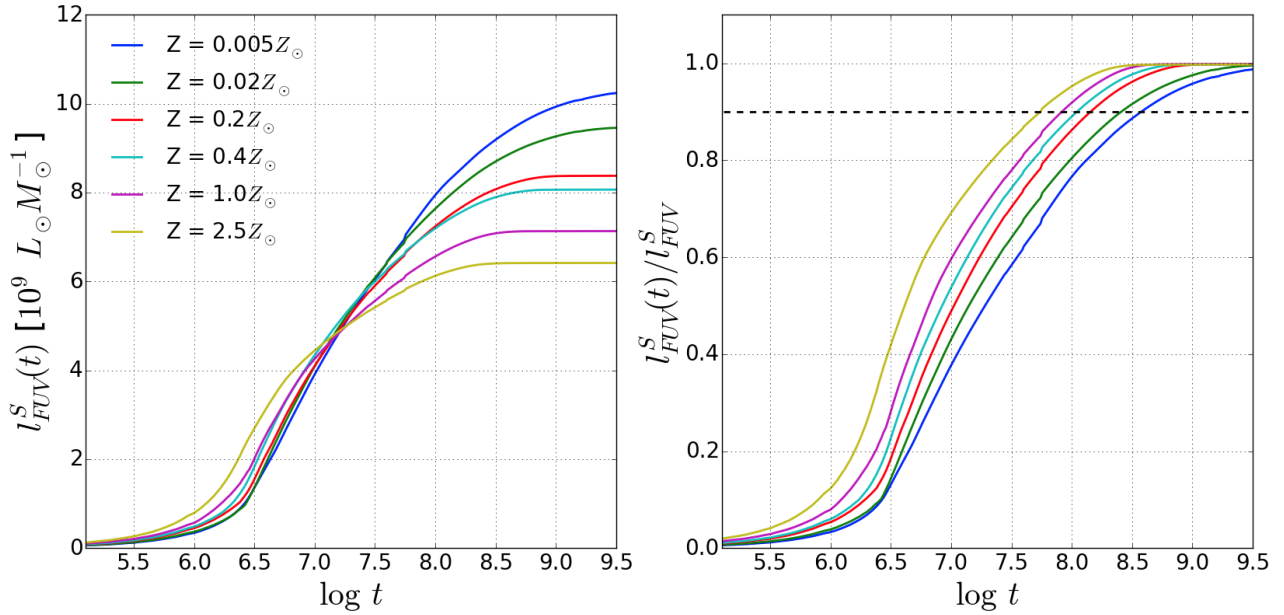$$l_{FUV}^S(90.48Myr) = 64.9208 \times 10^8 \, L_\odot M_\odot^{-1}. \tag{B.6}$$

Figure B.1 Left panel: The time-evolution of FUV luminosity of SSP models for six metallicities (from $0.005Z_\odot$ to $2.5Z_\odot$). Right panel: The same from left panel but normalized by the total value of l^S_{FUV}. The black dashed line shows the 90% of the total l^S_{FUV}.

SFR_{FUV}					
%	80	85	90	95	99
T (Myr)	38	55	90.48	160.9	321.02
$l^S_{FUV}(T)(10^8 L_\odot M_\odot^{-1})$	57.38	60.71	64.92	68.41	70.84

Table B.1 Calibration of SFR using the FUV indicator. The table lists different values (for solar metallicity) in function of the percentage of the total FUV luminosity.

Then, from equation B.4 we derive ψ_{FUV} ($\equiv$ SFR),

$$\frac{SFR_{FUV}}{M_\odot yr^{-1}} = 15.40337 \times \frac{L(FUV)}{10^{11} L_\odot}. \tag{B.7}$$

To derive the SFR we have chossen T at which $l^S_{FUV}(t)$ reaches the 90% of the total l^S_{FUV}, but you can choose another percentage to compute it. In Table B.1 we show several values.

Maybe you would like to choose another metallicity different from solar metallicity to calibrate the SFR and Table B.2 show T and value at with $l^S_{FUV}(t)$ reaches the 90% of the total value for different metallicities. The values obtained for T match with the life time of B stars.

SFR_{FUV} (90%)						
Z	$0.005Z_\odot$	$0.02Z_\odot$	$0.2Z_\odot$	$0.4Z_\odot$	$Z_\odot$	$2.5Z_\odot$
T (Myr)	404.14	286.12	160.90	113.91	90.48	57.09
$l^S_{FUV}(T)(10^8 L_\odot M_\odot^{-1})$	93.85	86.26	76.47	72.98	64.92	58.33

Table B.2 Calibration of SFR using the FUV indicator. The table lists values of $l^S_{FUV}(t)$ reaching 90% in function of metallicity.

We obtain an empirical (though model dependent) way of measuring the SFR (ψ) using the FUV luminosity, which was used in Cortijo-Ferrero et al. (2017).

C

List publications

The following list of scientific publications represents the different contributions done during the period of this thesis:

- CALIFA, the Calar Alto Legacy Integral Field Area survey. II. First public data release (Husemann et al., 2013)

- Resolving galaxies in time and space: II: Uncertainties in the spectral synthesis of datacubes (Cid Fernandes et al., 2014)

- The star formation history of CALIFA galaxies: Radial structures (González Delgado et al., 2014b)

- Insights on the Stellar Mass-Metallicity Relation from the CALIFA Survey (González Delgado et al., 2014a)

- CALIFA, the Calar Alto Legacy Integral Field Area survey. III. Second public data release (García-Benito et al., 2015)

- The CALIFA survey across the Hubble sequence. Spatially resolved stellar population properties in galaxies (González Delgado et al., 2015)

- Simultaneous spectroscopic and photometric analysis of galaxies with STARLIGHT: CALIFA+GALEX (López Fernández et al., 2016)

- Star formation along the Hubble sequence. Radial structure of the star formation of CALIFA galaxies (González Delgado et al., 2016)

- CALIFA, the Calar Alto Legacy Integral Field Area survey. IV. Third public data release Sánchez et al. (2016a)

- Star formation histories in mergers: the spatially resolved properties of the early-stage merger luminous infrared galaxies IC 1623 and NGC 6090 (Cortijo-Ferrero et al., 2017)

Bibliography

Abazajian, K. N., Adelman-McCarthy, J. K., Agüeros, M. A., et al. 2009, ApJS, 182, 543

Abel, T., Bryan, G. L., & Norman, M. L. 2002, Science, 295, 93

Abramson, L. E., Gladders, M. D., Dressler, A., et al. 2016, ApJ, 832, 7

Acquaviva, V., Gawiser, E., & Guaita, L. 2011, ApJ, 737, 47

Ahn, C. P., Alexandroff, R., Allende Prieto, C., et al. 2014, ApJS, 211, 17

Alongi, M., Bertelli, G., Bressan, A., et al. 1993, A&AS, 97, 851

Aumer, M. & White, S. D. M. 2013, MNRAS, 428, 1055

Baade, W. 1944, ApJ, 100, 137

Baldry, I. K., Glazebrook, K., Brinkmann, J., et al. 2004, ApJ, 600, 681

Balogh, M. L., Morris, S. L., Yee, H. K. C., Carlberg, R. G., & Ellingson, E. 1999, ApJ, 527, 54

Barway, S., Wadadekar, Y., Vaghmare, K., & Kembhavi, A. K. 2013, MNRAS, 432, 430

Bastian, N., Covey, K. R., & Meyer, M. R. 2010, ARA&A, 48, 339

Bell, E. F., Wolf, C., Meisenheimer, K., et al. 2004, ApJ, 608, 752

Bertin, E. & Arnouts, S. 1996, A&AS, 117, 393

Blanton, M. R. 2006, ApJ, 648, 268

Blanton, M. R., Hogg, D. W., Bahcall, N. A., et al. 2003, ApJ, 594, 186

Bloecker, T. 1995, A&A, 299, 755

Bressan, A., Chiosi, C., & Fagotto, F. 1994, ApJS, 94, 63

Bressan, A., Fagotto, F., Bertelli, G., & Chiosi, C. 1993, A&AS, 100, 647

Brinchmann, J., Charlot, S., White, S. D. M., et al. 2004, MNRAS, 351, 1151

Bromm, V. & Larson, R. B. 2004, ARA&A, 42, 79

Bruzual, G. & Charlot, S. 2003, MNRAS, 344, 1000

Bruzual A., G. 1983, ApJ, 273, 105

Bruzual A., G. & Charlot, S. 1993, ApJ, 405, 538

Burstein, D., Faber, S. M., Gaskell, C. M., & Krumm, N. 1984, ApJ, 287, 586

Calzetti, D., Armus, L., Bohlin, R. C., et al. 2000, ApJ, 533, 682

Cappellari, M., Bertola, F., Burstein, D., et al. 2001, ApJ, 551, 197

Cappellari, M. & Copin, Y. 2003, MNRAS, 342, 345

Cattaneo, A., Dekel, A., Devriendt, J., Guiderdoni, B., & Blaizot, J. 2006, MNRAS, 370, 1651

Chabrier, G. 2003, ApJ, 586, L133

Charbonnel, C., Meynet, G., Maeder, A., Schaller, G., & Schaerer, D. 1993, A&AS, 101, 415

Cicone, C., Maiolino, R., Sturm, E., et al. 2014, A&A, 562, A21

Cid Fernandes, R., González Delgado, R. M., García Benito, R., et al. 2014, A&A, 561, A130

Cid Fernandes, R., Gu, Q., Melnick, J., et al. 2004, MNRAS, 355, 273

Cid Fernandes, R., Mateus, A., Sodré, L., Stasińska, G., & Gomes, J. M. 2005, MNRAS, 358, 363

Cid Fernandes, R., Pérez, E., García Benito, R., et al. 2013, A&A, 557, A86

Cimatti, A., Brusa, M., Talia, M., et al. 2013, ApJ, 779, L13

Cimatti, A., Daddi, E., & Renzini, A. 2006, A&A, 453, L29

Conroy, C. 2013, ARA&A, 51, 393

Conroy, C., Gunn, J. E., & White, M. 2009, ApJ, 699, 486

Cooper, M. C., Newman, J. A., Croton, D. J., et al. 2006, MNRAS, 370, 198

Cortijo-Ferrero, C., González Delgado, R. M., Pérez, E., et al. 2017, MNRAS, 467, 3898

Cowie, L. L., Songaila, A., Hu, E. M., & Cohen, J. G. 1996, AJ, 112, 839

Croton, D. J., Springel, V., White, S. D. M., et al. 2006, MNRAS, 367, 864

Daddi, E., Cimatti, A., Renzini, A., et al. 2004, ApJ, 617, 746

Daddi, E., Dannerbauer, H., Stern, D., et al. 2009, ApJ, 694, 1517

Daddi, E., Dickinson, M., Morrison, G., et al. 2007, ApJ, 670, 156

Damen, M., Labbé, I., Franx, M., et al. 2009, ApJ, 690, 937

De Lucia, G., Springel, V., White, S. D. M., Croton, D., & Kauffmann, G. 2006, MNRAS, 366, 499

Dekel, A. & Birnboim, Y. 2006, MNRAS, 368, 2

Dressler, A., Kelson, D. D., Abramson, L. E., et al. 2016, ApJ, 833, 251

Dunne, L., Ivison, R. J., Maddox, S., et al. 2009, MNRAS, 394, 3

Elbaz, D., Daddi, E., Le Borgne, D., et al. 2007, A&A, 468, 33

Elbaz, D., Dickinson, M., Hwang, H. S., et al. 2011, A&A, 533, A119

Elmegreen, B. G., Bournaud, F., & Elmegreen, D. M. 2008, ApJ, 688, 67

Emsellem, E., Greusard, D., Combes, F., et al. 2001, A&A, 368, 52

Faber, S. M. 1972, A&A, 20, 361

Faber, S. M., Friel, E. D., Burstein, D., & Gaskell, C. M. 1985, ApJS, 57, 711

Faber, S. M., Willmer, C. N. A., Wolf, C., et al. 2007, ApJ, 665, 265

Fabian, A. C. 2012, ARA&A, 50, 455

Fagotto, F., Bressan, A., Bertelli, G., & Chiosi, C. 1994a, A&AS, 104

Fagotto, F., Bressan, A., Bertelli, G., & Chiosi, C. 1994b, A&AS, 105

Falcón-Barroso, J., Sánchez-Blázquez, P., Vazdekis, A., et al. 2011, A&A, 532, A95

Fardal, M. A., Katz, N., Weinberg, D. H., & Davé, R. 2007, MNRAS, 379, 985

Feulner, G., Gabasch, A., Salvato, M., et al. 2005, ApJ, 633, L9

Finlator, K., Davé, R., & Oppenheimer, B. D. 2007, MNRAS, 376, 1861

Foreman-Mackey, D., Hogg, D. W., Lang, D., & Goodman, J. 2013, PASP, 125, 306

Förster Schreiber, N. M., Shapley, A. E., Genzel, R., et al. 2011, ApJ, 739, 45

Fruchter, A. S. & Hook, R. N. 2002, PASP, 114, 144

Gallazzi, A., Brinchmann, J., Charlot, S., & White, S. D. M. 2008, MNRAS, 383, 1439

Gallazzi, A., Charlot, S., Brinchmann, J., White, S. D. M., & Tremonti, C. A. 2005, MNRAS, 362, 41

Ganda, K., Peletier, R. F., McDermid, R. M., et al. 2007, MNRAS, 380, 506

García-Benito, R., Zibetti, S., Sánchez, S. F., et al. 2015, A&A, 576, A135

Genzel, R., Burkert, A., Bouché, N., et al. 2008, ApJ, 687, 59

Girardi, L., Bressan, A., Chiosi, C., Bertelli, G., & Nasi, E. 1996, A&AS, 117, 113

Gladders, M. D., Oemler, A., Dressler, A., et al. 2013, ApJ, 770, 64

Gonçalves, T. S., Martin, D. C., Menéndez-Delmestre, K., Wyder, T. K., & Koekemoer, A. 2012, ApJ, 759, 67

González, V., Bouwens, R. J., Labbé, I., et al. 2012, ApJ, 755, 148

González Delgado, R. M., Cerviño, M., Martins, L. P., Leitherer, C., & Hauschildt, P. H. 2005, MNRAS, 357, 945

González Delgado, R. M. & Cid Fernandes, R. 2010, MNRAS, 403, 797

González Delgado, R. M., Cid Fernandes, R., García-Benito, R., et al. 2014a, ApJ, 791, L16

González Delgado, R. M., Cid Fernandes, R., Pérez, E., et al. 2016, A&A, 590, A44

González Delgado, R. M., Cid Fernandes, R., Pérez, E., et al. 2004, ApJ, 605, 127

González Delgado, R. M., García-Benito, R., Pérez, E., et al. 2015, A&A, 581, A103

González Delgado, R. M., Pérez, E., Cid Fernandes, R., et al. 2014b, A&A, 562, A47

Goodman, J. & Weare, J. 2010, Comm. App. Math. Comp. Sci, 5, 65

Gunawardhana, M. L. P., Hopkins, A. M., Bland-Hawthorn, J., et al. 2013, MNRAS, 433, 2764

Habing, H. J. 1995, Mem. Soc. Astron. Italiana, 66, 627

Habing, H. J. 1996, A&A Rev., 7, 97

Heavens, A. F., Jimenez, R., & Lahav, O. 2000, MNRAS, 317, 965

Hilz, M., Naab, T., & Ostriker, J. P. 2013, MNRAS, 429, 2924

Hopkins, A. M. & Beacom, J. F. 2006, ApJ, 651, 142

Hopkins, P. F., Bundy, K., Croton, D., et al. 2010, ApJ, 715, 202

Hubble, E. P. 1926, ApJ, 64

Hubble, E. P. 1936, Realm of the Nebulae

Husemann, B., Jahnke, K., Sánchez, S. F., et al. 2013, A&A, 549, A87

Johansson, P. H., Naab, T., & Ostriker, J. P. 2012, ApJ, 754, 115

Karim, A., Schinnerer, E., Martínez-Sansigre, A., et al. 2011, ApJ, 730, 61

Kauffmann, G., Heckman, T. M., De Lucia, G., et al. 2006, MNRAS, 367, 1394

Kauffmann, G., Heckman, T. M., White, S. D. M., et al. 2003, MNRAS, 341, 33

Kauffmann, G., White, S. D. M., & Guiderdoni, B. 1993, MNRAS, 264, 201

Kaviraj, S., Kirkby, L. A., Silk, J., & Sarzi, M. 2007a, MNRAS, 382, 960

Kaviraj, S., Rey, S.-C., Rich, R. M., Yoon, S.-J., & Yi, S. K. 2007b, MNRAS, 381, L74

Kelz, A., Verheijen, M. A. W., Roth, M. M., et al. 2006, PASP, 118, 129

Khochfar, S. & Silk, J. 2006, ApJ, 648, L21

Koleva, M., Prugniel, P., Bouchard, A., & Wu, Y. 2009, A&A, 501, 1269

Krajnović, D., Emsellem, E., Cappellari, M., et al. 2011, MNRAS, 414, 2923

Kroupa, P. 2001, MNRAS, 322, 231

Le Borgne, J.-F., Bruzual, G., Pelló, R., et al. 2003, A&A, 402, 433

Lee, K.-S., Ferguson, H. C., Wiklind, T., et al. 2012, ApJ, 752, 66

Lee, S.-K., Ferguson, H. C., Somerville, R. S., Wiklind, T., & Giavalisco, M. 2010, ApJ, 725, 1644

Lee, S.-K., Idzi, R., Ferguson, H. C., et al. 2009, ApJS, 184, 100

Leitherer, C. & Heckman, T. M. 1995, ApJS, 96, 9

Li, C. & White, S. D. M. 2009, MNRAS, 398, 2177

López Fernández, R., Cid Fernandes, R., González Delgado, R. M., et al. 2016, MNRAS, 458, 184

Madau, P. & Dickinson, M. 2014, ARA&A, 52, 415

Madgwick, D. S., Lahav, O., Baldry, I. K., et al. 2002, MNRAS, 333, 133

Magdis, G. E., Elbaz, D., Daddi, E., et al. 2010, ApJ, 714, 1740

Maraston, C. 1998, MNRAS, 300, 872

Maraston, C., Pforr, J., Renzini, A., et al. 2010, MNRAS, 407, 830

Martig, M., Bournaud, F., Teyssier, R., & Dekel, A. 2009, ApJ, 707, 250

Martin, D. C., Fanson, J., Schiminovich, D., et al. 2005, ApJ, 619, L1

Martin, D. C., Wyder, T. K., Schiminovich, D., et al. 2007, ApJS, 173, 342

Martins, L. P., González Delgado, R. M., Leitherer, C., Cerviño, M., & Hauschildt, P. 2005, MNRAS, 358, 49

McArthur, B. E., Endl, M., Cochran, W. D., et al. 2004, ApJ, 614, L81

Mendez, A. J., Coil, A. L., Lotz, J., et al. 2011, ApJ, 736, 110

Meurer, G. R., Heckman, T. M., & Calzetti, D. 1999, ApJ, 521, 64

Morrissey, P., Conrow, T., Barlow, T. A., et al. 2007, ApJS, 173, 682

Moustakas, J., Coil, A. L., Aird, J., et al. 2013, ApJ, 767, 50

Muñoz-Mateos, J. C., Gil de Paz, A., Boissier, S., et al. 2009, ApJ, 701, 1965

Naab, T., Khochfar, S., & Burkert, A. 2006, ApJ, 636, L81

Noeske, K. G., Weiner, B. J., Faber, S. M., et al. 2007, ApJ, 660, L43

Noll, S., Burgarella, D., Giovannoli, E., et al. 2009, A&A, 507, 1793

O'Connell, R. W. 1999, ARA&A, 37, 603

Ocvirk, P., Pichon, C., Lançon, A., & Thiébaut, E. 2006, MNRAS, 365, 74

Oemler, Jr., A., Dressler, A., Gladders, M. G., et al. 2013, ApJ, 770, 63

Oliver, S., Frost, M., Farrah, D., et al. 2010, MNRAS, 405, 2279

Oser, L., Ostriker, J. P., Naab, T., Johansson, P. H., & Burkert, A. 2010, ApJ, 725, 2312

Overzier, R. A., Heckman, T. M., Wang, J., et al. 2011, ApJ, 726, L7

Panter, B., Heavens, A. F., & Jimenez, R. 2003, MNRAS, 343, 1145

Papovich, C., Dickinson, M., & Ferguson, H. C. 2001, ApJ, 559, 620

Papovich, C., Finkelstein, S. L., Ferguson, H. C., Lotz, J. M., & Giavalisco, M. 2011, MNRAS, 412, 1123

Peebles, P. J. E. 1982, ApJ, 258, 415

Peng, Y.-j., Lilly, S. J., Kovač, K., et al. 2010, ApJ, 721, 193

Pérez, E., Cid Fernandes, R., González Delgado, R. M., et al. 2013, ApJ, 764, L1

Pérez-González, P. G., Rieke, G. H., Villar, V., et al. 2008, ApJ, 675, 234

Pforr, J., Maraston, C., & Tonini, C. 2012, MNRAS, 422, 3285

Pozzetti, L., Bolzonella, M., Lamareille, F., et al. 2007, A&A, 474, 443

Renzini, A. & Peng, Y.-j. 2015, ApJ, 801, L29

Rodighiero, G., Cimatti, A., Gruppioni, C., et al. 2010, A&A, 518, L25

Roth, M. M., Kelz, A., Fechner, T., et al. 2005, PASP, 117, 620

Salim, S., Rich, R. M., Charlot, S., et al. 2007, ApJS, 173, 267

Salpeter, E. E. 1955, ApJ, 121, 161

Sánchez, S. F., García-Benito, R., Zibetti, S., et al. 2016a, A&A, 594, A36

Sánchez, S. F., Kennicutt, R. C., Gil de Paz, A., et al. 2012, A&A, 538, A8

Sánchez, S. F., Pérez, E., Sánchez-Blázquez, P., et al. 2016b, RevMexAA, 52, 21

Sánchez-Blázquez, P., Peletier, R. F., Jiménez-Vicente, J., et al. 2006, MNRAS, 371, 703

Sandage, A. 1986, A&A, 161, 89

Schaerer, D., Charbonnel, C., Meynet, G., Maeder, A., & Schaller, G. 1993a, A&AS, 102, 339

Schaerer, D., Meynet, G., Maeder, A., & Schaller, G. 1993b, A&AS, 98, 523

Schawinski, K., Thomas, D., Sarzi, M., et al. 2007, MNRAS, 382, 1415

Schawinski, K., Urry, C. M., Lintott, C. J., et al. 2013, in American Astronomical Society Meeting Abstracts, Vol. 221, American Astronomical Society Meeting Abstracts #221, 225.06

Schawinski, K., Urry, C. M., Simmons, B. D., et al. 2014, MNRAS, 440, 889

Schawinski, K., Urry, C. M., Virani, S., et al. 2010, in IAU Symposium, Vol. 267, Co-Evolution of Central Black Holes and Galaxies, ed. B. M. Peterson, R. S. Somerville, & T. Storchi-Bergmann, 438–441

Schiminovich, D., Wyder, T. K., Martin, D. C., et al. 2007, ApJS, 173, 315

Schoenberner, D. 1983, ApJ, 272, 708

Searle, L., Sargent, W. L. W., & Bagnuolo, W. G. 1973, ApJ, 179, 427

Seibert, M., Martin, D. C., Heckman, T. M., et al. 2005, ApJ, 619, L55

Shapley, A. E., Steidel, C. C., Erb, D. K., et al. 2005, ApJ, 626, 698

Smit, R., Bouwens, R. J., Franx, M., et al. 2012, ApJ, 756, 14

Speagle, J. S., Steinhardt, C. L., Capak, P. L., & Silverman, J. D. 2014, ApJS, 214, 15

Stark, D. P., Ellis, R. S., Bunker, A., et al. 2009, ApJ, 697, 1493

Stark, D. P., Schenker, M. A., Ellis, R., et al. 2013, ApJ, 763, 129

Steinhardt, C. L., Speagle, J. S., Capak, P., et al. 2014, ApJ, 791, L25

Stoughton, C., Lupton, R. H., Bernardi, M., et al. 2002, AJ, 123, 485

Strateva, I., Ivezić, Ž., Knapp, G. R., et al. 2001, AJ, 122, 1861

Taylor, E. N., Hopkins, A. M., Baldry, I. K., et al. 2011, MNRAS, 418, 1587

Thomas, D., Maraston, C., & Bender, R. 2003, MNRAS, 339, 897

Tinsley, B. M. 1968, ApJ, 151, 547

Tinsley, B. M. 1978, ApJ, 222, 14

Tinsley, B. M. 1980, Fund. Cosmic Phys., 5, 287

Tojeiro, R., Heavens, A. F., Jimenez, R., & Panter, B. 2007, MNRAS, 381, 1252

Tojeiro, R., Wilkins, S., Heavens, A. F., Panter, B., & Jimenez, R. 2009, ApJS, 185, 1

Trager, S. C., Faber, S. M., Worthey, G., & González, J. J. 2000, AJ, 120, 165

Tremonti, C. A., Heckman, T. M., Kauffmann, G., et al. 2004, ApJ, 613, 898

Turnrose, B. E. 1976, ApJ, 210, 33

van den Bergh, S., Abraham, R. G., Ellis, R. S., et al. 1996, AJ, 112, 359

van Dokkum, P. G., Bezanson, R., van der Wel, A., et al. 2014, ApJ, 791, 45

Vassiliadis, E. & Wood, P. R. 1994, ApJS, 92, 125

Vazdekis, A. 1999, ApJ, 513, 224

Vazdekis, A., Coelho, P., Cassisi, S., et al. 2015, MNRAS, 449, 1177

Vazdekis, A., Sánchez-Blázquez, P., Falcón-Barroso, J., et al. 2010, MNRAS, 404, 1639

Walcher, C. J., Wisotzki, L., Bekeraité, S., et al. 2014, A&A, 569, A1

Walcher, J., Groves, B., Budavári, T., & Dale, D. 2011, Ap&SS, 331, 1

Willmer, C. N. A., Faber, S. M., Koo, D. C., et al. 2006, ApJ, 647, 853

Worthey, G. 1994, ApJS, 95, 107

Wuyts, S., Förster Schreiber, N. M., Lutz, D., et al. 2011, ApJ, 738, 106

Wyder, T. K., Martin, D. C., Schiminovich, D., et al. 2007, ApJS, 173, 293

Yi, S. K. 2003, ApJ, 582, 202

Yi, S. K., Peng, E., Ford, H., Kaviraj, S., & Yoon, S.-J. 2004, MNRAS, 349, 1493